Towards dedicated snow modelling in the Arctic that allows quantification of the impact of light absorbing impurities in snow

Auf dem Weg zu einer geeigneten Schneemodellierung in der Arktis, die eine Quantifizierung von lichtabsorbierenden Verunreinigungen im Schnee ermöglicht

Dissertation submitted by

Daniela Krampe

in partial fulfilment of the requirements for the degree of

Doctor of Natural Sciences (Dr. rer. Nat.)

to

Faculty 5

Geosciences

University of Bremen

Submission: 7 November 2022

Colloquium: 12 June 2023

Universität Bremen

ALFRED-WEGENER-INSTITUT
HELMHOLTZ-ZENTRUM FÜR POLAR- UND MEERESFORSCHUNG

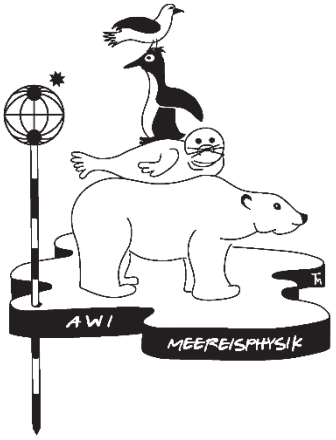

Subject Advisor: Dr. Frank Kauker and Dr. Andreas Herber
[Alfred Wegener Institute, Helmholtz Centre for Polar and Marine Research, Bremerhaven]

Supervisor: Prof. Dr. Olaf Eisen
[Alfred Wegener Institute, Helmholtz Centre for Polar and Marine Research, Bremerhaven]
[University of Bremen]

Second Reviewer: Prof. Dr. Marie Dumont
[Météo-France/CNRS, CNRM, Centre d'Etudes de la Neige /Snow Research Center, Grenoble]
[University of Grenoble Alpes]

The dissertation was written at the Sea Ice Physics section and Polar Meteorology section of the Alfred Wegener Institute, Helmholtz Centre for Polar and Marine Research, Bremerhaven.

Photo of a newly fallen snow crystal taken during MOSAiC (Multidisciplinary drifting Observatory for the Study of Arctic Climate) expedition, 14 February 2020 (Photo: Hannes Grische 2020).

"The world cannot live without the Arctic; it affects every living thing on Earth and acts as a virtual thermostat, reflecting sunlight and cooling the planet."

Philippe Cousteau, Jr.

Abstract

Snow is an important factor in the Earth System as it influences the global energy balance due to its high albedo. Light-absorbing impurities (LAI) in snow reduce its albedo, leading to enhanced absorption of shortwave radiation that warms the snowpack and stimulates feedback mechanisms that are partly responsible for faster warming of the Arctic than in any other part of the world. However, to date there is a lack of sufficient measurements to quantify the concentrations of LAI in Arctic snow, their seasonal evolution and trends. Therefore, it is difficult to investigate, quantify and understand the effects of LAI in snow on the evolution of snow properties, including the snow albedo, associated feedback mechanisms and the radiative forcing, especially in remote areas. To address this gap, models simulating the evolution of snow properties taken into account the effects of LAI on the radiative energy balance can be applied. However, reliable measurements to force these simulations, i.e. reliable deposition rates, are as well limited in time and space.

This dissertation has the ambitious goal to simulate reliably the impact of LAI on the radiative energy balance in snow. Several milestones had to be reached to achieve this goal. The first milestone was to find reliable forcing data for remote regions of the Arctic. The second milestone was to develop, for a snow model designed for application in the European Alps, fit-for-the-Arctic parameterisations that describe sufficiently well the evolution of snow properties. After reaching these milestones, the effects of LAI in snow, using exemplarily black carbon (BC), on the evolution of snow properties could be investigated. The analyses were performed at a site in northeast Greenland, using atmospheric in-situ and snow depth data from Villum Research Station (VRS) (2014 to 2018) together with additional snow measurements carried out during the Polar Airborne Measurements and Arctic Regional Climate Model Simulation Project (PAMARCMiP) campaign 2018, the modern global atmospheric reanalysis ERA5 and the regional atmospheric reanalysis CARRA-West, and the detailed snow model Crocus.

My results show that reanalyses are in principle able to represent prevailing atmospheric conditions, but suffer when resolving precipitation (amount and timing) and high wind speeds. Thereby, CARRA-West resolves small scale events and orography better than ERA5. When comparing CARRA-West and ERA5 forced simulations the performance vary from year to year. But overall, CARRA-West driven simulations perform slightly better than ERA5 driven simulations. Surprisingly, though, CARRA-West and ERA5 forced simulations agree better with snow measurements than simulations forced by atmospheric in-situ measurments.

In general, Crocus performs well with regard to snow depth evolution, while there are weaknesses in simulating vertical profiles of snow density and snow specific surface area (SSA). But, there are still shortcomings with respect to the simulation of snow depth. Snow depth decreases too rapidly in spring, possibly due to a combination of overestimated compaction and snow metamorphism formulations that are insufficient for Arctic conditions resulting in a too rapid decrease in SSA. This has implications for the simulation of snow albedo and hence the simulation of the effects of BC in snow. The study shows that the presence of BC reduces the surface snow albedo, which leads to a shortening of the snow season. Further effects are a decrease in snow depth and warmer ground temperatures. Efforts to improve model performance by introducing a new snow density parameterisation adapted to Arctic atmospheric conditions and modifications in a parameterisation influencing the upper snow density during strong wind events result in higher agreements between measured and simulated snow properties.

In conclusion, this dissertation substantially advances the understanding of the performance and sensitivity of the snow model Crocus in the Arctic, including knowledge gain on processes that are important in the Arctic. The results of this dissertation provide an improved understanding of the reasons for deviations between measured and simulated snow properties caused by the forcing data and model parameterisations. Thus, it provides a good basis for the design of future research studies and field campaigns to evolve further snow modelling in the Arctic. Reliable snow simulations in the Arctic are needed to analyse feedback mechanisms and processes leading to enhanced Arctic warming. Finally, this dissertation presents the prevailing BC concentrations in Greenlandic snow and demonstrates the effects different BC deposition rates have on the evolution of snow properties.

Zusammenfassung

Schnee ist ein wichtiger Faktor im Erdsystem, da er aufgrund seiner hohen Albedo die globale Energiebilanz beeinflusst. Durch lichtabsorbierende Verunreinigungen (LAI) wird die Albedo des Schnees verringert, wodurch mehr solare Einstrahlung absorbiert wird. Dadurch erwärmt sich die Schneedecke und es kommt zu Rückkopplungsmechanismen, die mit dazu beitragen, dass sich die Arktis schneller als jeder andere Teil der Welt erwärmt. Die vorhandenen Messungen sind jedoch nicht ausreichend, um die Konzentrationen von LAI, ihre jahreszeitliche Entwicklung und Trends zu quantifizieren. Daher ist es schwierig Auswirkungen von LAI im Schnee auf die Schneeeigenschaften, einschließlich der Schneealbedo, auf Rückkopplungsmechanismen und auf den Strahlungsantrieb zu quantifizieren und zu verstehen. Dies gilt insbesondere für abgelegene Gebiete. Um diese Lücke zu schließen, können Modelle eingesetzt werden, die die Entwicklung der Schneeeigenschaften unter Berücksichtigung der Auswirkungen von LAI im Schnee auf die Strahlungsenergiebilanz simulieren. Allerdings sind zuverlässige Messungen, die diese Simulationen antreiben wie z.B. zuverlässige Depositionsraten, zeitlich und räumlich begrenzt.

Diese Dissertation hat das ehrgeizige Ziel den Einfluss des LAI auf die Strahlungsenergiebilanz im Schnee zuverlässig zu simulieren. Um dieses Ziel zu erreichen, mussten mehrere Meilensteine erreicht werden. Der erste Meilenstein bestand darin verlässliche Antriebsdaten für abgelegene Regionen der Arktis zu finden. Der zweite Meilenstein betraf die Entwicklung von geeigneten Parametrisierungen, die die Entwicklung der Schneeeigenschaften für die Arktis unter Verwendung eines Schneemodells, das ursprünglich für die Anwendung in den europäischen Alpen konzipiert wurde, ausreichend gut beschreiben. Nach Erreichen dieser Meilensteine konnten die Auswirkungen der LAI im Schnee am Beispiel von schwarzem Kohlenstoff (BC) untersucht werden. Die Analysen wurden für einen Standort in Nordostgrönland durchgeführt, wobei in-situ Messungen von atmosphärischen Bedingungen und der Schneehöhe an der “Villum Research Station” (VRS) der Jahre 2014 bis 2018 verwendet wurden. Zusätzlich wurden Schneemessungen, die während der “Polar Airborne Measurements and Arctic Regional Climate Model Simulation Project” (PAMARCMiP) Kampagne 2018 durchgeführt wurden, sowie die moderne globale atmosphärische Reanalyse ERA5 und die regionale atmosphärische Reanalyse CARRA-West zusammen mit dem detailierten Schneemodell Crocus benutzt.

Meine Ergebnisse zeigen, dass Reanalysen prinzipiell in der Lage sind, die vorherrschenden atmosphärischen Bedingungen wiederzugeben, aber bei der Auflösung von Niederschlag (Menge und Zeitpunkt) sowie bei hohen Windgeschwindigkeiten Schwächen zeigen. Dabei löst CARRA-West kleinräumige Ereignisse und Orographie besser auf als ERA5. Beim Vergleich von Simulationen, die mit CARRA-West bzw. ERA5 angetrieben werden, variiert die Güte von Jahr zu Jahr. Insgesamt schneiden die Simulationen, die mit CARRA-West angetrieben werden, etwas besser ab als die Simulationen, die mit ERA5 angetrieben werden, Überraschenderweise stimmen die Simulationen, die mit CARRA-West und ERA5 angetrieben werden, besser mit Schneemessungen überein als Simulationen, die mit in-situ Messungen angetrieben werden.

Im Allgemeinen kann Crocus die Entwicklung der Schneehöhe gut simulieren, weist jedoch Schwächen bei der Simulierung von vertikalen Schneeprofilen der Dichte und der spezifischen Schneeoberfläche (SSA) auf. Es gibt aber auch Probleme bei der Simulation der Schneehöhe – die Schneehöhe nimmt im Frühjahr zu schnell ab. Dies liegt möglicherweise daran, dass für die Arktis ungeeignete Parametrisierungen zu einer zu hohen Schneeverdichtung und zu einer zu schnellen Schneemetamorphose führen. Dadurch nimmt die SSA zu schnell ab. Dies hat Auswirkungen auf die Simulation der Schneealbedo und damit auch auf die simulierten Effekte von BC im Schnee. Die Studie zeigt, dass BC die Oberflächenalbedo verringert, wodurch die Schneesaison verkürzt wird.

Zudem ist die Schneehöhe geringer und die Bodentemperatur ist höher. Anpasungen am Modell durch Einführung einer neuen, an die arktischen atmosphärischen Bedingungen angepassten Schneedichteparametrisierung und Änderungen von Parametrisierungen, die die obere Schneedichte bei Starkwindereignissen beeinflussen, führten zu einer höheren Übereinstimmung zwischen gemessenen und simulierten Schneeeigenschaften.

Diese Dissertation verbessert das Verständnis der Prozesse und der Sensitivität des Schneemodells Crocus in der Arktis erheblich, einschließlich des Erkenntnisgewinns über Prozesse, die in der Arktis wichtig sind. Die Ergebnisse dieser Dissertation ermöglichen ein besseres Verständnis, warum Abweichungen zwischen gemessenen und simulierten Schneeeigenschaften, die durch die Antriebsdaten und Modellparametrisierungen verursacht werden, bestehen. Damit bietet sie eine gute Grundlage für die Gestaltung zukünftiger Forschungsstudien und Feldkampagnen zur Weiterentwicklung der Schneemodellierung in der Arktis. Verlässliche Schneesimulationen in der Arktis sind notwendig, um Rückkopplungsmechanismen und Prozesse zu analysieren, die zu einer verstärkten Erwärmung der Arktis führen. Schließlich werden in dieser Dissertation die vorherrschenden BC Konzentrationen in grönländischem Schnee vorgestellt und die Auswirkungen möglicher Szenarien von BC Ablagerungsraten auf die Entwicklung der Schneeeigenschaften aufgezeigt.

Content

1 General introduction

1.1 Motivation: Arctic snow and its role in the earth's climate system

The Arctic is warming faster than any other part of the world (Bintanja and van der Linden, 2013). So far, not all of the interrelationships that lead to enhanced warming in the Arctic are fully understood and quantifiable (Bekryaev et al., 2010; Bintanja and van der Linden, 2013; Goosse et al., 2018; Wendisch et al., 2019). For many processes it is not yet clear how high their contribution to warming and thus to climate change actually is. These include the change in snow cover and the contribution of light-absorbing impurities in snow that reduce the albedo – the reflectivity – of the snow.

Snow during the boreal winter (winter on the Northern Hemisphere) covers about 14 % of the global land surface (Sturm et al., 1997; Domine et al., 2008). In addition, large parts of sea ice areas are covered with snow (Sturm et al., 1997). Thereby, seasonal snow covers the Arctic over several months (Liston and Hiemstra, 2011; Box et al., 2019; Lackner et al., 2022a) and undergoes strong temporal and spatial variations throughout the year (Cohen and Rind, 1991).

Snow consists mainly of ice crystals and air and is a porous medium (Domine et al., 2008). In addition, water vapour is part of snow (Sturm et al., 1997). Due to its composition, snow has a variety of special properties compared to other types of earth surfaces, for instance

- high albedo
- high emissivity
- low thermal conductivity and thus thermal insulation properties
- latent heat sink during melting

These properties change over the course of the year as snow undergoes different processes over time including snow metamorphism and redistribution by wind.

Further, snow acts as an interface between the atmosphere and the underlying ground. Thus, snow is of great importance for the earth's heat balance (Sturm et al., 1997) and there are many positive feedbacks within the climate system where snow is involved (Beniston, 2005; Brun et al., 2013). Despite their importance, we still lack a full understanding of the interactions between the Arctic snow cover and the atmosphere, hydrosphere and biosphere (see Figure 1.1) (Liston and Hiemstra, 2011).

In addition, there are also many other research areas and applications where snow plays an important role. For example, to analyse sea ice remote sensing reliable information about snow thickness and snow density is needed (King et al., 2020). Further, the distribution of plants is strongly connected to snow persistence (Rissanen et al., 2021). Snow also plays an important component in the study of vegetation composition and nutrient content of plants (Moriana-Armendariz et al., 2022) and in the research on fauna, as snow influences reproduction, predation, habitant selection, and migration of animals (Glass et al., 2021).

However, observations, models and reanalyses are not sufficient to provide a comprehensive picture of the Arctic that covers the full range of spatial and temporal variability, interactions and linkages of key processes (Liston and Hiemstra, 2011). Many snow characteristics, e.g., snow depth and snow water equivalent (SWE), are difficult to determine and with large uncertainties using for instance observations of satellite remote sensing to receive information (Sturm et al., 2010). Thus, due to short, incomplete and sometimes erroneous observation series that are limited in time and space, as well as uncertainties in the models and reanalyses, it is a challenge to expand the current understanding of the Arctic and its processes (Goosse et al., 2018; Przybylak and Wyszyński, 2020).

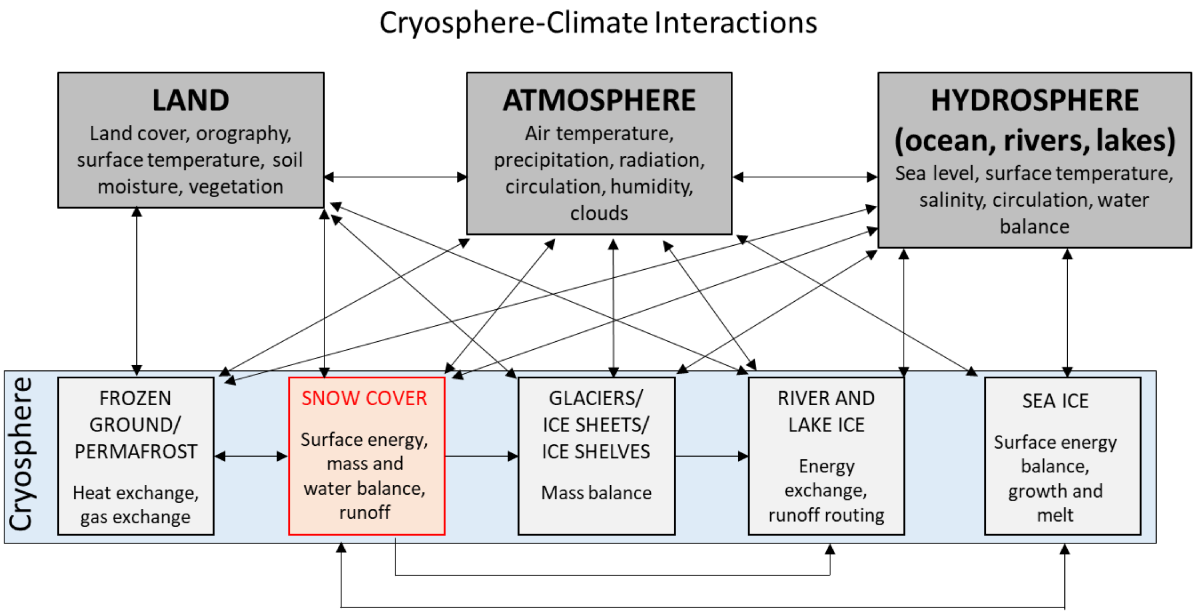

Figure 1.1: Schematic overview about some important cryosphere-climate interactions (modified after Armstrong and Brun (2008)).

1.2 Objectives and outline of this dissertation

This dissertation aims to expand our understanding of the role of snow in the coupled Arctic climate system. The focus is on the evaluation and on improvements of the snow model Crocus for processes in the Arctic. This is achieved by forcing the model with a set of different atmospheric datasets (reanalyses and in-situ measurements) in order to contribute to a comprehensive and complete time series of Arctic snow conditions throughout the year. The knowledge gained from the description of the full seasonal cycle helps to quantify reliably the influence of snow on global but also local scale in remote areas.

Finally, the outcome of the work will allow to estimate the impact of light absorbing impurities (LAI) using examplarily black carbon (BC) in the seasonal Arctic snow cover on the radiative energy balance, i.e., to quantify the contribution of these impurities on the radiative forcing. This topic becomes particularly relevant in respect to global warming and the resulting climate change. It is important to know the current implications of BC in snow, but also to predict the radiative forcing caused by LAI in the snow in the future, since, e.g., shipping traffic and thus exhaust gases are likely to increase with decreasing sea ice cover in the Arctic.

The research questions underlying the work of this dissertation are the following

R1: How do observed atmospheric conditions differ compared to a modern atmospheric reanalysis and connected to this how reliable are simulated snow properties in the Arctic?

In-situ observations, for atmospheric and snow quantities in the Arctic are often lacking a decent spatial and temporal coverage. In addition, reanalyses suffer from sparse coverage of observations to be assimilated and uncertain process formulations of the atmospheric model, especially in the Arctic. Furthermore, snow models are as well affected by inadequate or missing formulations of processes for polar applications, e.g., of metamorphism, blowing and drifting snow and vertical water vapour transport in the snowpack. All these factors introduce large uncertainties to the snow simulations.

Thus, in a first step, I investigate the differences in atmospheric variables, as e.g., air temperature and snowfall, between a widely used global reanalysis and in-situ observations to assess weaknesses and strengths in both datasets. In a next step, both datasets are used to force the detailed snow model Crocus,

developed for Alpine regions. The model output is compared to measurements of physical snow properties to evaluate the reliability of simulations of the Arctic snowpack. The study area is northeast Greenland.

R2: Can physical snow property simulation be improved by employing a local reanalysis having a higher spatial resolution than a global reanalysis?

Global reanalyses have a relative gross spatial resolution, e.g., 30 km. Thus, small scale atmospheric processes like local high wind speeds and local orography cannot be resolved. Local reanalyses having a much higher resolution, e.g., 2.5 km, should be able to describe these local atmospheric conditions better. As small scale events can have major effects on snow properties, simulations with higher resolved forcing data are expected to agree better with snow property measurements.

Thus, I analyse exemplarily the differences of atmospheric variables important for snow modelling between the widely used global and a newly introduced local reanalyses for the study site in northeast Greenland. This analysis is followed by the application of both reanalyses to force the snow model Crocus. Differences between the resulting simulated snow properties together with snow property measurements are evaluated.

R3: Can we improve Arctic snow modelling using a snow model developed for the European Alps by adapting the new snow density parametrisation and a parametrisation determining the effects of high wind speeds on upper snow layer density to Arctic conditions?

In the Arctic, it is colder and windier than in the European Alps. Thus, process formulations of the snow model Crocus have to be adapted to these Arctic conditions to receive reliable simulation of snow properties. For instance, Arctic atmospheric conditions lead to higher densities of newly fallen snow and the upper snow layers are stronger compacted by wind after deposition as observed in the European Alps. Thus, I introduce new parameterisations for calculating density of newly fallen snow, which are better suited for Arctic temperatures and I enhance the effect of strong wind on upper layer snow densities. Eventually, I compare the performance of these adapted parameterisations to measurements of the quantities but also to the performance of simulations with the default “European Alps” parameterisation.

R4: How high is the BC deposition rate in northeast Greenland and how do different BC deposition rates influence snow properties?

Finally, I used the developed “fit-for-the-Arctic-conditions” snow model Crocus for studies on BC in Arctic snow. BC in Arctic snow contributes to the warming of the Arctic by causing less incoming shortwave radiation to be reflected. This leads to a warming of the snowpack and associated feedback mechanisms. Therefore, BC in snow influences the global climate.

Here, I describe the prevailing conditions of BC at a site in northeast Greenland in spring 2018. I first present measured BC concentrations in surface snow and in vertical snow profiles. Then I apply the snow model Crocus to estimate deposition rates that fit best the measured BC concentrations in snow. Next, I use different increased deposition rates to determine the influence of possibly higher deposition rates in the future on snow properties.

Each research question R1 to R4 is analysed and answered in detail in Chapter 6 to Chapter 9, respectively. Figure 1.2 outlines the schematic overview of processes and methods studied in this dissertation, and presents a roadmap that outlines future research directions stimulated by the outcome of this work. Beginning with the default Crocus version that was developed for applications in the European Alps different adaptations were made to adapt the snow model to Arctic conditions. Thereby,

various parameterisations and thresholds were tested (marked in yellow) before some formulations were approved for adaptation (marked in orange). The middle panel "Crocus over Arctic bedrock" summarises the analyses performed. These analyses are prerequisite, before, in future, the snow model can be eventually coupled to a sea ice model (panel "Crocus over Arctic Sea ice MOSAiC"). For this and to evaluate the impact of BC on radiative forcing, the analyses performed in this dissertation, the MOSAiC data collection and lab analyses are required.

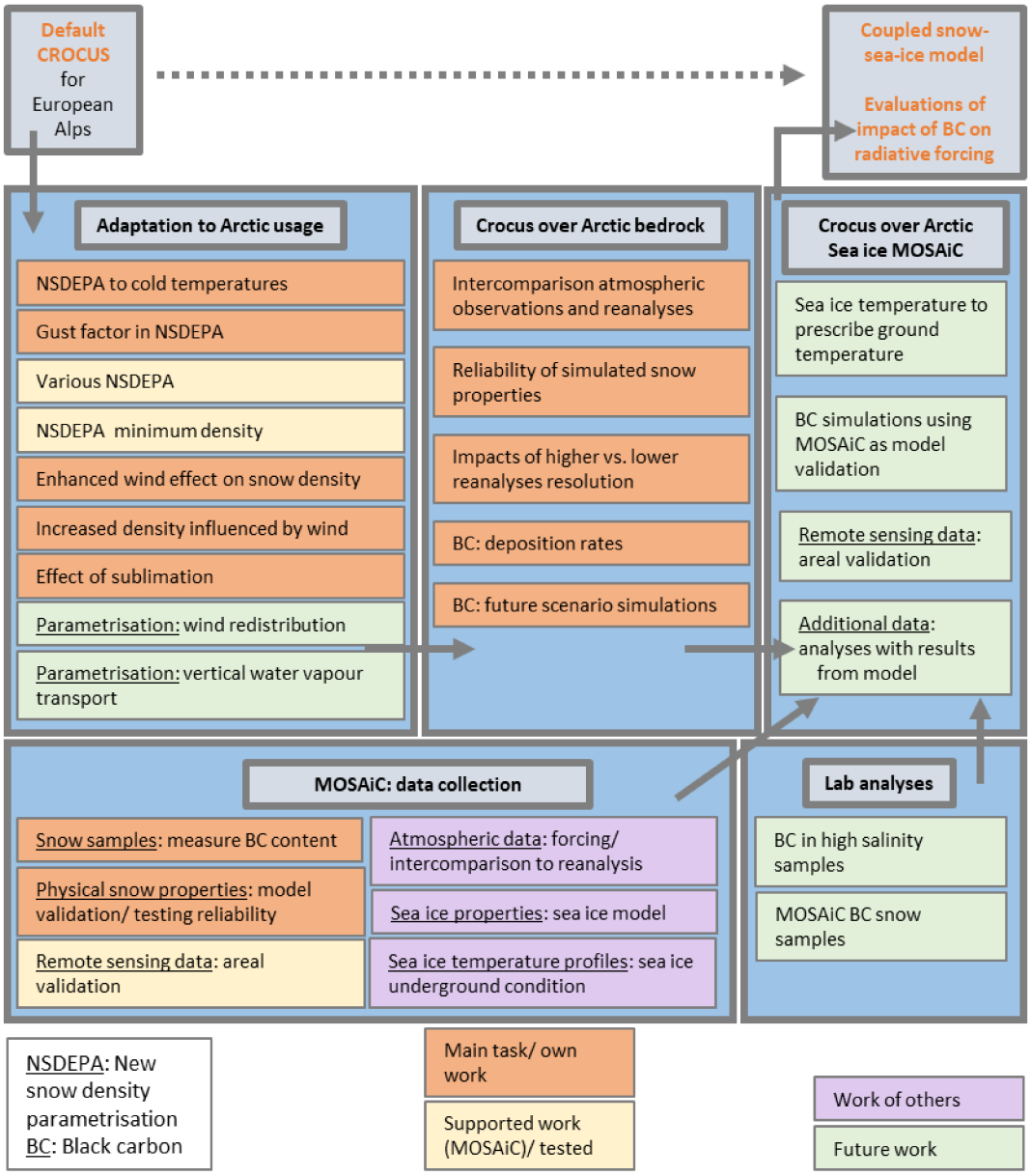

Figure 1.2: Schematic overview of processes and methods studied in this dissertation and outlines future research directions stimulated by the outcome of this dissertation (own drawing).

The structure of the dissertation is as follows

Chapter 2 discusses climate change in the Arctic, including feedback mechanisms and existing and projected changes in the Arctic climate. In particular, the changes and impacts of Arctic snow and the effects of black carbon particles in snow are addressed.

Chapter 3 introduces the most frequent form of solid precipitation - snow - and describes its importance for the global climate. Further, the spatial and temporal evolution of snow in the Arctic as well as the most important snow processes and physical properties for this dissertation are presented.

Chapter 4 gives an overview of the field measurements and instruments used to perform the studies in the dissertation. In addition, it presents the field campaign from which the data used were obtained.

Chapter 5 gives an overview of snow modelling before it presents the snow model Crocus and its usage in Polar Regions.

Chapter 6 addresses the first research question of this dissertation. This chapter has been submitted to the peer-reviewed journal Frontiers in Earth Science[1]. Parts of this chapter are published in The Cryosphere Discussion (https://doi.org/10.5194/tc-2021-100).

Chapter 7 deals with the second research question of the dissertation.

Chapter 8 deals with the third research question of the dissertation. Parts of this chapter are published in The Cryosphere Discussion (https://doi.org/10.5194/tc-2021-100).

Chapter 9 addresses the fourth research question of the dissertation.

Chapter 10 provides a summary of the key findings and limitations of this dissertation.

Chapter 11 gives suggestions for future research.

Remark: The Chapter 6 has been submitted and is written in collaboration with my co-authors and the Chapters 7, 8 and 9, are drafted journal articles. These Chapters are presented here in an unmodified form. Therefore, repetitions and inconsistences with the style of the rest of the dissertation are possible.

[1] After the submission of this dissertation, this manuscript has been published. The updated citation is Krampe D., Kauker F., Dumont M. and Herber A.: **Snow and meteorological conditions at Villum Research Station, Northeast Greenland: on the adequacy of using atmospheric reanalysis for detailed snow simulations.** Frontiers Earth Science, 11, https://doi.org/10.3389/feart.2023.1053918, 2023.

2 Climate change in the Arctic: An Overview

"The Earth is a fine place and worth fighting for."

Ernest Hemingway

The following subchapters describe recent and ongoing shifts due to climate change and the reasons for the enhanced temperature increase in the Arctic, before summarising the projected future climate change.

The increase in greenhouse gas concentration in the atmosphere is causing rising temperatures and climate change, which is already evident in many changes in the environment. The speed at which these changes are taking place is faster than ever before (Wendisch et al., 2017; Overland et al., 2019).

Carbon dioxide (CO_2), methane (CH_4) and nitrous oxide (N_2O) are important anthropogenic greenhouse gases. The increase in radiative forcing caused by these three greenhouse gases between 1750 and 2004 (254 years) was 2.2 W m^{-2}, compared to an increase of 2.3 W m^{-2} during the last glacial-interglacial transition lasting for 6000 years (Joos and Spahni, 2008). Anthropogenic CO_2 has increased and is likely to continue its trend, leading to additional global forcing (Overland et al., 2019). Thereby, atmospheric CO_2 concentration in 1750 was approximately 277 parts per million (ppm) (Joos and Spahni, 2008) and increased to 417.81 ppm in February 2022 (Dlugokencky and Tans, 2022).

There are different emission scenarios for simulating future climate, including scenarios in which emissions are reduced in the atmosphere (Overland et al., 2019). However, in all scenarios, including those with reduced emissions, many ongoing processes caused by rising temperatures, such as the melting of the Greenland ice sheet and sea level rise, are simulated for a certain period of time as a delayed response to the prevailing climate circumstance (Mudryk et al., 2018; Overland et al., 2019).

The effects of climate change are already clearly visible in the Arctic (Wendisch et al., 2017; Mudryk et al., 2018; Overland et al., 2019). The climate in the Arctic is unlike anything ever observed before. Some of the changes taking place in the Arctic are irreversible, such as the release of CH_4 stored in thawing permafrost (Overland et al., 2019).

Furthermore, there is indication that changes in the Arctic also affect the climate at low- and mid-latitudes through changes in atmospheric and oceanic circulation patterns (Wendisch et al., 2017; Mudryk et al., 2018; Overland et al., 2019). As a result of climate change, the temperature of the lower atmosphere is increasing, causing a decrease in air density and thus a lower pressure gradient between the Polar Regions and the lower latitudes. This impacts atmospheric circulation patterns, including the jet stream (Overland et al., 2019). The exact impacts on the climate in the lower latitudes are still an ongoing research topic (Wendisch et al., 2017; Mudryk et al., 2018; Overland et al., 2019; Wendisch et al., 2019). In addition to changes in atmospheric circulation patterns, changes in oceanic circulation pattern are also observed, e.g., the North Atlantic Oscillation and the Arctic Oscillation, causing, e.g., warmer winters over Eurasia (Chapin et al., 2005).

Seasonal temperature and precipitation patterns will change due to climate change. The effects will be most apparent in the transitional seasons of spring and autumn (Ernakovich et al., 2014). Snow cover is closely linked to temperature and precipitation (Matiu et al., 2021). Therefore, due to climate change, important factors that determine snow metamorphism and thus snow albedo, including air temperature and the temperature gradient between the snow surface and the ground, will change, possibly causing further feedbacks (Domine et al., 2006a).

Further, Box et al. (2019) found evidence of more moisture in the atmosphere, higher precipitation rates, increased river runoff, higher altitudes of glacier equilibrium lines and increased land ice melt from 1971 to 2017. In addition, sea ice thickness and cover have decreased, and snow melts earlier in spring resulting in a shorter period of snow cover in the Arctic (Mudryk et al., 2018; Box et al., 2019).

2.1 Recent and ongoing climate changes

Temperature

In the Arctic, surface air temperatures increased by +1.36°C century^{-1} over the period 1875 – 2008 (Bekryaev et al., 2010), about twice as much as in the Northern Hemisphere with +0.79°C century^{-1} (Bekryaev et al., 2010; Goosse et al., 2018; Przybylak and Wyszyński, 2020; Walsh, 2021) (see Table 2.1 for further studies and Figure 2.1). This stronger warming of the Arctic is called "Arctic Amplification" (Bekryaev et al., 2010; Wendisch et al., 2017; Przybylak and Wyszyński, 2020; Walsh, 2021; Rantanen et al., 2022) and is thought to be caused by positive feedbacks (Bekryaev et al., 2010; Overland et al., 2014; Pithan and Mauritsen, 2014) further described in subchapter 2.2.

Table 2.1: Surface air temperature warming in the Arctic.

Region	Period	Annual warming	Seasonal warming	Reference
Arctic	1875 - 2008	(+1.36°C century^{-1})	-	Bekryaev et al. (2010)
High Arctic[1]	1996 – 2015 relative to the reference period 1951 – 1990	+1°C	most increase in autumn (+1.9°C) and winter (+1.7°C), least increase during summer (+0.9°C)	Przybylak and Wyszyński (2020)
Marine Arctic[2]	1998 - 2018	-	warmer average surface air temperatures for the marine Arctic for winter (DJF) and summer (JJA)	Alekseev et al. (2020)
Arctic (>60°N)	1971 - 2017	+2.7°C (+0.6°C decade^{-1})	increase was stronger during the cold season (October – May) (3.1°C, 0.7°C/ decade) than in the warm season (June – September) (1.8°C, 0.4°C/ decade)	Box et al. (2019)
positive air temperature trends for 99 % of the Arctic (~>55°N)	1979 – 2009	(+0.38°C decade^{-1})	-	Liston and Hiemstra (2011)

[1]: The region of the High Arctic with the stations used is shown in Figure 1 in Przybylak and Wyszyński (2020).
[2]: Marine Arctic refers to the analyses of data from 41 stations (see Figure 1b in (Alekseev et al., 2020)) on islands and at the coast of the Arctic Ocean as well as adjacent seas.

The strength of the Arctic Amplification differs between studies due to different regions used for calculation and different periods of concern. Box et al. (2019) found most pronounced Arctic Amplification during the cold months (October – May) with warming that was 2.8 times the Northern Hemisphere warming for the period 1971 – 2017. Annually Arctic Amplification was 2.4 and for the warm season (June – September) Arctic Amplification was 1.7 (Box et al., 2019). For the period 1989 – 2018, Alekseev et al. (2020) found an annual Arctic Amplification of 2.91 (4.26 winter, 2.28 spring, 1.43 summer, 3.25 autumn) compared to the Northern Hemisphere and 4.32 (6.76 winter, 3.22 spring, 2.10 summer, 4.74 autumn) compared to global warming of surface air temperatures. Considering only the marine Arctic, Arctic Amplification is even higher (annual Northern Hemisphere 4.05, annual globe 6.02) (Alekseev et al., 2020). A recent study by Rantanen et al. (2022) found evidence of Arctic warming almost four times as high the global warming for the period from 1979 to 2021. Overall, the stronger increase in air temperatures of the Arctic compared to the Northern

Hemisphere or the globe was confirmed by many studies (e.g., Bekryaev et al., 2010; Box et al., 2019; Alekseev et al., 2020).

Until 2010, the warmest years observed in the northern polar region were 2003, 2005 and 2007 with mean annual temperatures of +1.72°C, +2.11°C and +2.18°C, respectively. These years coincide with the minimum sea ice extents (Bekryaev et al., 2010). However, the ten warmest years in the Arctic between 1900 and 2022 all occurred since 2011. This included 2021/2022 (October to September) being the sixth warmest year in the Arctic, with surface temperatures 0.73°C warmer than the 1991 – 2020 average (Ballinger et al., 2022). Thereby, winter temperatures in the Arctic have increased more than summer temperatures (see also Table 2.1) (Pithan and Mauritsen, 2014; Box et al., 2019; Przybylak and Wyszyński, 2020). However, there is regional variability in trends, e.g., caused by natural climate processes such as modes of atmospheric and oceanic circulation (Mudryk et al., 2018).

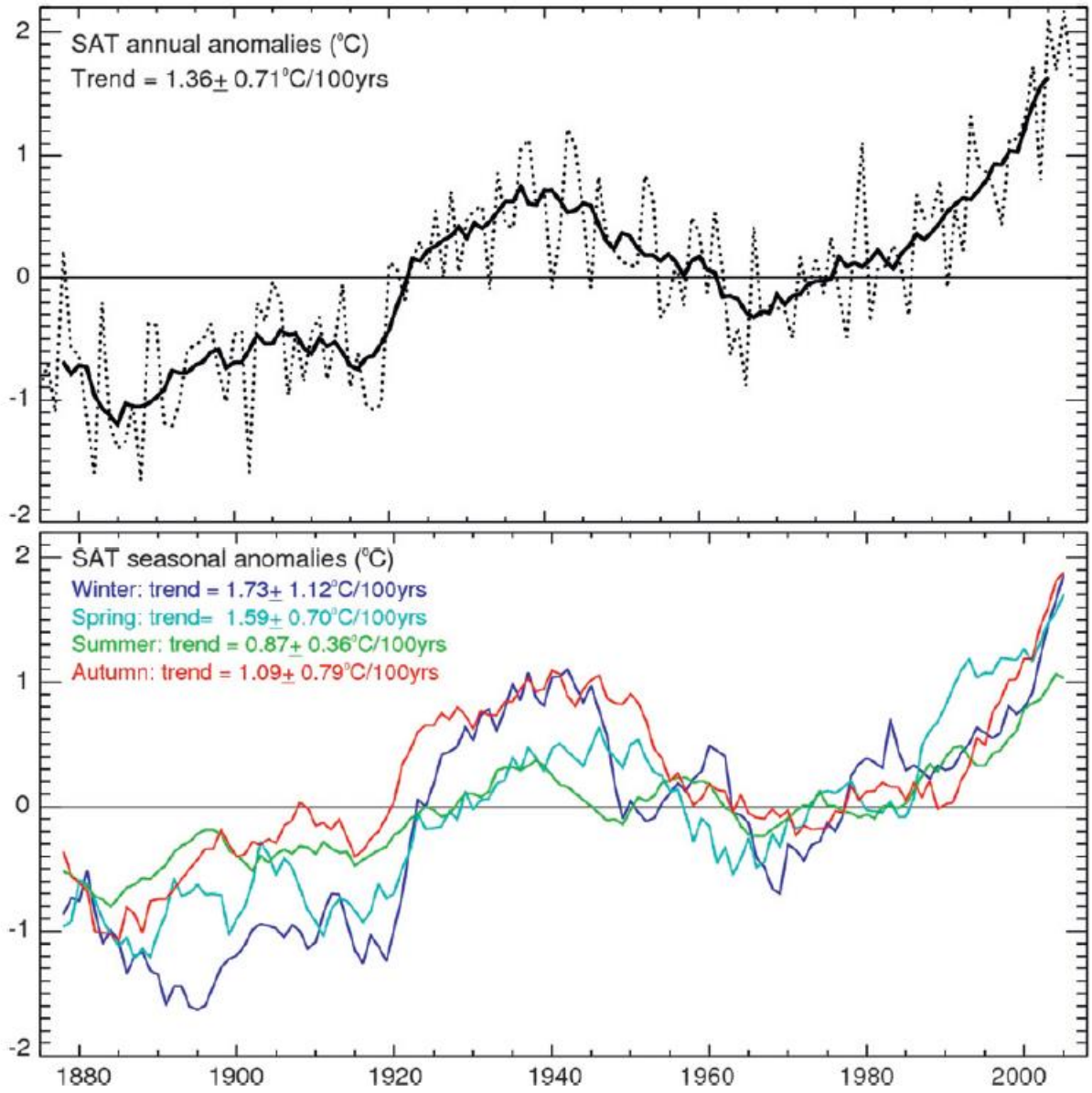

Figure 2.1: Annual and seasonal surface air temperature anomalies for the region north of 59°N. The dotted line shows unsmoothed values. The solid line shows a seven years running mean. Trends are for 1900 - 2008 (figure from Bekryaev et al., 2010).

Precipitation

Uncertainties regarding precipitation trends in the Arctic are large. However, Box et al. (2019) found increasing precipitation from 1971 to 2017 for areas north of 50°N. Here, the increase is higher for October to May (+6.8 %, increase of the eight months average by 225 mm) than for June to September (+4.7 %, increase of 168 mm on average over all four months). Between 1971 and 2017, annual precipitation in the Arctic (>60°N) increased by 6.2 % (1.3 % decade^{-1}) (Box et al., 2019).

Sea ice

Studies show a decrease in sea ice extent in recent years (Bintanja and van der Linden, 2013; Goosse et al., 2018; Mudryk et al., 2018). Thereby, the decline is greatest in late summer, but observed for all months of the year (Goosse et al., 2018).

Since 2007, minimum sea ice extent in September - using the National Snow and Ice Data Center (NSIDC) monthly sea ice index (Fetterer et al., 2017) - has been lower than since 1979, when satellite observations began. In 2009 – 2018, the observed decadal mean of sea ice minimum extent in September was 4.7 million km^2, which was 2.4 million km^2 (-31 %) less than in 1979 – 1988 (Landrum and Holland, 2020). The minimum summer sea ice extent was measured in 2012 (3.27 million km^2). Furthermore, the ten lowest summer sea ice extents since 1979 were observed between 2007 and 2020 (lowest extents in 2007, 2008, 2010 - 2012, 2015, 2016, 2018 - 2020) (Spreen et al., 2008 with actual time series data of the northern hemisphere until end of 2021 available at https://seaice.uni-bremen.de/data/amsr2/today/extent_n_19720101-20211231_amsr2.txt).

Further, the sea ice regime is shifting from thick multiyear sea ice towards thinner first year sea ice (Mudryk et al., 2018; Overland et al., 2019 and references therein). The amount of multiyear ice is 60 % lower than in the 1980s (Overland et al., 2019 and references therein).

2.2 Causes of Arctic Amplification

Multiple feedbacks between the atmosphere, land surfaces, the ocean and sea ice area cause the Arctic Amplification (Bekryaev et al., 2010; Goosse et al., 2018; Przybylak and Wyszyński, 2020; Walsh, 2021). To date, not all feedbacks and their relationships and respective contributions to climate change are fully understood (Overland et al., 2019; Wendisch et al., 2019). Therefore, the individual contributions of the various feedbacks are still controversial (e.g., Pithan and Mauritsen, 2014; Overland et al., 2019). Figure 2.2 provides the estimated radiative forcing caused by a number of feedbacks, some of which are described further below.

Some of the feedbacks causing the Arctic Amplification are the following

1) **snow/ice/surface-albedo feedback**
   (e.g., Chapin et al., 2005; Bekryaev et al., 2010; Goosse et al., 2018; Landrum and Holland, 2020)

   Melting of snow and ice leads to a reduction in the albedo of snow and ice (see Figure 3.1). Moreover, the underlying surfaces are exposed, having a much lower albedo and therefore absorbing more shortwave radiation and thus more energy than snow and ice (Goosse et al., 2018; Landrum and Holland, 2020). As a result, e.g., surface water of the ocean warms so that more heat is released into the atmosphere in autumn and thus sea ice formation begins later (Landrum and Holland, 2020). The effect of the snow-albedo feedback on the snow cover extent are strongest in spring (Hernández-Henríquez et al., 2015).

Arctic Amplification is also strongly related to sea ice melt. The extent of sea ice determines the surface albedo for large parts of the Arctic, as open water has a lower albedo than sea ice (see Figure 3.1). This influences the timing, magnitude and spatial pattern of warming during the time when the sun is above the horizon (Bekryaev et al., 2010).

2) longwave radiation feedback
(Chapin et al., 2005; e.g., Bekryaev et al., 2010; Bintanja and van der Linden, 2013; Alekseev et al., 2020; Landrum and Holland, 2020)

Both sea ice and snow insulate the underlying ocean or ground and prevent heat exchange between the underlying layers and the atmosphere. The thicker the sea ice or the snowpack, the higher is the insulating effect. Therefore, in winter, sea ice prevents heat release from the relative warm ocean towards the relative cold atmosphere (Bekryaev et al., 2010; Landrum and Holland, 2020). In this process, the extent of the sea ice is also of importance (Bekryaev et al., 2010).

The melting of sea ice leads to enhanced exposure of open water and thus to enhanced longwave and turbulent upward fluxes that increase the temperature of the atmosphere (Chapin et al., 2005; Bintanja and van der Linden, 2013). Enhanced atmospheric humidity, which increases longwave radiation, is also due to the melting of snow and ice, in addition to greater open water area (see also description of water vapour feedback) (Alekseev et al., 2020).

3) water vapour feedback
(e.g., Bintanja and van der Linden, 2013; Goosse et al., 2018; Walsh, 2021)

An increase in open water area also leads to an increase in evaporation and thus an increase in moisture with a maximum in autumn (Bintanja and van der Linden, 2013; Goosse et al., 2018; Walsh, 2021). In addition, enhanced latent heat transport towards the Arctic causes higher moisture (Bintanja and van der Linden, 2013; Walsh, 2021). Thereby, a warmer atmosphere is able to hold more moisture than a colder atmosphere. Since water vapour is a strong greenhouse gas, additional warming is introduced (Goosse et al., 2018; Walsh, 2021). More water in the atmosphere also means more clouds and an increase in downward longwave radiation (Bintanja and van der Linden, 2013; Walsh, 2021).

4) increased oceanic heat transport
(e.g., Bintanja and van der Linden, 2013; Goosse et al., 2018; Walsh, 2021)

Due to global warming, less heat is transported via the ocean currents from the Arctic towards the lower latitudes but more heat is transported towards the Arctic (Goosse et al., 2018; Walsh, 2021).

5) temperature feedback
(e.g., Pithan and Mauritsen, 2014)

Due to warmer temperatures, outgoing longwave radiation at the top of the atmosphere is increased, leading to heat loss (Pithan and Mauritsen, 2014).

6) Planck feedback
(e.g., Pithan and Mauritsen, 2014)

The higher the surface temperature, the more longwave radiation is emitted. This means that a forcing of, e.g., 1 W m^{-2} for a -30°C cold surface results in 0.31°C warming while it results in 0.16°C warming when the surface is 30°C warm. Thus, to balance external forcing the temperatures in the Arctic has to increase stronger than in other regions (Pithan and Mauritsen, 2014).

Further feedbacks not described in this work but elsewhere are, e.g., the transport of energy in the atmosphere (e.g., Bintanja and van der Linden, 2013; Goosse et al., 2018), increased amount of waves in the ocean, changes in wind pattern (e.g. Serreze et al., 1993), the release of methane (thawing of permafrost), the cloud feedback (e.g., Wendisch et al., 2019), the lapse rate feedback (e.g., Pithan and Mauritsen, 2014) and increased fresh water supply into the Arctic Basin (e.g., Box et al., 2019 and references therein).

There is evidence that the surface albedo feedback is one of the main drivers of Arctic Amplification (Pithan and Mauritsen, 2014). Changes in Arctic summer albedo are an important factor controlling high-latitude warming in recent years. Albedo decreases, e.g., due to shorter snow cover seasons and causes an increase in local warming of 3 W m^{-2} $decade^{-1}$, corresponding to a forcing caused by a doubling of CO_2 emissions. Apart from snow and sea ice melt, albedo changes are caused by vegetation changes in the Arctic, e.g., further northward migration of trees (Chapin et al., 2005). Another main driver of Arctic Amplification is the decrease in sea ice concentration and thickness, as it generates feedback mechanisms and affect atmospheric conditions in autumn and winter (Landrum and Holland, 2020).

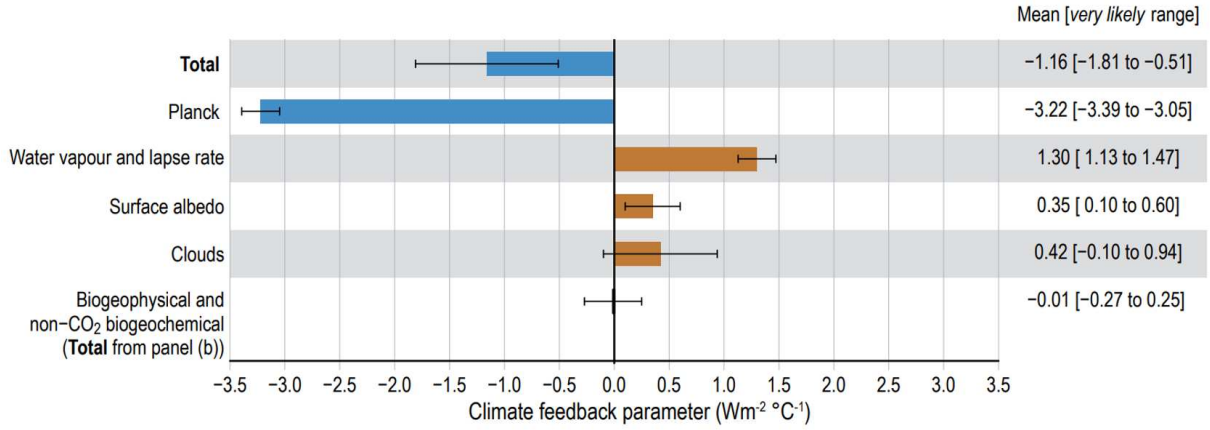

Figure 2.2: Estimates contribution of different feedback mechanisms on global temperature. Displayed are the mean feedback values (bars) and very likely ranges (uncertainty bar) (modified after Arias et al., 2021).

Alekseev et al. (2020) found that the Arctic winter warming is mainly controlled by enhanced atmospheric heat and moisture transport from the North Atlantic with additional oceanic heat transport towards the Norwegian and Barents seas. This is in line with the description by Box et al. (2019), naming the enhanced moisture in the Arctic and the delayed onset of sea ice growth in the Arctic as the main reasons for the highest temperature increase occurring in autumn and winter.

In this context, there are observations showing increasing surface and mid-tropospheric humidity from 1971 to 2017 through enhanced moisture transport from low latitudes to the Arctic and a longer period of open water area in the Arctic Ocean due to a delayed onset of sea ice formation. Also, an enhanced occurrence of low clouds was observed from June to September (Box et al., 2019 and references therein).

Further, warm air intrusions are observed in winter (Overland et al., 2019) and the ocean loses heat to the atmosphere (Pithan and Mauritsen, 2014). As sea ice melts, there is an increased upwards heat flux between the ocean and the atmosphere (Bekryaev et al., 2010).

Overall, winter warming is determined by the retreat of sea ice and associated feedbacks. The ice-albedo-feedback is responsible for about 25 % of winter warming, while the longwave radiation feedback causes about 75 % of the warming (Bintanja and van der Linden, 2013). In summer, the temperature increase is mainly controlled by additional radiative heat inputs to the surface energy balance, including the surplus due to the longwave radiation feedback (Alekseev et al., 2020). Changes due to climate warming will also affect the Arctic ecosystem, as there are numerous feedbacks, e.g., between temperature changes, the start of the growing season, flora and fauna (Ernakovich et al., 2014).

2.3 Future climate change

Representative concentration pathway (RCP) scenarios, called Shared Socio-economic Pathway (SSP) in the IPCC report currently worked on (Arias et al., 2021), describe a hypothetical future taking into account potential socioeconomic and technologic developments, energy and land use, greenhouse gases emissions and air pollutions. Four different RCP scenarios were defined: RCP 2.6, RCP 4.5, RCP 6.0 and RCP 8.5. The number stands for the additional radiative forcing, e.g., 8.5 W m^{-2} by 2100 (IPCC, 2014; Overland et al., 2014). The RCP 8.5 scenario, for example, is close to the current emissions, while the RCP 2.6 scenario requires removal of emissions from the atmosphere (Overland et al., 2014; Bintanja and Andry, 2017; Walsh, 2021).

Projected temperature

There is strong evidence that temperatures will increase considerably by the end of the 21st century (e.g., Ernakovich et al., 2014). All scenarios, including moderate mitigation scenarios, project further warming of the Arctic (Walsh, 2021). The projected air temperature under the different emission scenarios only becomes substantially different from about 2050 onwards (Overland et al., 2019).

For the RCP 8.5 scenario, a mean annual warming of 10°C is projected for areas north of 60°N until 2100, while for the RCP 2.6 scenario the projected warming is between 3 and 4°C. Considerable differences between the projected warming of both scenarios are visible, especially from mid-century onwards, meaning a future warming of the Arctic even under moderate conditions (Walsh, 2021). For ocean and land areas north of 70°N, projections show an increase in annual mean surface air temperatures of 8.5±2.1°C until 2100 using the RCP 8.5 scenario (Bintanja and Andry, 2017).

Using the Coupled Model Intercomparison Project 5 (CMIP5) class Multi-Model Large Ensemble (MMLE) Archive together with the RCP 8.5 scenario, Landrum and Holland (2020) found a stronger mean warming of the Arctic Ocean (12 – 28°C) than of the Arctic land masses (5 – 12°C) until 2100. Temperature rise in late autumn is projected to be +13°C by 2100 under the RCP 8.5 scenario and +7°C under the RCP 4.5 scenario in the Arctic. Spring temperatures are projected to be +5°C and +3°C warmer, respectively (Overland et al., 2014).

Projected precipitation

The warming of the atmosphere also causes changes in precipitation. Precipitation itself is influenced by “air temperature, surface fluxes, moisture advection, cloud microphysical processes, stability and orographic lifting of air masses” (Hernández-Henríquez et al., 2015).

In terms of precipitation projections there is a clear signal towards higher precipitation rates in the Arctic (Hernández-Henríquez et al., 2015; Bintanja and Andry, 2017; Walsh, 2021). This is in line with a warmer and more humid climate due to sea ice retreat, causing more open ocean water area in addition to enhanced transport of moisture from lower latitudes (Bintanja and Andry, 2017 and references therein; Walsh, 2021).

Under the RCP 8.5 scenario, precipitation is projected to increase by more than 20 % for subarctic land areas and by more than 40 % for the Arctic Ocean by 2100 (Walsh, 2021). Projected precipitation shows increasing precipitation rates of 50 % - 60 % by the end of the 21st century using CMIP5 models with the RCP 8.5 scenario (Bintanja and Andry, 2017).

Climate change is also altering the precipitation phase in the Arctic towards more liquid and less solid precipitation with drastic consequences for the "[…] energy balance, hydrological cycles and management, and ecology [..]" (Landrum and Holland, 2020 and references therein). The precipitation phase affects, e.g., river discharge, melting, surface albedo and the water and food supply (Bintanja and Andry, 2017 and references therein).

Snowfall decreased for 64 % of the Arctic area between 1979 and 2009 ranging from -3.03 cm decade^{-1} to +8.00 cm decade^{-1}, with a mean of -0.02 cm decade^{-1}. In general, snowfall fraction was 47 % of total Arctic precipitation between 1979 and 2009, with an overall decrease of 0.78 % decade^{-1}, ranging regionally from -5.41 % to +2.53 % (Liston and Hiemstra, 2011). Today, most precipitation north of 70°N falls as snow (65±5 %) (Bintanja and Andry, 2017).

Bintanja and Andry (2017) found that less precipitation than today will fall as snow even with increasing precipitation until 2100 for areas between 70° – 90°N. Due to increasing temperatures, a dominant part of the snowfall melts before it falls on the ground. The greatest shift towards increasing rainfall is projected for summer and autumn, as air temperatures are close to the melting point. But winter rainfall is also likely to increase (Bintanja and Andry, 2017).

Landrum and Holland (2020) found that until 2100 precipitation may fall as rain throughout the entire year in some areas of the Arctic under the RCP 8.5 scenario. In general, the snowfall season will be reduced by 2 – 4 months depending on the region (Landrum and Holland, 2020).

Projections indicate a rainfall fraction of 60 % until 2100 under the RCP 8.5 scenario, making liquid precipitation the predominate precipitation phase in the Arctic. In addition, under the RCP 4.5 scenario, rainfall fraction is projected to be higher than snowfall fraction by 2100. Thus, by the end of the 21st century, rain is likely to be the dominant precipitation phase in the Arctic (Bintanja and Andry, 2017).

Projected sea ice conditions

Projections for the future extent of Arctic sea ice, e.g., in summer, differ widely. There are models that predict a sea ice free ocean in summer already for the next decades, while other models still see some summer sea ice until the end of this century. This wide range reflects existing weaknesses of today's climate models in appropriately parametrising the processes that affect Arctic sea ice (Overland et al., 2014; Overland et al., 2019)

However, under the RCP 8.5 scenario, the fraction of thin sea ice in the central Arctic basin increases by more than 40 % until 2100. Since thin sea ice prevents less heat release from the warmer ocean towards the colder atmosphere than thick sea ice, the energy exchanges between the ocean and the atmosphere increases (Landrum and Holland, 2020).

3 Snow

3.1 Importance of snow in the Arctic

> *"Snowflakes are one of the nature's most fragile things,*
> *but just look what they can do when they stick together."*
>
> *Verna M. Kelly*

Snow covers the ground in the Arctic for a long period of the year. In this context, the time that the Arctic is covered with snow ranges from 219±50 days per year (Liston and Hiemstra, 2011) to at least half a year (Lackner et al., 2022a) to up to ten months (Mudryk et al., 2018; Box et al., 2019 and references therein).

However, snow cover and its properties are subject to strong temporal and spatial variations, stronger than any other changing surface conditions (see Chapter 3.2.2 and 3.2.3) (Cohen and Rind, 1991; Mudryk et al., 2018). Thereby, snow cover plays an important role in the global climate system, as it is part of climate feedbacks. Further snow is an important component in the Arctic hydrology and ecosystem (Mohammadzadeh Khani et al., 2022).

Due to its physical properties, snow has an enormous impact on the energy balance, the growing and melting of sea ice, and on flora and fauna, among others (Cohen and Rind, 1991; Liston and Hiemstra, 2011; Mudryk et al., 2018; Box et al., 2019 and references therein). The timing and duration of Arctic snow cover and snow properties play a major role in the global climate and global climate change with implications for physical and biological components and the economy (Liston and Hiemstra, 2011; Mudryk et al., 2018).

In the following, the links between snow and the water balance as well as impacts on the climate are briefly described. Next, a more detailed description of two important properties of snow, namely its high insulation and its high albedo, is given. As albedo is of great importance in the further course of this dissertation, it is described in more detail.

a) **water balance**

   Most precipitation in the High Arctic falls as snow, making snow to a main cryospheric feature of the region. Snow cover spans over all surfaces, from land to sea, lake and river ice (Mohammadzadeh Khani et al., 2022). Thereby, the amount of falling snow plays a crucial role for the catchment water balance. Snow acts as a water storage of freshwater during the Arctic winter. During the melt period in spring, water is released with a delay to the actual precipitation events. Therefore, snow influences the timing and magnitude of meltwater (Pomeroy et al., 2004; Liston and Hiemstra, 2011; Box et al., 2019 and references therein).

b) **some climatic impacts**

   There are indications that snow cover can reduce sea level pressure by up to 11 hPa and near surface air temperatures. The high albedo of snow leads to less shortwave radiation being absorbed (see description below), and latent heat is used during the melting of snow (latent heat of fusion for ice: 3.34×10^5 J kg^{-1} at 0°C), both of which lead to a drop in surface temperature (Cohen and Rind, 1991; Armstrong and Brun, 2008).

   Moreover, longwave radiation depends on temperature, therefore the emitted longwave radiation over a snow surface is low. In addition, snow cover appears to reduce cloud cover as it lowers the latent heat flux resulting in less surface evaporation and thus lower moisture content in the atmosphere (Cohen and Rind, 1991 and references therein).

By modifying the radiation balance, snow cover has huge effects on the surface energy balance. This leads to considerably altered air temperatures. This effect is especially pronounced during spring as solar radiation and snow cover are present (Chapin et al., 2005).

However, snow does not only have local or regional impacts on the prevailing climate. Simulations show that without snow cover, a warming in the mean annual surface air temperature of up to 5 K over northern North America and 8-10 K over Europe would occur during winter (Vavrus, 2007). These higher surface air temperature conditions would also influence the troposphere leading to changes in atmospheric circulation patterns. Further, the missing insulating effect of the snow cover would cause considerably lower soil temperatures and thus growing of permafrost areas (Vavrus, 2007). Also the water cycle would be affected through missing runoff and drier soils and sea ice would lose about 26 % of its mass without terrestrial snow cover (Vavrus, 2007).

c) **high insulation effect**

"The thermal conductivity is defined as the proportionality constant between the heat transport and the temperature gradient" (Sturm et al., 1997). Snow has a low thermal conductivity, for instance about ~0.1 W m^{-1} K^{-1} for newly fallen snow. In contrast, thermal conductivity of ice or wet soil is about 10 – 20 times higher. In addition, snow cover has a thermal conductivity that is about four times lower than frozen ground (Cohen and Rind, 1991; Armstrong and Brun, 2008; Langer et al., 2011a; Mudryk et al., 2018).

This low thermal conductivity of snow is caused by the fact that snow consists mainly of air (Armstrong and Brun, 2008; Domine et al., 2008). Thus, making snow an effective thermal insulator, reducing heat exchange via sensible heat between the lower atmosphere and the ground, ice or sea ice (Cohen and Rind, 1991; Armstrong and Brun, 2008; Langer et al., 2011a; Mudryk et al., 2018). Further, moisture transfer between the atmosphere and the underlying surface is reduced as well (Armstrong and Brun, 2008). Thereby, already a thin snow cover reduces the heat flux enormously leading in the case of sea ice to slower ice grow during autumn but to a delayed melting of sea ice in spring (Armstrong and Brun, 2008). Differences in the microstructure lead to differences of thermal conductivity in snow from different regions or different precipitation events (Sturm et al., 1997). The snow microstructure consists of grain size, shape and size distribution, pore size and shape, the size, shape and number of the bonds between grains and the type and form of larger structures, e.g. chains between grains (Shapiro et al., 1997; Johnson and Schneebeli, 1999; Lehning et al., 2002).

d) **high albedo**

Albedo is defined as "the ratio of the reflected to the incoming global shortwave radiation" (Armstrong and Brun, 2008). Surfaces with high albedo, e.g., snow and sea ice (see Figure 3.1), reflect most of the incoming shortwave radiation. Thus, only a small part is absorbed and leads to heating of underlying layers of snow, ice, soil or ocean and possibly to melting of snow and ice (Landrum and Holland, 2020). The albedo of snow is higher than that of sea ice (see Figure 3.1) (Goosse et al., 2018).

In general, snow albedo is dependent on snow type, grain size, surface roughness, impurity content and spectral distribution of the downwards radiation (Brun, 1989; Armstrong and Brun, 2008). Snow albedo depends, e.g., on the content of light absorbing impurities close to the snow surface as well as on the microstructure of the upper snow layers. Snow microstructure in turn is affected strongly by temperature, which is related to the energy and mass balance (Morin et al., 2020).

New snow has the highest albedo (~0.9) for most wavelengths of the solar radiation decreasing during the snow season (~0.8 – 0.85), whereby new snowfall increases snow albedo again (Perovich, 1996; Gardner and Sharp, 2010; Brown et al., 2021). During the course of the year albedo changes following changes in snow cover (Westermann et al., 2009). Thereby, a decrease in albedo from 0.9 to 0.5 results in fivefold increase of shortwave radiation absorption and thus heating of the snowpack (Armstrong and Brun, 2008). During snow melt albedo decreases. Warren (1982) found albedos in the range of 0.75 to 0.9 at the end of winter decreasing with snow melt in early spring to 0.6. Moreover, Langer et al. (2011a) found a reduction in the albedo from 0.8 to 0.2.

As snow melts due to increasing air temperatures, surfaces having a lower albedo than snow are exposed, absorbing more incoming shortwave radiation than snow covered surfaces, leading to more absorption of heat and therefore a warming of the surrounding and thus to even more snow melt. This effect is referred to as the "snow-albedo feedback" (see also Chapter 2.2) (Armstrong and Brun, 2008). Therefore, changes in snow albedo are co-responsible for rising temperatures in the Arctic (Chapin et al., 2005; Mudryk et al., 2018).

Thus, albedo is greatly influencing the net shortwave radiation and therefore the net radiation (Langer et al., 2011a; Morin et al., 2020). Therefore, it has huge effects on the energy balance (Morin et al., 2020). Even a shallow snow cover can have major impacts on the surface energy balance as its albedo is about four times higher than without snow cover (Langer et al., 2011a).

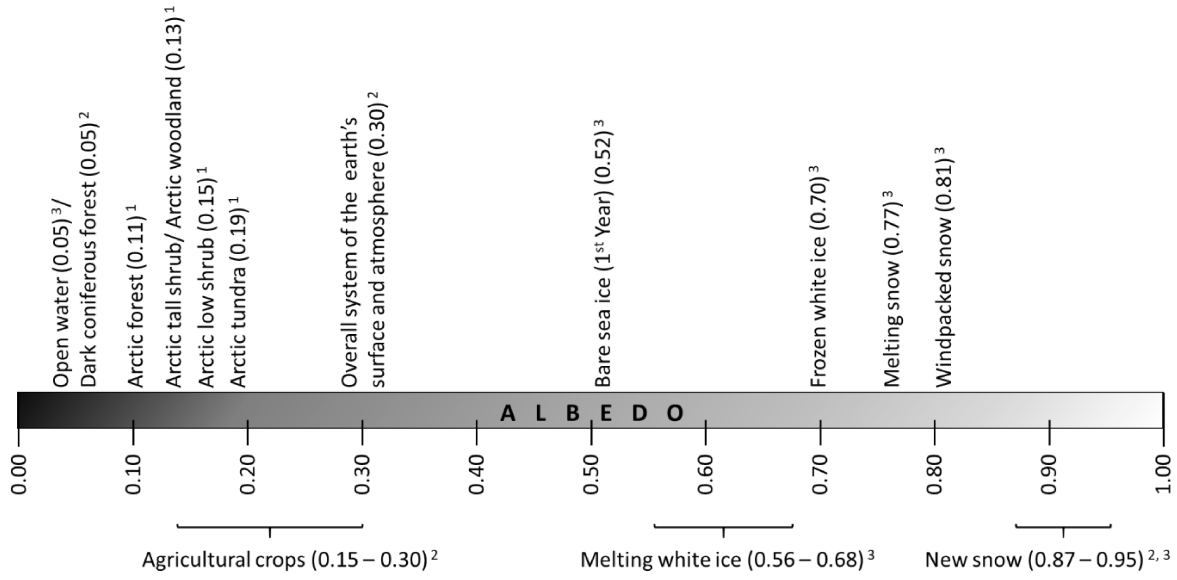

Figure 3.1: Observed albedo for different surfaces, open smooth water and different states of sea ice and snow. Data from [1]: Sturm (2005), [2]: Gebhardt et al. (2012) and [3]: Perovich (1996) and references therein (modified after Perovich, 1996).

3.2 Seasonal snow in the Arctic: An overview

3.2.1 Differences between Arctic and Alpine

> *"How the Arctic is unusual*
>
> *The Arctic climate exhibits many unique features.*
> *For example, the Sun does not rise high over the horizon, and seasonal variations in daylight are extreme (polar day and night)."*
>
> *Wendisch et al. (2017)*

Seasonal snow on the ground is mainly a result of numerous snowfall events leading to the formation of a layered snowpack. Further, refreezing rain and condensed water vapour form the snowpack (Colbeck, 1991; Domine et al., 2008). Thereby, snow stratification and snow characteristic vary around the globe, as climate variables, such as air temperature, humidity, precipitation and wind speed, influence snow properties and the temporal evolution of the snowpack (Colbeck, 1991; Sturm and Holmgren, 1998; Domine et al., 2008). This subchapter provides an overview of atmospheric conditions and snowpack characteristics of the European Alps and the Arctic as in the further course of this dissertation the snow model Crocus developed for applications in the European Alps (Chapter 5) is used for simulations at an Arctic site (Chapter 6 to Chapter 9). Further, this subchapter provides a summary of processes and characteristics that lead to different snow characteristics in the two regions.

3.2.1.1 European Alps

3.2.1.1.1 Atmospheric conditions

The greater region of the European Alps covers the region from about 4° – 18°E and 43° – 49°N (Auer et al., 2005; Isotta et al., 2014). The mountain ridge has the shape of an arc and extends about 1000 km (see Figure 3.2 (a) (Isotta et al., 2014) The mean elevation of the Alps is about 2500 m a.s.l. with the highest mountain Mont Blanc/ Monte Bianco peaking at 4810 m a.s.l. (Carturan et al., 2020).

The Alps are characterised by a complex orography with deep valleys and high mountains oriented in different directions (Böhm et al., 2001; Rauthe et al., 2013; Matiu et al., 2021). The climate is diverse, as the Alps form the transition zone between moderate humid climate caused by the Atlantic influence from the northwest, dry and winter cold but summer warm climate from continental east and humid and mild winters but dry summers from the Mediterranean region from the south (Böhm et al., 2001; Auer et al., 2005; Beniston, 2006; Rauthe et al., 2013; Adler et al., 2015; Matiu et al., 2021).

In general, in the European Alps the annual mean temperature (1901 – 2000) is 8°C while mean summer (July to August) temperature is 16.1°C and mean winter (DJF) temperature is 0°C (Casty et al., 2005). However, temperature ranges vary considerably: Average winter temperatures (December to January, 1981 – 2010) range between -5 and +5°C for altitudes below 1000 m, between -8 and +2°C for altitudes between 1000 m and 2000 m and between -14 to -2°C for altitudes between 2000 m and 3000 m, with temperatures between -10 and -5°C common for the latter (Matiu et al., 2021). During spring (March to May, 1981 – 2010) temperatures below 0°C are only common in regions above 2000 m altitude (Matiu et al., 2021).

Concerning precipitation, annual mean precipitation (1901 – 2000) is about 1200 mm (Casty et al., 2005). However, other studies found average annual precipitation in the Alps of about 2000 mm with higher values in high mountain regions. Isotta et al. (2014) provided a spatial distribution of the mean annual precipitation for the period 1971 – 2008, with annual precipitation ranging from 400 mm to more than 3000 mm (Figure 3.2 (b)). The spatial variability of precipitation, both horizontally and vertically, is already high over short distances due to the topography (Isotta et al., 2014; Carturan et al., 2020).

The pattern of seasonal variation of precipitation is more distinct: In general, precipitation is lower in winter and highest in summer (Frei and Schär, 1998). Casty et al. (2005) found precipitation amounts of 245 mm for winter and 352 mm for summer (1901 – 2000). Similar to Rauthe et al. (2013), who found most precipitation (120 mm) in June and lowest precipitation between October and May (below 85 mm) for the time period 1971 – 1990.

Since in the European Alps there is day and night all year-round and thus daily sunlight, the energy distribution is subject to a day-night-cycle. Thereby, e.g., during the night energy losses occur at the surface due to outgoing longwave radiation and energy surpluses occur at the surface during the day, leading to a pronounced air circulation directed down the valleys at night and up the valley during the day (Beniston, 2006).

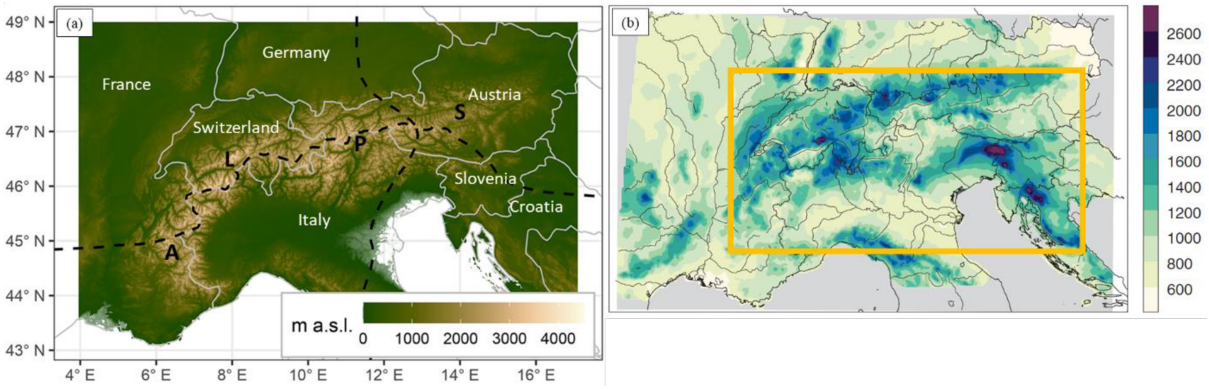

Figure 3.2: (a) Geographic location of the European Alps with topography displayed in colours as altitude in metres above sea level (a.s.l.). Topographic information from SRTM30 DEM (Shuttle Radar Topography Mission digital elevation model) with 1 km resolution. No information available for white parts. The dashed lines show the approximately position of the main climatic divides (Atlantic Ocean, Mediterranean Sea, European continent) from Auer et al. (2005) (modified after Matiu et al., 2021) (b) mean annual precipitation [mm] for the period 1971 – 2008. The orange box gives approximately the extend of the European Alps (modified after Isotta et al., 2014).

3.2.1.1.2 Snow conditions

In the Alps, snow depth increases with altitude. In the winter season (December to February) mean snow depth below 1000 m altitude is often below 40 cm, reaching values between 25 cm and 110 cm for altitudes between 1000 m and 2000 m and 50 cm to about 150 cm for altitudes between 2000 m and 3000 m (Matiu et al., 2021). In March, snow located in the higher altitudes of central Europe begin to melt while the main snow melt phase starts end of April often accompanied by rainfall (Holko et al., 2011). In the spring season (March to May) mean snow depth below 2000 m altitude is seldom above 80 cm. For altitudes above 2000 m mean snow depth is between 80 cm and 200 cm (Matiu et al., 2021). Figure 3.3 shows a typical site in the European Alps.

Figure 3.3: Typical Alpine study site in Col du Lautaret, France in February 2018 (Photo: Arttu Jutila).

Due to the high snow accumulation, a constant increase in density with depth is typical for Alpine snow, resulting in dense basal layers due to pressure metamorphism (see Figure 3.4 (a); see Chapter 3.3.1 for details) (Domine et al., 2019; Calonne et al., 2020). At the top of an Alpine snowpack often new snow can be found with densities around 50 kg m^{-3}, increasing towards 450 kg m^{-3} in the middle of the snowpack. Melt-freeze layers can be at the bottom of the snowpack and have densities around 350 kg m^{-3} (Calonne et al., 2020). However, early in the season, when snow height is low, depth hoar layers (see II.a in Chapter 3.3.1 for definition and details) with a low density may form and built the bottom of the snowpack (Domine et al., 2008; Calonne et al., 2020).

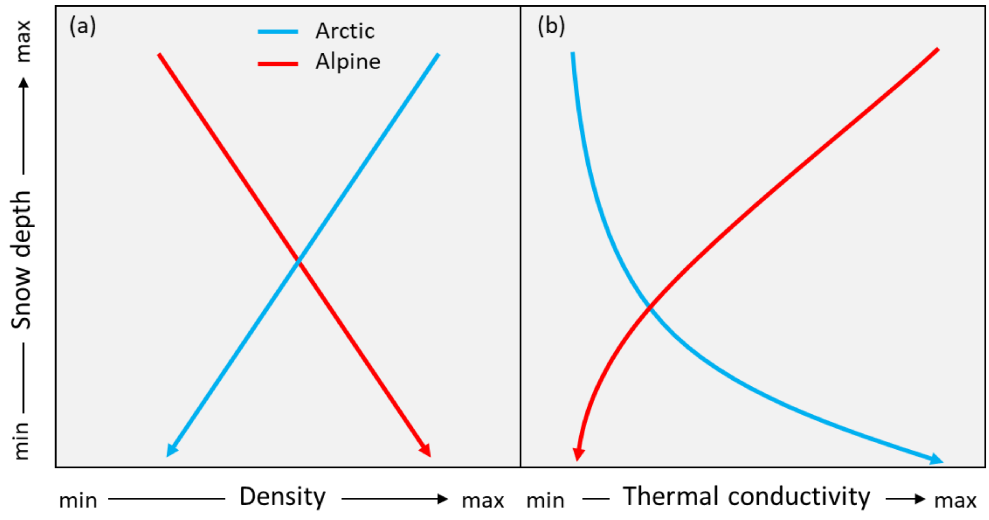

Figure 3.4: Typical vertical (a) snow density and (b) thermal conductivity profiles for Arctic and Alpine snowpacks (figure redrawn after Domine et al., 2019).

Melting and refreezing within the snowpack are common as well as short periods where snow on the ground is present (Jacobi et al., 2010; Essery et al., 2016; Leppänen et al., 2016). Further, Alpine snow is commonly close to its melting point (Jacobi et al., 2010; Essery et al., 2016). Therefore, Alpine snowpacks are warm and moist and have a comparable high liquid water holding capacity (Gascon et al., 2014). The commonly dense basal snow layers have a low permeability. However, over the entire snowpack densities are overall low and thus have a high permeability (Domine et al., 2007). Further, temperature gradients are usually low with values between 5 and 10°K m^{-1} (Domine et al., 2006b).

Typically thermal conductivity increases with depth in Alpine snowpacks (see Figure 3.4 (b)). Due to the relatively low thermal conductivity of the upper snow layers, temperature variations are only slowly transmitted towards the ground (Domine et al., 2019).

In the Alps, precipitation is high and frequent (Isotta et al., 2014). Thus, snow accumulation is high and typical snowpacks consist of many snow layers, some of which are thick. Since storms are seldom and snow accumulation is high, snowpacks are affected by wind to a small extend. Therefore, snow layers can be found that have never been affected by wind (Domine et al., 2007; Domine et al., 2008). Another consequence are fine-grained snow particles that are not wind packed. These layers are commonly separated by wind packed layers, melt-freeze crusts or ice layers (Domine et al., 2008).

3.2.1.2 Arctic

3.2.1.2.1 Atmospheric conditions

The Arctic includes a wide region defined in different ways. It is located around the North Pole and includes the Arctic Ocean and different landmasses. Common definitions of the Arctic are, e.g., the region north of the Arctic Circle, north of the Arctic tree line or regions in the high latitudes with summer temperatures of 10°C or less (see Figure 3.5) (National Snow and Ice Data Center, 2020).

Figure 3.5: Map of the Arctic. Different definitions of the Arctic are shown: Red line: 10°C isotherm in July, black circle: Arctic Circle, green line: Treeline, (modified after National Snow and Ice Data Center, 2020).

The climate in the Arctic is diverse as visualised in Figure 3.6. Mean annual air temperatures is clearly below zero but vary considerable between -18°C and -4°C. Mean annual precipitation is generally low and ranges between 80 mm and 300 mm (Eckerstorfer and Christiansen, 2011).

Due to the cold conditions, snowfall can occur all year-round in the Arctic. However, reliable precipitation measurements over extended periods are rare due to the remote location, low population and harsh conditions of the cold environment. In addition, snowfall variability is high and windy conditions contribute to the difficulty of performing high quality snowfall measurements (Homan and Kane, 2015).

In the Arctic, during summer there is 24 h incoming solar radiation leading to an energy input (Ernakovich et al., 2014) while in winter there is 24 h darkness and thus an absence of solar radiation, leading to an energy loss (see Chapter 3.2.3) (Colbeck, 1982).

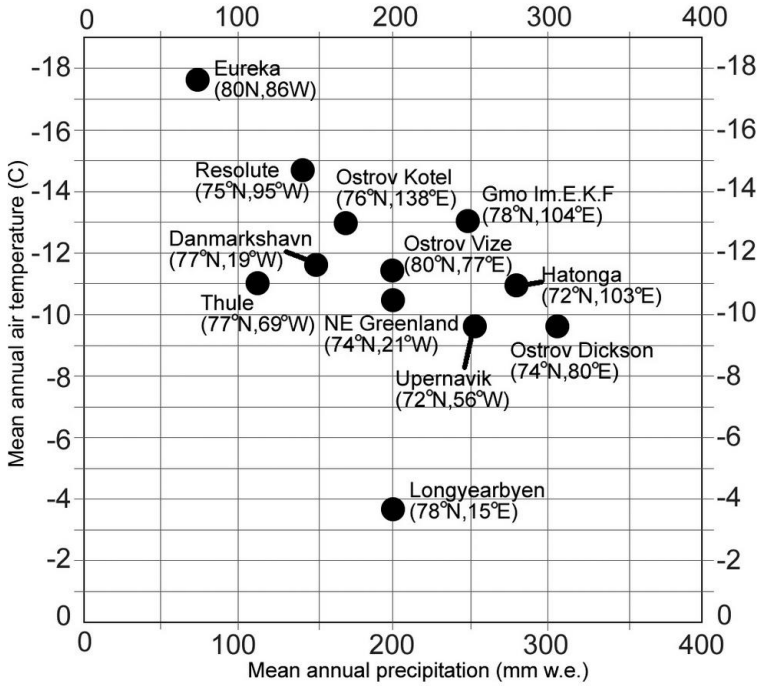

Figure 3.6: Mean annual temperature and precipitation for different stations in the Arctic in the year 2009 (figure from Eckerstorfer and Christiansen, 2011).

3.2.1.2.2 Snow conditions

Snow depth in the Arctic is commonly about 40 cm (Domine et al., 2006b) but can vary considerably. High wind speeds are common and lead to wind redistribution and transport-related sublimation. Therefore, snow distribution is considerable variable with usually snow being transported away from hilltops and windward slopes and being accumulated in depressions and leeward slopes (Homan and Kane, 2015). A picture of a typical Arctic study site is shown in Figure 3.7.

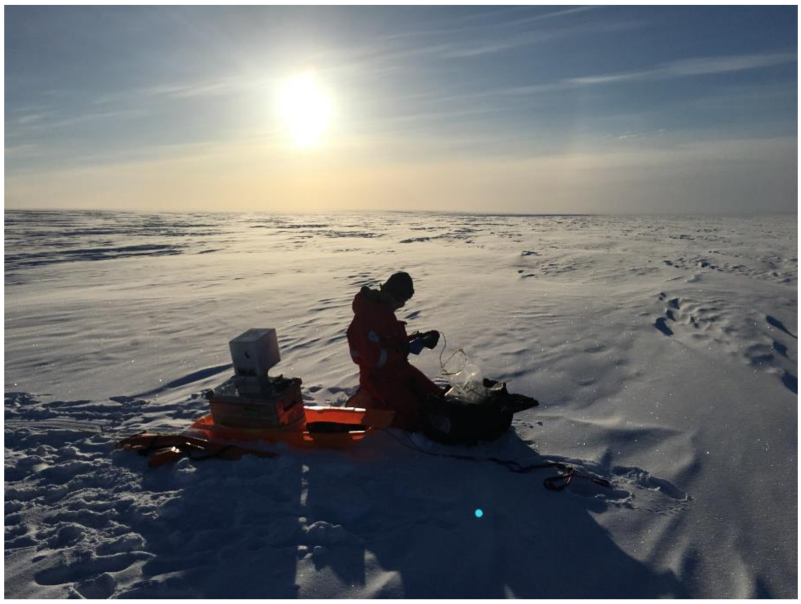

Figure 3.7: Typical Arctic study site close to Villum Research Station, Greenland in March 2018 (Photo: Andreas Herber).

Due to the cold air temperatures and the absence of solar radiation in winter, huge temperature gradients exist in the Arctic. Therefore, a strong vertical temperature gradient in the snowpack is a major determinant of snow metamorphism (Sauter and Obleitner, 2015), causing a strong vertical water vapour transport in the snowpack and thus a mass transfer from the bottom to the top. This process is needed to create the low density basal layers (depth hoar) typical for Arctic snowpacks (Domine et al., 2007; Domine et al., 2019).

Both the temperature gradient metamorphism and wind redistribution are typical characteristics of late winter Arctic snowpacks. Therefore, a typical Arctic snowpack consists of a basal low-density depth hoar layer and a top high-density wind slab layer (Sturm and Holmgren, 1994). Wind slabs contain of rounded grains due to sintering and mechanical rounding by wind (Domine et al., 2008; King et al., 2020). Typical densities for surface wind slabs are around 375±49 kg m^{-3} (King et al., 2020), while densities for basal depth hoar are around 248±27 kg m^{-3}. Therefore, usually density decreases with depth for an Arctic snowpack (see Figure 3.4 (a)).

Due to the relatively high thermal conductivity of the upper snow layers, temperature variations are transmitted quickly towards the ground (Domine et al., 2019). Basal snow layers have commonly relatively low densities and are thus highly permeable. However, overall Arctic snow has a relatively high density and therefore a comparably low permeability (Domine et al., 2007). The maximum liquid water holding capacity is comparably low due to cold and dry snow (Gascon et al., 2014).

3.2.2 Spatial distribution of Arctic snow

Both the spatial variability of snow thickness and melt are crucial elements of the nival system (Pomeroy et al., 2004). Knowledge of the spatial distribution of Arctic snow is essential for understanding climate-cryosphere interactions as snow and related feedbacks play a major role (Estilow et al., 2015). Furthermore, determining snow distribution is important for, e.g., the global energy balance, the food supply of Arctic animals such as caribou and muskoxen, and for the water balance as it is important for estimating the onset and amount of snow melt runoff (Liston and Sturm, 1998; Zweigel et al., 2021). As the snow cover influences the ground thermal regime, it also affects the ground temperature (Zweigel et al., 2021). Mean snow cover extent in the Arctic is largest in January - 47.4 million km^2 - and smallest in August - 3.0 million km^2 - (Estilow et al., 2015).

The interannual variability of seasonal snow cover is large (Pedersen et al., 2016b; Mott et al., 2018). Thereby, snow cover, snow depth, SWE (SWE: amount of water stored in the snow), and the timing of the snow season, determined by snow onset and snow melt, are not uniformly distributed over the surface. Instead, they are influenced by variations due to wind, vegetation, topography and snowfall (Liston and Sturm, 1998; Sturm and Benson, 2004; Pedersen et al., 2016b). Also, snow layers vary laterally due to wind redistribution, water percolation, local topography, vegetation and soil moisture (Sturm and Benson, 2004; Davesne et al., 2021). During the melting period, the snow cover becomes patchy, causing the snow properties, such as albedo, to vary considerably across small scales (Essery and Pomeroy, 2004).

Furthermore, annual precipitation varies considerably (Pedersen et al., 2016b). The amount of snowfall and the duration of the snow season are controlled by latitude, as it determines seasonal air temperatures. Thereby, a strong zonal gradient in mean snow cover duration exists. At a more regional scale, the distance to the ocean and the elevation determine the mean annual maximum accumulation (Brown et al., 2021).

Therefore, precipitation amounts within the Arctic underlie large regional differences. For maritime, coastal climates they found values of over 75 cm for the annual solid part of precipitation alone. In contrast, Liston and Hiemstra (2011) found annual water-equivalents for total precipitation of 10 – 30 cm for regions with dry, continental climates for the period 1979 – 2009. Thereby, low winter precipitation is typical for polar deserts in which no vegetation grows and which are widespread in the Arctic. Moreover, the distribution of precipitation varies across the region (Davesne et al., 2021).

However, snow accumulation is not equivalent to the amount of snowfall measured at a given location. Furthermore, snow depth measured at one point cannot be extrapolated to another point (Homan and Kane, 2015) because atmospheric circulation patterns and topography vary on the scale of kilometres. Both determine the amount of snowfall (Zweigel et al., 2021).

On a more local scale, i.e. in the range of tens to hundreds of meters, snow redistribution, further described in Chapter 3.3.2, leads to differences in snow distribution (Zweigel et al., 2021). For instance, snow depth varied between 0.3 m and 0.9 m on a 250 m transect with an elevation gradient ranging from 0 m a.s.l. (above sea level) to 420 m a.s.l., at Zackenberg, Greenland (Pedersen et al., 2016b). In general, Homan and Kane (2015) found evidence of higher spatial variability with increasing elevation.

Annual snow distribution patterns are similar because topography, which controls the locations of deposition and erosion during snow redistribution, along with slope, vegetation and consistent weather patterns, remain the same. Therefore, annual differences in snow depth vary overall but not relative to each other, and the overall snow depth pattern is the same each year (Homan and Kane, 2015; Pedersen et al., 2016b).

3.2.3 Temporal evolution of Arctic snow

> *"Presence and transformation of the snow pack change the physical properties of the atmosphere-ground interface, which in turn affects the above fluxes, thereby influencing the properties of the lower atmosphere."*
>
> *King et al. in Armstrong and Brun (2008)*

The terrestrial high Arctic is covered with snow eight to ten months a year. In general, snowfall in the Arctic is possible throughout the year (Homan and Kane, 2015). Snow accumulation extends over several months, e.g., from October to May in the Russian Arctic and from September to May in Zackenberg, Greenland (Bednorz and Wibig, 2016; Pedersen et al., 2016b). In Zackenberg, highest snow depth is reached between February and end of May (Pedersen et al., 2016b). Overall, most parts of the Arctic experience negative temperatures from October to May (Box et al., 2019).

Positive air and surface temperatures are frequent from June to September (Box et al., 2019). Snow melt is restricted to one or two months (Bednorz and Wibig, 2016). Thereby, 80 % of the total Arctic snow water is released within a few weeks in May and June, when energy input is large (Brown et al., 2021).

3.2.3.1 Overview: Energy- and mass balance

The processes within the snowpack are closely related to the energy and mass fluxes at the snow surface, and both influence each other. The timing and amount of snow melt are determined by the energy balance of the snowpack (Brown et al., 2021). The surface energy balance itself is mainly controlled by snow cover, cloud cover and ground temperature (Langer et al., 2011a).

The main contributor of the surface energy balance of a snowpack is provided by solar radiation (Warren, 1982; Lackner et al., 2022a). The occurrence of polar night and polar day as well as the presence of snow with the prevailing albedo determine the course of the shortwave radiation balance in the course of the year in the Arctic (Westermann et al., 2009; Lackner et al., 2022a).

More specifically, net short- (Q_S) and longwave (Q_L) radiation, sensible turbulent heat flux (Q_h), latent turbulent heat flux (Q_e), heat flux due to precipitation or blowing snow (Q_a) and the ground heat flux (Q_G) determine the energy balance of a snowpack at its snow-atmosphere interface (Mott et al., 2018; Lackner et al., 2022a). Outgoing longwave radiation is mainly controlled by the surface temperature (Westermann et al., 2009; Lackner et al., 2022a). The sensible turbulent heat flux arises due to temperature differences between the snow surface and the atmosphere. The latent turbulent heat flux depends on the water vapour pressure gradient between the snow surface and the atmosphere and includes the processes of sublimation, evaporation, and condensation, which are important for the mass balance (Westermann et al., 2009; Mott et al., 2018; Lackner et al., 2022a). Both turbulent fluxes are high when wind speed is high (Westermann et al., 2009; Lackner et al., 2022a). Turbulent heat fluxes can cause more than 50 % of the melting in regions with high wind speeds under humid air conditions or local changes in air temperature conditions (Mott et al., 2018 and references therein). Furthermore, higher temperature gradients between the surface and the atmosphere lead to a decrease in the sensible turbulent heat flux (Lackner et al., 2022a). The ground heat flux results from conduction (Mott et al., 2018).

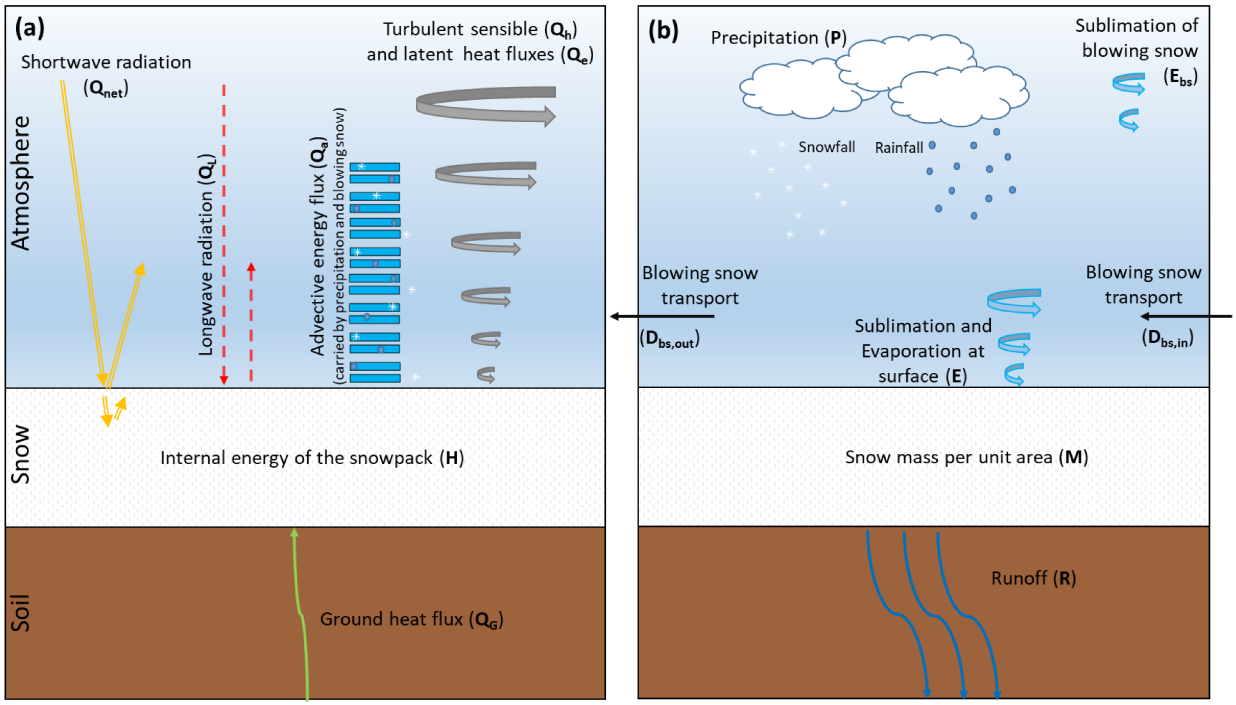

Figure 3.8: (a) Schematic illustration of the energy and (b) mass balance of a snowpack (own drawing modified after Armstrong and Brun, 2008).

Considering the snow surface as a whole, the net change rate over time t of the internal energy H can be calculated for a continuous snow cover according to Lackner et al. (2022a)

$$\frac{dH}{dt} = Q_{net} + Q_h + Q_e + Q_a + Q_G \tag{3.1}$$

with net radiation Q_{net} being calculated as follows (Langer et al., 2011a)

$$Q_{net} = Q_{SW,in} - Q_{SW,out} + Q_{LW,in} - Q_{LW,out} \tag{3.2}$$

and Q_h and Q_e being the sensible and the latent turbulent heat flux, Q_a the advective heat flux caused by precipitation and blowing snow, Q_G the ground heat flux, $Q_{SW,in}$ and $Q_{SW,out}$ the incoming and outgoing shortwave radiation and $Q_{LW,in}$ and $Q_{LW,out}$ the incoming and outgoing longwave radiation. All fluxes have the unit W m^{-2}. Positive fluxes are directed towards the surface.

The mass balance M [kg m^{-2} s^{-1}] of a snowpack is determined by the prevailing precipitation rate P, the redistribution of snow due to blowing snow D_{bs}, the sublimation rate during blowing snow E_{bs}, the sum of sublimation, evaporation and condensation at the snow surface E and the runoff rate R and can be calculated according to Armstrong and Brun (2008)

$$\frac{dM}{dt} = P - \nabla \bullet D_{bs} - E_{bs} \pm E - R \tag{3.3}$$

Thereby, losses from E_{bs} and enhanced sublimation in late winter, when the energy input from radiation increases and relative humidity is low, are the main components of sublimation in the Arctic (Brown et al., 2021).

The volumetric melt rate $Melt$ [m s^{-1}] can be calculated after Boike (2003)

$$Melt = \frac{Q_M}{\rho_W \, L_f} \tag{3.4}$$

with Q_M being the melt energy [W m^{-2}], ρ_W the density of water [kg m^{-3}] and L_f the latent heat of fusion for ice [J kg^{-1}].

3.2.3.2 Energy fluxes in the course of the year

Summer

The Arctic summer is characterised by a snow free ground and high incoming shortwave radiation (Westermann et al., 2009; Langer et al., 2011a). In addition, incoming shortwave radiation is present for 24 h, resulting in energy input (Ernakovich et al., 2014). Therefore, the main energy source in summer is the net shortwave radiation (Westermann et al., 2009) also visible in Figure 3.9. The incoming shortwave radiation can reach values of above 300 W m^{-1} under cloud free conditions and decreases to 20 W m^{-1} under cloudy conditions for a site northern Siberia, for example (Langer et al., 2011a).

The high positive net shortwave radiation is countered by the net longwave radiation, the sensible and latent heat flux, and the ground heat flux (Westermann et al., 2009; Langer et al., 2011a). Thawing of the active layer of permafrost plays an important role in energy consumption. Westermann et al. (2009) found that this process consumes 15 % of the net shortwave radiation in July and August at a site in Svalbard. At the beginning of the summer season, the average ground heat flux is highest due to a pronounced temperature gradient in the ground and an incipient thawing of the active layer (Westermann et al., 2009).

Both the sensible and latent heat fluxes show a pronounced diurnal cycle (Westermann et al., 2009; Langer et al., 2011a). The maximum of both fluxes occurs during midday, when net radiation is highest, while the minimum occurs around midnight with values close to zero, when the sun angle is lowest (Westermann et al., 2009).

Autumn

In autumn, temperatures drop steadily and it starts to freeze and snow (Langer et al., 2011a). The sun angle starts to decrease (Langer et al., 2011b). Some snow may cover the ground, but a continuous snow cover does not yet form (Westermann et al., 2009; Langer et al., 2011a).

Net radiation is positive but lower than in summer and shows a distinct diurnal cycle (Langer et al., 2011a). This is because the net shortwave radiation is lower than in summer due to lower sun angles (Westermann et al., 2009). The average sensible heat flux is negative and the average ground heat flux is positive, both resulting in an energy surplus towards the ground (Westermann et al., 2009; Langer et al., 2011a).

Shortly before the onset of polar night, net radiation is negative. Thereby, the contribution of the net shortwave radiation is neglectable because the albedo is already high due to snow cover. The energy loss is mainly compensated by the ground heat flux and to a lesser extent by the sensible heat flux (Langer et al., 2011b).

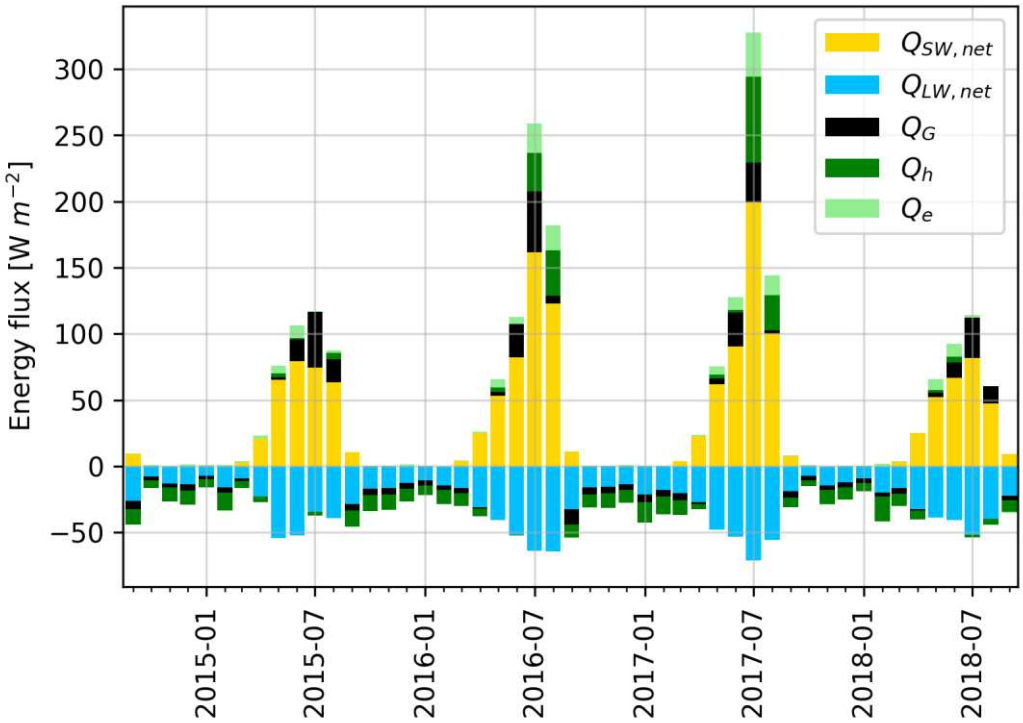

Figure 3.9: Monthly energy balance simulated with the snow model Crocus forced with ERA5 atmospheric data for Villum Research Station. Note that heat flux from rain is missing. $Q_{SW,net}$: Net shortwave radiation, $Q_{LW,net}$: Net longwave radiation, Q_G: Ground heat flux, Q_h: Sensible turbulent heat flux, Q_e: latent turbulent heat flux (own drawing).

Winter

In winter there is polar night without incoming shortwave radiation (Figure 3.9). Therefore, the radiation balance is only determined by the longwave radiation, which is clearly negative, resulting in negative net radiation. The energy loss at the surface is most pronounced on clear and cold nights (Colbeck, 1991; Westermann et al., 2009; Langer et al., 2011b; Lackner et al., 2022a). The amount of incoming and outgoing longwave radiation follows the temperature variations, while the net longwave radiation is quite stable (Lackner et al., 2022a).

The sensible heat flux and the ground heat flux resulting from active layer refreezing compensates for the energy losses (Westermann et al., 2009; Langer et al., 2011b; Lackner et al., 2022a). The sensible heat flux is lower in mid-winter than in early winter (Langer et al., 2011b). The turbulent sensible and latent heat fluxes are low during the polar night (Westermann et al., 2009; Mott et al., 2018). In general, the role of sensible heat flux is more important than that of latent heat flux during most of the winter (Lackner et al., 2022a).

Towards the end of winter, the importance of the ground heat flux decreases and the sensible heat flux is the dominant part counteracting the energy losses. The latent heat flux remains neglectable (Langer et al., 2011b).

As soon as there is sunlight again, net shortwave radiation increases considerably. However, the prevailing snow cover with its high albedo reflects a large part of the incoming shortwave radiation (Westermann et al., 2009; Lackner et al., 2022a).

Spring

Once there is no longer a continuous snow cover, the spatial variability of the surface energies already increases on a metre scale, especially due to differences in the surface albedo. In addition, a strong surface temperature gradient can form, as the maximum temperature of 0°C applies to snow surfaces but warmer snow free surfaces are present in the surrounding area. The turbulent sensible and latent heat fluxes as well as the longwave radiation over the different ground surfaces also differ (Mott et al., 2018).

During the spring season, positive net radiation predominates and thus an energy surplus from the atmosphere towards the snowpack (Lackner et al., 2022a). The net shortwave radiation is the main energy source. Additional incoming energy comes from the sensible heat flux (Westermann et al., 2009; Mott et al., 2018 and references therein). The sensible heat flux increases when snow-free areas are present (Langer et al., 2011a). Net longwave radiation is the dominant factor for energy losses. In addition, much energy is used for the phase change from solid to liquid during snow melt (Westermann et al., 2009; Langer et al., 2011a).

3.3 Snow processes

In this subchapter the processes snow metamorphism, sublimation and wind redistribution by blowing and drifting snow are described. Table 3.1 provides definitions for these processes.

Table 3.1: Definitions of snow processes discussed in this subchapter.

Process	Definition	Reference
Metamorphism	Change in snow microstructure and hence in snow properties over time due to thermodynamic imbalance	e.g., Colbeck (1982), Flin and Brzoska (2008), Domine et al. (2008)
Blowing snow	Transport of snow particles through wind close to the ground	e.g., World Meteorological Organization (2021a)
Drifting snow	Transport of snow particles through wind in moderate to great heights above the surface	e.g., World Meteorological Organization (2021b)
Sublimation	Phase change from solid (e.g., snow) to gaseous aggregate state, leading to a transport of water from the surface into the atmosphere	e.g., Mott et al. (2018), Sexstone et al. (2016), Pomeroy et al. (1997)

3.3.1 Snow metamorphism

The type of newly fallen snow can be divided according to the shape of the snow crystals. The shape of new snow depends on the atmospheric conditions, e.g., temperature and supersaturation, prevailing during the formation of the snow particle (see Figure 3.10) (Nakaya, 1954; Colbeck, 1982). For temperatures below -25°C dendritic snow, columns and bullet combinations are commonly observed in the Arctic. For temperatures that are more moderate plates, columns and needles are typical. For temperatures above 0°C wet snow consisting of particles of all shapes can be found (Legagneux et al., 2002).

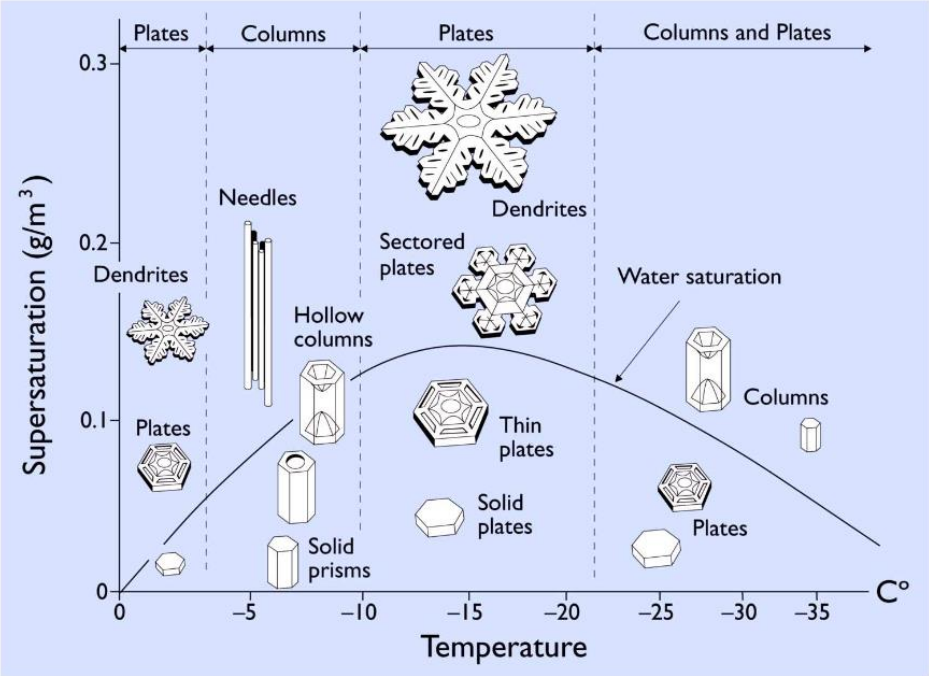

Figure 3.10: Snow crystal morphology after research conducted by Ukichiro Nakaya in the 1930s. Newly fallen snow particles formed in air are shown as a function of temperature and water vapour supersaturation. Supersaturation exists when air humidity is above 100 %. The water saturation curve represents typical supersaturation in a dense cloud (figure from Libbrecht, 2012).

Snow metamorphism refers to the change of snow microstructure and therefore snow properties over time, i.e. snow can evolve from newly fallen snow over firn to ice (Colbeck, 1982; Domine et al., 2008). The physical properties of snow are controlled by the snow type and hence by the metamorphism the snow has undergone (Colbeck, 1982).

Metamorphism is a rapid process compared to the time the snow is present and takes place continuously (Colbeck, 1991). Snow that is older than one day, but sometimes only older than a few hours, is already undergoing metamorphosis, which is evident in changes in the shape of the snow particles (Legagneux et al., 2002; Domine et al., 2007). In this process, rounded edges are typical of snow that is beginning to metamorphose (Cabanes et al., 2002; Legagneux et al., 2002).

Metamorphism itself is controlled by the ambient temperature, the liquid water content and the temperature gradient, which in turn are handled by the energy and mass balance (Brun, 1989). Thereby, high wind speeds and high temperature gradients lead to rapid metamorphism and thus to heavily metamorphosed snow within a few days (Domine et al., 2007). In addition, the overburden pressure of overlying snow layers and the time since deposition lead to an increase in snow density (Sommerfeld and LaChapelle, 1970; Colbeck, 1982; Sturm et al., 1997; Judson and Doesken, 2000). Snow metamorphism is fastest at temperatures around 0°C and slowest at -40°C (Sommerfeld and LaChapelle, 1970; Judson and Doesken, 2000; Legagneux et al., 2002).

Another factor is the presence of liquid water in a snowpack that is at its melting point (called wet snow). Wet snow undergoes so-called wet metamorphism (Colbeck, 1982, 1991), which also reduces the albedo (Sauter and Obleitner, 2015). In contrast, snow without liquid water and at temperatures below the melting point is called dry snow and undergoes dry metamorphism (Colbeck, 1982).

Thus, in simple terms, a distinction is made between two types of snow metamorphism

I. **Wet metamorphism**: taking place at air temperatures around 0°C where liquid water is present (e.g., Colbeck, 1982; Domine et al., 2008)

II. **Dry metamorphism**: taking place at air temperatures below the freezing point and therefore without liquid water (e.g., Colbeck, 1982; Domine et al., 2008)

During **wet snow metamorphism**, the snow particles become rounded as water is transported from convex to concave snow particles, where it refreezes (Domine et al., 2008). In this process, liquid is easy to move when the water content is high, whereas when the liquid water content is low liquid may be trapped and difficult to move. Thus, metamorphism is slow when the liquid water content is low resulting in faster vanishing of the dendritic grain shape (see Figure 3.11) of the snow particles the more water is present (Brun, 1989; Domine et al., 2008). Wet snow metamorphism forms snow particles that are called melt forms (Niwano et al., 2012).

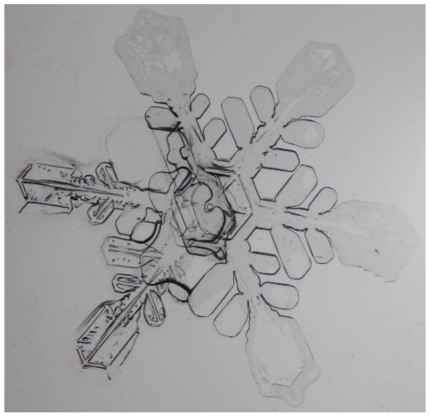

Figure 3.11: Photo of a new dendritic snow crystal taken during MOSAiC (Multidisciplinary drifting Observatory for the Study of Arctic Climate) expedition, February 2020 (Photo: Hannes Grische 2020).

Dry snow metamorphism can be further divided into

II.a. **Snow temperature gradient metamorphism**: A high temperature gradient (see description below) leads to vertical water vapour transport (Sommerfeld and LaChapelle, 1970; Colbeck, 1982; e.g. Domine et al., 2008). This type of metamorphism is able to create depth hoar layers (Sommerfeld and LaChapelle, 1970). Depth hoar is a form of highly metamorphosed snow that develops under high temperature gradients within the snowpack. Large, faceted crystals, which may also be hollow or cup-shaped, are typical for depth hoar (Legagneux et al., 2002). Since the top of underlying grains is warmer than the bottom of the overlying grains, water can sublime from the lower, warmer grain to the upper, colder grain (Sommerfeld and LaChapelle, 1970). In addition, the formation of faceted crystals, which is the early stage of depth hoar, is possible (Niwano et al., 2012).

II.b. **Equi-temperature metamorphism**: Due to a low temperature gradient (below 5 K m^{-1}) the main transport of water vapour is not caused by the temperature gradient (Sommerfeld and LaChapelle, 1970; Lehning et al., 2002; e.g. Domine et al., 2008). Instead, the decrease in curvature is the main driver for the exchange of water molecules as it leads to differences in saturation pressure that leads to exchanges in water molecules by vapour diffusion (Sommerfeld and LaChapelle, 1970) This leads to a transport of latent and sensible heat (Colbeck, 1991). During this process, particles break causing smaller and more grains. Over time the shape of the snow particles becomes equi-dimensional and grains become larger (Sommerfeld and LaChapelle, 1970). Typical snow particles formed by this type of metamorphism are decomposed, fragmented or rounded (Niwano et al., 2012).

II.c. **Wind snow metamorphism:** During wind events, the snow particles break leading to smaller grain sizes. Further, the snow particles become rounder and sinter quickly. Thereby, the density of the layers formed by these snow particles increases, as the particles can be packed closer together and a strong bonding between them exists (Colbeck, 1982, 1991; Keenan et al., 2021; Warren, 1982; Bormann et al., 2013). These wind-hardened snow layers are called wind slabs or wind crusts when they are thin (Colbeck, 1982, 1991; Sturm and Holmgren, 1994). Thereby, snowpacks are denser at windier sites than at sites with lower wind speeds (Sturm and Holmgren, 1998).

Since the **temperature gradient** within a snowpack is of great importance for the type of metamorphism, its formation and further related processes are described here.

> Temperatures in dry snowpacks tend to increase from the snow surface towards the basal layers. This causes a temperature gradient and an equalising movement resulting in an upward flow of heat. Due to the temperature gradient, there is also a vapour density gradient and a similar upward transport of water vapour occurs (Colbeck, 1983; Domine et al., 2008). Typical values for temperature gradients in the Arctic range from 10 to 30 K m^{-1} (Domine et al., 2008). For a 1 m thick snowpack with 0°C at the snow-ground interface and -15°C at the snow-atmosphere interface produces, for example, a water vapour pressure gradient of 444 Pa m^{-1} (Domine et al., 2008).
>
> Sublimation in the lower layers on warmer snow particles and condensation in the upper layers on colder snow particles maintain the vertical mass transport (Colbeck, 1983; Domine et al., 2008). Snow particles grow by condensation of water vapour on the bottom of the particles, which is colder compared to the ambient temperature, while they become smaller by sublimation on the top, which is warmer compared to the ambient temperature (Flin and Brzoska, 2008).
>
> However, temperature and vapour gradient are not uniform in a snowpack, but can vary considerably in the different snow layers, since thermal conductivity and permeability depend on the snow density (Colbeck, 1991). The higher the temperature gradient, the higher the rate of metamorphism (Colbeck, 1983).

In heavely metamorphosed snow the original crystal shape can no longer be identified (Legagneux et al., 2002; Domine et al., 2007). Metamorphosed snow can be a few days or several months old (Domine et al., 2007). It is often found in deep or basal snow layers (Legagneux et al., 2002; Sturm et al., 2010). In general, basal layers often consist of faceted crystals that persist in regions with low temperature gradients and therefore missing vertical water vapour transport, e.g., in the Alps, but transform into depth hoar within a maximum of three weeks in regions with high temperature gradients, e.g., in the Arctic (Domine et al., 2007).

The state of metamorphism of a snow layer determines the snow properties. For example, an increase in density over time leads to a decrease in the pore space between snow grains and thus to a decrease in snow depth (Judson and Doesken, 2000). Due to metamorphism, grain size and impurity content increase over time, resulting in a decrease in snow albedo, which determines the energy balance at the snow surface (see Chapter 3.2.3) (Domine et al., 2006a). Changes in size, shape and cohesion of snow grains influence, e.g., temperature gradient and temperature (Colbeck, 1982, 1983).

In general, the proposed snow metamorphism schemes are not exclusively found in a snowpack or a snow layer, as nature does not know such sharp divisions, but the actual snow metamorphism is rather a mixture of the proposed schemes (Sommerfeld and LaChapelle, 1970; Colbeck, 1982). Already newly fallen snow is most likely a mixture of different snow crystal types, e.g., plates, needles, as they are exposed to different conditions on their way through the atmosphere. This also applies to snow on the ground, as different atmospheric conditions over the course of a year reveal different metamorphic processes that snow on the ground undergoes from the time after it is deposited (Colbeck, 1982).

3.3.2 Snow redistribution by drifting and blowing snow

Snow redistribution due to wind creates a heterogeneous snow distribution as snow is removed in some areas but accumulated in other areas (Brun et al., 2013). Thus, snow redistribution leads to regional snow depth variability and the formation of snow deposition features such as snow dunes that can range from sub-metres to several tens of metres and beyond (Sturm and Holmgren, 1994; Sturm and Benson, 2004; Mott et al., 2018 and references therein). However, snow is preferentially deposited on leeward sides of, e.g., ridges or local depressions (Liston et al., 2016; Mott et al., 2018 and references therein). But snow redistribution can also cause a flattening of the surface (Mott et al., 2018 and references therein).

During drifting and blowing snow events, snow is redistributed on a scale of a few metres to hundreds of metres by creep, saltation and turbulent suspension (see Table 3.2 for definitions) (Liston et al., 2016; Mott et al., 2018 and references therein). Thereby, the World Meteorological Organisation (WMO) defines drifting snow as “an ensemble of snow particles raised by the wind to small heights above ground” (World Meteorological Organization, 2021b). In contrast, the WMO defines blowing snow as “an ensemble of snow particles raised by the wind to moderate or great heights above the ground” (World Meteorological Organization, 2021a). The difference between drifting and blowing snow lies therefore in the height at which the snow is transported. As drifting snow is transported in lower layers, visibility at eye level is not affected, whereas with blowing snow, visibility at eye level is usually severely impaired, depending on the intensity of the event (World Meteorological Organization, 2021a, 2021b).

Table 3.2: Mechanisms of wind transport of snow.

Mechanisms	Definition	Wind speed and transported load	Reference
Creep	Rolling of usually bigger particles along the surface	For new dry snow from 5 ms^{-1}; small amount of snow is transported	e.g., Mott et al. (2018), Liston et al. (2016)
Saltation	Bouncing transport of particles in a 5 to 10 cm thick layer with frequent surface contact due gravity and wind drag	Usually smaller amount of snow is transported than due to suspended snow transport	e.g., Mott et al. (2018), Liston et al. (2016)
Suspension	Suspended transport of small particles up to several hundred metre high	Higher wind speeds, long distances from tens to hundreds of metres	e.g., Mott et al. (2018), Liston et al. (2016)

Wind transport requires that the shear of the wind on the snow surface exceeds a threshold value, which depends on the type of surface snow, to overcome the resistance of the snow particles to be transported (Vionnet et al., 2013; Liston et al., 2016). Sufficient wind speeds are particularly likely in flat or wind exposed areas (Mott et al., 2018). The wind speed threshold for transport generally increases with time the snow was deposited and air temperature, which determines, e.g., snow hardness (Liston et al., 2016).

Other factors controlling the probability of blowing or drifting snow transport include the microstructure of snow crystals, the snow surface roughness and cohesion (Liston et al., 2016; Mott et al., 2018). Cohesion increases with snow density, snow grain size and liquid water content, with dry, dendritic newly fallen snow being the easiest to mobilise (Mott et al., 2018 and references therein).

As snow particles are transported, they collide with each other. Laboratory experiments show that snow particles deposit partly at the collision point at wind speeds of 2 m s^{-1} and 3 m s^{-1}, but are transported further at wind speeds above 5 m s^{-1} (Sato et al., 2008). In general, the higher the wind speed, the more snow load is transported downwind (Liston et al., 2016).

The frequency of wind induced snow transport is subject to annual and interannual variabilities. These are caused by the probability of strong winds and snowfall occurring throughout the year and the changes in snow properties over time. For example, wet snow e.g., common during spring, has clearly higher cohesive forces between snow grains than dry snow leading to a lower probability of snow drift or blowing snow (Vionnet et al., 2013).

During precipitation that is accompanied by drifting or blowing snow redistribution, an immediate integration of the newly fallen snow into the existing snowpack at the place of precipitation does not always occur (Keenan et al., 2021). Due to wind redistribution and fast metamorphism, newly fallen snow layers are present only for a short time (Derksen et al., 2014). However, when denser layers are deposited over a lower density layer, they can preserve the lower density layer (Dominé et al., 2002).

The physical properties of snow, such as the roughness of the snow surface, are altered during snow redistribution (see II.c in Chapter 3.3.1) (Mott et al., 2018). Furthermore, the snow particles are sorted gravitational during wind deposition. This results in smaller particles being closer to the snow surface (Warren, 1982). Thus, the snow surface has a higher albedo than a surface without wind effects. Albedo increases with smaller grain sizes because a photon must travel shorter distances through the snow before being scattered, decreasing the probability of absorption (Warren, 1982; Gardner and Sharp, 2010).

3.3.3 Sublimation

Snow sublimation can be separated into three different features (Mott et al., 2018 and references therein)

(1) Sublimation at the snow surface

(2) During blowing snow events

(3) In connection with vegetation

In the non-forested Arctic, sublimation appears at the snow surface and during blowing snow events. It is controlled by air temperature, humidity, solar radiation, particle size and wind speed among other variables of the surface energy balance (Liston and Sturm, 1998; Gordon et al., 2006; Liston and Hiemstra, 2011; Vionnet et al., 2014; Mott et al., 2018). Thereby, Figure 3.12 presents the relationship between wind speed and sublimation rates calculated using different parameterisations for an Arctic site in Canada for constant solar radiation, relative humidity and air temperature. In addition, Liston and Sturm (1998) found an increase of 10 % in sublimation for wind speed of 5.4 m s^{-1} compared to 4.0 m s^{-1}.

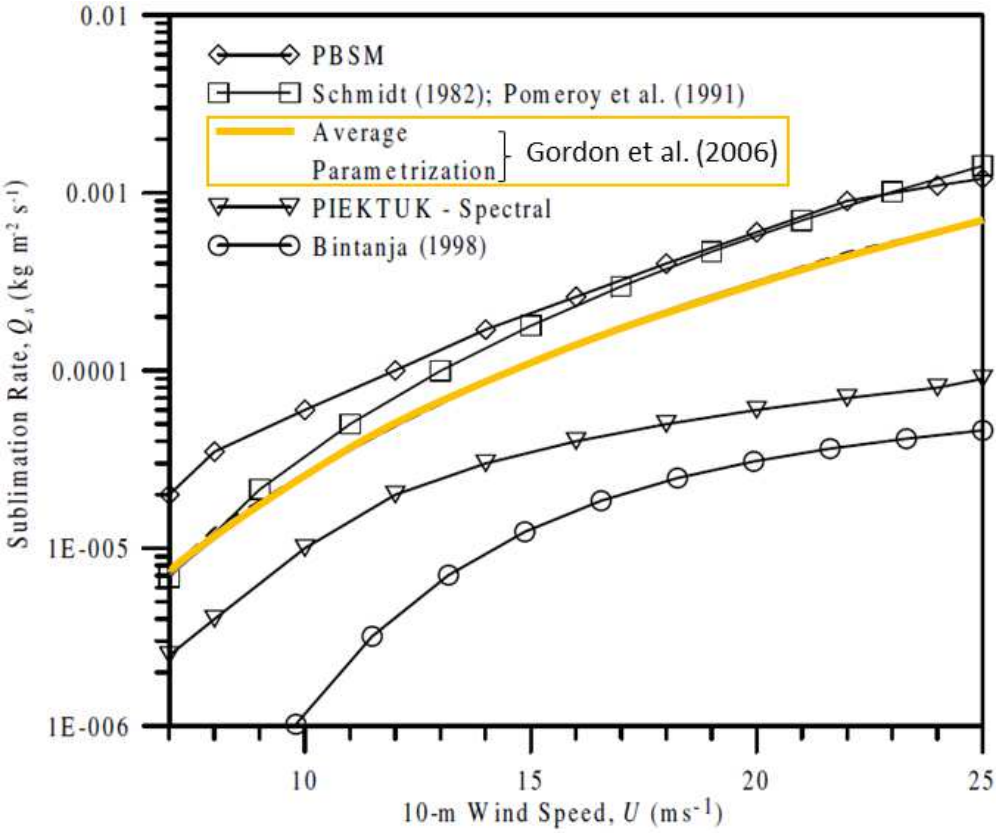

Figure 3.12: Sublimation rates calculated after different parameterisations for a fetch of 500 m in the Canadian Arctic, incoming solar radiation of 120 W m^{-2}, relative humidity of 70 %, relative humidity with respect to ice of 77 % and air temperature of -10°C at 2 m height (see Gordon et al. (2006) for more details). The yellow line visualises the parameterisation used in the snow model Crocus, as described in Chapter 5.2 (modified after Gordon et al., 2006).

The importance of sublimation for the snow mass balance (see Chapter 3.2.3.1) depends on the accumulated snowfall within a year. In years with low snowfall sublimation likely plays a more important role than in years with high snowfall (Sexstone et al., 2016). Several studies from Liston and Sturm (1998, 2002; 2004) show the importance of snow sublimation for the Arctic water balance, as sublimation accounts for between 10 % and 50 % of total winter precipitation.

Sublimation of snow leads to a latent heat flux towards the atmosphere and thus causes an energy loss for the snowpack (see equation (3.1)). While the intensity of sublimation depends on meteorological conditions, sublimation increases humidity and decreases temperature of the lower boundary layer. From the mass balance point of view of the snowpack sublimation leads to the transport of water from the solid snow surface or blowing snow particle towards gaseous water in the atmosphere causing a mass loss for the snowpack (see equation (3.3)) (Mott et al., 2018).

Blowing snow sublimation

The highest proportion of sublimation (78 %) is caused by blowing snow sublimation (Vionnet et al., 2013). Several studies analysed total mass loss due to blowing snow sublimation resulting in 9 % to 41 % for the regions Alaska (Liston and Sturm, 1998, 2002), Canadian Prairies (Pomeroy and Gray, 1995) and Trail Valley Creek, Canada (Pomeroy et al., 1997), whereby most studies showed around 20 % losses.

Wind leads to enhanced sublimation under unsaturated ambient air conditions with respect to ice causing rounding of the snow crystals and a destruction of microstructures (Cabanes et al., 2002; Dominé et al., 2002; Vionnet et al., 2013; Lafaysse et al., 2017). Thereby, conditions during wind induced sublimation

are favourable for rapid sublimation "because of the high ratio of particle surface area to mass, excellent ventilation of blowing snow particles and atmospheric water vapour deficit" (Pomeroy et al., 1997).

During wind induced snow transport, sublimation is highest close to the ground, where most snow particle are transported, and decreases with altitude (Vionnet et al., 2014). Thereby, snow mass is lost, as sublimation lowers the snow concentration in the atmosphere and alters accumulation. Due to the gross snow mass loss through sublimation, it plays a major role in the spatial distribution of snow, especially at the end of winter (Liston and Sturm, 1998; Vionnet et al., 2014). Further, sensible heat is lost to the atmosphere, while wind induced sublimation acts as a source for water vapour (Vionnet et al., 2013).

Further, within the surface boundary layer relative humidity increases with respect to ice during wind induced sublimation, whereby the increase is greatest close to the surface and decreases with height. The same is true for potential temperature causing also an increase in the potential temperature gradient leading to a more stable surface boundary layer (Vionnet et al., 2013).

Sublimation at the snow surface

"By surface snow sublimation, we refer solely to the turbulent mass exchanges between the surface of the snowpack and the atmosphere, excluding the sublimation associated with blowing snow event" (Brun et al., 2013). For the Colorado Rocky Mountains surface sublimation amounted to 13 % to 17 % of winter precipitation (Sexstone et al., 2016).

Higher wind speeds enhance surface sublimation due to higher turbulences at the surface layer (Sexstone et al., 2016). Dryer and warmer air conditions lead to a higher sublimation rate (Liston and Sturm, 1998; Mott et al., 2018 and references therein). Another factor controlling surface sublimation is the vapour pressure gradient from the surface towards the atmosphere, which builds up when the snow surface is comparably warm and humidity low (Pomeroy et al., 1997; Sexstone et al., 2016).

Sublimation at the snow surface undergoes a diurnal cycle, like wind speed, net radiation, air temperature snow surface temperature and relative humidity, which determine the amount of snow lost through sublimation (Brun et al., 2013; Sexstone et al., 2016; Mott et al., 2018 and references therein). Surface sublimation is therefore highest during early afternoon when surface promoting conditions prevail. Further, surface sublimation is higher during the melting period than during the snow accumulation period and in general increase with time of the snow season (Sexstone et al., 2016).

3.4 Physical snow characteristics

In the following subchapter, further information about snow density and specific surface area (SSA) is given, as these are two important snow variables analysed in this dissertation. Both snow variables were measured during a campaign in spring 2018 in northeast Greenland (see description in Chapter 4) and are used to investigate the performance of the snow model Crocus (see description in Chapter 5).

3.4.1 Snow density

Density is defined as total mass per volume and has the unit kg m^{-3} (Fierz et al., 2009). The initial density of the newly fallen snow and the prevailing metamorphism state of the snow particle (see Chapter 3.3.1) determine snow density.

Factors leading to high densities include high precipitation rates, warm air temperatures, strong winds and long lasting snow seasons (Bormann et al., 2013). In this context, densification rates increase around mid to late spring as internal seasonal snow melt processes lead to increased densification (Bormann et al., 2013). This is due to the presence of liquid water and refreezing (Sturm and Holmgren, 1998).

Density of snow varies spatially. The spatial variability of snow density is introduced, e.g., by regional differences in solar radiation and wind exposure, aspect, slope and the presence and type of vegetation (see Chapter 3.2) (Sturm et al., 2010; Bormann et al., 2013). Thereby, higher bulk densities and lower snow depth can be found in regions with high wind speeds, e.g., Arctic, than in wind protected areas (Sturm et al., 1997; Domine et al., 2008; Sturm et al., 2010). "Bulk density" refers to the average density over all snow layers in the full vertical profile of a snowpack (Sturm and Holmgren, 1998).

In general, seasonal snow density in the Arctic ranges from about 10 kg m^{-3} for newly fallen snow of dendritic shape to 610 kg m^{-3} for dense wind slab layers (Sturm et al., 1997; Domine et al., 2008 and references therein). However, the average snow density of an Arctic snowpack is in the range of 200 kg m^{-3} to 400 kg m^{-3}, and thus air is the main component of the snow (Domine et al., 2008). For Svalbard, Sauter and Obleitner (2015) found snow densities in the upper layers ranging from 100 kg m^{-3} to 200 kg m^{-3}.

Factors controlling new snow density are degree of riming, grain size and shape. In general grain sizes are smaller when falling at colder air temperatures and can lead to higher densities as they can be packed closer together than bigger snow particles (Judson and Doesken, 2000). Judson and Doesken (2000) found a weak correlation between new snow density and air temperature, whereby density decreased with temperature between 0°C and -20°C.

Domine et al. (2008) found typical newly fallen snow densities between 10 kg m^{-3} to 200 kg m^{-3} for different regions. Judson and Doesken (2000) reported snow densities for newly fallen snow between 10 kg m^{-3} and 350 kg m^{-3} measured in the United States. Thereby, they found lower new snow densities at sites with trees and sheltered from wind (10 kg m^{-3} to 257 kg m^{-3}). At sites with frequent storm occurrence new snow densities were above 100 kg m^{-3}. In general, 72 % of all new snow densities were between 50 kg m^{-3} and 100 kg m^{-3} (Judson and Doesken, 2000).

Depth hoar that underwent high temperature gradient metamorphism (see II.a in Chapter 3.3.1) has low densities around 200 kg m^{-3} (Domine et al., 2008). But also higher densities for depth hoar of up to 350 kg m^{-3} were reported for instance by Sturm et al. (1997). Snow layers affected by wind drift (see II.c in Chapter 3.3.1) typically have densities in the range of 300 kg m^{-3} to 600 kg m^{-3} (Sturm et al., 1997; Domine et al., 2008).

3.4.2 Snow specific surface area (SSA)

Defined after Fierz et al. (2009) "[T]he classical grain size […] of a snow layer is the average size of its grain. The size of the grain or particle is its greatest extension measured in millimetres." In snow models it was common to use grain size and semi-empirical shape variables, e.g., dendricity defined as "the ratio of the square of the perimeter of a grain to its area" (Bartlett et al., 2008) and sphericity defined as "the ratio of rounded versus angular shapes" (Lefebre et al., 2003), to parametrise snow processes such as metamorphism (Vionnet et al., 2012; Carmagnola et al., 2014). However, such snow variables are difficult to measure in the field, their determination is often subjective and observer dependent and these variables are difficult to relate to other snow variables (Carmagnola et al., 2014; Leppänen et al., 2016). Instead, the optical grain size, which is the ratio of the spheres that have the same albedo, can be easily quantified and linked to other snow properties and is therefore used in newer versions of snow models (Carmagnola et al., 2014; Calonne et al., 2020), which consider optical grain size as equal to the effective grain size (Carmagnola et al., 2014).

The effective grain size is the diameter of independent spheres with the same surface area to volume ratio as the snow (Grenfell and Warren, 1999; Gallet et al., 2009). It is inversely proportional related to SSA (Gallet et al., 2009; Kinar and Pomeroy, 2015). The relationship is as follows

$$SSA = \frac{6}{\rho_{ice}\, d_{eff}} \tag{3.5}$$

whereby d_{eff} is the effective grain size and ρ_{ice} the density of ice (917 kg m^{-3} at 0°C) (Gallet et al., 2009).

Thereby, SSA is the surface area of a defined snow volume accessible to gases divided by its mass expressed in the following equation (Legagneux et al., 2002; Taillandier et al., 2007; Gallet et al., 2009; Libois et al., 2013)

$$SSA = \frac{S}{M_a} = \frac{S}{\rho_{ice}\, V} \tag{3.6}$$

with S being the surface area, M_a the mass and V the volume of the snow particles. SSA has the units m^2 kg^{-1} or m^2 m^{-3} as it can be referred to the total surface area of the air/ice interface per unit mass or per ice volume. Multiplying the density of ice to SSA related to unit mass, the SSA related to unit volume can be calculated (Fierz et al., 2009).

A high correlation between SSA and snow spectral albedo in the shortwave infrared was found by Domine et al. (2006a). This builds the base for the development of instruments measuring SSA in the field using an optical method by applying its reflectance, e.g., IceCube (A2 Photonic Sensors, 2016; Gallet et al., 2009; see Chapter 4.3). Indeed, Domine et al. (2006a) concluded that snow spectral albedo in the shortwave infrared is physically mainly controlled by SSA thus making it to a good variable to determine shortwave infrared reflectance.

Dry new snow, especially dendritic snow, has a high SSA of about 74.1 ± 26 m^2 kg^{-1} on average, whereas snow falling above 0°C has a lower SSA of about 50.3 ± 11.2 m^2 kg^{-1} on average. Variability within the SSA of new snow is caused by sublimation during precipitation. Other factors determining new snow SSA are ice nuclei concentrations, cooling rate, available moisture, the temperature profile of the atmosphere and breaking of snow particles during wind events (Domine et al., 2007).

After deposition, near surface SSA undergoes daily, weekly and seasonal variations (Libois et al., 2015). Measured SSA show values ranging from 224 m^2 kg^{-1} for diamond dust (i.e. tiny ice crystal precipitation mostly formed under clear sky conditions (Walden et al., 2003; Intrieri and Shupe, 2004)) to 2 m^2 kg^{-1} for melt-freeze layers (Domine et al., 2007; Domine et al., 2012).

In general, SSA decreases over time due to snow metamorphism (see Chapter 3.3.1) causing increasing snow density and grain size (Legagneux et al., 2002; Domine et al., 2007; Fierz et al., 2009; Carmagnola et al., 2014). Factors leading to changes in SSA over time are air temperature and absorption of solar radiation that are especially important during spring and summer (Libois et al., 2015). Thereby, the higher the temperature the faster decreases SSA (Taillandier et al., 2007).

Snowfall and diamond dust events lead to fast increase in surface SSA as the deposited snow particles have high SSA (90 – 120 m² kg^{-1}). Libois et al. (2015) found a decrease of SSA after a snowfall event from 90 to 30 m² kg^{-1} within 10 days. Further, strong winds lead to a fast decrease of surface SSA by blowing away new snow layers with a high SSA and exposing older snow layers with a lower SSA (Domine et al., 2006a; Libois et al., 2015). Thus, rapid decrease of surface SSA are caused by erosion of snow while slow decrease of surface SSA is due to metamorphism (Libois et al., 2015).

Another important relationship exists between SSA and albedo (Domine et al., 2006a). As SSA decreases, snow albedo decreases (Carmagnola et al., 2014). Therefore, higher surface SSA leads to a stronger absorption of energy than lower surface SSA impacting the energy balance of the snow surface (Taillandier et al., 2007; Tuzet et al., 2020).

In terms of climate change, variations in SSA can trigger both positive and negative effects in the radiative forcing. If all other circumstances concerning SSA remain the same, the following considerations can be made: As SSA decreases with increasing temperature, snow albedo decreases causing a positive feedback. Further, with increasing precipitation temperature gradients between the snow surface and the soil may decrease potentially to such an extent that the metamorphism regime (from temperature gradient to isothermal conditions) changes. This results in a slower decrease in SSA and thus in albedo, causing a negative warming feedback (see Chapter 2.2) (Taillandier et al., 2007).

3.5 Arctic snow in a changing climate

3.5.1 Recent, present and future changes

These subchapters provide an overview of changing snow conditions and the impacts of BC in snow on the radiative forcing. In this subchapter, recent, present and future changes in Arctic snow cover and snow properties are presented. Future warmer air temperatures will have the effect that even at higher altitudes and further north there will be more areas where the snow cover is sensitive to temperature variations, e.g., due to intrusions of warm air (Mudryk et al., 2018).

Snow mass and snow cover extent

Estimates of the annual maximum total snow mass reached in March for the years 1980 – 2018 for the Northern Hemisphere above 40°N excluding Alpine regions are 2846 Gt – 3062 Gt, resulting in a SWE of 90 mm water equivalent (w.e.) to 97 mm w.e. (Pulliainen et al., 2020). In general, March snow mass is declining for the period 1980 – 2018 in the Northern Hemisphere (-49 Gt decade^{-1}), but trends depend on the region. In regions of Siberia and at coastal regions, e.g., around the Arctic Ocean, the trend is towards more snow mass, while in Europe, Yukon, Alaska and around Hudson Bay snow mass is declining. Further, Pulliainen et al. (2020) found a coupling between high snowfall amounts and the absence of sea ice cover.

A decline in snow cover has been observed in recent decades (Hernández-Henríquez et al., 2015; Box et al., 2019; Overland et al., 2019). The observation of maximum decline varies across studies. Overland et al. (2019) reported a maximum decline in spring, while Hernández-Henríquez et al. (2015) found a maximum decline in mid-June. However, the development of the snow cover extent depends on elevation and latitude (Hernández-Henríquez et al., 2015).

In the time period from 1972 – 2006, spring snow cover in the Northern Hemisphere decreased by 1.28 x 10^6 km^2 (Déry and Brown, 2007). Further, Box et al. (2019) found a reduction in snow cover extent of more than 30 % in May to June from 1971 to 2017 on Arctic land areas.

The trend towards a decline in snow cover extent accelerated between 2007 and 2014. High latitudes (60 N - 70°N) are affected strongest. In these regions changes in the surface energy balance are therefore expected to be highest (Hernández-Henríquez et al., 2015). There is evidence that a decrease in snow cover has similar effects on warming as a decrease in sea ice extent (Bekryaev et al., 2010 and references therein).

The trend of decreasing snow cover extent is projected to continue (Overland et al., 2019). For the Canadian Arctic, for example, snow loss is projected for the coming years, especially in October to November and May to June, while changes in winter snow cover extent are small, as winter temperatures are projected to stay below the freezing point in the coming years (Mudryk et al., 2018).

Snow season

The amount of solid precipitation, together with air temperatures and solar radiation, control the length of the snow season (Liston and Hiemstra, 2011). There is common evidence that the snow cover season in the Arctic has declined in recent decades (Chapin et al., 2005; Liston and Hiemstra, 2011; Box et al., 2019), leading to earlier warming of the lower atmosphere through sensible heat (Chapin et al., 2005).

The snow season is reduced by earlier melting in spring and later formation of a snow cover in autumn (Chapin et al., 2005; Liston and Hiemstra, 2011; Hernández-Henríquez et al., 2015; Box et al., 2019 and references therein; Wendisch et al., 2019). Thereby between 1979 and 2009, snow cover formation was delayed on average by 1.3 days decade^{-1} in 65 % of the Arctic, ranging regionally from -10.8 days decade^{-1} to +14.1 days decade^{-1}. Complete melting of the snow cover in spring occurred on average 1.3 days decade^{-1} earlier for 80 % of the Arctic, ranging from -9.9 days decade^{-1} to +3.7 days decade^{-1} (Liston and Hiemstra, 2011). Similarly, Box et al. (2019) reported the time snow covers the ground in spring declined by 15.5 days (3.4 days decade^{-1}) in the Arctic (>60°N) between 1972 and 2017, with strongest changes observed at high latitudes and altitudes, where warming in the Arctic is greatest.

Projections show shorter seasons when snow or ice cover the land and ocean, as the onset of ice and snow cover formation is delayed and melting starts earlier. For example, a 10 % – 20 % shorter snow season is projected by 2050 under the RCP 4.5 scenario (Overland et al., 2019).

Snow properties

Analyses for the years 1979 to 2018 revealed an increase in days with wet snowpacks, probably caused by warmer air temperatures in spring and autumn. In autumn, increased rain also causes more frequent wet snowpacks (Royer et al., 2021).

For the same period, increases in near surface density (spring: +0.58 kg m^{-3} year^{-1}, September: +0.45 kg m^{-3} year^{-1}, October: +0.34 kg m^{-3} year^{-1}) were found during melt and rain on snow events, as well as in bulk density (+0.51 kg m^{-3} year^{-1}) (Royer et al., 2021). Snow density in the Arctic also increased between 1979 to 2009, with values ranging regionally from -21.0 kg m^{-3} decade^{-1} to +15.4 kg m^{-3} decade^{-1} (Liston and Hiemstra, 2011). An increase in snow density also affects other properties of snow, such as the insulating effect or thermal conductivity, which is enhanced by a more frequent occurrence of wet snow (Royer et al., 2021).

Another aspect that is altered due to climate change is, e.g., snow sublimation, which decreased in 77 % of the Arctic between 1979 and 2009 (Liston and Hiemstra, 2011). Further, there may be more ice layers within the snowpack in the future because of rain on snow events and because of an increase in winter thaw events (Box et al., 2019 and references therein). Already over the last decade, decreasing winter sea ice has led to more frequent warm air intrusions in winter and rain on snow events early in the season (Landrum and Holland, 2020).

In summary, changes in Arctic snow cover, its duration and properties vary regionally (Liston and Hiemstra, 2011; Mudryk et al., 2018). There are regions with increasing SWE and longer snow covered periods between 1979 and 2009, while others have experienced a decline. However, the overall trend in the Arctic is clear: Arctic snow cover extent and duration are decreasing, with earlier melting in spring and later formation of snow cover in autumn, and lower maximum winter SWE (Liston and Hiemstra, 2011; Mudryk et al., 2018). Thereby, 75 % of the Arctic area showed a reduction of snow cover season by -2.6 days decade^{-1}, regionally ranging from -17.0 days decade^{-1} to +8.1 days decade^{-1} (Liston and Hiemstra, 2011).

3.5.2 Black Carbon (BC) in Arctic Snow

BC particles in Arctic snow are among those responsible for the rapid rise in temperatures in the Arctic. BC particles are the component of atmospheric aerosol with the strongest sunlight absorption (Flanner et al., 2007; Bond et al., 2013; AMAP, 2015; Schulz et al., 2019). The origin of BC particles is incomplete combustion (Warren, 1984). BC particles are produced by anthropogenic sources, e.g., burning of coal and oil, diesel engines, agriculture caused bush fires, e.g., for land conversion rotational agriculture, and from natural sources, e.g., forest fires (Warren, 1984; Bond et al., 2013; Barlow et al.,

2020). Thereby, the amount of BC in the environment is dominated by anthropogenic sources (Laborde et al., 2012). In 2004, the following amounts of emissions caused global BC concentrations: 34 % wildfires, 1 % shipping, and 65 % other anthropogenic sources (Browse et al., 2013).

The produced particles can be distributed regionally and intercontinentally via long distance transport (up to several thousands of kilometres) until they are removed from the atmosphere by wet deposition and by dry deposition (Doherty et al., 2010; Bond et al., 2013; Sinha et al., 2018; Yang et al., 2019; Mori et al., 2020). In the Arctic, BC sources are limited. Thus, most of the BC particles found in the Arctic are transported to the Arctic from the mid-latitudes (Bond et al., 2013). According to Stohl (2006) there are three different transport ways that can bring BC particles into the Arctic: "low-level transport followed by ascent in the Arctic, low-level transport alone, and uplift outside the Arctic, followed by descent in the Arctic." Thereby, not all pathways are possible for a transport from all regions and for all seasons. The transport from North America and Asia mostly occurs via the "uplift" pathway. Transport from Europe occurs along all three pathways during winter but during summer there is no "low level transport alone" (Stohl, 2006).

One reason for that is a "dome" of cold air in winter and spring that makes transport from the lower-latitudes towards the Arctic more difficult. Due to its regional extension, air masses from Eurasia can enter the Arctic troposphere during that time easier than from North America (Bond et al., 2013). In addition, during the time the polar dome is present in the Arctic, BC produced in the Arctic accumulates in the polar boundary layer (Mori et al., 2020).

In general, the time BC particles need to reach the Arctic in winter is usually short: 25 % reach the Arctic within 4 days, 50 % need 9 days and 15 % need longer than 20 days. Furthermore, in winter BC particles in near surface air are about a week old while they are only about 3 days old in altitudes of 5 km - 8 km (Stohl, 2006).

Fossil-fuel pollution seems to be the main source for BC particles in Svalbard, Tromsø, Norway, and Western Russia, whereas biomass burning is likely the main source for Greenland (in spring) and the Alaskan/Canadian Arctic (Doherty et al., 2010; Mori et al., 2020). In summer, boreal fires are an important source of BC particles. Thereby, the BC amount from boreal fires is clearly lower than that from anthropogenic emissions. In contrast to most anthropogenic sources, particles coming from boreal fires are produced higher up north (Stohl, 2006).

Atmospheric BC concentration undergoes a seasonal cycle. For instance, for a site in Svalbard, Gogoi et al. (2018) found maximum BC concentrations in the atmosphere in spring (median ~29 ng m^{-3}) and minimum concentration during summer (median ~11 ng m^{-3}). Daily mean values reached values higher than 150 ng m^{-3}. This higher atmospheric BC concentration in spring and lower concentrations in summer and during the polar day is typical for the Arctic (Donth et al., 2020). In the Arctic, annual spring variations in the amount of tropospheric BC are related to annual variations in open biomass burning (Ohata et al., 2021).

Modern high-resolution regional chemical transport models can simulate parts of the processes, e.g., the timing of deposition events, possible pathways and sources of BC particles, but are still insufficient to simulate realistic BC deposition rates. They tend to underestimate BC deposition by a factor of 2 - 100. Furthermore, the simulations suffer on uncertainties in forcing data such as emission rates of wildfires and ambiguity in the parameterisation of wet removal of aerosols add to the weaknesses of the models (Thomas et al., 2017). In many models, the sensitivity of BC on global atmospheric absorption is assumed too low. The shortcomings of the models are caused as well by underestimation of BC concentration in the atmosphere and issues in simulating absorption due to BC mixed with other particles correctly (Bond et al., 2013). Nevertheless, Ohata et al. (2021) found that model simulations of atmospheric BC mass concentrations are in agreement with observations when emissions are mainly caused by anthropogenic sources but underestimate the concentration when the main source of BC is open biomass burning.

Beside the atmospheric influence from BC, there is also a strong effect after deposition in snow. BC belongs to the so-called light absorbing impurities (LAI), which reduce the reflectivity and thus the albedo of surfaces (Warren, 1984; Flanner et al., 2007; Bond et al., 2013; Doherty et al., 2013; Sinha et al., 2018; Yang et al., 2019). Apart from BC, LAIs include, for instance, dust, and volcanic ash as well as living particles such as algae. Thereby, the effect BC has on snow albedo is about 50 times stronger than dust and 200 times stronger than ash for the same mass of LAI (Warren, 1984). For this reason, it was decided that only BC from the LAIs is further addressed in this dissertation. As a follow-up work, other LAIs may be considered in the future. BC in snow leads to increased absorption of radiation, contributing to a warming of the snowpack, the underlying layers and the surface air. Therefore, this process is called "snow darkening". The reduction of snow albedo accelerates snow melt due to enhanced radiative forcing. Thus, BC in the Arctic contributes to warming in the Arctic and can influence the global climate (Budyko, 1969; Flanner et al., 2007; Doherty et al., 2010; Bond et al., 2013; Doherty et al., 2013; Gogoi et al., 2018; Sinha et al., 2018; Yang et al., 2019).

Due to its high albedo snow absorbs solar radiation in the visible and near-ultraviolet range only to a small fraction. BC particles influence the albedo of snow and ice in the wavelength range where the absorption of ice is lowest ($\lambda < 0.9$ µm) (Warren, 1982; Doherty et al., 2010; Gardner and Sharp, 2010). Thus, already small concentrations of BC particles can change the amount of absorbed solar radiation at those wavelengths drastically (Doherty et al., 2010; Bond et al., 2013; Jacobi et al., 2019).

Deposition of BC is caused by two different mechanisms, either by precipitation called "wet deposition" or by sedimentation or turbulent diffusion called "dry deposition" (Doherty et al., 2013; Tuzet et al., 2017; Jacobi et al., 2019). Considering that BC is chemically inert, dry and wet deposition is the only sink of BC in the atmosphere (Yang et al., 2019). Thereby, BC is removed from the atmosphere within a few days to weeks (Bond et al., 2013). Model simulations estimate a lifetime of atmospheric BC north of 66.5°N in April of 11.9±2.8 days and the annual average lifetime to 11.5 days to 12.1 days (Ohata et al., 2021 and references therein).

The deposition of BC in snow is influenced by the BC concentration in the atmosphere, the aging of BC, how efficiently BC is removed from the atmosphere by wet deposition and the prevailing meteorological conditions (Gogoi et al., 2018). Thereby, inversions in the boundary layer during winter and spring that often occur in the Arctic limits turbulent exchange, i.e. dry deposition. In addition, wet deposition is restricted due to a dry atmosphere. Therefore, aerosols have a high lifetime during winter in the Arctic (Stohl, 2006). In falling snow, only the wet deposition rate controls the BC concentration (Sinha et al., 2018).

There is a lack of knowledge concerning the processes and impacts of deposition, which is also caused by a lack of BC flux measurements (Sinha et al., 2018; Mori et al., 2020). Several studies found that most BC content in snow is caused by wet deposition (e.g. ,Flanner et al., 2007; Sinha et al., 2018; Yang et al., 2019; Mori et al., 2020). Nevertheless, the knowledge about other environmental processes that might impact the BC concentration in snow is still limited (Bertò et al., 2021).

Mori et al. (2020) found from simulations that removal of atmospheric BC by wet deposition accounts for about 90 % of the total deposition. Thereby, observations for Barrow, Alaska, show that 50 % of the total annual deposition occured during three months in summer when precipitation rates were high emerging from biomass burning (Mori et al., 2020). Yang et al. (2019) found even higher fractions of wet deposition over the Arctic of up to 98 % of total deposition.

For a site near Ny-Ålesund, Svalbard, Sinha et al. (2018) found wet deposition rates of 0.328±0.055 mg m^{-2} in falling snow, 0.491±0.093 mg m^{-2} for a glacier site and 0.21±0.4 mg m^{-2} for a site in a valley for September 2012 to April 2013. For Barrow, Alaska, Mori et al. (2020) measured the highest median monthly wet deposition flux of 0.24±0.20 mg m^{-2} $month^{-1}$ in summer (2013 - 2017) and much lower values in spring (0.056 mg m^{-2} $month^{-1}$) due to differences in monthly precipitation. For October to April, they found low wet deposition rates due to low precipitation rates. Furthermore, they

calculated an annual BC wet deposition amount of 1.35 mg m^{-2}, whereby about half (0.71 mg m^{-2}) occurred during three months in summer.

The climatic effects of BC in the Arctic are still under discussion and are subject to large uncertainties. This is because the mechanisms are complex and not fully understood. This applies in particular for the processes after deposition of BC in snow (Bertò et al., 2021). These factors include BC particle redistribution and relative humidity. These variables are related to snow sublimation and the formation of surface hoar as well as evaporation of wet snow, which all influence the relative BC concentration (Doherty et al., 2013; Gogoi et al., 2018; Sinha et al., 2018; Bertò et al., 2021). The post-depositional processes, snow melt and sublimation lead possibly to a relative increase in BC mass in the snowpack when water mass is removed (Bertò et al., 2021).

One process that is especially present during snow melt is scavenging of BC (Warren, 1984; Flanner et al., 2007; Doherty et al., 2010; Doherty et al., 2013; Bertò et al., 2021). Scavenging of BC happens when liquid water percolates through the snow, transporting BC particles from the upper snow layers to the underlying snow layers (Tuzet et al., 2017). Thereby, BC particles accumulate in surface snow as meltwater is more efficiently transported from the surface than BC particles because BC particles are hydrophobic. Thus, during the melting season, BC concentration in the upper snowpack is enhanced as water mass is lost (Warren, 1984; Flanner et al., 2007; Doherty et al., 2010; Doherty et al., 2013; Bertò et al., 2021).

Doherty et al. (2013) estimated BC scavenging fractions for BC of about 10 % – 30 % for sites in Alaska and Norway and of about 20 % – 30 % for a site in Greenland. This process leads to a positive feedback as it acclearates the decreases of the snow albedo leading in turn to acclearated snow melt (Flanner et al., 2007; Doherty et al., 2010; Doherty et al., 2013).

The effect of lowering the snow surface albedo due to BC particles is also related to snow age, as it determines the effective radius of snow particles and therefore snow reflectance. Aged snow has larger grain sizes (and thus smaller SSA) than newly fallen snow (having higher SSA). Thereby, in snow with a larger effective radius the same amount of BC particles reduces the albedo more than in snow with smaller effective radius. Because snow with a larger effective radius has a smaller extinction coefficient and scatters more light in the forward direction, visible light can penetrate deeper into the snowpack. In contrast, snow with smaller particles backscatters the incident radiation more than larger snow particles. With increasing path length of the photons in snow with larger grain size the probability of being absorbed by BC particles rises (Warren, 1982; Flanner et al., 2007; Gardner and Sharp, 2010; Donth et al., 2020). For instance, for a BC concentration in snow of 50 ng g^{-1} and a snow grain radius of 100 µm (new snow) the albedo reduction is 0.03 while for a grain radius of 1000 µm (old melting snow) the albedo decreases by 0.08 (Doherty et al., 2010; Donth et al., 2020).

As the snow absorbs more sunlight due to these post-depositional processes, there is a positive feedback mechanism: the snow absorbs more heat leading to accelerated metamorphism, which causes a faster growth of snow grains (snow grain size increases), and thus darker snow surface. This is visualised in Figure 3.13. Furthermore, sublimation due to warming snow is increased, which leads as well to accumulation of BC particles at the snow surface (Flanner et al., 2007; Bond et al., 2013; Tedesco et al., 2016).

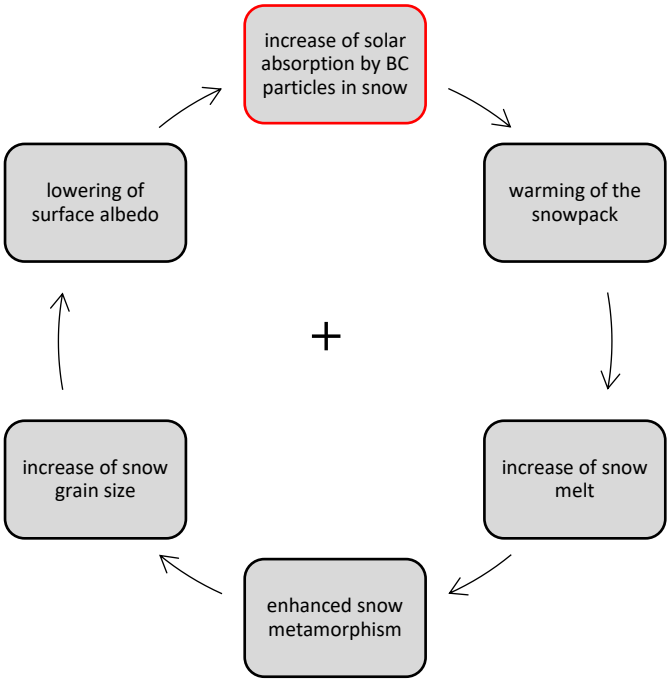

Figure 3.13: Positive feedback mechanism after deposition of black carbon in snow (own drawing).

While atmospheric BC shows the above described seasonal cycle, BC in snow seems to be not fully linked to this. For a site in Barrow, the BC concentration in ambient air near the surface showed a seasonal variation, while the BC concentration in rain and snow did not. The BC concentration in rain and snow was high in early winter, spring and midsummer and was generally uncorrelated with BC concentration in ambient air near the surface (Mori et al., 2020). In addition, the maximum BC concentrations in the snow on the Greenland ice sheet are reached in summer (~June - August) (Polashenski et al., 2015). Also, other studies found that the BC concentration in the upper snowpack is not directly linked to the BC load in the atmosphere (Bertò et al., 2021). Sinha et al. (2018) suggested that the BC concentration in the snowpack is not only controlled by the concentration in the boundary layer but also by the concentration in the upper atmospheric layers because they found weak correlations between the BC concentration in snow and in the boundary layer.

Since 1989, the BC concentration in the Arctic atmosphere have decreased considerably, which is also reflected in the BC concentrations in snow. However, differences in measurement methods for BC concentration in snow might also have caused lower observed BC concentrations in snow (Doherty et al., 2010). Nevertheless, a BC content of 0.1 parts per million by weight (ppmw) in snow can lead to a reduction in albedo of several percent (Warren, 1982). Already in the early days, Warren (1984) wrote in his review that weight fractions of BC in snow where measured (1 to 6 x 10^{-8}). Thereby, a weight fraction of 5 x 10^{-8} can already reduce the albedo of new snow by 2.5 % and of metamorphosed snow by 7 %.

In general, BC concentrations in surface snow at lower latitudes are higher than at higher latitudes (see also Table 3.3). For the west Arctic (west from the North pole), BC concentrations increase with distance to the North Pole from ~5 ng g^{-1} to ~10 ng g^{-1} for lower latitudes and from ~8 ng g^{-1} for Arctic Alaska/Canada to 14 ng g^{-1} for sub-Arctic Canada. For Greenland, a median BC concentration of 3 ng g^{-1} was found. BC concentrations in the east Arctic (Tromsø, Norway, Russia) are about twice as high as for the Canadian Arctic located on the same latitude. In general, BC concentrations in the European Arctic vary more than in Arctic Canada or the Arctic Ocean (Doherty et al., 2010).

A daily mean solar radiation forcing of +0.2 W m^{-2} is reached for a BC concentration of 5 ng g^{-1} in surface snow and a minimum solar zenith angle of 55° when no atmospheric BC is assumed. These conditions represent typical summer conditions with a clear sky atmosphere. In general, for a BC concentration of 5 ng g^{-1} in surface snow representing clean conditions in the Arctic and a SSA of 20 m^2 kg^{-1} the radiative forcing is between +0.4 W m^{-2} and +0.7 W^2 m^{-2} (Donth et al., 2020).

However, events like forest fires can cause BC-rich layers. For instance, BC particles originating from a forest fire in Canada were transported through the troposphere and deposited in snow over the Greenland ice sheet in summer 2013. The formed layer had peak BC concentrations from 2.8 ng g^{-1} to 43 ng g^{-1} (mean 15 ng g^{-1}) (Thomas et al., 2017). BC concentrations during melt can exceed 200 ng g^{-1} on the melting surface snow. Doherty et al. (2013) found BC concentration in melt layers of up to 20 ng g^{-1} and in the snow layers below of 1 ng g^{-1} for a site in Greenland. Thereby, new snow had a concentration of 1 ng g^{-1} – 2 ng g^{-1}.

Table 3.3: Black carbon (BC) content in surface snow in various regions of the world continued after Tuzet et al. (2020), own table.

Regions	**Typical BC content [ng g^{-1}]**	**References**
Antarctic Plateau	0.2 – 0.6	Grenfell and Warren (1999); Warren et al. (2006)
Arctic	8-60	Doherty et al. (2010); Mori et al. (2019)
Greenland	0.8 – 4.5	Doherty et al. (2010); Mori et al. (2019); Polashenski et al. (2015)
Svalbard	0.2 – 13	Bertò et al. (2021); Gogoi et al. (2018); Doherty et al. (2010)
China	20 – 2000	Wang et al. (2013); Ye et al. (2012)
North America	5 – 70	Painter et al. (2012); Doherty et al. (2014)
French Alps	0 – 80	Tuzet et al. (2020)
Swiss Alps	0 – 50	Gabbi et al. (2015)
Arctic Ocean	7	Doherty et al. (2010)
Arctic Canada	8	Doherty et al. (2010)
Subarctic Canada	14	Doherty et al. (2010)

Flanner et al. (2007) simulated radiative forcing caused by BC in surface snow considering different values for, e.g. emissions and scavenging ratio, leading to a central, high and low estimate. They found that BC leads globally to an annual mean radiative forcing of +0.054 W m^{-2} (0.007 W m^{-2} - 0.13 W m^{-2}) for a strong boreal fire year with high BC emissions from biomass burning and +0.047 W m^{-2} (0.007 W m^{-2} - 0.12 W m^{-2}) for a weak boreal fire year considering fossil fuel, biofuel and biomass burning. If only fossil fuel and biofuel sources are considered, the radiative forcing is +0.043 W m^{-2}, showing that 80 % of the forcing is due to anthropogenic sources. Furthermore, simulations showed that the radiative forcing is maximal when the snow starts to melt in spring.

Flanner et al. (2007) simulated a global warming of 0.15°C (0.10°C) for strong (weak) boreal fire years due to effects of BC in snow. The annual mean albedo for a strong (weak) boreal fire year is 0.047 (0.017) smaller. Simulations using the strong fire year BC values show a radiative forcing of 1.5 W m^{-2} during June to July for areas between 80°N and 90°N.

In summary, radiative forcing due to BC particles in snow is highest when it falls together with (Flanner et al., 2007; Doherty et al., 2010; Donth et al., 2020)

(1) high BC surface concentrations in the upper snow layers being the case in spring and occurs with the start of the melt season;
(2) coarse grained snow (e.g., during melting, aged snow) having a lower albedo than fine grained snow and a higher effect for the same BC content;
(3) earlier melt and thus earlier expose of underlying surfaces with lower albedo;
(4) accumulation of BC particles during snow melt;
(5) low zenith angle;
(6) high amount of incoming solar radiation.

These conditions are reached in spring and summer, especially during the melting period (Donth et al., 2020).

4 Field measurements

> *"An experiment is a question which science poses to Nature and a measurement is the recording of Nature's answer."*
>
> *Max Planck*

The following subchapter provides a general overview on snow measurements as used for the studies presented within this dissertation. Therefore, the focus is on the physical snow property analysis performed in the field as well as on the analysis of snow samples in the lab. A brief overview on the field campaign during which the measurements were taken is included at the end.

4.1 Snowpits

Snowpit analysis are a common procedure to determine snow properties and the stratigraphy of a snowpack as presented by, e.g., Leppänen et al. (2016), Calonne et al. (2020), King et al. (2020). The term snowpit refers to a usually rectangular hole in the snowpack that commonly extends to the ground and is dug on an undisturbed snow surface with a shovel (Fierz et al., 2009; Kinar and Pomeroy, 2015). The snowpit wall, a smooth vertical wall of snow on which the measurements are taken, is exposed shaded from the sun (Fierz et al., 2009; Leppänen et al., 2016).

In a traditional snowpit focussing on the physical analysis of the snowpack, the following parameters are measured: snow depth and snow layer thickness with a ruler, grain shape and size by visual classification, snow hardness using the hand hardness index, snow density using a density cutter and snow temperature using a penetration thermometer (Fierz et al., 2009; Kinar and Pomeroy, 2015).

In addition, the snow wall is often used to determine the liquid water content of the snowpack by using, e.g., a snow fork, the SWE by taking snow cores and SSA by measuring either the infrared reflectance of the snow surface (measured by IceCube, Chapter 4.3) or the bonding force (measured by the SnowMicroPen (SMP), Chapter 4.4). In order to put the measurements into a local context, photos of the surrounding area of the snowpit, the sampled snow wall as well as of the defined snow layers are taken (Leppänen et al., 2016). In addition to physical snow measurements, chemical snow samples can be collected for later analyses in the lab (Armstrong and Brun, 2008).

4.2 Density Cutter

To measure snow density manually, a density cutter in combination with a scale can be used. There are different types and shapes of density cutters such as cylinder-, wedge-, or box-type cutters (Proksch et al., 2016). For this dissertation, all density cutter measurements were carried out with a box-type cutter with a size of 6 cm x 3 cm x 5.5 cm resulting in a sample volume of 100 cm^3. Thus, the vertical resolution is 3 cm. The measurement error of the box-type density cutter is about 10 %, however, the density is often overestimated for compacted snow densities and underestimated for low densities and fragile snowpacks (e.g., depth hoar) (Proksch et al., 2016; Calonne et al., 2020).

4.3 IceCube

The IceCube (see Figure 4.1) is a commercial instrument manufactured by A2 Photonic Sensors that provides SSA. The hemispherical reflectance of snow using shortwave infrared is related to snow SSA, as visualised in Figure 4.2 (Grenfell and Warren, 1999). The IceCube uses this relation to obtain SSA from hemispherical reflectance of a snow sample illuminated by a laser diode at a wavelength of 1310 nm. The reflectance is recorded as voltage using a signal-to-reflectance relationship. From the recorded reflectance, SSA is obtained using a radiative transfer model (Gallet et al., 2009; A2 Photonic Sensors, 2016).

The measurement error for SSA below 60 $m^2 kg^{-1}$ is about 10 % (Gallet et al., 2009; A2 Photonic Sensors, 2016; Calonne et al., 2020), whereby the manufactory gives an uncertainty of ±10 % for SSA values between 2 $m^2 kg^{-1}$ and 160 $m^2 kg^{-1}$. Within the calculation of the accuracy, uncertainties due to the reflectance measurement, the crystal shape, the calibration curve and systematic errors are taken into account (Gallet et al., 2009). A recent study from Martin and Schneebeli (2022) compared the indirect measurements of SSA with the IceCube with direct micro computed tomography (micro-CT) measurements. They found an overestimation of SSA measured with the IceCube of 20 – 52 % for snow with an SSA of 5 – 25 $m^2 kg^{-1}$ due to the destruction of the snow during the sampling preparation.

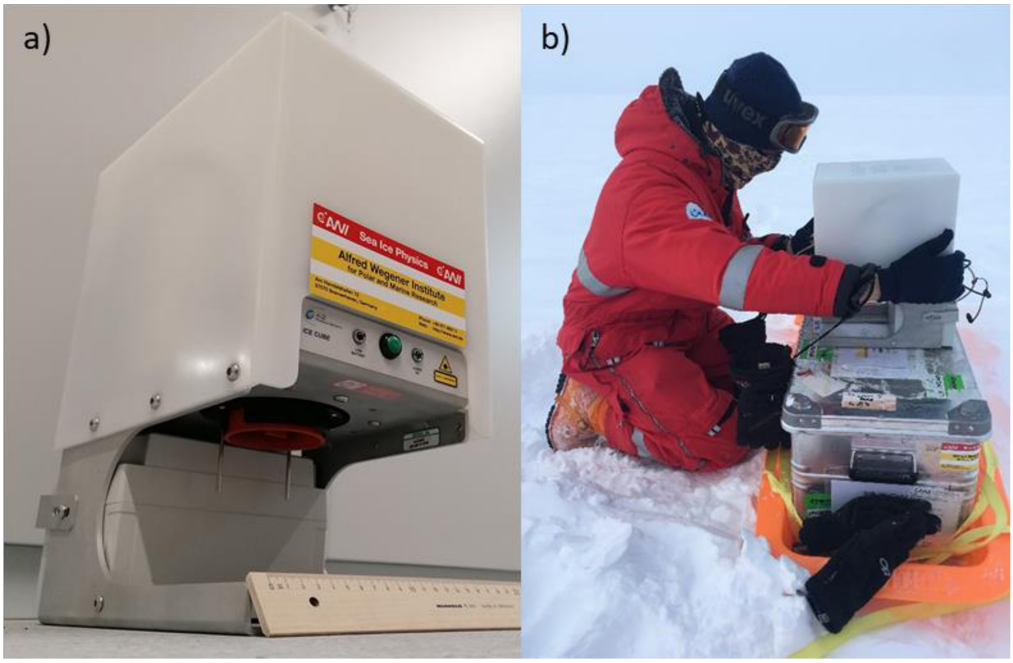

Figure 4.1: (a) The IceCube instrument (Photo: Daniela Krampe). (b) Scientist measures specific surface area using the IceCube in the field (Photo: Andreas Herber).

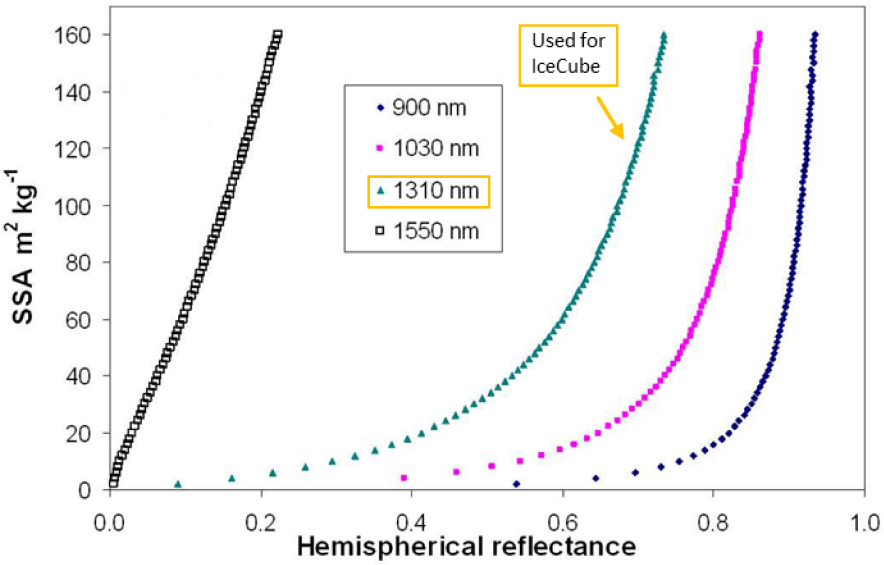

Figure 4.2: Relationship between snow specific surface area and hemispherical reflectance for different shortwave infrared wavelengths (modified after Gallet et al., 2009).

Each measurement day needs to be started with a respective instrument calibration procedure using six reference plates with different reflectance levels (see Figure 4.3), from which a calibration curve is created. The snow sample is then collected in a circular sample holder with a diameter of 6 cm and a vertical resolution of 2.5 cm (see Figure 4.4) (Leppänen and Kontu, 2018). To obtain reliable SSA values, a smooth surface of the snow sample is required. In some cases, e.g., for brittle depth hoar or large grains, it may be difficult to ensure a flat surface and instead hollows or protruding grains may occur, increasing the uncertainty of the measurement (Gallet et al., 2009; Leppänen et al., 2016).

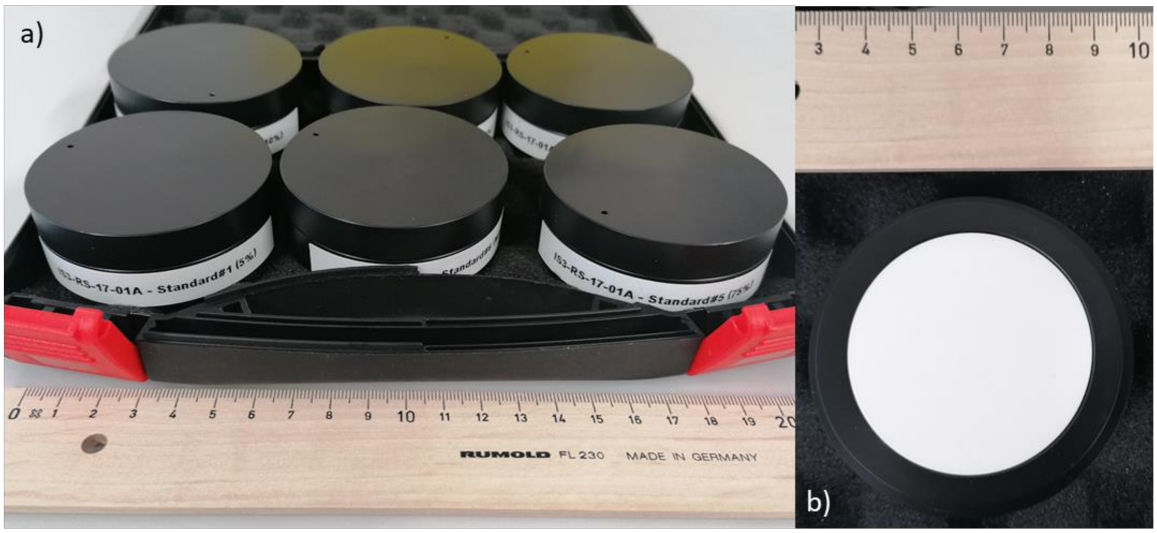

Figure 4.3: (a) The six reference plates with different reflectance level for calibration of the IceCube. (b) Reference plate for calibration of the IceCube (Photos: Daniela Krampe).

Figure 4.4: Snow sample holder for IceCube measurements and tools to receive the snow sample (Photo: Daniela Krampe).

4.4 SnowMicroPen (SMP)

The SnowMicroPen (SMP) is a digital cone penetrometer (Schneebeli et al., 1999; Calonne et al., 2020), which measures a vertical penetration force resistance profile while penetrating through the snowpack. A rod with a 5 mm diameter cone at its tip is lowered electrical into the snowpack at a constant speed. During the propagation into the snowpack the resistance force exerted on the cone is measured (Schneebeli et al., 1999; Calonne et al., 2020).

To obtain snow density and SSA from penetration force different parameterisations have been developed in the last years, based on different snowpack properties and different versions of the SMP. Proksch et al. (2015) developed parameterisations for the SMP version 2 by calibrating a statistical model using micro-CT measurements of snow density and SSA from Alpine, Arctic and Antarctic snowpacks. To calculate snow density [kg m^{-3}] following Proksch et al. (2015) the following parameterisation can be used

$$\rho_{SMP} = a_1 + a_2 \ln(F) + a_3 \ln(F)\, L + a_4\, L \tag{4.1}$$

with a_1 = 420.47 kg m^{-3}, a_2 = 102.47 N^{-1}, a_3 = -121.15 N^{-1} mm^{-1}, a_4 = -169.96 mm^{-1}, F being the penetration resistance force [N] and L the length of the microstructure [mm].

For SSA the following equation can be used after Proksch et al. (2015)

$$SSA_{SMP\_P} = \frac{4\left(1 - \phi_i^{SMP}\right)}{I_c^{SMP}} \tag{4.2}$$

With the volume fraction of ice ϕ_i^{SMP} calculated as

$$\phi_i^{SMP} = \frac{\rho_{SMP}}{\rho_{ice}} \tag{4.3}$$

with ρ_{ice} being the density of ice (917 kg m^{-3}) and the slope of the correlation function I_c^{SMP} at the origin calculated as

$$I_c^{SMP} = c_1 + c_2\, L + c_3 \ln(F) \tag{4.4}$$

with c_1 = 0.131 mm, c_2 = 0.355 mm^{-1} and c_3 = 0.0291 N^{-1}.

Several studies show that the calculations of snow density and SSA after Proksch et al. (2015) for the most recent version of the SMP, version 4, deviates from density cutter and IceCube measurements (King et al., 2020; Royer et al., 2021). Therefore, Calonne et al. (2020) used density cutter and IceCube measurements from the Swiss Alps to formulate a new statistical model for the SMP version 4 to obtain snow density and SSA from measured penetration resistance force. To calculate snow density after Calonne et al. (2020) the following values for equation (4.1) are used: a_1 = 295.8 kg m^{-3}, a_2 = 65.1 N^{-1}, a_3 = -43.2 N^{-1} mm^{-1}, a_4 = 47.1 mm^{-1}.

To calculate SSA the following parameterisation can be used after Calonne et al. (2020)

$$SSA_{SMP\_C} = b_1 + b_2 \ln(L) + b_3 \ln(F) \tag{4.5}$$

with b_1 = 0.57 m^2 kg^{-1}, b_2 = -18.56 mm^{-1} and b_3 = -3.66 N^{-1}.

Another recalibrated parameterisation of Proksch et al. (2015) to obtain snow density were proposed by King et al. (2020) for the SMP version 4 used for snow on Arctic sea ice. The recalibration was based on density cutter measurements, revealing in equation (4.1) with a_1 = 312.54 kg m^{-3}, a_2 = 50.27 N^{-1}, a_3 = -50.26 N^{-1} mm^{-1}, a_4 = -85.35 mm^{-1}.

In general, the calculated snow density determined from SMP measurements have an uncertainty of about 10 % (Proksch et al., 2015; King et al., 2020). However, the accuracy depends on the snow type, as measurements in fragile depth hoar have a lower accuracy (14 %) than measurements of rounded (10.7 %) or faceted (8.6 %) snow (King et al., 2020).

There are several advantages using SMP measurements in addition to traditional snowpit measurements. With the SMP many measurements can be conducted within a short time. Thus, a high spatial coverage of snow microstructure characteristics can be achieved. In addition, the SMP delivers measurements in a millimetre-scale range and supplies therefore a high vertical resolution of snow microstructure (Calonne et al., 2020; King et al., 2020).

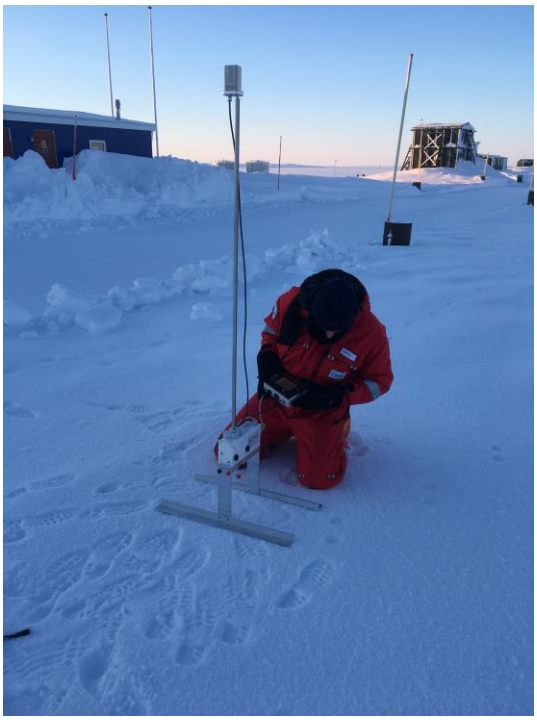

Figure 4.5: Preparation of the SnowMicroPen at Villum Research Station, Greenland (Photo: Andreas Herber).

4.5 Single Particle Soot Photometer (SP2)

To measure the concentration of refractory BC (rBC) in snow the Single Particle Soot Photometer (SP2) originally developed for rBC measurements in the atmosphere, is also a widely used instrument to analyse BC concentrations in snow, e.g., Zanatta et al. (2021), Mori et al. (2019), Jacobi et al. (2019). The instrumental measurement set-up, as the measurements were carried out for this work, is shown in Figure 4.6.

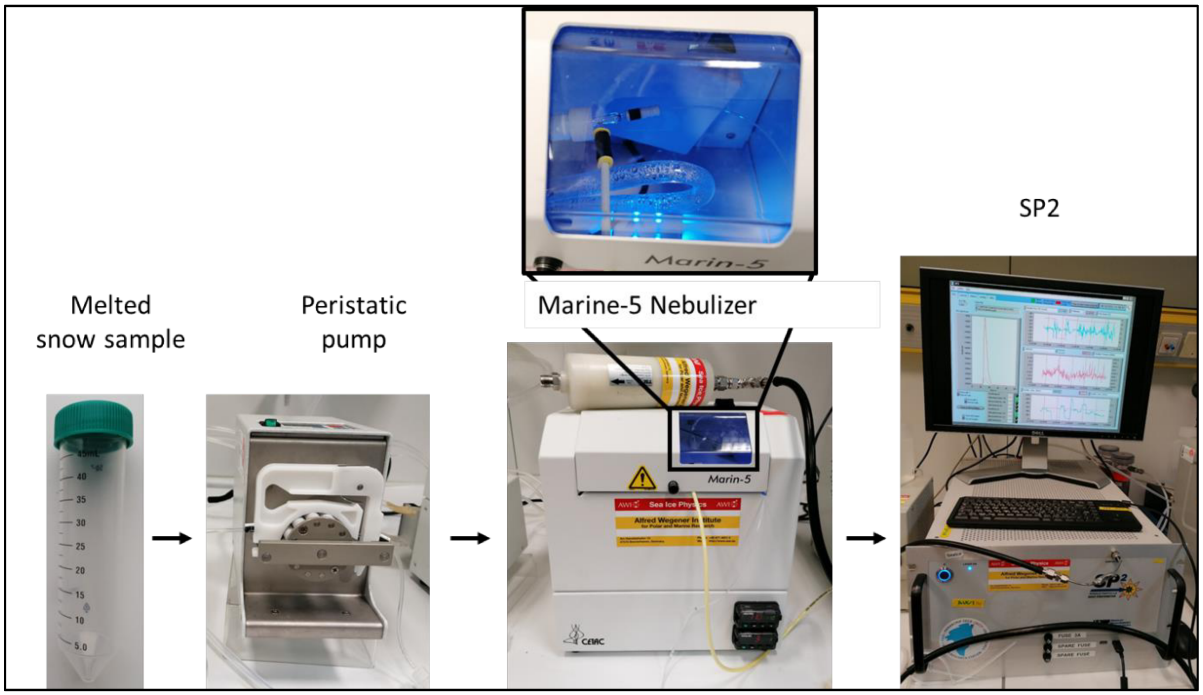

Figure 4.6: Instrumental measurement set-up in the lab to analyse snow samples for black carbon concentration. The photo above the Marine-5 nebulizer is a close-up of the nebulizer chamber (Photos: Daniela Krampe).

The SP2 instrument was developed by the Droplet Measurement Technologies Incorporated in the USA. This measurement technique belongs to the so called laser-induced incandescence techniques (Schwarz et al., 2010; Laborde et al., 2012; Zanatta et al., 2021). The SP2 measures indirectly the BC mass concentration of individual aerosol particles (Schwarz et al., 2010; Laborde et al., 2012; Mori et al., 2016). By doing so, the instrument uses a high intensity, Nd:YAG (Neodymium-doped Yttrium Aluminium Garnet; Nd:$Y_3Al_5O_{12}$; a crystal) intra-cavity laser with a wavelength of 1064 nm having a Gaussian intensity profile (Schwarz et al., 2010).

The BC particles entering the laser beam, heat up by absorbing the laser light reaching temperatures as high as the vaporisation temperature of BC of about 3700 K - 4300 K (Schwarz et al., 2010 and references therein). During evaporation, BC particles emit thermal radiation in the visible wavelength range, which is detected by the instrument. The intensity of this light is proportional to the particle mass, so that after an empirical calibration of the device with BC particles of known particle mass, the mass of the individual BC particles can be determined (Schwarz et al., 2010 and references therein).

For the calibration of the SP2, commercial BC such as fullerene soot and Aquadag® are used. Thereby, the sensitivity of the SP2 is not the same for all BC types leading to uncertainties in the measurements if the chemical composition differs from the BC type used for calibration (Laborde et al., 2012). Due to instrumental limitations, the SP2 is able to measure the BC mass of the individual in the range of 0.3 fg - 300 fg (femtogram; 1.0 x 10^{-18} kg), which translates to a range of approximately 70 nm - 800 nm of BC core equivalent diameter assuming spherical particles.

Before the BC concentration can be measured, the snow sample has to be melted shortly before the measurements, e.g., in a warm water bath, which had a temperature of 25°C for this work (Zanatta et al., 2021). Then, the sample is transported via a peristatic pump that ensures a constant liquid flow rate and transports the melted snow sample into a concentric nebulizer, e.g. Marine-5.

The Marine-5 nebulizer (Mori et al., 2016; Zanatta et al., 2021) is a concentric pneumatic nebulizer containing a heating-cooling cycle system and was developed by Teledyne Technologies in the USA. The nebulizer produces droplets with the help of dry air with a constant flow rate (Mori et al., 2016) and

dries these by first warming them to 110°C and cooling them afterwards to 5°C (Zanatta et al., 2021). Through this process water vapour condenses and is drained (Mori et al., 2016). From the nebulizer dry air with aerosols remains and flows into the SP2. During nebulization of the snow sample, about 50 % - 60 % (Katich et al., 2017) of rBC are lost and therefore cannot be detected by the SP2, whereas Zanatta et al. (2021), who also analysed the BC samples used in this dissertation, found a detection rate of 57 % - 66 % for samples they analysed with the same instrument as used for our samples.

4.6 Field campaign: PAMARCMiP

For the analyses performed within this dissertation, measurement data from the PAMARCMiP (Polar Airborne Measurements and Arctic Regional Climate Model Simulation Project) 2018 campaign were used. PAMARCMiP is part of the ArctiC Amplification: Climate Relevant Atmospheric and SurfaCe Processes, and Feedback Mechanisms (AC^3) project. The campaign took place in March and April 2018 around the Villum Research Station in northeast Greenland (see Figure 6.1). During the campaign, airborne observations and ground-based measurements were conducted to learn more about the physical and optical properties of snow, sea ice and the atmosphere (Donth et al., 2020; Mei et al., 2021; Ohata et al., 2021).

For the purpose of this dissertation, the following measurements of the physical snow properties snow depth, snow density and SSA were used together with analyses of BC concentration of snow samples:

1) **23 March 2018** transect between locations 1 to 5 (see Figure 4.7)

   SMP measurement transect to obtain the spatial variability of snow properties

   Used instruments

   - Density: SMP
   - SSA: SMP

   Unfortunately, due to the cold temperatures during the field campaign, the SMP version 4 failed end of March 2018 and was no longer usable from this point on. SMP measurements were conducted on 22 March, 23 March, 26 March and 27 March on land. Due to thick ice lenses and compact snow, the SMP could not penetrate the entire snow profile. The total snow depth was not measured at the SMP measurement sites. I chose the 23 March 2018 for analyses because on this day more than five SP measurements penetrated deeper than 40 cm into the snow, which was not the case for the other measurement days.

2) **3 April 2018** at locations 1 to 5 (see Figure 4.7)

   Vertical profiles of snow density, SSA and snow samples for BC analysis taken every 10 cm starting at the ice/ground interface in addition to measurements at the snow surface; snow depth.

   Used instruments

   - Density: snow density cutter
   - SSA: IceCube
   - BC: small vials with a volume of 50 mL (see Figure 9.2)

   The 3 April 2018 was the only date during the campaign where detailed snow measurements were conducted on land over the entire snow profile on several locations. Thus, these measurements were chosen for further analyses.

A schematic illustration of the snow measurements and a photo of a snowpit conducted during PAMARCMiP 2018 are shown in Figure 4.8.

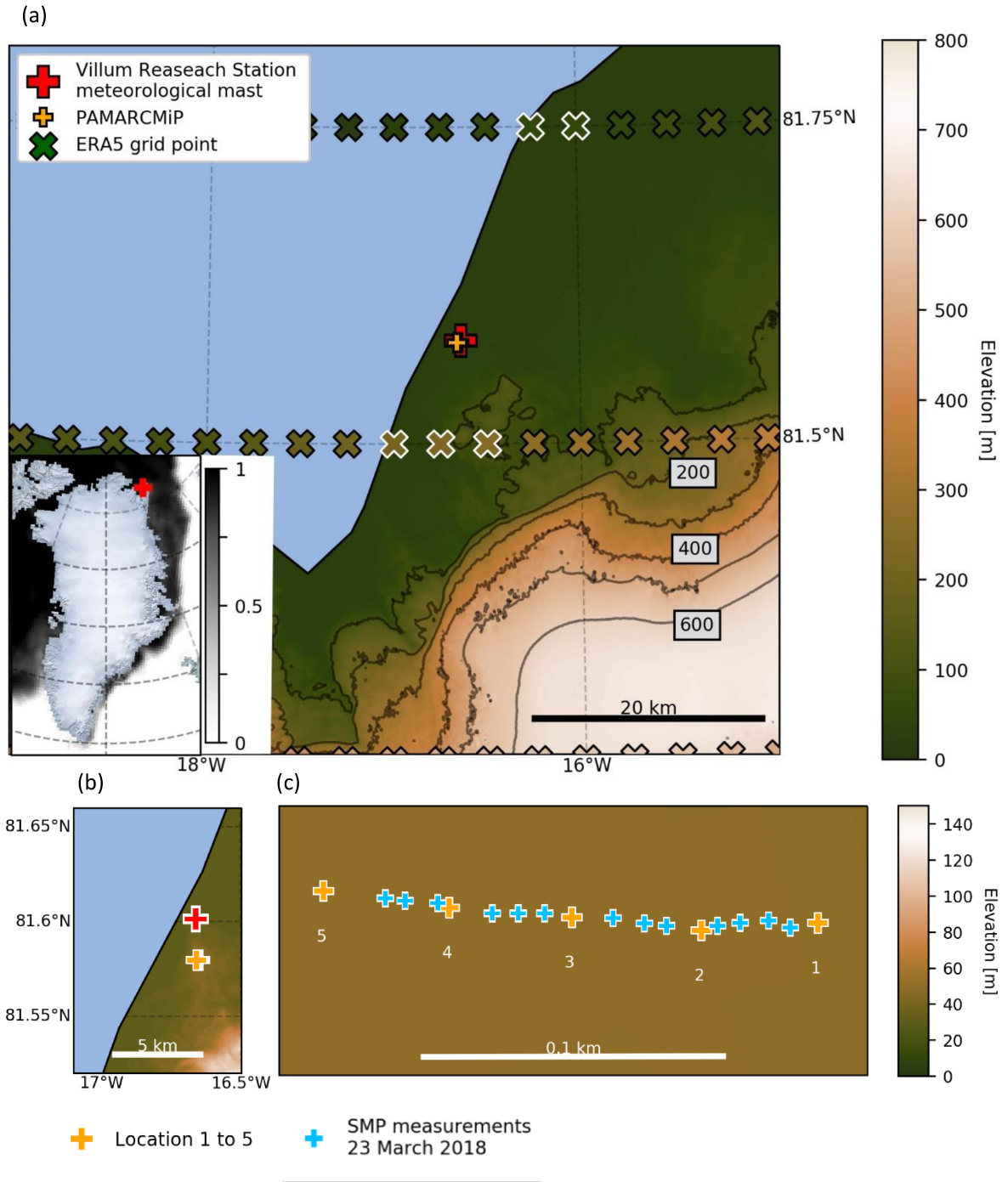

Figure 4.7: Overview map showing location of meteorological mast of Villum Research Station (red cross), measurement location during PAMARCMiP (yellow cross), ERA5 grid cell centres and terrain elevation (both using the same colour bar, the crosses are filled with colours according to the ERA5 elevation) in northeast Greenland (Digital elevation model: Howat et al. (2015), Howat et al. (2014)). Crosses with white boundaries are the ERA5 grid cells used in this study. Small inserted panel at left bottom: Sea ice concentration from 15 March 2018 (Maslanik and Stroeve, National Snow and Data Center, updated yearly). (b) Zoom in of (a) showing the position of the measurements in relationship to the location of Villum Research Station. (c) Zoom in of (b) showing SnowMicroPen (SMP) measurement positions as well as locations 1 to 5 for detailed snowpit measurements during the PAMARCMiP (Polar Airborne Measurements and Arctic Regional Climate Model Simulation Project) 2018 campaign used for studies presented in this dissertation. The background is the ocean in blue (Own drawing).

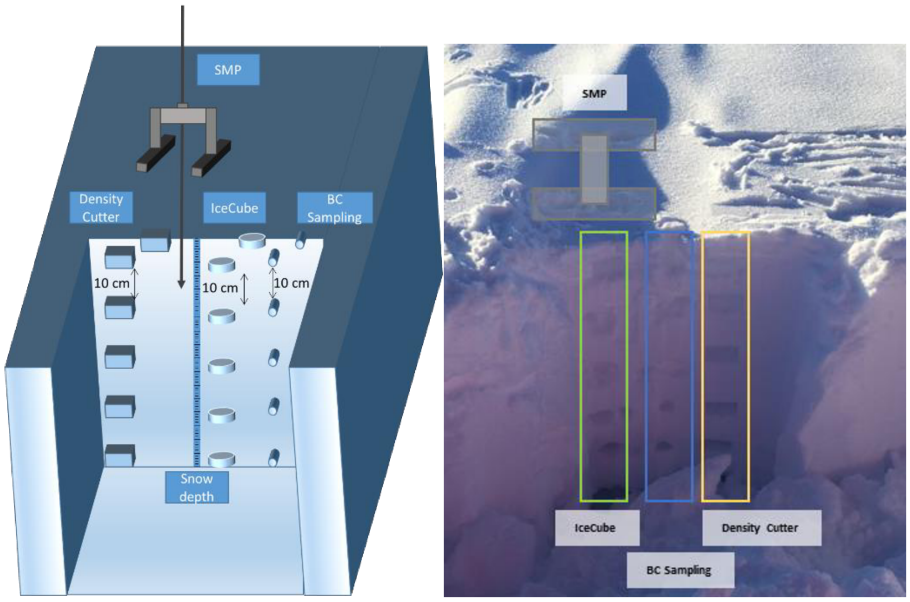

Figure 4.8: Left: Schematic of the snowpit measurements (Own drawing). Right: Photo of a snowpit measured during the PAMARCMiP (Polar Airborne Measurements and Arctic Regional Climate Model Simulation Project) 2018 campaign with positions of IceCube, black carbon (BC) and density cutter sampling as well as measurement position of the SnowMicroPen (SMP) (Photo: Andreas Herber).

5 Snow modelling

"Essentially, all models are wrong, but some are useful."

(George E. P. Box, Robustness in the strategy of scientific model building, 1979)

As explained above, snow is important because it is strongly influencing, e.g., the surface energy balance in the Arctic. Especially in remote locations continuous time series of snow measurements are rare and difficult to conduct. Snow models are an important tool to fill this gap. Snow models are used for various applications: for hydrological simulations (Wever et al., 2014), avalanche forecast and mass balance research (Bartelt and Lehning, 2002; Vionnet et al., 2012), snow science and snow engineering applications (Bartelt and Lehning, 2002), environmental studies (Liston et al., 2016) or for investigations of impacts of snow cover variability (Royer et al., 2021).

Thereby, the degree of model complexity varies (Wever et al., 2014). There are single-layer snow models, intermediate complex snow models and detailed snow models. Single-layer snow models are often used in numerical weather prediction and climate models, representing the main snow properties of, e.g., high albedo and low thermal conductivity parametrised by fixed coefficients representing mean conditions. In contrast to single layer snow models, intermediate snow models are able to represent some specific internal processes of the snowpack, e.g., settling or refreezing. Detailed snow models like Crocus and SNOWPACK handle explicitly internal snow processes accounting for the layering of a snowpack and its microstructure affecting, for instance, the layer density, the layer heat conduction and albedo. However, detailed models are computationally expensive (Vionnet et al., 2012) and many of the process formulations are not well validated, especially in high latitudes. Often, detailed snow models are used in "single-point" mode, but can also be used spatially distributed.

Crocus is a one-dimensional physical snowpack model, applied operationally by Météo France but also in polar research studies (e.g., Sauter and Obleitner, 2015; Barrere et al., 2017) (see Chapter 5.1 and 5.2. for details). Also, SNOWPACK is a one-dimensional physical snowpack model, developed originally for Swiss avalanche forecasts, i. e., for the European Alps (Bartelt and Lehning, 2002) but is also used for studies over sea ice (Wever et al., 2020).

Another widely used snow model for polar applications is SnowModel (Snow-Evolution MODELing System), e.g., Pedersen et al. (2015), Boelman et al. (2019), Loe et al. (2020), by Liston and Elder (2006). It was developed for investigating snowpacks in different climates and landscapes. As SNOWPACK and Crocus, the snow model SnowModel (Liston and Elder, 2006 and references therein) is spatially distributed and multi-layered.

Crocus is coupled to the ISBA (Interactions between Soil, Biosphere, and Atmosphere) model (Langlois et al., 2009; Domine et al., 2019), while SNOWPACK and SnowModel are not coupled to any land surface model. Thus, Crocus is able to explicitly take mass and energy exchanges between the ground and the snow into account (Langlois et al., 2009; Vionnet et al., 2012).

Recently, a parameterisation for the impact of light absorbing impurities on snow evolution and snow properties has been implemented in Crocus (Tuzet et al., 2017; Tuzet et al., 2020), in contrast to SNOWPACK and SnowModel. Since the impact of BC on the radiative forcing in the Arctic is part of this dissertation and the coupling to the land surface model is a clear advantage, the snow model Crocus was chosen for this dissertation. Another reason I prefer using Crocus is the ability to use an ensemble version of Crocus in the future to account for modelling errors and to examine the effects of different model parameterisations (Lafaysse et al., 2017).

5.1 The snow model Crocus

In this subchapter some details on the snow model Crocus are given. Figure 5.1 provides an overview of state variables and main processes considered in the model. Even more detailed information can be found in the work of Brun et al. (1992) and Vionnet et al. (2012).

A finite-element grid is used to resolve the snowpack vertically. Thereby, layer thickness, heat content, density and age characterise each snow layer (Vionnet et al., 2012). Snow layers can dynamically change over time in number and thickness allowing for a reliable representation of the natural snowpack. This dynamical scheme was originally developed for Crocus (Brun et al., 1992).

Newly fallen snow is considered as dry snow and can fall at surface air temperatures below +2°C. Wet newly fallen snow does not exist in the model (Langlois et al., 2009). Thereby, the density of newly fallen snow is calculated by

$$\rho_{new} = a_\rho + b_\rho\left(T_a - T_{fus}\right) + c_\rho U^{1/2} \tag{5.1}$$

where T_a is the surface air temperature [°C], T_{fus} the melting point temperature for water [°C], U the wind speed [m s^{-1}] and a_ρ, b_ρ and c_ρ are empirical constants (109 kg m^{-3}, 6 kg m^{-3} K^{-1}, and 26 $m^{-7/2}$ $s^{-1/2}$, respectively). The minimum new snow density is set to 50 kg m^{-3} (Vionnet et al., 2012).

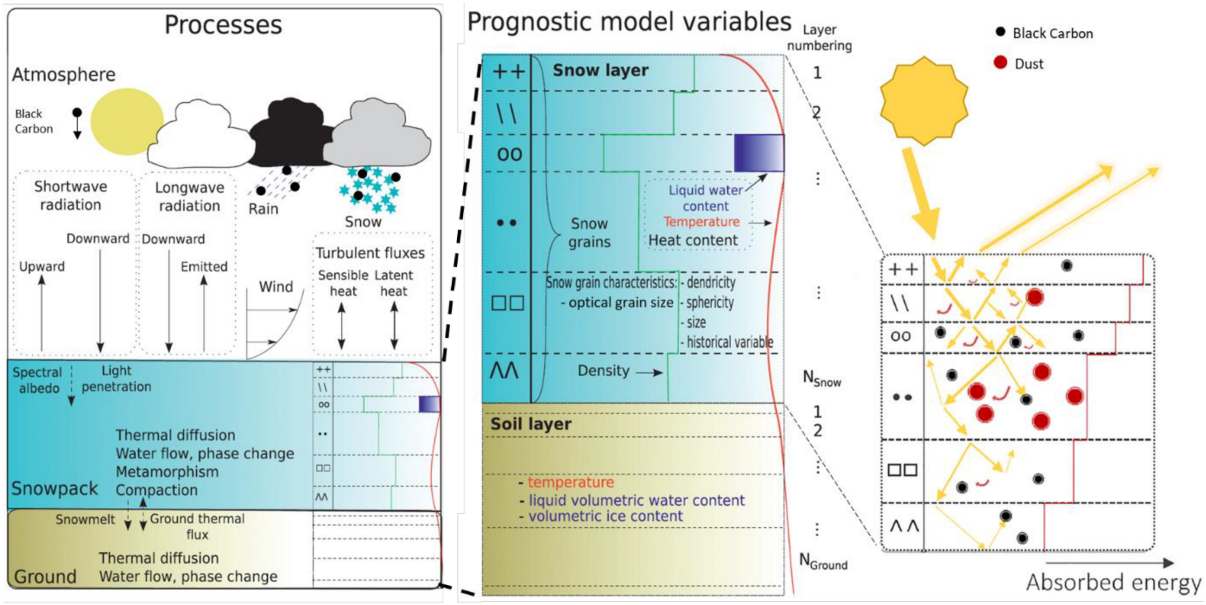

Figure 5.1: State variables and main processes considered in the snow model Crocus and the multilayer soil model ISBA (Interactions between Soil, Biosphere, and Atmosphere) and visualisation of black carbon effects in the model (modified after Tuzet et al. (2017) and Vionnet et al. (2012)).

During a snowfall event, one or several new snow layers can form depending on the amount of snowfall (Vionnet et al., 2012; Morin et al., 2020). If a snow layer is already present at the ground, layers are merged when snow properties are similar. Over time snow settles and snow layers get thinner due to snow metamorphism and snow compaction (Vionnet et al., 2012).

The compaction of snow due to the weight of overlaying snow layers is calculated as

$$\Delta Z = -\frac{\sigma Z}{\eta}\Delta t \tag{5.2}$$

with Z being the layer thickness [m], σ the vertical stress [N m^{-2}] due to the weight of snow layers above, Δt the time step [s] and η the snow viscosity [kg s^{-1} m^{-1}] (Vionnet et al., 2012). Thereby, snow viscosity

is controlled by snow density, temperature, liquid water content and snow microstructure (Carmagnola et al., 2014).

Metamorphism is parametrised in the here used Crocus version in terms of the optical grain size d_{opt}, considered to be equal to the effective grain size (closely linked to SSA, see Chapter 3.4.2 and equation (3.5)), and sphericity *s,* representing the shape of the snow particle with values between 0 (faceted particle) and 1 (round particle). This parameterisation developed by Carmagnola et al. (2014) is named C13, hereafter. To parametrise snow metamorphism, Crocus differentiates between dendritic and non-dendritic snow characterised by d_{opt} whereby the empirical constant β is set to 10^{-4} m (Carmagnola et al., 2014)

$$dendritic: d_{opt} < \beta\,(4 - s) \tag{5.3}$$

$$non - dendritic: d_{opt} \geq \beta\,(4 - s) \tag{5.4}$$

Wet snow metamorphism is solely controlled by the liquid water content (see Table 5.2 for equations) (Brun, 1989; Vionnet et al., 2012; Carmagnola et al., 2014). For the parameterisations used with the metamorphism scheme C13, Carmagnola et al. (2014) reformulated the parameterisations provided in Vionnet et al. (2012) in terms of d_{opt} and *s* and replaced dendricity δ and grain size g_s [m] with

$$\delta = \frac{\frac{d_{opt}}{\beta} - 4 + s}{s - 3} \tag{5.5}$$

and

$$g_s = \beta\,(4 - s) \tag{5.6}$$

The advantage of using C13 is the use of the optical grain size instead of dendricity and grain size in the model formulations. The measurement of the optical grain size is simpler, objective and can be more easily related to other variables (see Chapter 3.4.2.). In addition, most equations are simplified (Carmagnola et al., 2014). Hereafter, the model as presented by Vionnet et al. (2012) is called original version and with the metamorphism scheme C13 is called default version (Table 5.1).

Table 5.1: Definition of the terms “Original version” and “Default version” used to describe different versions of the snow model Crocus in this dissertation.

Term	Description and reference
Original version	the snow model Crocus as described in Vionnet et al. (2012)
Default version	as original version but using the optical grain size instead of dendricity and grain size in the model formulations; Carmagnola et al. (2014)

Table 5.2: Parameterisation of wet snow metamorphism. θ is the mass liquid water content, t time [days], v the equivalent volume of snow grain, v_0' and v_1' empirical constants. Note that the grain size g_s is rewritten for the metamorphism scheme C13 as function of sphericity (see equation (5.6)) and dendricity δ is rewritten as a function of sphericity s and optical grain size d_{opt} (see equation (5.5)) (Vionnet et al., 2012; Carmagnola et al., 2014).

	Non-dendritic snow	**Dendritic snow**
$0 \leq s < 1$	$\frac{\Delta g_s}{\Delta t} = 0$ $\frac{\Delta s}{\Delta t} = \frac{1}{16}\theta^3$	$\frac{\Delta \delta}{\Delta t} = -\frac{1}{16}\theta^3$
$s = 1$	$\frac{\Delta s}{\Delta t} = 0$ $\frac{\Delta v}{\Delta t} = v_0' + v_1'\theta^3$	$\frac{\Delta s}{\Delta t} = \frac{1}{16}\theta^3$

Dry snow metamorphism caused by temperature gradient G is divided into three temperature gradient regimes (Brun et al., 1992; Vionnet et al., 2012; Carmagnola et al., 2014)

1. weak temperature gradient: $G \leq 5$ K m^{-1}
2. middle temperature gradient: 5 K m^{-1} < $G \leq 15$ K m^{-1}
3. strong temperature gradient: $G > 15$ K m^{-1}

The equations of the dry snow metamorphism parameterisation for the default version can be found in Table 5.3. Thereby, d_{opt} increases with metamorphism causing SSA to decrease (Carmagnola et al., 2014).

Table 5.3: Parameterisation of dry snow metamorphism (setup C13). *f*, *w*, *h* and ϕ in the third line are empirical functions to predict depth hoar growth rates. *t* is expressed in days and $T_{decay} = e^{-6000\text{K}/T_{st}}$ with T_{st} being the snow temperature [K] (Carmagnola et al., 2014).

∇T	**Non dendritic snow**	**Dendritic snow**
$G \leq 5$ K m^{-1}	$\frac{\Delta d_{opt}}{\Delta t} = -2\beta s \frac{\Delta s}{\Delta t}$ $\frac{\Delta s}{\Delta t} = 10^9 T_{decay}$	$\frac{\Delta d_{opt}}{\Delta t} = \beta\left[-2\,10^8 T_{decay}(s-3) + \frac{\Delta s}{\Delta t}\frac{\frac{d_{opt}}{\beta}-1}{s-3}\right]$ $\frac{\Delta s}{\Delta t} = 10^9 T_{decay}$
$5 < G \leq 15$ K m^{-1}	$\frac{\Delta d_{opt}}{\Delta t} = -2\beta s \frac{\Delta s}{\Delta t}$ $\frac{\Delta s}{\Delta t} = -2\,10^8 T_{decay} G^{0.4}$	$\frac{\Delta d_{opt}}{\Delta t} = \beta\left[-2\,10^8 T_{decay} G^{0.4}(s-3) + \frac{\Delta s}{\Delta t}\frac{\frac{d_{opt}}{\beta}-1}{s-3}\right]$
$G > 15$ K m^{-1}	if $s > 0$: $\frac{\Delta d_{opt}}{\Delta t} = -2\beta s \frac{\Delta s}{\Delta t}$ and $\frac{\Delta s}{\Delta t} = -2\,10^8 T_{decay} G^{0.4}$ if $s = 0$: $\frac{\Delta d_{opt}}{\Delta t} = \frac{1}{2} f(T) h(\rho) w(G) \phi$ and $\frac{\Delta s}{\Delta t} = 0$	$\frac{\Delta s}{\Delta t} = -2\,10^8 T_{decay} G^{0.4}$

Sublimation at the snow surface is determined through the latent heat flux and changes the thickness of the surface snow layer. To calculate the surface latent and sensible heat fluxes aerodynamic resistance together with the turbulent exchange coefficient C_H are applied (Touzeau et al., 2018). C_H relies on the Richardson number R_i (which determines the stability of the atmosphere close to the snow surface) and the surface roughness (Lafaysse et al., 2017 and references therein). Rougher surfaces reveal higher turbulent fluxes, while lower atmospheric stability (lower R_i) causes higher C_H (Lafaysse et al., 2017).

In the latent heat flux Q_e [W m^{-2}] evaporation in the top snow layer and sublimation are included. It is calculated as

$$Q_e = \rho_a \left(\text{K}\, L_f + L_v\right) C_H\, U\, [q_{sat}(T_s) - q_a] \tag{5.7}$$

with K being the ratio of solid and liquid phase of the turbulent mass exchange between snow surface and atmosphere, L_f the latent heat of fusion [J kg^{-1}], L_v the latent heat of vaporisation [J kg^{-1}], ρ_a the air density [kg m^{-3}], C_H the turbulent exchange coefficient, U the wind speed [m s^{-1}], $q_{sat}(T_s)$ [kg kg^{-1}] the saturation specific humidity over a flat ice surface at the snow surface temperature T_s and q_a the atmospheric specific humidity [kg kg^{-1}] (Vionnet et al., 2012).

The sensible heat flux Q_h [W m^{-2}] is determined by

$$Q_h = \rho_a\ C_p\ C_H\, U \left(\frac{T_s}{\pi_s} - \frac{T_a}{\pi_a}\right) \tag{5.8}$$

with C_p being the air specific heat [J K^{-1} kg^{-1}], π_s and π_a the Exner functions $\pi = (p\ /\ p_0)^{R_G\ /\ C_{pd}}$ for the surface and atmosphere, respectively, with p being the surface air pressure, p_0 the reference atmospheric pressure, R_G the specific gas constant, C_{pd} the specific heat capacity for the surface and the atmosphere, respectively (Vionnet et al., 2012).

I use a Crocus version, where LAI and their radiative impacts are explicitly considered, as I concentrate on the effects of BC in the third part of the dissertation.

To take the radiative effects of BC into account, the radiative transfer model Two-stream Analytical Radiative TranfEr in Snow model (TARTES) (Libois et al., 2013) is used instead of the albedo scheme after Brun et al. (1992). TARTES applies the asymptotic analytical radiative transfer theory (AART) (see e.g., Kokhanovsky and Zege, 2004) together with the δ-Eddington approximation (see e.g., Jiménez Aquino and Varela, 2005) to obtain the spectral absorption of the sunlight in a snowpack. The variables SSA, density, snow layer thickness and impurity content as well as solar zenith angle and spectrally resolved diffuse-to-total-irradiance ratio are needed by TARTES (Tuzet et al., 2017).

In AART the geometric snow grain shape is parametrised with the help of the absorption enhancement parameter B and the asymmetry factor g. B "[…] quantifies the lengthening of photon paths inside a snow grain due to internal multiple reflections […]" (Libois et al., 2013) while "g corresponds to the average cosine of the angle of deviation of scattering by snow grains" (Libois, 2014). These wavelength λ dependent parameters characterise the effects of the shape of the ice matrix and are calculated after Tuzet et al. (2020) (adapted from (Libois, 2014)) by

$$B(\lambda) = B_0 + 0.4\ (r_i(\lambda) - 1.3) \tag{5.9}$$

$$g(\lambda) = g_0 - 0.38\ (r_i(\lambda) - 1.3) \tag{5.10}$$

whereby r_i is the real part of ice refractive index, B_0 the enhancement parameter set to 1.6 in the default Crocus version and g_0 the asymmetry factor set to 0.845. Thereby, the size of snow grains is assumed to be larger than the wavelength (Kokhanovsky and Zege, 2004; Libois et al., 2013).

The asymmetry factor can have values between $-1 \leq g \leq 1$, whereby $g = 0$ means isotropic scattering, $g = 1$ means a completely forward scattering and $g = -1$ completely backward scattering. An asymmetry factor of $g = 0.9$ corresponds to a grain size radius of $r > 50$ µm (Warren, 1982).

After Kokhanovsky and Zege (2004) in AART the albedo α of a semi-infinite scattering medium illuminated by a diffuse source can be calculated as

$$\alpha = \exp\left(-4\sqrt{\frac{1-\omega}{3\,(1-g)}}\right) \tag{5.11}$$

with ω being the single scattering albedo. This equation is used in a simplified way in TARTES assuming convex snow particles

$$\alpha \cong \exp\left(-8\sqrt{\frac{B\,\xi}{3\,\rho_{ice}\,SSA\,(1-g^G)}}\right) \tag{5.12}$$

with ξ being the wavelength dependent ice absorption coefficient ($\xi = \frac{4\,\pi\,X}{\lambda}$, with the wavelength dependent imaginary part of the ice refractive index X) and g^G the geometric asymmetry factor controlled by the shape and real part of the ice refraction index. g^G "[…] quantifies the forward-scattering of light by the snow grain" (Libois et al., 2013).

In Crocus, impurities are entrained through wet and dry deposition into the snowpack. Once deposited in the snowpack, scavenging events as well as direct (i.e. darkening of the snow and thus lowering of snow albedo) and indirect (alteration of snow properties, e.g., lowering of near-surface SSA leading to a reduction of near-infrared albedo) effects of impurities are simulated. A prognostic variable is implemented representing the mass of BC in each snow layer, whereby it is described by its optical and scavenging properties (Tuzet et al., 2017).

The change in mass content M_p [g m^{-2}] due to wet deposition is

$$\Delta M_p = W_i\,\Delta t \tag{5.13}$$

with W_i being the wet deposition flux [g m^{-2} s^{-1}] and Δt the time step [s]. Wet deposition during snowfall leads to the creation of a new snow layer containing the BC mass content, while during rainfall the content is added to the surface snow layer (Tuzet et al., 2017).

In contrast to wet BC deposition, dry BC deposition is potentially distributed over several near-surface snow layers due to wind pumping. Therefore, the dry deposition mass distribution $M_{t+\Delta t,l}$ [g m^{-2}] for near-surface layers l is parametrised by an e-folding depth-scale

$$M_{t+\Delta t,l} = M_{t,l} + D\,\frac{e^{-(z_l\,/\,h_e)}}{\sum_{k=1}^{N} e^{-(z_k\,/\,h_e)}\,\Delta z_k}\,\Delta t \tag{5.14}$$

with D being the dry deposition flux [g m^{-2} s^{-1}] and h_e the e-folding depth scale set to 5 mm while z_l is the layer depth defined as the distance between the snow surface and the midpoint of the lth layer. N is the number of snow layers and z_k the thickness of the kth layer (Tuzet et al., 2017).

The BC content at the snow surface layer increases during melting, because the BC content of the melted snow layers is added to the uppermost non-melted snow layer. For the process of scavenging of BC the handling of water percolation in the model is important.

For the water percolation in Crocus a simple bucket approach is used. Each snow layer is characterised by a volumetric liquid water content and has a maximum volumetric liquid water holding capacity. If the water content exceeds the holding capacity, the water – together with the BC particles contained in the meltwater when scavenging is activated – percolates into the underlying snow layer (Lafaysse et al., 2017; Tuzet et al., 2017).

5.2 Crocus in Polar Regions

Although developed for applications in the Alps Crocus was used in recent years as well in the Arctic (Essery et al., 2016; Barrere et al., 2017; e.g., Domine et al., 2019) and in the Antarctic (Gallet et al., 2014a; Gallet et al., 2014b; e.g., Libois et al., 2014). In the following, I focus on process formulations in the default Alpine version of Crocus that needs attention when engaging Crocus in high-latitudes. I will point to limitations in simulating polar snowpacks and will present adaptations made by other researcher groups on the model to improve its performance in high-latitudes. In the following chapters, Chapter 6, Chapter 7, Chapter 8 and Chapter 9 adaptations I made are presented.

For polar applications, the impact of wind drift on the density and compaction of the upper snow layers has been implemented. Thereby, the change of snow particle shape as well as its fragmentation is taken into account (Vionnet et al., 2013).

In the original version of Crocus, snow grains are described by dendricity δ, sphericity *s,* and grain size g_s. New snow crystals (see Figure 3.11) have a dendricity of 1 due to a high amount of remaining initial geometry while metamorphosed snow has a dendricity of 0. Metamorphosed snow has a sphericity of 1 as the ratio of rounded to angular shapes is high while new snow has a sphericity of 0.5. Over time dendricity decreases and sphericity increases (Vionnet et al., 2013). In terms of the optical grain size d_{opt} (default version) these values correspond to 10^{-4} m for new snow (the empirical constant β, compare equations (5.3) and (5.4)) (Carmagnola et al., 2014).

For falling snow particles, the dendricity δ_{fall} and sphericity s_{fall} are parametrised as a function of 5 m height wind speed U

$$\delta_{fall} = \min[max(1.14 - 0.07\,U, 0.2), 1] \tag{5.15}$$

$$s_{fall} = \min[max(0.035\,U + 0.43, 0.5), 0.9] \tag{5.16}$$

For $U \leq 2$ m s^{-1} newly fallen snow crystals reaching the surface are considered to conserve its properties ($\delta_{fall} = 1,\ s_{fall} = 0.5$). Snow crystals start to fragment for $U > 2$ m s^{-1} ($\delta_{fall} < 1,\ s_{fall} > 0.5$) and for wind speeds $U \geq 6$ m s^{-1} snow transport occurs in addition (Vionnet et al., 2013).

As high wind speeds are much more common in polar than in Alpine regions (Sturm and Holmgren, 1998; Homan and Kane, 2015) the parameterisation of wind effect on snow is essential to be implemented when applying Crocus there. Snow erosion is active when the driftability index S_I

$$S_I = -2.868\exp(-0.085\,U) + 1 + M_{ob} \tag{5.17}$$

is positive, where M_{ob} is a mobility index. Then snowdrift is assumed and fragmentation of surface snow grains is applied. Thereby, new snow particles of low density are easier to mobilise and have higher driftability indexes than older snow that has already undergone sintering cohesion. Furthermore, wet snow layers or crusts at the surface inhibit snow drift (Vionnet et al., 2012; Vionnet et al., 2013).

When using Crocus' default version setup compaction during snowdrift is calculated for dendritic and non-dendritic snow following Carmagnola et al. (2014) and Royer et al. (2021)

$$dendritic: \frac{\Delta\, d_{opt}}{\Delta\, t} = \beta \left[\frac{\delta}{2\,\tau_i}\,(s-3) + \frac{1-s}{\tau_i}\,(\delta-1)\right] \tag{5.18}$$

$$non-dendritic: \frac{\Delta\, d_{opt}}{\Delta\, t} = -2\,\beta\,\mathrm{s}\,\frac{1-s}{\tau_i} \tag{5.19}$$

and

$$\tau_i = \frac{\tau}{W_E\,\Gamma_{i,drift}} \tag{5.20}$$

with t being time in hours, τ_i a time scale for the change of snow grains under wind transport that depends on the constant τ (set to 48 h) and the grain driftability $\Gamma_{i,drift}$. W_E allows for tuning and is set to 1 in Crocus' the default version. The maximum snow density ρ_{max} for which an impact due to snowdrift occurs is set to 350 kg m^{-3} in the default version (Royer et al., 2021). Effects of compaction and fragmentation propagate through the snowpack until some conditions are no longer met (e.g., the density has reached ρ_{max} or the wind speed is below the transport threshold of 6 m s^{-1}) (Vionnet et al., 2013).

During blowing snow events, enhanced sublimation takes place. Then the sublimation rate Q_{Sub} [kg m^{-2} s^{-1}] is calculated following Gordon et al. (2006)

$$Q_{Sub} = A\left(\frac{T_0}{T_a}\right)^{\gamma} U_t\,\rho_a\,q_{si}\,(1-Rh_i)\left(\frac{U}{U_t}\right)^{E_S} \text{ for } U > U_t \tag{5.21}$$

whereby T_a is the air temperature [K] and U the wind speed [m s^{-1}]. U_t is a threshold wind speed where wind drift occurs dependent on the mobility index M (see equation (5.17)). q_{si} is the saturation specific humidity with respect to ice at temperature T_a [kg kg^{-1}] and Rh_i relative humidity with respect to ice. A, γ and E_S are dimensionless constants set to 0.0018, 4 and 3.6, respectively, T_0 the triple point temperature 273.15 K, and ρ_a the air density [kg m^{-3}].

As Crocus was developed for applications in the Alps, the parameterisation of processes is mainly based on empirical experiments conducted in the French Alps primarily at Col de Porte (45.3° N, 5.8° E, 1324 m a.s.l.) (Essery et al., 2016). As snowpacks in the Arctic and the European Alps differ from each other considerably (see Chapter 3.2.1), limitations in simulated processes and weaknesses in simulating snow properties are expected.

In the snowpack of polar regions, high temperature gradients between the snow surface and the ground are commonly causing strong upward vertical water vapour fluxes and thus lead to mass transfer from the bottom towards the top (see Chapter 3.3.1). Note that simulating vertical water vapour transport is essential to accurately simulate depth hoar in the snowpack (Domine et al., 2019), but depth hoar is simulated by Crocus without it.

While the exchange of water vapour between the atmosphere and the snow surface is taking care of in the model, thermal conductivity is implemented following Yen (1981). Here, it is assumed that thermal conductivity depends solely on density, which monotonously increases with depths. This formulation is not adequate to simulate vertical water vapour transport (Gallet et al., 2014b; Domine et al., 2019). First attempts to consider the vertical water vapour transport in snow models are made by Schürholt et al. (2022), Jafari et al. (2022), Simson et al. (2021), Jafari et al. (2020) and Touzeau et al. (2018). Furthermore, for polar regions the influence of condensation and sublimation on the microstructure of snow is insufficiently realised (Gallet et al., 2014b).

These processes have impacts on changes on SSA and roughness (Gallet et al., 2014b) and lead to issues in simulating thermal conductivity, temperature gradients and snow metamorphism (Domine et al., 2019). Due to these numerous issues density and thermal conductivity change with depths in the snowpack is reversed with respect to observations in Arctic simulations (Jacobi et al., 2010; Domine et al., 2016a; Domine et al., 2019).

Nevertheless, Jacobi et al. (2010) were able to simulate depth hoar layers at the bottom of a snowpack and generated sufficient temperature profiles with quick temperature changes at the surface and smoother changes at the bottom of the snowpack for a site in Alaska. They achieved this by reducing the thermal conductivity during winter months (see Table 5.4). Also, Brun et al. (2013) managed to simulate depth hoar during extreme temperature gradients in northern Eurasia. They relate this to the coupling of Crocus with the ISBA soil model.

Still, Jacobi et al. (2010) found that simulated temperatures are generally colder than observed, whereby there is a higher agreement of simulated and observed snow temperatures towards the basal layers. There seems to be convective processes that are not fully understood (like wind pumping at low wind speeds) leading to cooling events that are not reproduced by the model to the same extend as observed.

Domine et al. (2019) found differences in snow surface temperatures of up to 4°C between observations and simulations associated with differences in snow stratigraphy. In contrast Sauter and Obleitner (2015) simulated good representation of snow surface temperature and its temporal variability with largest deviations in winter. As reasons for deviations in winter they named possible undetected riming of the sensor or model uncertainties. Also, Gallet et al. (2014b) sufficiently simulated the snow surface temperatures for applications at Dome C, Antarctic.

Brun et al. (2013) simulated sufficiently (bias: -0.5 K, r: 0.675 compared to monthly observations) soil temperatures in -20 cm depth of the soil for more than 250 stations in northern Eurasia. Also, Domine et al. (2019) found that simulated ground temperatures for an Arctic site in Canada agree well with observations apart from too rapid freezing and thawing of the ground. They suspect too high simulated thermal conductivity of basal layers as reason for too rapid freezing. Furthermore, snow temperatures at the snow-ground interface tend to be warmer than observations for sites in Arctic Finland. The occurrence of more pronounced cold spikes in simulations was found at the beginning of the freeze up period as well as warmer temperatures of the ground towards spring. However, simulated ground temperatures agree generally well with observations (Essery et al., 2016).

Also, the parameterisation of new snow density and metamorphism was developed for the Alps. When using it for applications in the Arctic settling and compaction of the upper snow layers is systematically underestimated and reveals too low densities at the top of the snowpack (Sauter and Obleitner, 2015). Studies show, that the default version of Crocus is insufficient to simulate observed surface snow densities and tends to underestimate surface snow density in the Antarctic (Keenan et al., 2021).

Underestimations of snow depth can also cause an underestimation of snow density, as the weight of the overlaying snow contributes to compaction and, hence, to higher snow densities (Vionnet et al., 2012). Erroneous simulated densities as well evolve from model deficiencies in the formulation of snow redistribution by wind and percolation of meltwater (Gascon et al., 2014). Brun et al. (2013) studied the performance of Crocus for more than 250 stations in northern Eurasian for snow density. Spatial variability of bulk density is simulated well. However, they found that simulated densities at stations where snow redistribution is common are too low compared to observations.

Regarding snow depth, many studies show a sufficient performance of Crocus when applied to polar regions (Jacobi et al., 2010; Brun et al., 2013; Essery et al., 2016; Luijting et al., 2018). Deviations between observations and simulations occurred, e.g., during winter when observed decreasing snow depth events were not present in the model (Luijting et al., 2018). Again, a reason for the overestimation of snow depth could be the use of too low new snow densities according to Essery et al. (2016). Snow depth decrease due to erosion during blowing snow events not parametrised in the model causes

deviations as well (Luijting et al., 2018). Over a snow season all these biases accumulate. Deviations between model and observations can also be caused, of course, due to biases in the forcing data (Luijting et al., 2018). However, the decrease in snow depth is faster in simulations than observations (Essery et al., 2016) or melting occurs too early and simulated snow depths are lower than observed (Jacobi et al., 2010).

To receive reliable simulation results many studies using Crocus in the Arctic scaled forcing variables, e.g., the snowfall forcing the model is scaled to match measured SWE for instance Essery et al. (2016) or used the changes in measured snow depth to calculate SWE rates that are used to force the model instead of using snowfall from atmospheric reanalyses or weather stations for instance Sauter and Obleitner (2015).

Brun et al. (2013) found good performance of Crocus when enhanced sublimation due to blowing snow events is employed in terms of snow depth, SWE and snow cover duration. Also, the simulated begin of the melting season is close to the observed timing (Brun et al., 2013; Essery et al., 2016).

When the maximum liquid-water-holding-capacity in the model is reached, water at ice layers percolates through the layer, rather than forming lateral water flows or accumulating above the ice layer. This prevents the building of thick ice-layers that are impermeable to water (Gascon et al., 2014).

Beside the above described adaptations there are more studies that tried to improve the parameterisation of physical processes in polar regions (e.g., Jacobi et al., 2010; Sauter and Obleitner, 2015; Royer et al., 2021). Table 5.4 tries to give an overview about modifications without claim of completeness.

The key message of this chapter is that the model includes some processes essential for simulating polar snowpacks, such as compaction and sublimation during wind drift, but other processes such as the redistribution of snow due to wind drift and the vertical water vapour transport are still missing or need to be adapted. A lot of work still has to be performed before the model can sufficiently simulate vertical profiles of physical snow properties. Thereby, many small steps towards more sufficient parameterisations of snow properties and processes are necessary before polar snowpacks can be simulated reliably. Modifications listed in Table 5.4 and the manuscripts presented in the following Chapters, Chapter 6, Chapter 7, Chapter 8 and Chapter 9 are attempts to achieve this goal.

Table 5.4: Examples of adaptations made to Crocus to better represent polar conditions.

Reference	Region	Adaptation	For tuning of which snow variable?
Sauter and Obleitner (2015)	Svalbard on glaciers	new snow density parameterisation (change of factor in default parameterisation) $a = 300$ kg m^{-3} (default: $a = 109$ kg m^{-3}	near surface density (underestimation of settling and compaction)
		water percolation and refreezing water contributes to runoff at snow-ice layer interfaces rather than percolating through the next layer → preventing percolation into glacier and enhanced refreezing	formation of superimposed ice
Royer et al. (2021)	circumpolar Arctic area	new snow density parameterisation (change of factor in default parameterisation) $c = 52$ kg m$^{-7/2}$ s$^{-1/2}$ (default: $c = 26$ kg m$^{-7/2}$ s$^{-1/2}$)	near surface density (underestimation of wind effect on density)
		increase wind effect from 1 to 3	underestimation of wind compaction
		maximum density impacted by wind from 350 kg m^{-3} to 600 kg m^{-3}	Several studies show higher surface densities (see references in Royer et al. (2021))
		following Gouttevin et al. (2018): deactivation of wind compaction, increasing of viscosity under vegetation	vegetation trapping effect (low basal densities)
		thermal conductivity of snow: default after Yen (1981) changed to parameterisation after Sturm et al. (1997)	better suitable parameterisation of thermal conductivity in snow for Arctic snow
Jacobi et al. (2010)	Alaska	reduction of ground heat fluxes depending on the month of the year between December (30 %) and April (80 %)	simulating decrease of thermal conductivity during winter
Barrere et al. (2017)	Bylot Island, Canada	addition of a 10 cm thick surface litter	improvements in upper (10 cm) soil temperature and water content
		addition of organic carbon within the soil profile	improvements in upper (10 cm) soil temperature and water content
		increase the maximum density for wind-induced snow compaction, from 350 to 600 kg m^{-3}	Increasing density of wind-compacted snow layers
Domine et al. (2016b)	Bylot Island, Canada	increasing viscosity of dry snow in the presence of shrubs, deactivation of wind effects in shrubs, decreasing of albedo	simulating effects of vegetation
Gallet et al. (2014b)	Dome C, Antarctic	changed the simulated densities of the upper 2 cm to measured densities that were higher than simulated ones	improvements in microstructure simulations
Libois et al. (2014)	Dome C, Antarctic	new snow density is set to 170 kg m^{-3}	increase of new snow density to measurements
		SSA of new snow is set to 100 m^2 kg^{-1} (maximum default: 65 m^2 kg^{-1})	adaptation to measurements
		increase of maximum density due to compaction by wind to 450 kg m^{-3}	Increasing density of wind-compacted snow layers
		adaptation of the aggregation scheme for numerical layers	handling of prevailing low precipitation amounts

6 On the adequacy of using atmospheric reanalysis for detailed snow simulations[2]

This chapter is currently under review as

Krampe, D.[1], Kauker, F.[1,2], Dumont, M.[3], and Herber, A.[1]: **Snow and meteorological conditions at Villum Research Station, northeast Greenland: On the adequacy of using atmospheric reanalysis for detailed snow simulations,** Frontiers in Earth Science, in review, 2022.

Parts of this chapter are published in a preprint in The Cryosphere Discussion as

Krampe, D.[1], Kauker, F.[1,2], Dumont, M.[3], and Herber, A.[1]: **On the performance of the snow model Crocus driven by in situ and reanalysis data at Villum Research Station in northeast Greenland**, The Cryosphere Discuss. [preprint], https://doi.org/10.5194/tc-2021-100, 2021.

[1] Alfred-Wegener-Institut Helmholtz-Zentrum für Polar- und Meeresforschung, Department of Climate Science, Bremerhaven, Germany
[2] Ocean Atmosphere Systems GmbH, Hamburg, Germany
[3] Univ. Grenoble Alpes, Université de Toulouse, Météo-France, CNRS, CNRM, Centre d'Études de la Neige, 38000 Grenoble, France

Author contributions

DK carried out the analysis, performed the model simulations, drafted the manuscript and prepared the figures. FK helped with fruitful discussions of the analysis and designed the methodology of the sensitivity survey. All authors contributed to the editing of the manuscript. AH helped with the observational design of the study. FK and MD assisted with the numerical design. AH was leading the PAMARCMiP campaign.

[2] After the submission of this dissertation, this manuscript has been published. The updated citation is Krampe D., Kauker F., Dumont M. and Herber A.: **Snow and meteorological conditions at Villum Research Station, Northeast Greenland: on the adequacy of using atmospheric reanalysis for detailed snow simulations.** Frontiers Earth Science, 11, https://doi.org/10.3389/feart.2023.1053918, 2023.

Abstract

Reliable and detailed measurements of atmospheric and snow conditions in the Arctic are limited. While atmospheric modern reanalyses could potentially replace the former, the latter can be principally simulated by dedicated snow modelling. However, because the uncertainties of reanalyses and modelling are exceptionally large at high latitudes, a thorough analysis of the performance of atmospheric reanalyses and the snow model simulations are required. Specifically, we aim to answer the following questions for Villum Research Station (VRS), northeast Greenland:

(1) What are the predominant snow and meteorological conditions?

(2) What are systematic differences between the modern atmospheric reanalysis ERA5 and in situ measurements?

(3) Can the snow model Crocus simulate reliably snow depth and stratigraphy?

We systematically compare atmospheric in situ measurements and ERA5 reanalysis (November 2015 - August 2018) and evaluate simulated and measured snow depth (October 2014 - September 2018). Moreover, density and specific surface area (SSA) are determined from detailed vertical profiles exemplarily for two days.

We found good agreement between in situ and ERA5 atmospheric variables except for precipitation, wind speed, and wind direction. ERA5's resolution is too coarse to resolve the topography in the study area adequately, leading presumably to the detected biases.

Crocus can simulate satisfactorily the evolution of snow depth, but simulations of SSA and density profiles for both forcings are biased compared to measurements. Unexpectedly, measured snow depth agrees better with ERA5 driven simulations than with simulations forced with in situ measurements.

In conclusion, ERA5 has great potential to force snow models but the use of Crocus in the Arctic is affected by limitations. These limitations strongly affect the accuracy of the vertical profiles of physical snow properties.

6.1 Introduction

The availability of snow data, especially snow depth and physical snow properties in the Arctic, is temporally and spatially limited. However, snow plays a crucial role in the Arctic, as it covers the ground most of the year as well as the sea ice during the cold season. Snow depth, snow cover duration as well as snow properties such as density, specific surface area (SSA: Ice-air interface surface area divided by snow mass, (Calonne et al., 2020)), thermal conductivity and albedo have climatic, ecology and socioeconomic impacts (Sturm et al., 1997; Hall, 2004; Callaghan et al., 2011; Box et al., 2012). Changes in snow cover alter the exchange of energy and mass e.g. by modifying the albedo of the surface as well as the sensible, latent and ground heat fluxes and thus also the length of the growing season (Stiegler et al., 2016). Snow also affects the flora and fauna. It is an important habitat for Arctic animals from the smallest like lemmings to the biggest animals the polar bears (Schmidt et al., 2012; Liston et al., 2016; Domine et al., 2018a; Boelman et al., 2019).

Despite its importance, the description of snow in current models, e.g. sea ice-ocean models, is simple as in most cases a fixed density for all layers is assumed (e.g. Uotila et al. (2019)). These simplifications strongly limit the value of the output of these systems. In addition, for numerical weather predictions more accurate snow models allowing for snow metamorphism that work not only in the mid-latitudes but also in the Arctic are strongly needed to represent high-latitude – mid-latitude linkages that affect the weather over e.g. Europe. Coupling of already existing snow models could help to overcome these issues (e.g. Day et al. (2020)).

Snow models are important tools to gain information about the snowpack evolution where snow measurements are seldom (Bartelt and Lehning, 2002; Liston and Elder, 2006; Vionnet et al., 2012). One snow model used for the Arctic is Crocus, e.g. Jacobi et al. (2010), Carmagnola et al. (2014), Essery et al. (2016), Barrere et al. (2017). For this study, we use the snow model Crocus due to the implementation of light absorbing impurities and related processes in snow (Tuzet et al., 2017), which we aim to use for future studies. The assessment of the performance of Crocus in the Arctic in previous studies shows that bulk variables are reasonably simulated while vertical profiles of snow properties are deficient e.g. due to the absence of water vapour transport (Domine et al., 2016b; Barrere et al., 2017; Domine et al., 2019).

However, complete and sufficiently long time series of meteorological measurements, especially reliable precipitation data, to force snow models are limited in the Arctic (Boelman et al., 2019). Therefore, snow models are often driven by atmospheric reanalyses delivering complete time series of meteorological data for given locations or areas (Barrere et al., 2017; Gouttevin et al., 2018; Domine et al., 2019). Such reanalyses data are physically consistent, which cannot be guaranteed for in situ observations (Hersbach et al., 2020). Since 2016, data from the next generation global atmospheric reanalysis ERA5 (European Centre for Medium-Range Weather Forecasts (ECMWF) ReAnalysis-5th Generation (ERA5) atmospheric reanalyses data set) are available (Hersbach et al., 2020). Some studies already evaluated the performance of ERA5 in the Arctic (Wang et al., 2019; Delhasse et al., 2020a). However, more studies are needed to investigate strengths and weaknesses of the reanalysis accurately.

So far, nobody has investigated the prevailing snow and atmospheric conditions at Villum Research Station (hereafter VRS). For the first time, ERA5 is being used to force the snow model Crocus in the Arctic. Therefore, in this paper we aim to answer the following main questions:

(1) What are the snow and meteorological conditions at VRS, northeast Greenland?

(2) What are systematic differences between ERA5 and in situ measurements in northeast Greenland regarding variables needed to drive snow models at an Arctic site?

(3) Can Crocus simulate reliably snow depth evolution and the vertical profiles of snow density and SSA at an Arctic site in northeast Greenland, when forced with atmospheric in situ data or ERA5?

We use in situ observations from Greenland at VRS, where meteorological data from November 2015 to August 2018 and snow depth from August 2014 to September 2018 were measured. In addition, during a campaign in spring 2018 numerous snow parameters, as snow depth, snow density and SSA were measured.

6.2 Data and methods

First, measured atmospheric and snow condition will be presented. Then differences in atmospheric in situ measurements and the modern reanalyses ERA5 will be analysed before both datasets are used to drive the snow model Crocus. Finally, the results of the simulations will be analysed and compared to in situ snow measurements.

6.2.1 Study site

The study site is located in the surroundings of the atmospheric measurement mast at VRS (81°34’ N, 16°38’ W, 37 m above sea level) in northeast Greenland (Figure 6.1). The Wandel Sea in the north, a local ice cap called Flade Isblink in the south and east and fjords in the west surround the low land (Rasch et al., 2016). The Greenlandic ice sheet is located at a distance of more than 100 km to the southwest (Gryning et al., 2021).

The observed annual mean temperature is -21°C. July is the warmest month (4°C) and March the coldest (-26°C) (Rasch et al., 2016; Gryning et al., 2021). The annual precipitation is 188 mm (Rasch et al., 2016). From mid-October to end of February there is polar night while from mid-April to beginning of September there is polar day (Nguyen et al., 2013).

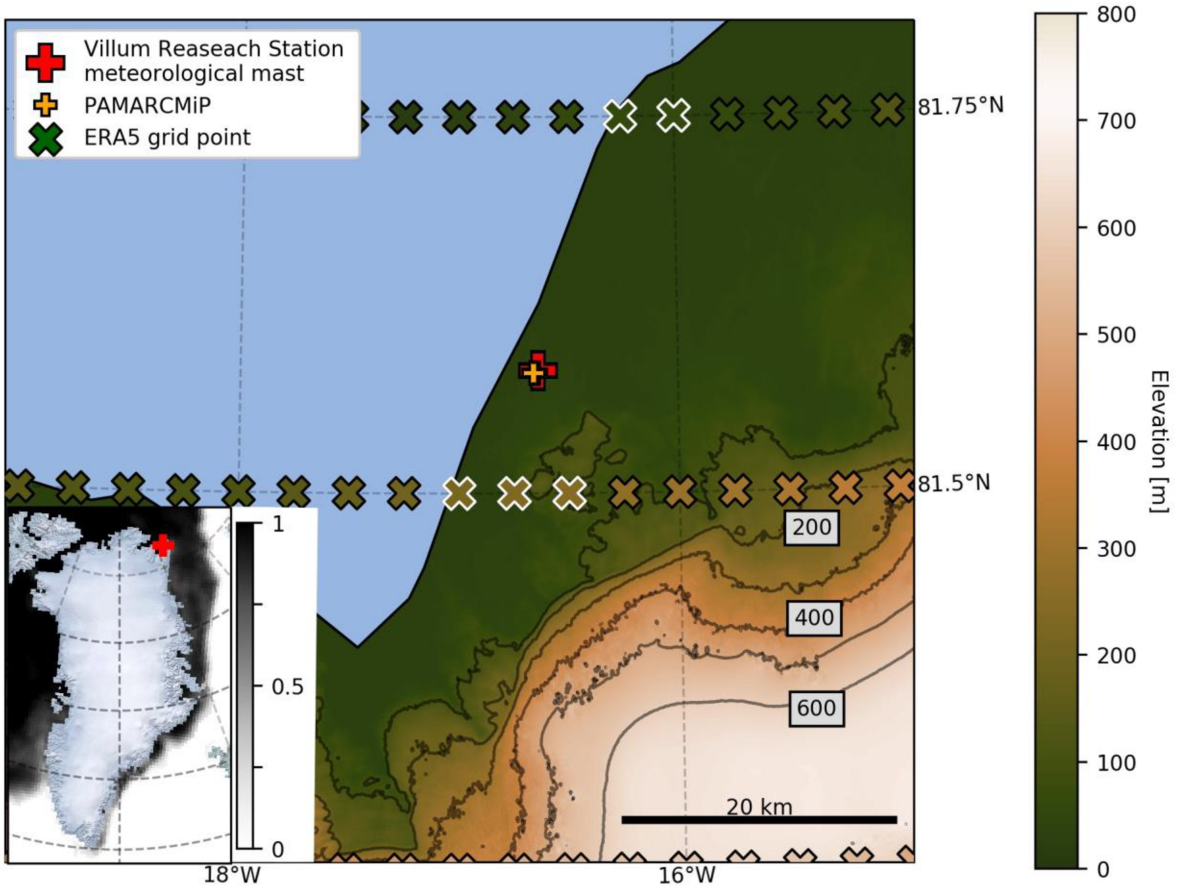

Figure 6.1: Map showing location of meteorological mast of Villum Research Station (red cross), measurement location during PAMARCMiP (yellow cross), ERA5 grid cell centres and terrain elevation (both using the same colour bar, the crosses are filled with colours according to the ERA5 elevation) in northeast Greenland (Digital elevation model: Howat et al. (2015), Howat et al. (2014)). Crosses with white boundaries are the ERA5 grid cells used in this study. Small inserted panel at left bottom: Sea ice concentration from 15 March 2018 (Maslanik and Stroeve, National Snow and Data Center, updated yearly).

6.2.2 In situ measurements

Meteorological data were measured at an automatic weather station (Villum Reserach Station, 2021). We choose the study period to compare atmospheric variables of ERA5 and in situ and simulated snow depth according to the availability of measured forcing variables between 27 November 2015 and 8 August 2018. Table 6.1 gives an overview on the installed meteorological sensors and their accuracy. In the Appendix an overview about the different time periods used for validation and simulations in this study is delivered (Table B.1).

Table 6.1: Meteorological sensors installed at Villum Research Station (Yankee Environmental Systems, 2012; ASIAQ, 2014).

Variable	Device	Accuracy	Sensor height [m]	Missing measurements
Air temperature	ROTRONIC - HC2-S3C03-PT15	± 0.1°C	3	1.9 %
Relative humidity	ROTRONIC - HC2-S3C03-PT15	± 1 %	3	2.9 %
Wind speed	Vector Instrument - A100R	±0.1m s^{-1}	9	5.9 %
Wind direction	Vector Instrument - W200P	±2°	9	5.1 %
Surface air pressure	Vaisala - PTB110	± 1.0 hPa	2	1.4 %
Incoming shortwave radiation	Kipp&Zonen - CNR4	<5 %	3	19.0 %
Incoming longwave radiation	Kipp&Zonen - CNR4	<10 %	3	5.6 %
Precipitation	Yankee Environmental Systems - TPS-3100	±0.5 mm h^{-1}	3	35.2 %

In situ snow depth was measured at VRS from 26 August 2014 to 30 September 2018 (ASIAQ, 2014). In addition, we conducted snow measurements during the **P**olar **A**irborne **M**easurements and **A**rctic **R**egional **C**limate **M**odel **Si**mulation **P**roject (PAMARCMiP) campaign, in a distance less than 500 m away from VRS, between 10 March and 8 April 2018. Measurements included, snow density, SSA and snow depth. The meteorological situation during and shortly before the campaign is described in Sect. 6.3.2.2.

Vertical profiles of snow density and SSA were retrieved from a SnowMicroPen (SMP) Version 4, a snow penetrometer measuring the bonding force between snow grains with a vertical resolution of 1.25 mm (Schneebeli et al., 1999). Note, there are different parameterisations to obtain density and SSA from penetration force and hence calculating snow density and SSA from penetration force introduces uncertainties.

While the parameterisation from Proksch et al. (2015) was developed for an older SMP version, the parameterisations from Calonne et al. (2020) and King et al. (2020) were developed for the SMP Version 4, used here. However, calibrations of the individual parameterisations were made for different regions. For the development of the parameterisation, Proksch et al. (2015) used data from the European Alps and the Arctic, while measurements for the parameterisation after Calonne et al. (2020) were from the Swiss Alps and therefore only for warm snow. The density parameterisation of King et al. (2020) was developed using measurements from Arctic snow on sea ice.

As snow from different regions (e.g. Arctic and Alps, land and sea ice) is not similar, we tested all these parameterisations. Three parameterisations were applied for density and SSA was obtained based only on Calonne et al. (2020) and Proksch et al. (2015), as King et al. (2020) did not provide any SSA parameterisation.

Results are shown in Figure 6.2. While density calculated after Calonne et al. (2020) and King et al. (2020) differ only slightly, densities after Proksch et al. (2015) were considerably higher in the upper part of the profiles and generally more variable over the entire profile (Figure 6.2 shaded areas). However, density after King et al. (2020) is lower than obtained from the other parameterisations especially in the lower part. SSA after Calonne et al. (2020) differed strongly from Proksch et al. (2015) and is clearly higher and more variable over the entire profile.

After comparing the results for all parameterisations, we used results after Calonne et al. (2020) for the comparison with simulations. Calonne et al. (2020) provides parameterisations for density and SSA and is developed for the SMP version we used in the field. Further, calculated density is overall in good

agreement with density calculated after King et al. (2020). However, our comparison shows that results should be interpreted with care.

Due to thick ice layers within the snowpack, the SMP could not penetrate the full vertical profile and snow depth measurements were not possible. The maximal penetration depth of the SMP measurements on 23 March 2018 was about 0.8 m.

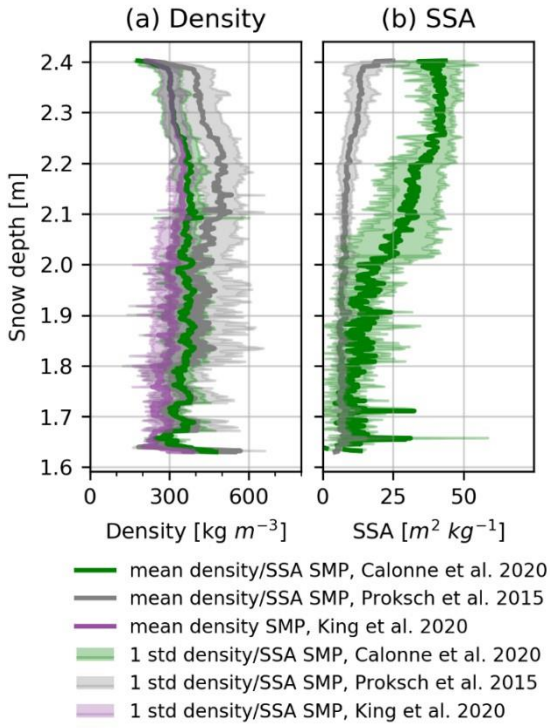

Figure 6.2: Comparison of SnowMicroPen (SMP) parameterisations of Calonne et al. (2020), Proksch et al. (2015) and King et al. (2020) (only density) to obtain (a) snow density and (b) specific surface area (SSA) from penetration force measured on 23 March 2018. The shaded areas represent the standard deviation range.

In addition, on 3 April 2018, total snow depth was measured with a ruler, and every 0.1 m of the profile, snow density was measured with a density cutter (60x30x56 mm^3) and SSA with an IceCube3 at five locations. The optical system IceCube measures the hemispherical infrared reflectance of snow and converts the reflectance in SSA (Zuanon, 2013). Table 6.2 provides further details on the instruments used for the measurements.

Table 6.2: Instruments used to measure snow physics at Villum Research Station and during PAMARCMiP campaign.

Variable	Device	Accuracy	Measurement date
Snow depth	Campbell - SR50A	±1 cm (ASIAQ, 2014)	26 Aug 2014–30 Sep 2018
Snow density and specific surface area	SnowMicroPen	Arctic mean relative error ~15 % (from Proksch et al. (2015), note that here we use Calonne et al. (2020), but no accuracy is delivered by Calonne et al.	23 March 2018
Snow density	Density Cutter	±10 % (Domine et al., 2016a)	3 April 2018
Specific surface area	IceCube3	±10 % (A2 Photonic Sensors, 2016)	3 April 2018

6.2.3 Modelling

6.2.3.1 The snow model Crocus

We used the multilayer snow model Crocus (Brun et al., 1992; Vionnet et al., 2012) in single-column mode. The snow model is embedded in the surface scheme SURFEX (version 8.1) and is coupled to the soil model ISBA-DF (Boone et al., 2000). The snow model can deal with up to 50 dynamical snow layers. Layer thickness, heat content, density and age characterise each snow layer. The number of the snow layers is dynamical, i.e. layers can run empty (zero thickness).

Crocus describes the evolution of the snowpack by taking the energy- and mass balance of the snowpack into account. Implemented processes are surface melting, internal melting and refreezing, snow metamorphism, near-surface densification due to wind, enhanced sublimation for strong winds, fragmentation and compaction due to snowdrift, settling due to the weight of overlying snow layers and solar absorption in the snowpack. Snow compaction and microstructural changes due to wind drift in Crocus occur when wind speed exceeds a transport threshold depending on snow properties. Commonly, this threshold is at 6 m s^{-1} (Vionnet et al., 2013). These wind drift effects are passed on to the underlying layers with an exponential decay until the precalculated layer's transport threshold falls below the wind speed. Snow redistribution is not taken into account (Vionnet et al., 2013).

Crocus is driven by surface fluxes derived from air temperature, specific humidity, wind speed, incoming direct and diffuse shortwave and longwave radiation, rain- and snowfall rate and surface air pressure. In addition to the atmospheric forcing, the model uses the terrain information aspect, slope and altitude as well as optionally wet and dry deposition coefficients of black carbon (BC) or other light absorbing impurities (Tuzet et al., 2017). A detailed description of the model can be found in Vionnet et al. (2012).

6.2.3.2 Model simulations setup

ERA5

The global atmospheric reanalysis ERA5 is available in the Climate Data Store of Copernicus on a regular latitude-longitude grid at 0.25° x 0.25° resolution and has a temporal resolution of one hour (Hersbach et al., 2020). For VRS the grid cell size is 5 km along the longitude and 31 km along the latitude. The output of the simulations driven by ERA5 are representable on spatial scales of at least one grid cell size, i.e. on 5 km x 31 km.

Instead of interpolating spatially to the location of VRS, we took the nearest available grid cell (mid-point at 81.5° N 16.75° W, 185 m above sea level), which is about 10 km south from VRS. This is done to avoid spatial interpolation of the atmospheric variables, which might destruct their physical consistency. We ran the model with atmospheric input from the four other nearest neighbour grid cells to VRS located on land (Figure 6.1). The results of the additional simulations were taken as a metric for the co-location error, i.e. were deemed to give information of the representativeness of the ERA5 data (see Loew et al. (2017) for an introduction of the terminology used).

Due to a constant negative offset throughout the years in ERA5's surface air pressure, probably caused by orographic effects (see Sect. 6.3.2.1), we adjusted ERA5 surface air pressure by adding the mean difference between in situ air pressure and ERA5 air pressure. To reduce spin-up effects, introduced through the unknown initial conditions of the soil, we run a longer simulation from January 2010 to December 2019 and used the initial conditions on 31 December 2019 for a second pass of the period. This second pass simulation is called ERA5 control run (ERA5-CTRL). An overview of all model simulations performed is given in Table 6.3. Simulations to analyse the impact of individual forcing variables on the simulated snow depth (ERA5-sens, see Sect. 6.2.3.3) used ERA5-CTRL forcing but with disturbances on each individual forcing variable.

In situ measurements

For the simulations driven by measured atmospheric data, meteorological data from VRS were used. To force Crocus, we resampled the data to hourly mean or hourly accumulated data, respectively.

We used ERA5 data to fill in missing data (about 5 %) for all in situ variables, except for precipitation. The amount and timing of precipitation events were too diverse between ERA5 and in situ measurements to fill the missing data. In addition, an overestimation of precipitation would be introduced when filling missing precipitation data with ERA5 precipitation, most likely because of the different spatial scales of precipitation in ERA5 and the in situ data (the latter containing much smaller scales). Therefore, we deliberately set missing precipitation data to zero knowing that this is causing an underestimation of the accumulated precipitation. Additionally, we examined the timing and length of the precipitation data gaps. There are many short gaps over the entire study period, as visible in Figure B.1 (in the Appendix).

The in situ control simulation (Insitu-CTRL) is forced with in situ measurements from VRS from 27 November 2015 to 8 August 2018, except for the measured longwave radiation, which was replaced by the corresponding ERA5 variable for the whole study period because of the systematic errors in this measurements (see Figure B.2 in the Appendix for a comparison of measured and ERA5 longwave radiation). To reduce spin-up effects for the in situ simulation, we used the archived initial conditions from 26 November 2015 of ERA5-CTRL, as initial conditions for the in situ simulation.

Table 6.3: Overview of all conducted model simulations (LWdown: Longwave radiation downwards, PSurf: Surface air pressure).

Name of simulation (acronym)	**Forcing data**	**Timeframe**	**Adaptations**
ERA5 control (ERA5-CTRL)	ERA5 data	2010–2020	PSurf offset adapted to in situ data
ERA5 sensitivity (ERA5-sens)	as in ERA5-CTRL	2010–2020	as ER5-CTRL but one simulation for each forcing variable is disturbed by + one-tenth standard deviation
In situ control (Insitu-CTRL)	in situ data, LWdown from ERA5	Nov 2015–Aug 2018	LWdown from ERA5

6.2.3.3 Sensitivity simulations

To understand the difference between the simulated snow depths we used the approach of partial disturbances. With this approach, we were able to quantify the contribution of every forcing variable to the difference in the simulated snow depth between ERA5-CTRL and Insitu-CTRL.

We used ERA5-CTRL as baseline simulation for our sensitivity survey because of its consistency and completeness of all forcing variables. From the ERA5 data, we calculated the daily standard deviation from January 2010 to August 2020 for every forcing variable. We used this longer time period to get more robust estimates of the standard deviations. We added one-tenth of the standard deviation to the individual variable as typical disturbance d_i while all other variables were unchanged in each simulation of ERA5-sens. Then, we determined the difference between the simulated snow depth for each of the ERA5-sens simulations and the ERA5-CTRL simulation. The sensitivity $e(x_i)$ for every forcing variable is defined as:

$$e(x_i) = \left(m(x_i + d_i) - m(x_i) \right) / d_i, \tag{6.1}$$

with d_i being one-tenth of the standard deviation from the ERA5 ith forcing variable.

We estimated the influence of each forcing variable on the snow depth difference between Insitu-CTRL and ERA5-CTRL as:

$$m(x_i') - m(x_i) = e(x_i)(x'_i - x_i), \tag{6.2}$$

with $m(x_i')$ - $m(x_i)$ being the mean bias of in situ and ERA5 simulated snow depth and x_i' - x_i the mean difference between the *i*th in situ and the corresponding ERA5 forcing variable. For a perfect linear model, the sum of $m(x_i')$ - $m(x_i)$ over all forcing variables x_i would be equal to the snow depth difference between Insitu-CTRL and ERA5-CTRL. However, because of the non-linearities in the model the sum approximates the "real" difference of both simulations but allows us to identify the main sources of the difference between Insitu-CTRL and ERA5-CTRL with respect to the simulated snow depth.

6.3 Results

6.3.1 Measured conditions at Villum Research Station

6.3.1.1 Overview: In situ atmospheric measurements

An overview about the atmospheric conditions of the study period (27 Nov 2015 – 8 Aug 2018) is given in Figure B.2 in the Appendix. The mean air temperature during the study period is -14.5°C. Thereby, the maximum air temperature is 14.1°C (26 July 2016) and the minimum temperature -41.1°C (10 March 2017).

In general, positive monthly mean temperatures are measured between June and August (2016: June 0.4°C, July 5.8°C, Aug 3.4°C; 2017: June 0.9°C, July 5.5°C, Aug 2.8°C, 2018: July 2.5°C). Mean seasonal air temperatures are the following: December to February: -25.0°C, March to May: -20.4°C, June to August: 2.6°C, September to November: -13.7°C. Thereby, direct incoming shortwave radiation is present from February until October, whereby maximum incoming radiation is reached in June in all years (2016: 345.8 W m^{-2}, 2017: 338.9 W m^{-2}, 2018: 351.1 W m^{-2}).

Rainfall is measured in 2016 in the months June to September, in 2017 in May to September and in 2018 in February, May, July and August. Thereby, maximum rainfall occurs in June 2017 (38.6 mm). Other months where more than 30 mm rainfall is present are July 2016 (37.6 mm), July 2017 (34.7 mm).

There is no month without snowfall. Minimum snowfall shows up in July in all three years (2016: 5.6 mm w.e., 2017: 14.4 mm w.e., 2018: 3.5 mm w.e.). Highest snowfall does not always occur in the same month. Months with snowfall higher than 100 mm w.e. appear in December 2015 (135.3 mm w.e.), May 2017 (140.2 mm w.e.) and in February 2018 (571.0 mm w.e.). By far the largest accumulated monthly snowfall during the study period takes place in February 2018.

6.3.1.2 Measured snow depth

Snow depth varies considerably even on small spatial scales. With the SA50A-sensor, we can only measure point snow depth. On 3 April 2018, snow depth in the vicinity of VRS varied between 0.60 m and 1.17 m with a standard deviation of 0.22 m. This might be caused by several small depressions and bumps that influenced local snow depth.

As can be seen in Figure 6.3 and Table 6.4, snow cover started to form in late August in all years. Snow cover lasted until mid-July of the following year for the snow seasons 2014/15 and 2015/16, until late June for the snow season 2016/17, and until early August for 2017/18.

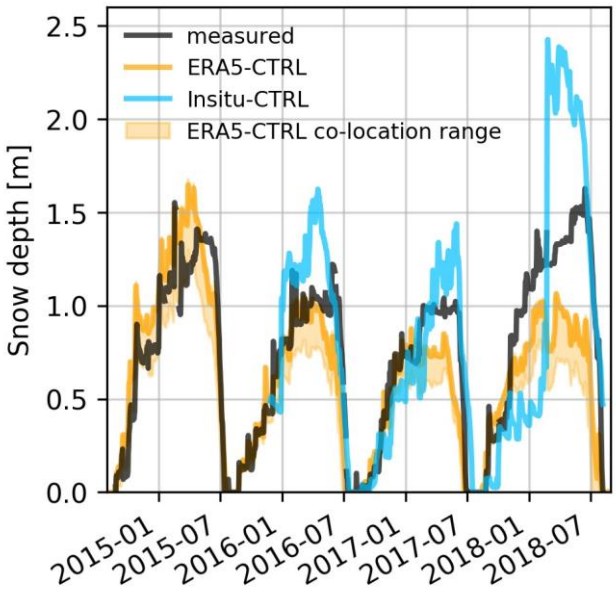

Figure 6.3: Snow depth at Villum Research Station from August 2014 to August 2018 covering four entire snow seasons. Measured snow depth (black line) and simulated by ERA5-CTRL (orange line - closest ERA5 grid cell to Villum Research Station) and by Insitu-CTRL (blue line – no data available before 27 November 2015 and after 7 August 2018). The orange shaded area visualises minimum and maximum snow depth of simulations at the four additional ERA5 grid cells nearest to Villum Research Station located on land and serve to illustrate the potential influence of the co-location error.

The date and the height of the maximum snow depth varied considerably between the snow seasons with the highest maximum snow depth during the entire study period of 1.62 m (15 June 2018) and the lowest maximum snow depth of 1.03 m (23 April 2017). The long-term mean snow depth during the snow season was 0.74 m.

Table 6.4: Measured start and end dates of snow season for each year of the study period, defined as the first date on which snow depth exceeds or falls below 0.05 m, respectively. Height and date of maximum snow depth.

	Snow season start date (first date > 5 cm)	**Snow season end date** (last date > 5 cm)	**Maximum snow depth and date**
2014/15	28 Aug 2014	13 July 2015	1.54 m 18 Feb 2015
2015/16	27 Aug 2015	13 July 2016	1.22 m 28 May 2016
2016/17	after 25 Aug 2016 (nans until 28-Sep-2016 (11 cm))	27 June 2017	1.03 m 23 April 2017
2017/18	too many false and missing data	05 Aug 2018	1.62 m 15 June 2018

6.3.1.3 Measured snow density

Mean snow density over all profiles measured with the SMP on 23 March 2018 was 307 kg m^{-3} (standard deviation: 33 kg m^{-3}), while the SMP was only able to penetrate a maximum of about 0.8 m from the top of the snow layer due to thick ice lenses. The SMP measurements (Figure 6.2) showed a pronounced increase in the density from about 180 kg m^{-3} to about 300 kg m^{-3} in only a few centimetres down from the snow surface. This density peak could reflect a surface wind slab layer, which density cutter measurements cannot resolve.

The snow density cutter measurements on 3 April 2018 (Figure 6.4) result in a mean density of 291 kg m^{-3} (standard deviation: 67 kg m^{-3}). During the snowpit surveys, measurements over the full profiles were possible and we found thick ice layers in the lower 0.4 m in 40 % of the snowpits and 0.3 m to 0.4 m thick compacted snow layers about 0.2 m below the snow-atmosphere interface in another 40 % of the snowpits.

We observed a decrease in density towards the basal layers. In addition, observations during fieldwork indicate a bottom depth hoar layer in our profiles. Our density observations reflect the typical stratigraphy of an Arctic snowpack: a basal depth hoar layer with low density (150–200 kg m^{-3}) and high density at the top wind slab snow layers (exceeding 400 kg m^{-3}).

6.3.1.4 Measured snow SSA

On 23 March 2018 the mean SSA measured with the SMP (Figure 6.2) was 24 m^2 kg^{-1} (standard deviation: 12 m^2 kg^{-1}) for the top 0.8 m. At the top layer the mean surface SSA was 44 m^2 kg^{-1} (standard deviation: 7 m^2 kg^{-1}). SSA was stable over the top 0.15 m and halved over the next 0.4 m (25 m^2 kg^{-1}) while it was stable again over the following 0.35 m.

Also, the IceCube measurements from 3 April 2018 (Figure 6.4) showed a decrease in SSA from the surface towards the middle part of the snow layers continued by an almost constant course to greater depth. Thereby, mean SSA was 34 m^2 kg^{-1} (standard deviation: 11 m^2 kg^{-1}). However, amplitudes of the decrease and the absolute value of SSA between all snow profiles differed considerably.

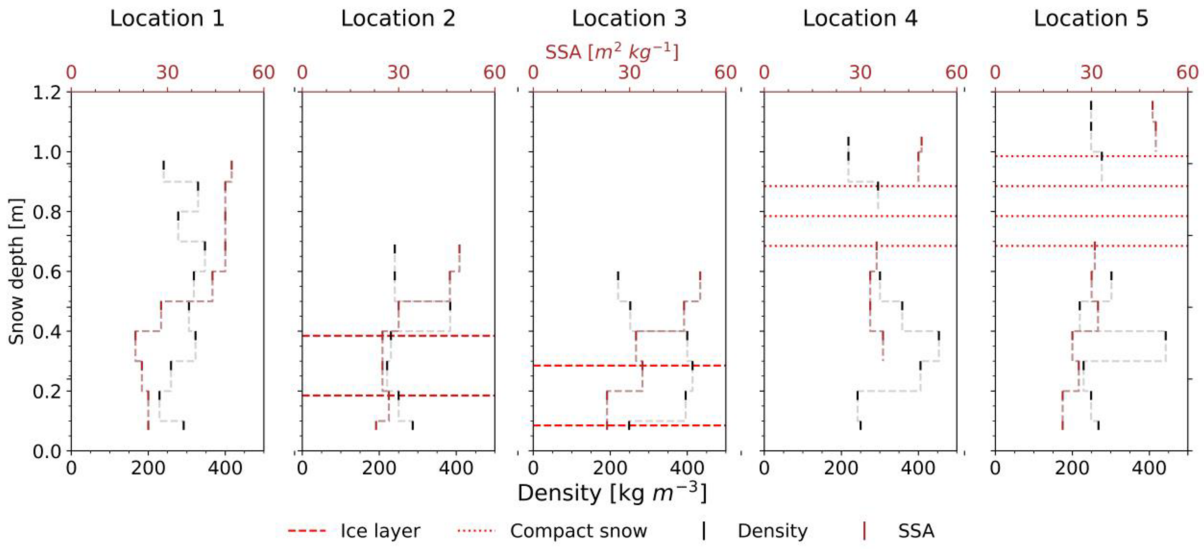

Figure 6.4: Observed snow densities with the density cutter in black and specific surface area with the IceCube in brown. Measurements from 3 April 2018. Note the difference snow depth of the five profiles.

6.3.2 Comparison of atmospheric in situ measurements and reanalysis data

6.3.2.1 Entire study period

Figure 6.5 shows scatter plots of daily anomalies of the atmospheric forcing variables from ERA5 and the in situ data. Observed direct shortwave radiation, diffuse shortwave radiation, specific humidity and air temperature agreed well. Mean biases were small and the Pearson correlation coefficients (r) were between 0.84 and 0.91. ERA5 underestimated the air temperature by 1.0°C and the specific humidity by 0.0002 kg kg^{-1} compared to the in situ data. Longwave radiation showed a poor correlation (r: 0.28) and a high root mean square difference (RMSD): 60.5 W m^{-2}), which we attribute to measurement errors in the in situ longwave radiation clearly visible in Figure B.2 in the Appendix.

Atmospheric surface pressure correlated well with in situ surface pressure (r: 0.99) but showed a systematic offset of 19 hPa. We attribute this bias to the altitude difference of the ERA5 nearest grid cell to VRS of about 150 m caused by the relatively coarse resolution of ERA5. ERA5 surface air pressure of the four grid cells closest to VRS showed a large spread (mean surface air pressure difference -9 hPa, standard deviation: 13 hPa).

Rain- and snowfall showed mean biases of 0.1 mm day^{-1} and 0.6 mm day^{-1} w. e. (water equivalent) and poor correlations of 0.15 and 0.13, respectively. Observed and ERA5 precipitation differed strongly not only in the amount but also in the timing of extreme events. In situ precipitation was generally higher than ERA5 precipitation. ERA5 rainfall tended to be weaker than in situ rainfall.

In situ measurements showed clearly more snowfall over the entire study period than ERA5 (70 % of total measured snowfall). In contrast, the frequency of ERA5 snowfall was more than three times higher than the frequency of in situ snowfall, i.e. ERA5 showed many small snowfall events. The proportion of snowfall in total precipitation was lower for in situ measurements (90 %) than for ERA5 (95 %), probably due to the higher elevation of the nearest grid cell.

ERA5 and measured wind direction showed as well large deviations. Measured preferred wind direction was from the south-west while ERA5's preferred wind direction was from the south (Figure B.3 in the Appendix). The mean wind speed from ERA5 over the entire study period was slightly higher than measured (0.2 m s^{-1}). However, ERA5 underestimated the occurrence of wind speeds higher than 6 m s^{-1}.

In summary, there was a good match between atmospheric measurements and ERA5 for the variables incoming direct and diffuse shortwave radiation, incoming longwave radiation (except the period of obvious measurement errors) and specific humidity. Air temperature and surface air pressure agreed well in general but altitudinal differences between actual topography and ERA5 resolved topography have to be taken into account. Lower wind speeds were reproduced well by ERA5 but there were underestimations of higher wind speeds. Rainfall and snowfall showed considerable differences in frequency and amount. In our study, the use of longwave radiation from ERA5 instead of observations for the in situ forcing enabled us to circumvent measurement errors in this variable.

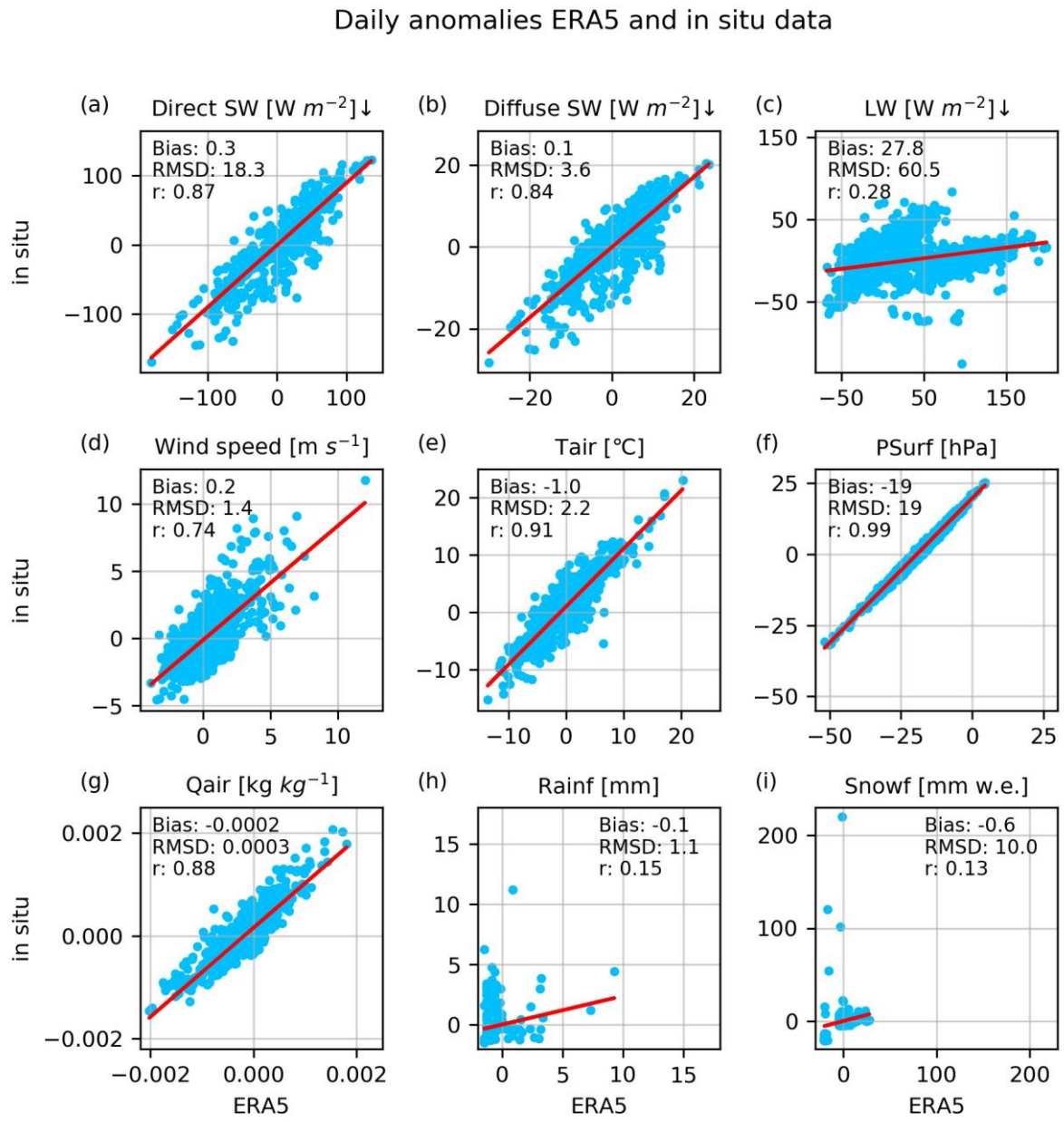

Figure 6.5: Scatter plots of ERA5 and in situ daily anomalies. Metrics inserted into each panel are the mean bias defined as ERA5 – in situ, root mean squared difference (RMSD) and correlation coefficient (r). The red line depicts the regression line. (a) Direct incoming shortwave radiation (SW), (b) diffuse incoming SW, (c) incoming longwave radiation (LW), (d) wind speed, (e) air temperature (Tair), (f) surface air pressure (PSurf), (g) specific humidity (Qair), (h) rainfall (Rainf) and (i) snowfall (Snowf) in mm w.e. (water equivalent).

6.3.2.2 During and shortly before the PAMARCMiP campaign

In the second half of February 2018 there was a remarkable period of exceptional weather conditions lasting about two weeks (Figure 6.6), where even air temperatures above freezing temperature were present in hourly data. The mean daily air temperatures between 17 February 2018 and 27 February 2018 were about 20°C warmer than in the weeks before and after. Also, February's mean air temperatures were about 8°C warmer than in 2016 and 2017 (2016: -26.7°C, 2017: -26.3°C, 2018: -18.2°C). 2018 is the only year where rainfall was present in February. In 2016 and 2017 the earliest rain occurred in June (2016) and May (2017).

During the PAMARCMiP campaign, air temperature was about -20°C. A high pressure system located over the North Pole together with several weak low pressure systems over northeast Greenland controlled the synoptic situation during the campaign (see also Nakoudi et al. (2020)).

The warm event was accompanied by remarkably strong winds. Hourly in situ wind speeds exceeded 20 m s^{-1}. During the time of the snowpit survey observed wind speeds were slightly below 6 m s^{-1} with some hours above 6 m s^{-1} at the beginning of the campaign. During the warm and strong wind event, wind direction was mainly from south to southeast, shifting towards southwest afterwards.

ERA5 underestimated snowfall during the first warm event. Between 17 Feb 2018 and 27 Feb 2018, ERA5 snowfall was about 5 % of the in situ snowfall (ERA5: 28 mm, in situ: 530 mm). Due to the short periods of air temperature above the freezing temperature there was also some rainfall measured. ERA5 rainfall during that time was close to zero at 81.5° N, 16.75° W, while neighbouring grid cells showed a similar amount of rainfall of 1 mm as the in situ measurements.

Apart from the first warm event the amount of precipitation in both datasets were similar, but the timing of precipitation events differed strongly. During PAMARCMiP, in situ measurements showed a snowfall event lasting over several days, which is not present in ERA5. Instead, ERA5 showed snowfall about a week before the campaign. Field observations during PAMARCMiP confirmed strong snowfall events.

In summary, ERA5 is able to catch the heat waves and strong winds in the second half of February 2018. Most variables match well during this period apart from precipitation and some minor deviations in wind direction and hourly wind speed during peak times, where hourly ERA5 wind speed underestimates.

Since ice layers were detected in the snowpack during PAMARCMiP we analysed the occurrence and timing of rain on snow events to investigate whether rain on snow events were responsible for the ice layers. For this purpose, we looked at rainfall events where there was ≥0.05 m of snow on the ground for the period where precipitation was measured (26 November 2015 to 8 August 2018, 987 days). During this period, there were 861 days with snow depth ≥ 0.05 m. On 52 days, i.e. in about 5 % of the time there were rain on snow events (mean daily rainfall 2.2 mm, standard deviation: 3 mm). They occurred dominantly at the end of the snow season (see Figure B.4 in the Appendix). However, 2018 was the only year during the study period, where rain and therefore rain on snow events were present already in February. Therefore, we assume that the ice layers found are caused not only by melting and refreezing of snow but also by rain on snow events.

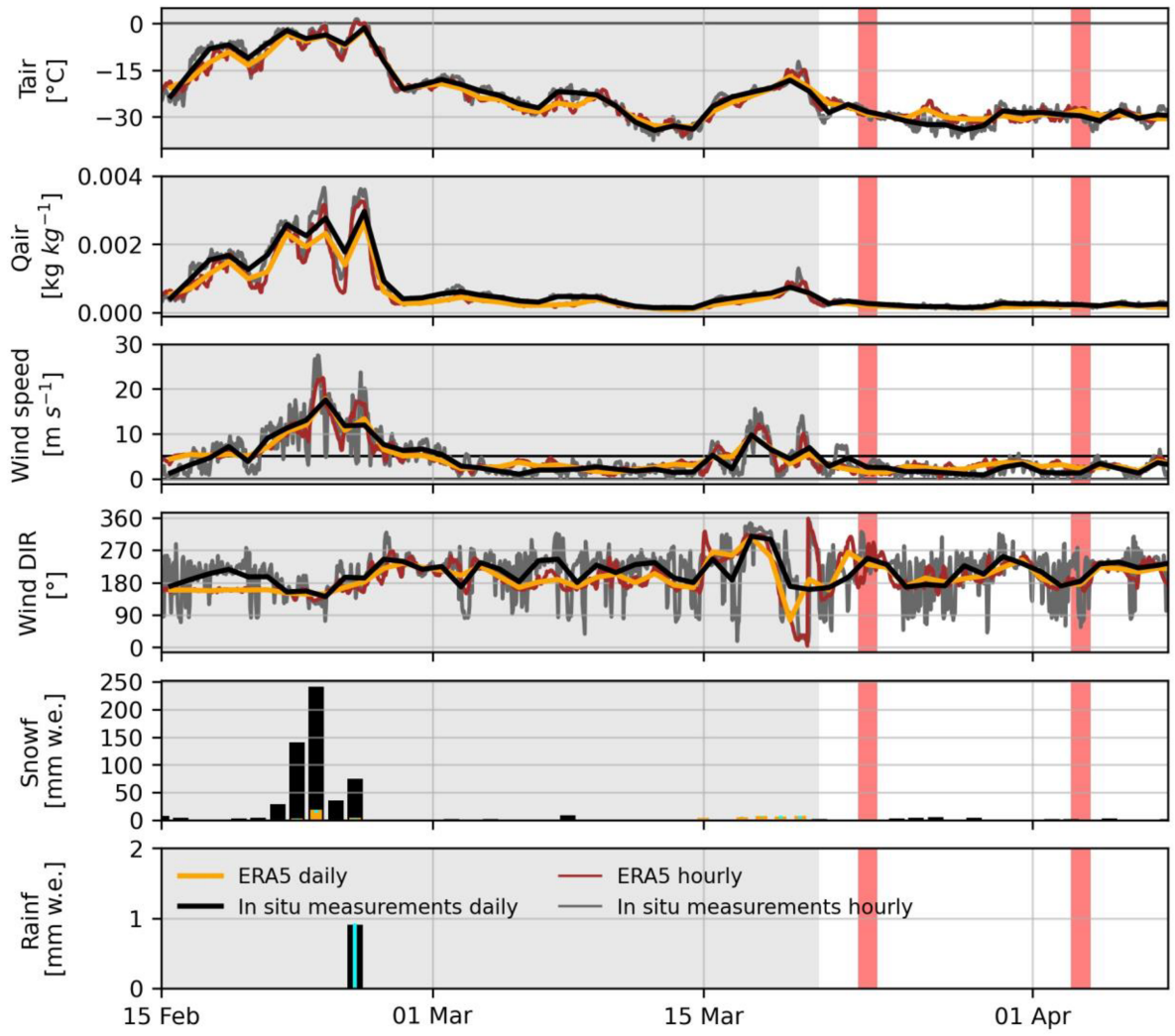

Figure 6.6: Atmospheric development from 15 February 2018 to end of PAMARCMiP campaign 8 April 2018. PAMARCMiP time is shown as the white and red area, whereby the red area is the time of the snowpit measurements. Cyan vertical lines in the panels for snow- and rainfall show the co-location error of ERA5. In case of rainfall the vertical line indicates the occurrence of rainfall on neighbouring grid cells (see text).

6.3.3 Snow simulations at Villum Research Station

In the last subsections, we examined the differences between atmospheric measurements and ERA5. This first step is important to understand the differences in snow simulation results that arise from the different forcings. With this background, in the following subsections we examined the simulated snow properties using these atmospheric data to force the snow model Crocus and compared it with the presented snow measurements.

6.3.3.1 Simulated snow depth

Overall ERA5-CTRL simulated the snow depth for the winter-centred years 2015/16, 2016/17 and 2017/18 in good agreement with the measurements (RMSD: 0.29 m) (Figure 6.7a). Until early spring, the measured snow depth was within the co-location error of the ERA5-CTRL simulations. Melting started too early compared to the measurements (Figure 6.3). Date and amount of the maximum snow depth showed some moderate differences.

While the onset of snow accumulation in 2017/18 of ERA5-CTRL was in good agreement with the observation, the simulation underestimated the snow depth from November 2017 onwards strongly. From late February to mid-March 2018, ERA5-CTRL showed even a slight reduction while the measured snow depth is growing, which further increased the difference between simulated and measured snow depth. Over the entire study period, the mean bias between ERA5-CTRL's snow depth and the observation was -0.17 m (Figure 6.7a).

The snow depth simulated by Insitu-CTRL overestimated the maximum snow depth in all three years. However, for the in situ forced simulation the initial values (e.g. snow depth) was taken from the spin-up run with ERA5-CTRL forcing on 26 November 2015 as no snow depth measurements were available before 27 November 2015. Therefore, in 2015/16 Insitu-CTRL was certainly impacted by the initial values and was difficult to evaluate, especially the simulated maximum snow depth.

The end of the snow season of 2015/16 agreed well with the snow depth measurements (Figure 6.3). In Insitu-CTRL the onset of snow accumulation and snow depth of the year 2016/17 matched well until late spring. Later in the year the accumulation events were too strong leading to an overestimation of the snow depth. The end of the snow season occurred somewhat later than observed in 2017.

In 2017/18, Insitu-CTRL overestimated the maximum snow depth by almost a meter and showed a later than measured increase in snow depth. Also, the in situ simulations clearly underestimated the snow depth at the beginning of the snow season 2017/18 until the strong precipitation event in February. From late February to early March, there was a distinct increase in snow depth of about 1.5 m within a few days. This event led to an overestimation of snow depth after the event (see Figure B.2 in the Appendix). Even if over the entire study period the mean bias between Insitu-CTRL and the observed snow depth was low (0.06 m), the RMSD is larger as in ERA5-CTRL (0.39 m versus 0.29 m). The explained variance, which is the proportion of variance in the observation that can be explained by the simulation was 23 % (Figure 6.7) while it was 73 % in the ERA5-CTRL simulation.

Figure B.2 in the Appendix shows that the monthly snow depth disagreements between measured and both simulated snow depths were highest during the melting season. Furthermore, the snow depth deviations were higher for the simulations driven by atmospheric in situ data than for the ERA5 driven simulations. Especially in 2018, in situ simulation strongly underestimated snow depth before February and overestimated snow depth afterwards.

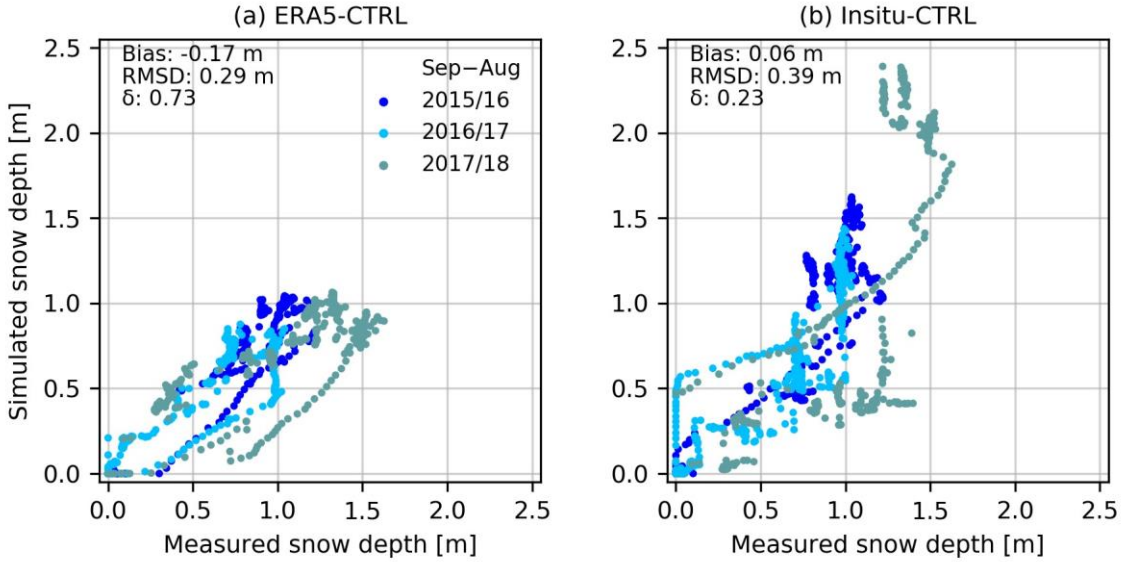

Figure 6.7: Scatter diagram of measured and simulated daily snow depth between 27 November 2015 and 8 August 2018. The different colours visualise different years. Metrics displayed are the mean bias, root mean squared difference (RMSD) and explained variance δ.

As the sensitivity survey (Table 6.5) showed, the differences between the in situ and ERA5 forcing in snowfall and specific humidity but also to a lower degree air temperature were dominantly causing the deviation between the simulated snow depth of Insitu-CTRL and ERA5-CTRL. The remaining forcing variables had minor impact.

The large response to the differences in specific humidity turned out to be an artefact of the linearisation. The experiment was rerun with a disturbance of 0.0002 kg kg^{-1} and resulted in a difference in snow depth of 0.17 m. This shows the limits of our approach – the sensitivity calculated for a disturbance of one-tenth of the standard deviation of the variability of the specific humidity was overestimated. Adding up the impacts on the snow depths of the perturbations on snowfall, specific humidity (0.0002 kg kg^{-1}) and air temperature amounted to 0.28 m and compared well with the mean difference in snow depths between Insitu-CTRL and ERA5-CTRL of 0.23 m, i.e. these forcing variables were causing the difference.

In summary, ERA5 simulated snow depth surprisingly clearly outperformed in situ simulated snow depth. Taking into account the considerable spatial snow depth variability, simulated ERA5 snow depth, which represents a mean of the grid cell, agreed unexpectedly well with the point measurements at VRS. We found that up to 73 % of the variance measured could be described by the ERA5 forced simulations. This is a high value for any kind of simulation of the earth system. The in situ simulations snow depth's showed larger deviations from the measured snow depth than the ERA5 simulation (only up to 23 % explained variance). The simulated in situ snow depth considerably overestimated. We did not expect that result as atmospheric forcing was measured nearby and we treated missing precipitation measurements as no precipitation. Hence, we expected an underestimation of snow depth rather than an overestimation.

One reason for differences in snow depth between ERA5 and in situ forced simulations and the measurements is attributed to variations in the snow densities. Hence, we calculated the snow water equivalent from measured snow depth by assuming a snow density of 250 kg m^{-3} and compared it with the simulated snow water equivalent. This confirmed that main differences in simulated and measured snow depth are due to different precipitation rates. However, we would need snow water equivalent measurements or higher vertically and temporally resolved snow density measurements to compare accurately snow water equivalents of simulations and measurements, which are unfortunately not available.

Table 6.5: Results of sensitivity survey. CTRL refers to the control simulations described in Sect. 6.2.3.2. Mean difference between in situ and ERA5 2015 – 2018 refers to the atmospheric forcings while remaining columns refer to the simulations. DIR_SWdown: Direct incoming shortwave radiation, SCA_SWdown: Diffuse incoming shortwave radiation, LWdown: Incoming longwave radiation, Tair: Air temperature, PSurf: Surface air pressure, Qair: Specific humidity, Rainf: Rainfall and Snowf: Snowfall in water equivalent (w.e.). Values below $1x10^{\pm4}$.

	Mean difference between in situ and ERA5 2015 - 2018	**One-tenth of standard deviation ERA5**	**Snow depth difference between ERA5-sens and ERA5-CTRL 2015 – 2018 [m]**	**Impact on snow depth difference between Insitu-CTRL and ERA5-CTRL 2015 – 2018 [m]**
DIR_SWdown [W m^{-2}]	-0.3	3.35	-0.007	0.001
SCA_SWdown [W m^{-2}]	-0.1	0.60	0.001	-0.0002
LWdown [W m^{-2}]	0	2.74	-0.01	0
Wind speed [m s^{-1}]	-0.2	0.17	-0.02	0.016
Tair [K]	1.0	0.42	-0.04	-0.091
PSurf [hPa]	0.01	0.80	0	0
Qair [kg kg^{-1}]	0.0002	4e-05	0.05	0.250
Qair 2e-04 [kg kg^{-1}]	0.0002	2e-04	0.17	0.167
Rainf [mm]	0.1	0.05	-0.0002	-0.001
Snowf [mm w.e.]	0.6	0.31	0.11	0.201

6.3.3.2 Simulated snow density profiles

Overall, simulated and measured density profiles showed a poor agreement for the CTRL simulations (Figure 6.8a and Figure 6.9a). Simulated snow densities, both in ERA5-CTRL and Insitu-CTRL were much lower than measured with the SMP or with the density cutter. This was especially true for the upper part of the profiles.

Density variations with depth within the snowpack were mostly small. Simulated snow densities showed a clear densification with depth and did not capture the snow density decrease from 388 kg m^{-3} to 270 kg m^{-3} measured with the density cutter in the lower part of the snowpack (e.g. below 0.3 of normalised snow depth, Figure 6.9a).

SMP measurements showed a pronounced increase in the density from 180 kg m^{-3} to 300 kg m^{-3} over a few centimetres below the snow surface, which density cutter measurements could not resolve. Both simulations (ERA5-CTRL and Insitu-CTRL) were not able to capture this density increase near the surface (Figure 6.8a).

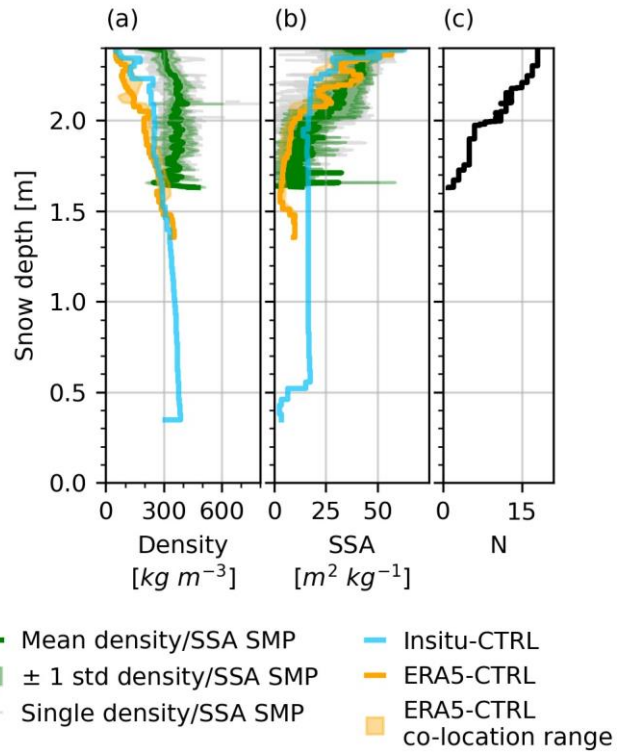

Figure 6.8: Simulated and measured snow density and specific surface area (SSA) on 23 March 2018. Measured density and SSA are derived after Calonne et al. (2020) from the SnowMicroPen (SMP). (a) displays snow density, (b) SSA and (c) the sampling frequency of SMP measurements. Snow depth baseline is the maximum snow depth during PAMARCMiP campaign of all measurements and simulations (2.4 m) as the SMP did not penetrate the entire snowpack (see also explanation in the Appendix). Single density/SSA SMP shows measured single SMP profiles. The meaning of the colours are expressed in the legend.

Vertical mean density in Insitu-CTRL was higher than in ERA5-CTRL on 23 March 2018 and 3 April 2018. In Insitu-CTRL (Figure 6.9a) thick snow layer of recent snowfall was visible at the top of the profile (1–0.85 of normalised snow depth). Also, density in ERA5-CTRL indicated some recent snowfall but less pronounced compared to Insitu-CTRL (Figure 6.9a, 1–0.9 of normalised snow depth).

6.3.3.3 Simulated SSA profiles

Overall, SSA measured by the SMP and simulated were in some agreement when the sample variability of the measurements is taken into account (the simulated SSA was within the range spanned by ±1 standard deviation of the sampling variability). SSA in ERA5-CTRL was much more variable in depth than Insitu-CTRL on 23 March 2018 (Figure 6.8b). SSA in ERA5-CTRL showed three peaks while SSA in Insitu-CTRL was more uniform in depth. SSA measured with the SMP showed a huge standard deviation, which led to some match with simulated SSA even if both simulated profiles differed by about 10 m^2 kg^{-1} on average.

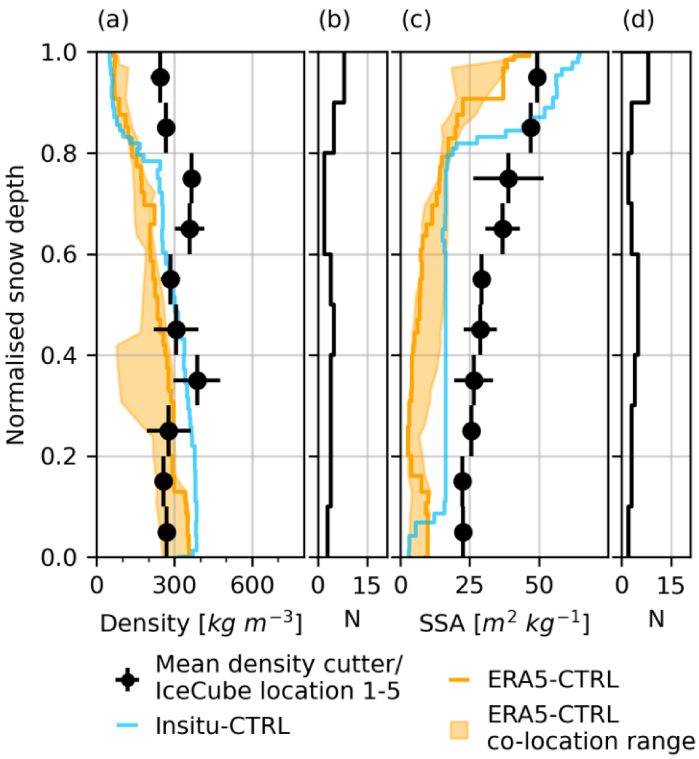

Figure 6.9: Simulated and measured snow density from density cutter and specific surface area (SSA) from IceCube on 3 April 2018. (a) snow density, (c) SSA and (b) and (d) the sampling frequency of density cutter measurements and IceCube measurements, respectively.

The vertical profiles of the SSA of both simulations were similar in form to the observations taken with the IceCube on 3 April 2018 (Figure 6.9c). All profiles showed a decrease in SSA from the surface towards the middle part of the snow profile continued by an almost constant course to greater depth.

However, amplitudes of the decrease and the absolute value of SSA differed considerably. ERA5-CTRL started at the surface with a realistic SSA of 47 m^2 kg^{-1} but decreased stronger than the measurements with depth. Therefore, ERA5-CTRL underestimated SSA over the entire snow profile and showed mostly values below Insitu-CTRL. It decreased from the top of the snowpack until 0.6 m, followed by a constant middle part with SSA lower than 10 m^2 kg^{-1}. SSA increased in the lower part of the profile until the ground, which contradicts the measurements. SSA in Insitu-CTRL showed an overestimation of surface SSA of about 15 m^2 kg^{-1} but it decreased stronger than measured before it became rather stable from 0.8 to 0.1 m while the measurement showed a slight decrease over the whole profile with higher SSA than Insitu-CTRL.

Overall, ERA5-CTRL and Insitu-CTRL could capture the gross profile of measured SSA. ERA5-CTRL started with more realistic surface SSA than Insitu-CTRL. However, both simulations failed to reproduce the details in the measured SSA profiles. Moreover, the SSA decreasing rates from top to bottom of the profiles were different for simulations and measurements.

6.4 Discussion

6.4.1 Comparison of atmospheric in situ measurements and reanalysis data at Villum Research Station

The advantages of ERA5 is its physical consistency, the completeness of the set of needed variables, and the completeness in time. These are features that are not guaranteed in case of in situ measurements. However, the reanalysis is only able to resolve processes, which are within the scales of the model resolution or even larger (Minola et al., 2020). Precipitation on a kilometre scale can already vary

significantly (Betts et al., 2019). Therefore, ERA5 cannot resolve local precipitation events as for instance visible in the atmospheric data during PAMARCMiP where ERA5 underestimates precipitation during the warm event in the second half of February 2018.

Atmospheric variables measured at VRS are point measurements representing local conditions. ERA5 on the other hand represents mean values in a grid cell. Due to the relatively coarse resolution of ERA5, the orographic relief is much smoother than in reality. This causes altitudinal differences and leads to different values e.g. in surface air pressure than observed. After correcting for this altitudinal differences ERA5 air pressure variations agree well with measurements, which is in line with the findings of Delhasse et al. (2020a).

We find a good correspondence between measured and ERA5 air temperatures, shortwave and longwave radiation with only minor differences in agreement with other studies (Betts et al., 2019; Wang et al., 2019; Delhasse et al., 2020a). Differences in observed and ERA5 surface air temperature can also result from the elevation difference between VRS and the ERA5 grid cell.

Differences in topography also affect wind speed and wind direction (Delhasse et al., 2020a). Higher obstacles to the southeast from VRS, not resolved by ERA5, are impacting wind direction and wind speed. In addition, the vertical interpolation from higher levels to the surface causes differences in wind speed and wind direction between the reanalysis and in situ measurements. This can be problematic in terms of snow modelling, as wind is an important variable to simulate snow density due to wind compaction, enhanced sublimation and wind redistribution at higher wind speeds.

In our study, generally ERA5 overestimates wind speed (mean over the whole study period) while Betts et al. (2019) found an underestimation for the Canadian Prairies. Delhasse et al. (2020a) identified an underestimation over stations located in the ablation area of the Greenland Ice Sheet but mostly overestimation for stations located in the accumulation area Delhasse et al. (2020b). However, we identify wind speed underestimation for higher wind speeds ($> \sim 6$ m s^{-1}) in agreement with Betts et al. (2019) and Delhasse et al. (2020a).

Our analyses of the wind direction show strong differences between reanalysis and in situ data, although without impact on our simulations because we do not prescribe an aspect ratio. However, the difference between measured and ERA5 wind direction might have to be taken into account for other studies. Especially when it comes e.g. to modelling of snow redistribution by snowdrift, wind direction plays an important role and has to be handled with care.

Furthermore, large measurement gaps in in situ precipitation are problematic. We underestimate the precipitation accumulated over time because we replaced these gaps by zero precipitation. Nonetheless, the in situ simulations clearly overestimate the snow depth, i.e. our simulations suggest that the in situ precipitation is not consistent to the measured snow depth. False precipitation measurements can be caused by snowdrift, which is falsely detected as local precipitation.

We consider the uncertainties caused by filling gaps of the remaining forcing variables with ERA5 as neglectable. ERA5 shortwave radiation agrees well with observations (19.0 % missing values) and Crocus shows a minor impact of differences in in situ and ERA5 shortwave radiation. The measurement gaps of the other variables are below 6.0 % and therefore considered as unproblematic. However, our sensitivity study shows that Crocus is strongly impacted by the deviations between in situ measurements and ERA5 in snowfall, specific humidity, air temperature and wind speed.

Because the snow season 2017/18 shows the most pronounced deviation of measured and simulated snow depth (larger for the in situ than for the reanalysis simulations), we had a closer look into this season. We compared the monthly cumulative in situ precipitation with the monthly cumulative precipitation of ERA5 and GPCP (Global Precipitation Climatology Project, Adler et al., 2016) (see Figure B.5 in the Appendix). During the first five months (September 2017 to January 2017), in situ precipitation is slightly lower than GPCP precipitation and ERA5 precipitation. This can be explained

by the setting of gaps in measured precipitation to zero that we performed. In February 2018 there is a high precipitation event during the exceptional warm event lasting over several days with daily precipitation of up to 240.7 mm. This event is not seen in ERA5 or GPCP. It is also not reflected in the measured snow depth, which only rises slightly during that time. However, as also wind speed was extreme and the precipitation instrument in general is known as reliable even in windy conditions (Nitu et al., 2018), we cannot exclude that this was a local precipitation event which was not captured by the reanalyses products and that additional snowfall was blown away. However, the high snowfall event in February 2018 leads to the sudden increase of snow depth in the simulations forced by in situ data not seen in the simulations forced by ERA5.

6.4.2 Snow simulations at Villum Research Station

6.4.2.1 Simulated snow depth

We can show that Crocus is in principle able to simulate reliably snow depth evolutions for an Arctic site when uncertainties of the atmospheric forcing are small. If the results can be transferred to other locations is, of course, questionable and will be part of future research. Other studies have come to the same conclusion but in contrast to our study most studies also adjusted the forcing data (Jacobi et al., 2010; Sauter and Obleitner, 2015; Barrere et al., 2017; Luijting et al., 2018), e.g. scale measured snowfall to the maximum measured snow water equivalent measurement. This does not allow for a proper analysis of the quality of the model.

We found that ERA5 considerably underestimates snow accumulation during the warm air intrusion in spring 2018 and for other major precipitation events, which accumulates as well to a strong underestimation of snow depth throughout the snow season in 2018. In our study, deviations in simulated and measured snow densities contributed to differences in snow depth between simulations and measurements. Also, Luijting et al. (2018) found accumulated over- and underestimations of snow depth of about 1 m over a snow season.

We found highest impacts on the in situ and ERA5 forced simulations with regard to the snow depths for snowfall rate, specific humidity and air temperature. Sauter and Obleitner (2015) showed that uncertainties in forcing can lead to more than 3 m deviation in snow depth after one year. This again highlights how problematic biases due to missing data, snowdrift and riming on instruments and measurement uncertainties in the measured data are.

Snow redistribution due to strong winds is not implemented in the model and could be another reason for deviations between observed and simulated snow depth (see also Luijting et al. (2018)). In the Arctic, snow redistribution is important. However, we investigated the correlation of wind speed above 6 m s^{-1} and snowfall for both forcing datasets and calculated a Pearson correlation of 0.46 and 0.51 for in situ and ERA5 data, respectively. From this we conclude that the impact of snowdrift at our location is probably not large and that therefore the timing of snow incorporated into the snowpack is not a decisive process for the snow density profile at VRS. Otherwise, we would have expected a higher correlation between high wind speeds and precipitation for in situ data (containing the effect of wind drift) than for the ERA5 data.

However, the impact on density and increased sublimation due to snowdrift is implemented into Crocus and leads to distinctively lower snow depths in our simulations. Nevertheless, the parameterisation of increased sublimation during snowdrift requires more attention, which is beyond the scope of this paper.

Crocus reproduces well the observed onset of snow accumulation in our study, while melting starts earlier than observed. Reasons for the discrepancies in the timing and development of thawing could be a higher simulated thermal conductivity of the basal snow layer and a lower simulated thermal conductivity of the near-surface layers.

Further, the measured snow depth is a point measurement. Already the measured snow depth in the detailed snow profiles close to the location of atmospheric measurements showed deviations due to spatial variability. Also other studies found differences of 0.45 m to more than 1 m in snow accumulation within a radius of a few kilometres (Domine et al., 2016a; Pedersen et al., 2016a). Reasons for this include snow redistribution by wind, microtopographic relief and vegetation (Liston and Sturm, 2002; Barrere et al., 2017).

6.4.2.2 Simulated snow density and SSA profiles

We find considerable differences between measured density profiles and both CTRL simulations while Essery et al. (2016) found a strong correlation between simulated and observed snow density profiles (r=0.74). We see a constant increase in density with depth. This is typical for Alpine snowpacks, where dense basal layers are common while density in Arctic snowpacks usually decreases with depths (Domine et al., 2019).

Our simulations overestimate density for upper snow layers and underestimate density for basal snow layers. This correspondents with results from other studies (Jacobi et al., 2010; Gascon et al., 2014; Barrere et al., 2017; Domine et al., 2019). Our results show clearly that an important process determining the snow stratigraphy in the Arctic is missing in Crocus. Barrere et al. (2017) and Jacobi et al. (2010) considered the main reason for the inverted density profiles in the lack of a parameterisation of upward water vapour transport due to strong temperature gradients occurring in the Arctic.

Moreover, the presumably too high precipitation in the in situ data, which was measured about one month before the measurements of the vertical snow profiles, is not visible in the snow depth measurements. In the in situ simulations, however, it leads to higher snow masses and consequently to increased compaction compared to the ERA5 density profile, which was forced by much lower precipitation.

In addition, the top low density in the in situ simulation (1.0 to 0.85 normalised snow depth in Figure 6.9a), results from an in situ precipitation event in late March. About a week earlier a precipitation event occurred in the ERA5 data and was therefore already subject to changes in density.

A realistic simulation of snow density is crucial since there are strong functional relationships within the model parameterisations but also in nature between individual variables. For example, snow density, SSA, thermal conductivity and temperature gradient are linked (Vionnet et al., 2012; Carmagnola et al., 2014; Domine et al., 2019). Thus, one incorrectly simulated variable affects the reliability of other physical snow variables (Domine et al., 2019). As density is a key variable, we anticipate that differences in simulated and measured densities can partly explain differences in simulated and measured SSA.

SSA is parameterised in Crocus as an inverse function of the optimal diameter (Carmagnola et al., 2014). Therefore, an inverted stratification of snow density leads to a lower SSA and thus to a lower albedo simulated with Crocus (Domine et al., 2019). In reality, differences in SSA of snow profiles can also result from variations in snow depth, density and temperature (Jacobi et al., 2010; Carmagnola et al., 2014). SSA further depends on wind speed and temperature gradient (Carmagnola et al., 2014; Domine et al., 2019).

In addition, flaws in the forcing data can lead to erroneous simulated densities and SSA as visible in deviations in ERA5-CTRL and Insitu-CTR in SSA (Figure 6.9). We find discrepancies between simulations of SSA and IceCube measurements, which is in agreement with Carmagnola et al. (2014). Strong temperature gradients in the Arctic's snow layer not captured by Crocus (Domine et al., 2019) could partly explains differences in our simulated and measured SSA profiles.

6.5 Conclusion

Working with snow in the Arctic is challenging due to limited availability of measured snow data. Detailed snow models can help to overcome this problem and can assist to interpret the measurements but require carefully prepared forcing data to ensure high quality of simulated snow data. Using the snow model Crocus, we can show that already relatively small deviations in solid precipitation, specific humidity and air temperature lead to considerable differences in simulated snow depth.

In situ atmospheric and snow measurements in the Arctic are rare, incomplete, and have to cope with difficult measurement conditions such as riming on the instruments and strong winds. However, models need complete time series to drive them. Here we present in situ atmospheric measurements for 2015 to 2018 and compare them with the modern atmospheric reanalysis ERA5 before driving the snow model Crocus with these datasets. We also analyse snow depth measurements (2014 – 2018) and detailed vertical density and SSA profiles of a campaign in spring 2018. These profiles show the typical stratification of Arctic snow and the influence of a recent warm air intrusion event with high wind speeds on the snow stratification.

Our study demonstrates that the reanalysis ERA5, except for precipitation, wind speed, and wind direction, agrees well with atmospheric measurements at VRS in northeast Greenland. ERA5 is also "physically consistent" because it is itself output of a numerical atmospheric model. This does not necessarily apply for the observations due to measurement errors and co-location errors. At least partly this explains higher agreement of simulated and measured snow depth under ERA5 forcing than under in situ forcing, a result we had not expected.

Due to the relatively coarse resolution of ERA5, topography is not resolved in detail. Presumably, for that reason, ERA5 cannot reproduce small-scale local precipitation events. Observed and reanalysis precipitation also do not match in time. Differences in topography influence wind direction and wind speed, thus ERA5 underestimates higher wind speeds in particular. Due to differences in elevation between the grid cell and the observation site, there are differences in air temperature and surface air pressure.

Overall, our study shows that ERA5 is capable to replace in situ measurements to force snow models where observations are limited, considering the highlighted systematic differences and limitations of in situ data and the reanalysis. We stress the importance of quality control of all in situ data in order to take advantages of observational data over reanalyses in modelling meaningful snow related quantities. Our study site is located in an area influenced by orography. We expect higher agreement of ERA5 and observations for flat areas as widely common in the Arctic such as over sea ice.

Concerning our research question, whether the snow model Crocus can reliably simulate snow depth evolution as well as snow density and SSA profiles, we cannot give a conclusive answer. Crocus can simulate the gross evolution of snow depth, but not of SSA and snow density of an Arctic snowpack sufficiently. Thereby the ERA5 simulations outperforms the in situ simulations.

Here, we present for the first time snow and atmospheric conditions for VRS and use ERA5 to force the snow model Crocus in the Arctic. Our study shows that Crocus has great potential for simulating snow conditions in the Arctic. The model can contribute to complement temporally and spatially limited observed snow depth measurements through representative simulations. Simulated and observed snow densities and SSA show deviations of which the user needs to be aware. Having that in mind, Crocus can give added value to the evolution and the range of the prevailing density and SSA.

7 Performance of high resolution versus medium resolution forcing for snow modelling

Investigating the performance of high resolution versus medium resolution reanalysis forcing for snow modelling in northeast Greenland

Abstract

The resolution of atmospheric medium resolution reanalyses is often too coarse to resolve small scale events and local topography. This affects atmospheric variables such as air temperature, air pressure and wind speed. Therefore, the following two hypotheses are investigated

(1) Using a high resolution reanalysis leads to more accurate representation of atmospheric conditions and thus to more realistic simulated snow properties.

(2) Accounting for enhanced sublimation during wind drift is important to capture snow depth evolution and depends strongly on a realistic wind speed distribution.

For this, I compared atmospheric variables from the high resolution reanalysis CARRA[3] with the medium resolution reanalysis ERA5[4] and put them into context with in-situ measurements from Villum Research Station in northeast Greenland. Further, I forced the snow model Crocus with both reanalyses and analysed simulated snow depth and vertical profiles of snow density and snow specific surface area (SSA). Finally, the effects of enhanced sublimation during wind drift and the simulated energy balance were investigated.

As a result, CARRA reliably resolves local topography. The correlation of daily mean wind speed with measurements is improved, but both reanalyses underestimate daily maximum wind speed, although the maximum wind speed of CARRA is higher than that of ERA5. Humidity shows large differences between the reanalyses and snowfall is poorly resolved in both, although the total amount of snowfall is almost consistent to the measurements.

For simulations of the snow depth evolution, I find varying performances among the years simulated. While ERA5 is superior in 2014/15, CARRA is superior in 2017/18. Vertical profiles of snow density and specific surface area are poorly resolved in both simulations based on measurements of five vertical snow profiles of one day.

The higher resolution of CARRA leads to some improvements, including a better representation of spatial and temporal variability including small scale events. However, reliable representation of snowfall remains a concern. Further, the snow depth decreases earlier in spring as measured independently of the used reanalyses probably due to model shortcomings. Possible reasons are the formulation of compaction and enhanced sublimation during wind drift.

In conclusion, CARRA resolves local events better as ERA5, but issues remain in the representation of maximum wind speed and snowfall. The performance of Crocus forced by the reanalyses varies from year to year. For simulations in the Arctic, the enhanced sublimation formulation included in the model

[3] CARRA: Copernicus Arctic Regional Reanalysis
[4] ERA5: ECMWF ReAnalysis-5th Generation (ERA5) atmospheric reanalyses data set

leads to considerable reduction in the bias of snow depth. Model parameterisations that could cause snow depth decrease to start too early should be further analysed in future studies.

7.1 Introduction

Since continuous time series are needed to drive a snow model, often reanalyses are used, providing all the basic atmospheric variables needed to force snow models, including data for remote areas such as the Arctic (e.g., Barrere et al. (2017), Domine et al. (2019)). Comparisons of extreme wind of different reanalyses and satellite data show that a horizontal resolution of at least 15 km is necessary to capture all extreme wind characteristics for the Euro-Atlantic sector of the Arctic. A horizontal resolution of 30 km is suitable to capture the distribution and magnitude of high wind speeds, but a resolution of 15 km is required to capture mesoscale wind systems, although still insufficient to resolve small-scale wind systems (Gutjahr and Heinemann, 2018). Due to smaller Rossby wave radii at more northerly latitudes, the higher north, the higher the resolution has to be to resolve the mesoscale wind system.

In general, reanalyses seem to miss important circulation mechanisms responsible for high wind speeds connected to errors in representing the atmospheric boundary layers (Kislov and Matveeva, 2016). Analyses of extreme wind speeds for the European Arctic show, that medium horizontal resolution reanalyses underestimate high surface wind speed frequency and intensity in comparison to observations (Kislov and Matveeva, 2016; Krampe et al., 2021).

Reanalyses also have systematic weaknesses in resolving regional topography due to too coarse resolution which smoothes the land surface. This results in systematic biases of surface air pressure and air temperature. Furthermore, precipitation pattern of reanalyses do not match with measurements (Essou et al., 2016; Chen et al., 2021; Krampe et al., 2021; Køltzow et al., 2022). When reanalyses are used to force snow models, these imperfections influence the simulation of important physical snow properties, e.g., snow depth, snow density and specific surface area (SSA).

Enhanced sublimation during strong wind events is considered an important process for snow evolution events (Essery et al., 1999; Liston and Sturm, 2004; Vionnet et al., 2014). Thus, it can be expected that higher resolution reanalyses, which better represent high wind speeds, are beneficial for the representation of enhanced sublimation during wind drift. In addition, sublimation depends on air temperature, humidity, surface roughness and the distance to open water among others (Essery et al., 1999; Liston and Sturm, 2004). Little is known about the amount of winter sublimation in the Arctic, as observations are sparse. In general, sublimation shows a high spatial and temporal variability.

Sublimation estimated by simulations range from rather low values of 12 % - 23 % of total precipitation, e.g. for the Greenland ice sheet, to 15 % - 50 % of the total snow cover, e.g. in the Canadian Arctic. However, in field surveys in Alaska, observations also found sublimation of 100 % (Essery et al., 1999; Liston and Sturm, 2004 and references therein). Already Essery et al. (1999) found that considering sublimation in Arctic snow simulations is important as otherwise simulated snow depth exceeds the measurements clearly.

To improve Crocus' performance in simulating snow depth, snow density and snow SSA at an Arctic site in northeast Greenland the following two hypotheses are tested

(1) The use of a high resolution reanalysis as atmospheric forcing leads to more accurate representation of atmospheric conditions than medium horizontal resolution reanalyses and thus to more realistic simulations of snow properties.

(2) Including enhanced sublimation during wind drift, which depends strongly on a realistic wind speed distribution, is important to capture snow depth evolution.

To examine the hypotheses, I employed data from the reanalyses ERA5 (European Centre for Medium-Range Weather Forecasts (ECMWF) ReAnalysis-5th Generation (ERA5) atmospheric reanalyses data set) and CARRA-West (Copernicus Arctic Regional Reanalysis; hereafter CARRA) as well as snow and atmospheric measurements at Villum Research Station (VRS) located in northeast Greenland.

7.2 Methods

7.2.1 Study Design

I investigated whether atmospheric high resolution reanalyses have a more realistic representation of especially wind speed and precipitation but also other atmospheric variables, where medium horizontal resolution reanalyses showed weaknesses in earlier studies (Kislov and Matveeva, 2016; Gutjahr and Heinemann, 2018; Krampe et al., 2021). For this, I compared the two reanalyses CARRA and ERA5 with ground based in-situ measurements exemplary at an Arctic site in northeast Greenland called Villum Research Station (VRS).

(1) Comparing an atmospheric high resolution reanalysis (CARRA) and a medium resolution reanalysis (ERA5) with in-situ measurements from an Arctic site.

Next, I used the snow model Crocus (Brun et al., 1992; Vionnet et al., 2012) to simulate snow properties at VRS driven by both reanalyses. Additionally, the impacts of the model's parameterisation for increased sublimation during snow drift are evaluated and differences between ERA5 and CARRA driven simulations with respect to the energy fluxes are analysed.

(2) Evaluating the snow depth, snow density and SSA as well as the effect of enhanced sublimation during wind drift and differences of the energy balance for ERA5 and CARRA driven simulations.

7.2.2 Comparing atmospheric high and medium resolution reanalyses with in-situ measurements

The atmospheric reanalysis CARRA has a resolution of 2.5 km and is available for Greenland, Iceland and East-Canada every 3 h (Copernicus Climate Change Service, 2020), while ERA5 is a global atmospheric reanalysis with a resolution of 31 km x 5 km at northern Greenland and is available hourly (Hersbach et al., 2020). For comparison with in-situ measurements, I used near surface air temperature, air pressure, wind speed, humidity and snowfall measurements from VRS (81°34' N, 16°38' W, 37 m above sea level) in northeast Greenland (for more information about the set up of the weather station and the measured data see Krampe et al. (2021)). I used the grid point 81.5° N 16.75° W, 185 m above sea level for ERA5 and 81.56° N 16.71° W, 40 m above sea level for CARRA. For atmospheric analyses, I used the time from 27 November 2015 to 8 August 2018, for which measurements exists. For comparison between reanalyses and in-situ data I calculated mean bias (reanalysis – in-situ measurements), root-mean-square deviation (RMSD) and performed linear regressions.

7.2.3 Snow model Crocus driven by CARRA and ERA5

I used the detailed multilayer SURFEX/ISBA-Crocus snow model Version 8.1 (Brun et al., 1992; Vionnet et al., 2012), which is described in detail in Chapter 5. In the default version Crocus takes empirically surface snow compaction and fragmentation due to blowing snow into account when a threshold commonly set to 6 m s^{-1} is exceeded (Vionnet et al., 2013). In addition, enhanced sublimation (i.e. snow mass loss) due to blowing snow is taken into account. The total sublimation of blowing snow Q_{Sub} [kg m^{-2} s^{-1}] is calculated as (Gordon et al., 2006; Brun et al., 2013)

$$Q_{Sub} = A \left(\frac{T_0}{T_a}\right)^{\gamma} U_t \, \rho_a \, q_{si} \, (1 - Rh_i) \left(\frac{U}{U_t}\right)^{Es} \text{ for } U > U_t \quad (7.1)$$

with T_a being the air temperature [K] and U the wind speed [m s^{-1}]. U_t is a threshold wind speed for snow transport. q_{si} is the saturation specific humidity with respect to ice at temperature T_a [kg kg^{-1}] and Rh_i relative humidity with respect to ice. A, γ and E_S are dimensionless constants set to 0.0018, 4 and 3.6, respectively, T_0 the triple point temperature 273.15 K, and ρ_a the air density [kg m^{-3}].

I used ERA5 data to force Crocus after applying a spin-up phase from 2010 to 2019 to account for model adjustments mainly needed to adjust the soil temperature. The here analysed simulation is created by a second pass of the forcing period with the initial state taking from 2019 of the spin-up simulation. Detailed information about the preparation of the ERA5 forcing file and the model setup are described in Krampe et al. (2021) and Chapter 6. I followed the same procedure for creating the CARRA simulations.

Offsets, for instance in snow depths and snow density over a season, can accumulate, resulting in large offsets between measurements and simulations. Thus, I calculated snow depth differences accumulated over one month for 1 September 2014 to 31 August 2018 to evaluate the effect of using a higher resolution reanalysis on the simulation on snow depth. In addition, I compared simulated and measured density and SSA profiles on 3 April 2018 measured with a density cutter (60x30x56 mm^3) and an IceCube (see Chapter 4 for further details), respectively during the **P**olar **A**irborne **M**easurements and **A**rctic **R**egional **C**limate **M**odel **S**imulation **P**roject (PAMARCMiP). For more details on the snow measurements taken and snow and atmospheric conditions see Krampe et al. (2021) and Chapter 6.

For analyses, I used the following simulations

(a) ERA5-CTRL: Simulations driven by ERA5 using the same setup as described in Krampe et al. (2021)
(b) CARRA-CTRL: Simulations driven by CARRA using the same setup as ERA5-CTRL
(c) ERA5-noENSUBL: as (a) but without enhanced sublimation during wind drift
(d) CARRA-noENSUBL: as (b) but without enhanced sublimation during wind drift

7.3 Results

7.3.1 Comparing atmospheric high and medium resolution reanalyses with in-situ measurements for 26 November 2015 to 8 August 2018

Air temperature

Overall, ERA5 and CARRA surface air temperatures agreed well with measurements (Figure 7.1). Over the entire study period, ERA5 underestimated air temperature by -0.95°C due to a cold bias in summer while CARRA overestimated air temperature by +1.39°C due to a warm bias in winter. However, note that for ERA5 orography a too high terrain altitude at the study location was used (ERA5: 185 m above sea level, actual terrain altitude: 37 m above sea level), while CARRA's surface altitude (40 m) was in agreement with the actual terrain measurements

Air pressure

As visible in Figure 7.1 (and in Figure C.1 in the Appendix) ERA5 showed a systematic underestimation of air pressure (Bias: -19 hPa) due to the altitude mismatch of 148 m. The bias in surface air pressure was lower in May to October than in the other months. CARRA agreed well with measured surface air pressure (Bias: 0 hPa) as CARRA's surface altitude was in agreement with the actual terrain altitude (altitude mismatch: 3 m). The months June to September showed a slight overestimation.

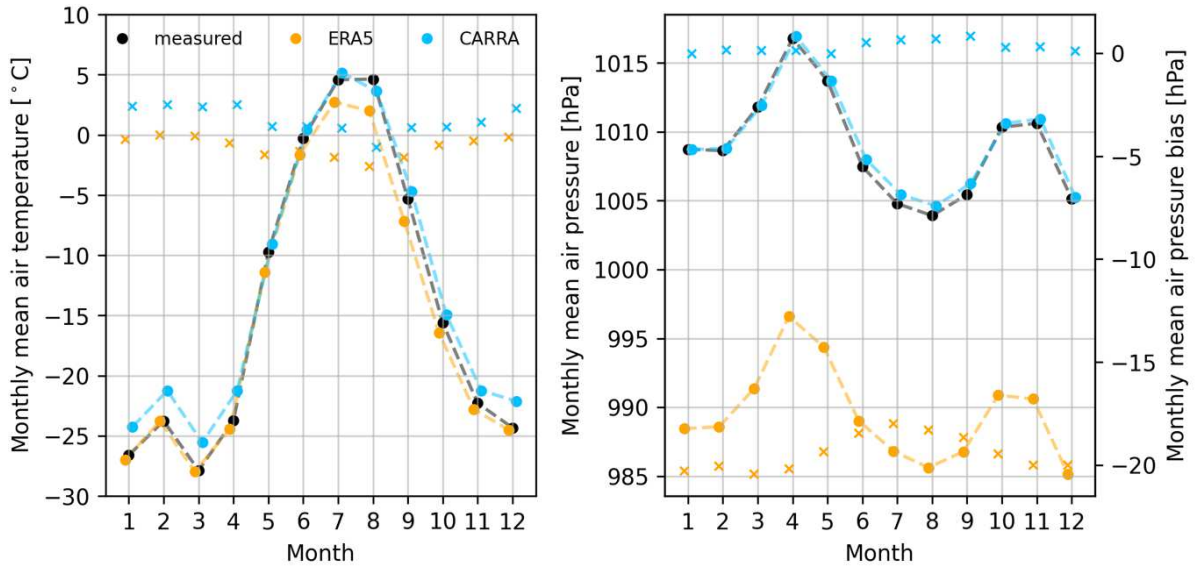

Figure 7.1: Monthly comparison of CARRA and ERA5 with in-situ measurements of left: air temperature and right: air pressure, whereby crosses represents air temperature and pressure biases (reanalysis - in-situ measurement).

Wind speed

Figure 7.2 shows the daily mean wind speed and the daily maximal wind speed for every month gathered over all years for ERA5, CARRA and measured wind speed. For October to April ERA5 slightly underestimated measured mean daily wind speed (Bias: 0.35 m s^{-1} to 0.85 m s^{-1}) while it overestimated wind speed for June to September (Bias: -0.12 m s^{-1} to -0.69 m s^{-1}). The bias over the entire study period showed a slight overestimation of daily mean wind speed of 0.2 m s^{-1} (RMSD: 1.4 m s^{-1}, r: 0.74).

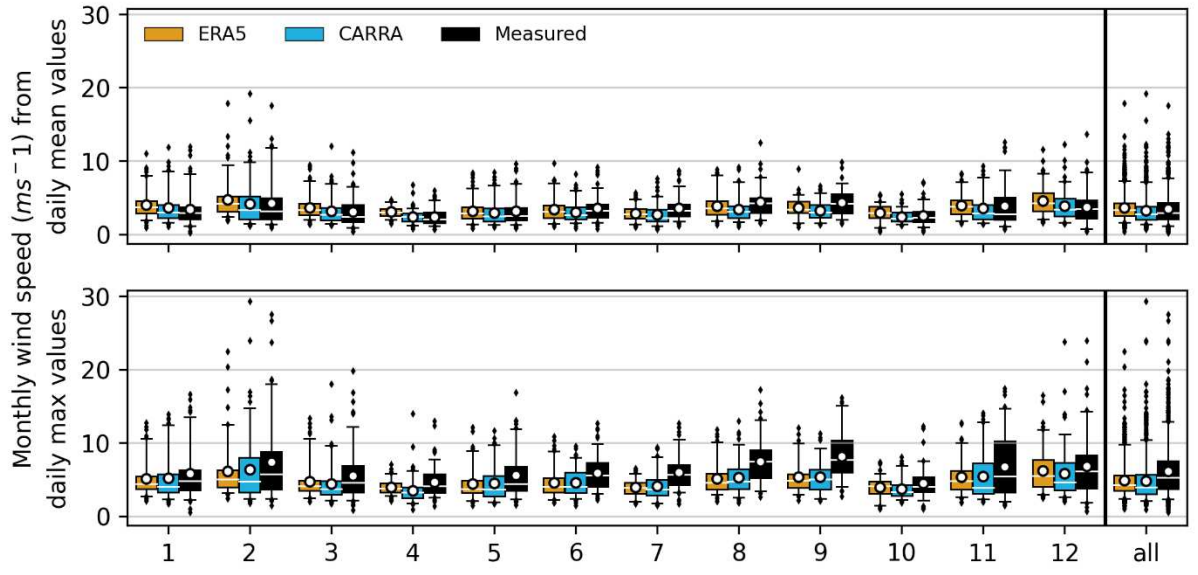

Figure 7.2: Boxplot of monthly wind speed (January to December) calculated from daily mean values over approximately three years from CARRA, ERA5 and measurements. Top: daily mean, Bottom: daily maximum. White dots: mean, white horizontal lines: median, black horizontal lines: 25 % and 75 % percentiles, respectively. The whiskers are the proportion of the interquartile range (5 – 95 %). More extreme points are marked as outliers.

CARRA underestimated daily mean wind speed from November to January and in March/April (Bias: 0.01 m s^{-1} to 0.22 m s^{-1}), while it overestimated wind speed in January and from May to October

(Bias: -0.09 m s^{-1} to -1.04 m s^{-1}). Thereby, the bias over the entire study period showed a slight underestimation of daily mean wind speed of -0.3 m s^{-1} (RMSD: 1.2 m s^{-1}, r: 0.80). Thus, CARRA showed a higher correlation with in-situ daily mean wind speed than ERA5.

In general, daily wind speed was highest in February for all three datasets and overall higher in winter (November to March) than in summer (April to June). However, daily measured mean wind speed was below 5 m s^{-1} in every months (see Figure C.2 in the Appendix).

While both reanalyses represented well daily mean wind speed, maximum wind speed was clearly underestimated in both reanalyses and in all seasons. While in-situ measurements had a mean maximum daily wind speed of 6.1 m s^{-1}, the values for ERA5 and CARRA were clearly lower (4.9 m s^{-1} and 4.8 m s^{-1}, respectively). Maximum daily wind speeds were highest for CARRA (29.3 m s^{-1}), while ERA5 and in-situ measurements showed highest values of 22.5 m s^{-1} and 27.5 m s^{-1}, respectively. Correlations between in-situ measurements and CARRA daily maximum wind speeds are slightly higher (r: 0.84) than for ERA5 (r: 0.80) (see Figure C.3 in the Appendix).

Humidity

The atmospheric datasets showed huge differences in terms of humidity. Figure 7.3 shows the time series for the entire study period for relative humidity for all three datasets. ERA5 showed a distinct seasonal cycle, which is almost not visible in the CARRA data. In-situ measurements showed only a weak seasonal cycle.

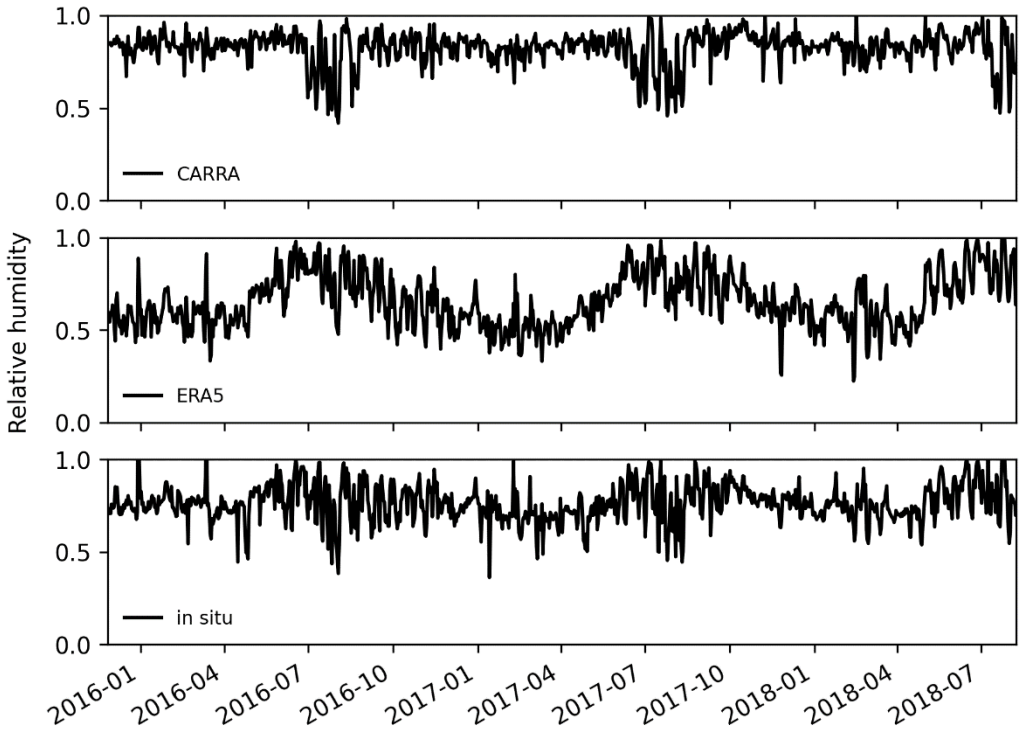

Figure 7.3: Time series of relative humidity. Top: CARRA, middle: ERA5, bottom: in-situ measurements.

Specific humidity (Figure 7.4) is low from November to April due to cold temperatures and increases towards the summer months with increasing temperatures. Accordingly, specific humidity is maximal in July for all three datasets and variations were higher during the warmer months (May to September) than during the colder months (October to April).

CARRA overestimated specific humidity from January to May and again from September to December. In contrast, ERA5 underestimated specific humidity in all months, but especially from May to September. The long-term mean bias based on daily mean data of CARRA is 0.10 g kg^{-1} with respect to the in-situ data (RMSD: 0.26 g kg^{-1}) and of ERA5 -0.18 g kg^{-1}.(RMSD: 0.28 g kg^{-1}).

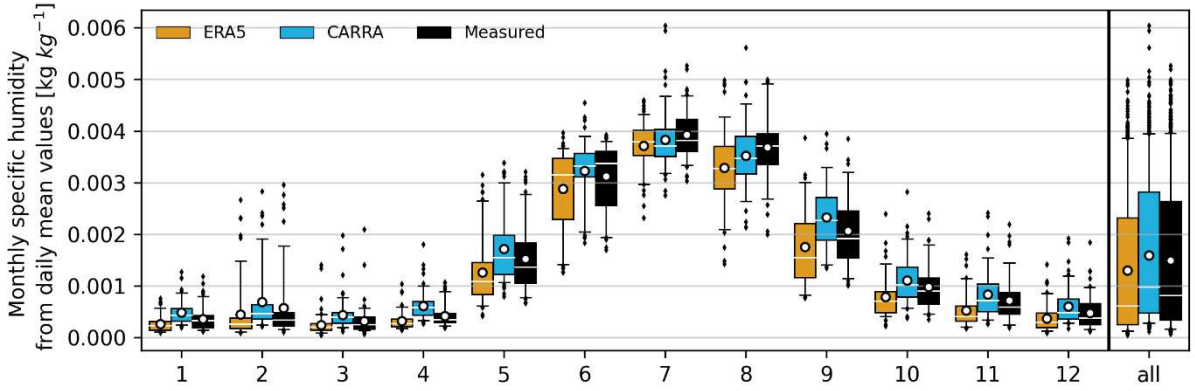

Figure 7.4: Monthly specific humidity (January to December) averaged from daily mean values over approximately three years from CARRA, ERA5 and measurements. White dot: mean, white line: median, black horizontal lines: 25 % and 75 % percentiles, respectively. The whiskers are the proportion of the interquartile range (5 – 95 %). More extreme points are marked as outliers.

Snowfall

Daily mean monthly snowfall biases were small for ERA5 and for CARRA. However, as visible in Figure 7.5, median values as well as quartiles and minimum and maximum values deviated clearly from measured snowfall for both reanalyses. ERA5 and CARRA both underestimated snowfall in spring but overestimated snowfall in autumn. Thereby, during spring the monthly snowfall bias was highest for both reanalyses, while it was smallest in summer (June/August) as snowfall was low in general during summer. The high bias in February with a mean outside the quantiles is caused by a considerable heavy precipitation event in February 2018, which resulted in 571.0 mm w.e. snowfall in this month (see Chapter 6).

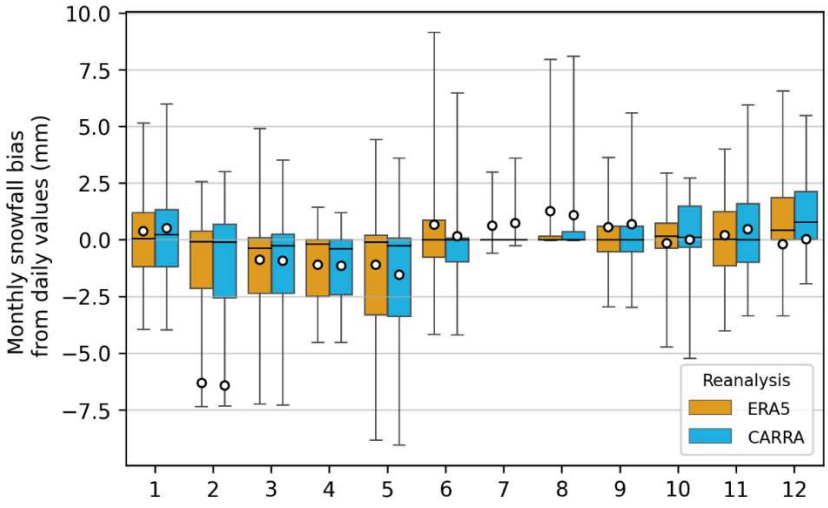

Figure 7.5: Boxplots of monthly snowfall bias (January to December) averaged over approximately three years from CARRA and ERA5 compared to measured snowfall (snowfall threshold: +1°C). White dot: mean, black line, black horizontal lines: 25 % and 75 % percentiles, respectively. The whiskers show the maximum and the minimum of the data.

Mean biases, RMSD and correlation between ERA5 and CARRA showed a high agreement between both reanalyses for daily cumulative snowfall (Bias: -0.0 mm w.e., RMSD: 1.3 mm w.e., r: 0.96). Compared to in-situ measurements both reanalyses performed poorly with similar high mean biases and RMSD and low correlations of 0.13 (ERA5) and 0.06 (CARRA) (Figure C.1).

7.3.2 Model simulations

7.3.2.1 Simulations ERA5 versus CARRA

It is evident that both reanalyses underestimated, overestimated or overlooked certain events responsible for changes in measured snow depth, e.g. compaction, melting, and snowfall events. There were several minor events that were not captured by ERA5-CTRL or CARRA-CTRL (Figure 7.6). I took a closer look at some characteristic events to see if simulations forced with the reanalyses were able to reproduce these events.

1. There was a large offset in snow depth between measurements and simulated snow depth in January 2015 for both reanalyses. Several events in autumn 2014 led to this deviation. During the first event, both reanalyses reproduced the increase in snow depth but slightly overestimated it. While in the measurements snow depth decreased afterwards to the same snow depth as before the event, this was not the case in the simulations. Both reanalyses reproduced the timing and extent of the next event well. Furthermore, both reanalyses satisfactorily simulated the increase in snow depth during the third event in autumn and reproduced a decrease afterwards. However, CARRA-CTRL simulation clearly underestimated the decrease. The decrease during the first event seems to be caused by melting (decrease in snow water equivalent (SWE)), while the decrease during the other two event was mainly caused by compaction in the model (no decrease in SWE). The increase of the fourth event was well captured by CARRA-CTRL but the timing was earlier than in the measurements. The timing of ERA5-CTRL was good but the increase in snow depth was underestimated.

2. There was a snow depth peak in September 2016 in the measurements before the actual snow accumulation season began. ERA5-CTRL was not able to simulate this peak. In the simulation with CARRA-CTRL, the peak was simulated but overestimated. The subsequent melt rate was of about the same amount as in the measurements but due to the overestimation of the peak, snow depth did not melt completely, leading to an overestimation of the subsequent snow depth evolution of CARRA-CTRL. I excluded this event from CARRA-CTRL by setting the snow depth back to zero after this event. However, differences remained. The offset in snow depth thus seems to be related to model parameterisations.

Events like the ones described above led to an accumulation of deviations between simulated and measured snow depth over time.

While snow depth simulations forced with ERA5-CTRL were closer to the measurements in the snow season 2014/15 in autumn, CARRA-CTRL forced snow depth simulations clearly outperformed ERA5-CTRL in the snow season 2017/18. In the snow season 2017/18 ERA5-CTRL's simulated snow depth reached only 1.06 m maximum snow depth in contrast to CARRA-CTRL, which reached about 1.38 m maximum snow depth. In the snow season 2014/15, simulated snow depth was similar for both reanalyses until autumn and again from June onwards. In between, most of the time the simulations overestimated measured snow depth (CARRA-CTRL stronger than ERA5-CTRL) before it came to an underestimation of simulated snow depth in spring (ERA5-CTRL stronger than CARRA-CTRL).

In the snow season 2017/18, ERA5-CTRL and CARRA-CTRL snow depth were close to each other in early autumn (and close to the measurements) but started to deviate in late autumn. While ERA5-CTRL underestimated measured snow depth (which stayed for the rest of the year), CARRA-CTRL was in good agreement with the measurements until the onset of continuous snow depth decrease in the simulations, which happened in the simulations already in late April about a month too early compared with the measurements.

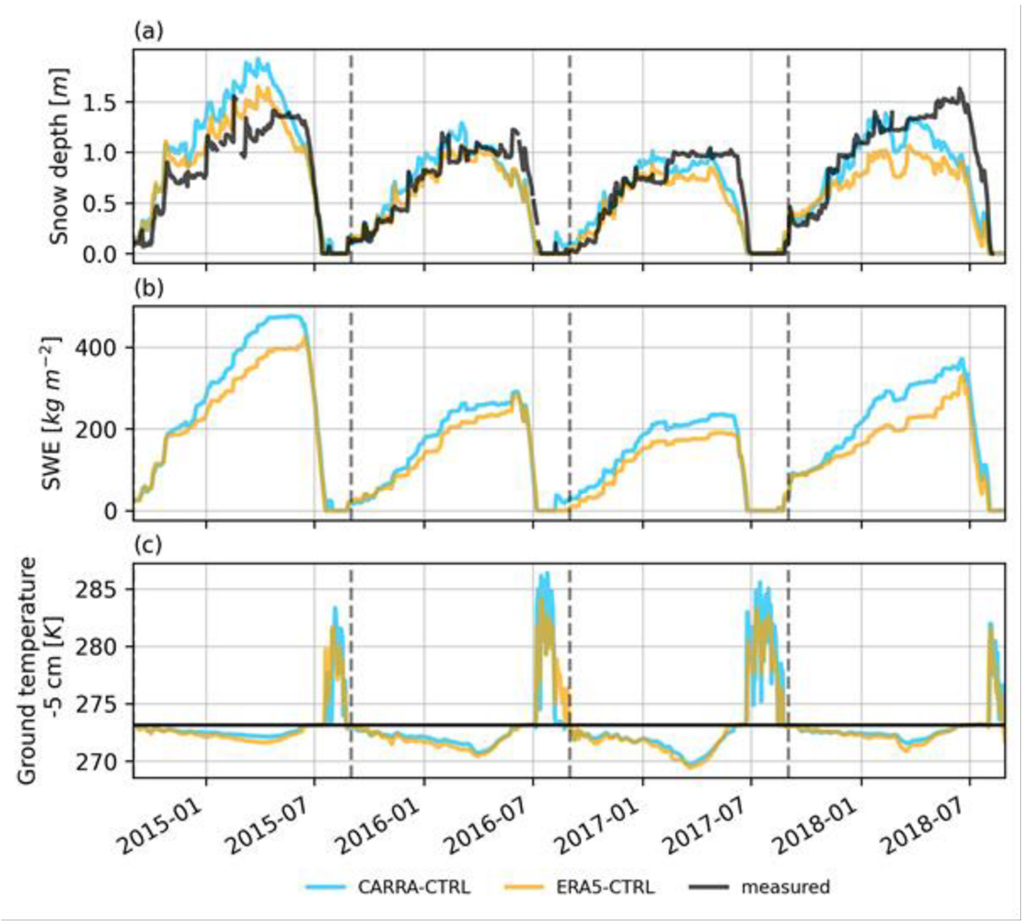

Figure 7.6: Time series for (a) snow depth (b) snow water equivalent (SWE) and (c) ground temperature at -5 cm from 1 September 2014 to 30 August 2018. (a) simulated with ERA5 forcing, CARRA forcing and measured (b) and (c) simulated with ERA5 forcing and CARRA forcing. Vertical dashed lines denote 1 September of each simulation year.

Simulations forced with both reanalyses overestimated snow depth in the first two months of snow accumulation (September, October). When comparing monthly snow depth anomalies (Figure 7.7) it is obvious that snow depth simulations forced with ERA5-CTRL tended to underestimate measured snow depth while CARRA-CTRL tended to overestimate measured snow depth from November to April. In May and June, both reanalyses strongly underestimated measured snow depth. The too early start of snow depth decrease in spring and thus underestimation of snow depth was evident in all years and for both reanalyses (Figure 7.7). As shown in Figure 7.7 deviations were caused in May and June. In general, the higher spatial resolution of CARRA-CTRL was reflected in greater interannual variability of snow depth than in ERA5-CTRL.

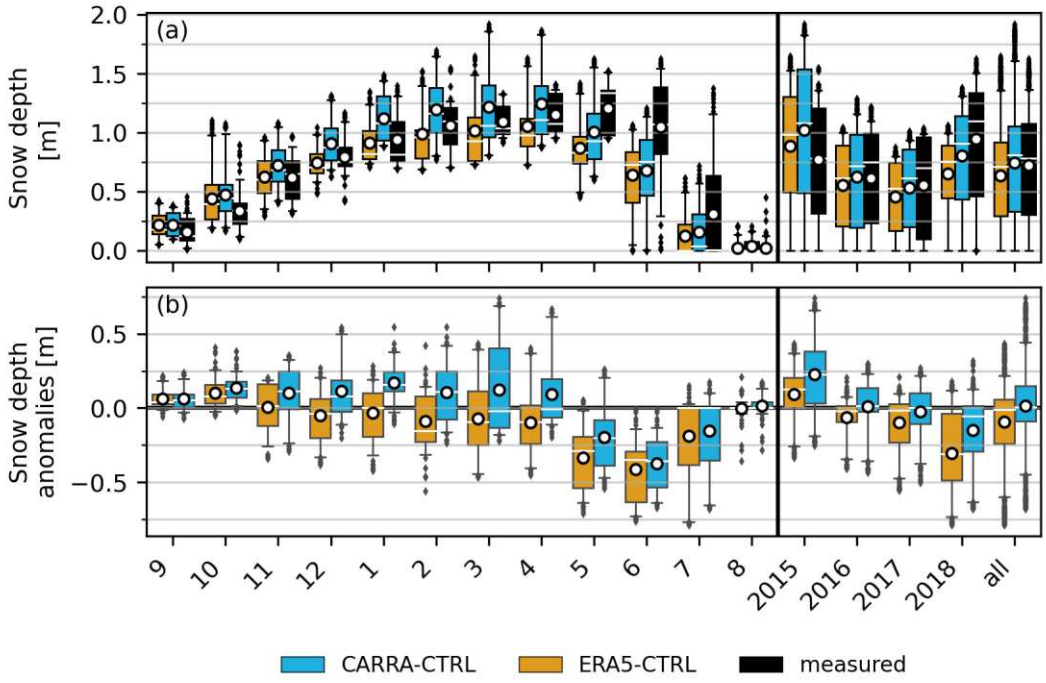

Figure 7.7: Boxplots of simulated snow depth with CARRA and ERA5 forcing and measured (a) long-term mean snow depth distribution calculated from daily mean data per month (left) and per year and for all simulated years (right) (b) as (a) but for the anomalies (simulation – measurements). White dot: mean, white line: median, black horizontal lines: 25 % and 75 % percentiles, respectively. The whiskers are the proportion of the interquartile range (5 – 95 %). More extreme points are marked as outliers.

The warmer air temperatures of CARRA-CTRL led to slightly higher ground temperature than ERA5 CTRL especially during summer (Figure 7.6 (c)). As soon as the snow depth began to decrease in spring, the insulation between the atmosphere and the ground decreased. Since SWE did not also decrease at the beginning, the snow depth decreased at the beginning mainly due to compaction. Denser snow has a higher thermal conductivity than snow with lower density. Therefore, the rising air temperatures from April onwards also led to an increase in ground temperatures. Ground temperature became positive when there was no more snow on the ground.

As visible in Figure 7.6, peaks in the snow depth time series during the time of snow accumulation were not present in the SWE time series. In conclusion, most simulated snow depth decreases until the melt onset in spring were caused by compaction rather than melting in the simulations. This indicates that the formulation of compaction in the model is not sufficient for the Arctic. Further, the shape of the SWE time series corresponds well to the shape of the snow depth measurements, also during the melting phase. This indicates, that the snow mass is simulated correctly and the mismatch in snow depth before the melt onset is rather related to issues in the formulation of snow compaction than in too early melting. Since I do not have any SWE measurements, I cannot compare this behaviour with measurements and thus cannot analyse this issue further.

Measurements from different snow profiles allowing for a comparison of snow properties with the simulations over the entire vertical snow profile exist only on 3 April 2018. The vertical snow density profile simulated with ERA5-CTRL and CARRA-CTRL showed almost no difference (Figure 7.8 (a)). Both simulated vertical density profiles underestimated snow density in the upper snow layers, agreed well with observations in the middle snow layers and overestimated density in the lower snow layers. As there are no significant difference between snow density simulated by ERA5-CTRL and CARRA-CTRL, I refer to Krampe et al. (2021) for more detailed analyses of measured and simulated ERA5-CTRL snow density.

Simulations of the vertical SSA profile on 3 April 2018 forced with ERA5-CTRL and CARRA-CTRL shows some differences (Figure 7.8 (b)). ERA5-CTRL SSA started with realistic surface SSA values of about 48 $m^2\ kg^{-1}$ while CARRA-CTRL overestimated surface SSA (~56 $m^2\ kg^{-1}$). Simulated and measured SSA decreases with depth. From 1.0 to 0.8 normalised snow depth, both reanalyses decreased stronger than measurements leading to an underestimation of SSA over the entire profile for both simulations. CARRA-CTRL decreased more than ERA5-CTRL leading to an agreement of both simulated SSA from 0.85 to 0.65 normalised snow depth. From here, ERA5-CTRL is smaller than CARRA-CTRL SSA causing CARRA-CTRL SSA to be slightly closer to the measurements than ERA5-CTRL until 0.15 normalised snow depth, where ERA5-CTRL SSA increases again while measurements and CARRA-CTRL simulation did not change. Here, the shape of the profile of CARRA-CTRL agreed better with measurements – it shows the reduction for greater depth while ERA5-CTRL shows an increase – although ERA5-CTRL is in that depth closer to the measurements.

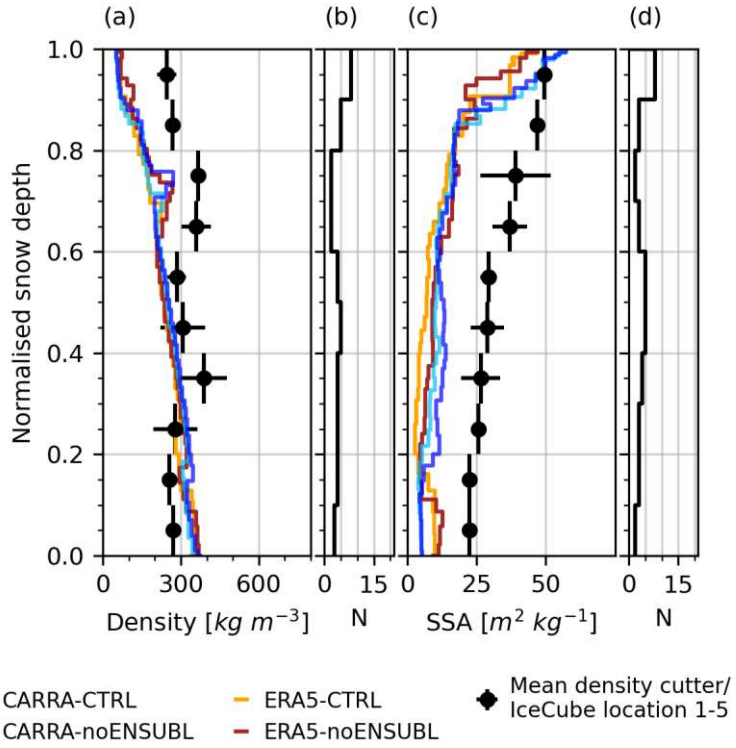

Figure 7.8: (a) Snow density and (c) snow specific surface area (SSA) on 3 April 2018 simulated with ERA5 forcing and CARRA forcing (both simulations with and without enhanced sublimation during wind drift) and measured. (b) and (d) show the sample frequency of density cutter and IceCube measurements, respectively.

7.3.2.2 Effects of enhanced sublimation during snow drift events

As sublimation is important in the Arctic, I used the implemented parameterisation for enhanced snow sublimation during wind drift in the CTRL-simulations with Crocus. Additionally, I ran simulations without enhanced sublimation during wind drift to analyse the impact of enhanced sublimation.

Figure 7.9 shows that without enhanced sublimation during snow drift snow depth and SWE was higher than in the CTRL-simulations in all years. Thereby, snow depth and SWE for the ERA5-noENSUBL were higher than for CARRA-noENSUBL. In the snow season 2017/18 both noENSUBL-simulations did not melt completely at the end of the snow season in contrast to both CTRL-simulations.

The differences in SWE between CARRA-noENSUBL and CARRA-CTRL and between ERA5-noENSUBL and ERA5-CTRL were about the same in the individual years. However, the impact when forced by ERA5 was much larger (about 70 kg m^{-2} in SWE) when compared to the impact when forced by CARRA (about 45 kg m^{-2}). This can be attributed to the lower humidity of ERA5 leading to greater enhanced sublimation during high wind speeds compared to the CARRA-simulations.

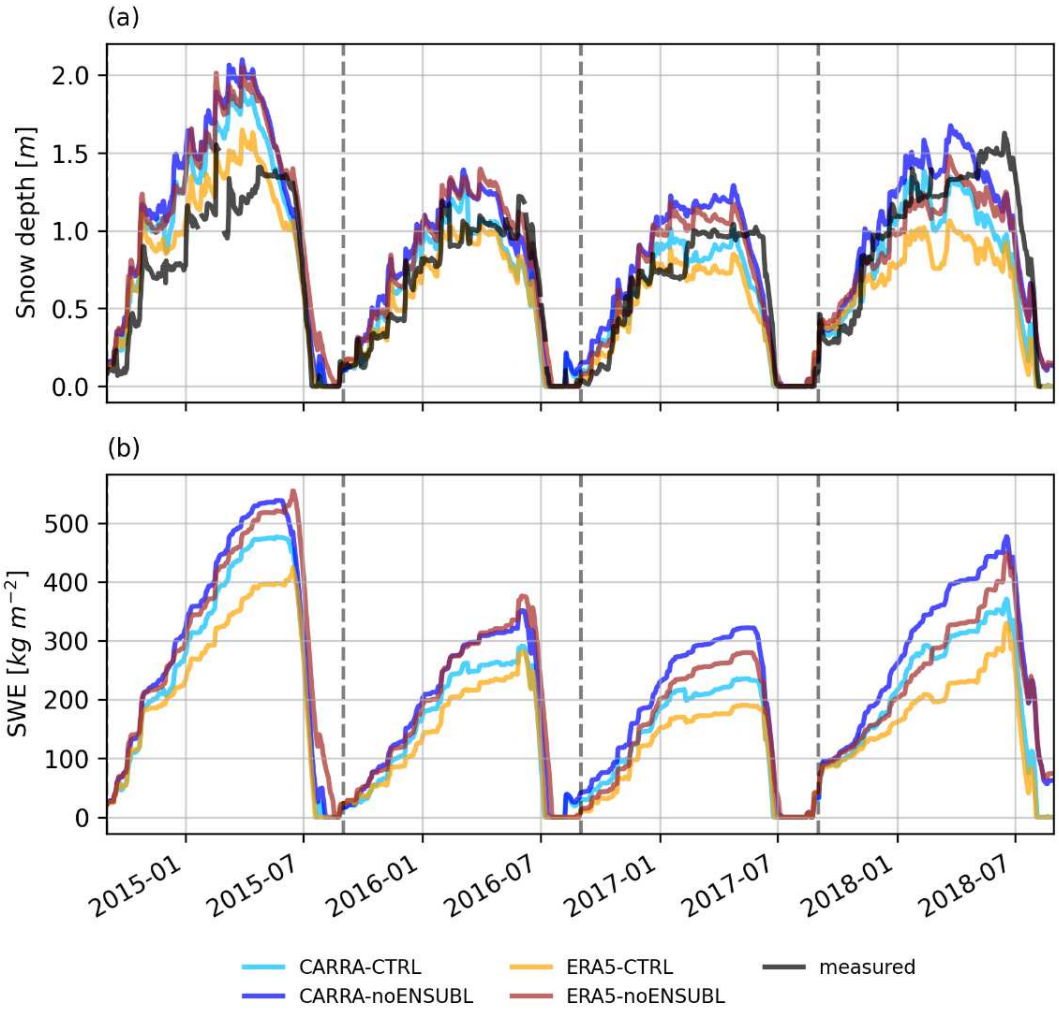

Figure 7.9: Time series of (a) snow depth, (b) snow water equivalent (SWE) and (c) ground temperature 5 cm into the soil from 1 September 2014 to 30 August 2018. Simulations with and without enhanced sublimation during wind drift forced by CARRA and ERA5 are shown as well. In the case of snow depth also measurements are shown. Vertical dashed lines denote 1 September of each simulation year.

In general, the noENSUBL-simulations had a higher agreement with the measurements during the time of continuous snow depth decrease in spring. This was also the case in 2017/18, when snow depth of ERA5-noENSUBL and CARRA-CTRL where similar before the continuous snow depth decrease in spring.

I used the RMSD and the coefficient of determination (R^2) as metrics to evaluate the performance of the simulations with respect to snow depth. R^2 determines the proportion of variation in the dependent variable (here: simulations) that is predicted from the independent variable(s) (here: measurement). A value of one means perfect fit and a value of, e.g., 0.7, means that a simulation can describe 70 % of the variance of the measurements (Steel and Torrie, 1960; Glantz and Slinker, 1990; Draper, Norman R. and Smith, Harry, 1998).

In the light of these two metrics, the CTRL-simulations performed better than the noENSUBL-simulations, whereby CARRA-CTRL simulations had the best agreement with measured snow depth (Table 7.1). However, R^2 was high for all simulations (ERA5-CTRL: 0.69, CARRA-CTRL: 0.71, ERA5-noENSUBL: 0.69, CARRA-noENSUBL: 0.61). The same was true for the RMSD, which was lowest for CARRA-CTRL (0.25 m) and highest for CARRA-noENSUBL (0.29 m). However, values were close for all simulations and varied strongly from year to year.

As I showed in Chapter 7.3.2.1 the model has weaknesses in simulating the correct timing of the start of the snow depth decrease in spring, leading to deviations of simulated and measured snow depth in the melting season. In addition, already in Figure 7.9 it is apparent that the performance of the different model simulations for individual years differ. Thus, I also calculated R^2 and RMSD from September to April for the individual years leaving out the melting season. The time series examined are shown in Figure C.4 to Figure C.7 in the Appendix, respectively. Again, the CTRL-simulations were superior over the noENSUBL-simulations, whereby the differences were more pronounced than when considering the entire study period. Only in 2017/18 ERA5-noENSUBL had a higher agreement with measurements than ERA5-CTRL in terms of R^2 (0.90 vs. 0.50) and a lower RMSD as ERA5-CTRL (0.13 m to 0.28 m).

For September 2014 to April 2015 the performance for ERA5-CTRL (R^2: 0.69, 0.22 m) was clearly better than for the other simulations having negative R^2 and RMSD about twice as high. For September 2015 to April 2016 the CTRL-simulations (R^2: ERA5-CTRL: 0.96, CARRA-CTRL: 0.85) agreed considerably better than the noENSUBL-simulations (R^2: ERA5-noENSUBL: 0.59, CARRA-noENSUBL: 0.54). For this period, especially the performance of ERA5-CTRL had a high agreement with the measurements, which was also reflected in a considerable low RMSD of 0.07 m.

For September 2016 to April 2017 both CTRL-simulations had a high agreement with measured snow depth, whereby CARRA-CTRL had a higher agreement (R^2: ERA5-CTRL: 0.82, CARRA-CTRL: 0.84). The performance of CARRA-noENSUBL was poor (R^2: 0.40). For September 2017 to April 2018 CARRA-CTRL had the best performance with a high R^2 of 0.92 and a low RMSD of 0.11 m. ERA5-CTRL clearly had weaknesses (R^2: 0.50) while the performance of ERA5-noENSUBL had a R^2 of 0.90.

Table 7.1: Coefficient of determination (R^2) and root mean square difference (RMSD) calculated for the snow depth simulations compared to the snow depth measurements.

	Coefficient of determination (R^2)				
	Sep 2014 – Aug 2018	**Sep 2014 – April 2015**	**Sep 2015 – April 2016**	**Sep 2016 – April 2017**	**Sep 2017 – April 2018**
ERA5-CTRL	0.69	0.69	0.96	0.82	0.50
ERA5-noENSUBL	0.69	-0.42	0.59	0.69	0.89
CARRA-CTRL	0.71	-0.03	0.85	0.84	0.92
CARRA-noENSUBL	0.61	-0.85	0.54	0.40	0.77
	RMSD [m]				
ERA5-CTRL	0.26	0.22	0.07	0.14	0.28
ERA5-noENSUBL	0.26	0.47	0.22	0.18	0.13
CARRA-CTRL	0.25	0.40	0.13	0.13	0.11
CARRA-noENSUBL	0.29	0.54	0.23	0.25	0.19

Simulated vertical density profiles forced with ERA5-noENSUBL and CARRA-noENSUBL only showed small differences to snow density simulated with the CTRL-simulations on 3 April 2018 (Figure 7.8). The simulated vertical SSA profile of ERA5-noENSUBL showed a continuous decrease of SSA from the surface to about 0.8 normalised snow depth while ERA5-CTRL showed a rapid decrease. Below 0.8 normalised snow depth, ERA5-noENSUBL SSA is mostly higher than for ERA5-CTRL. SSA from CARRA-CTRL and CARRA-noENSUBL are rather similar until 0.55 normalised snow depth. Below that depth, SSA from CARRA-noENSUBL is slightly higher than for CARRA-CTRL until about 0.2 normalised snow depth, when SSA from both simulations is similar again. The difference between noENSUBL-SSA and CTRL-SSA caused a slightly higher agreement with measured SSA in the middle snow layers. The underestimation in the upper snow layers was higher in the ERA5-noENSUBL simulation.

7.3.2.3 Simulated energy balances

Figure 7.10 shows the monthly mean energy fluxes for ERA5-CTRL and CARRA-CTRL. Shortwave radiation was only present when the sun is over the horizon (March to August) and was slightly higher in ERA5-CTRL than in CARRA-CTRL. This was especially visible in June 2015, August 2016, July 2017 and August 2018. Snow depth was almost not present during these months. Therefore, the energy surplus of ERA5-CTRL in comparison to CARRA-CTRL probably did not influence simulations largely.

There were months when CARRA-CTRL and ERA5-CTRL had clearly different energy balances as, e.g., in August 2016. The fluxes of shortwave radiation, sensible turbulent heat flux, and latent turbulent heat flux are considerably higher in ERA5-CTRL than in CARRA-CTRL in that month.

Overall, differences in longwave radiation were apparent in May 2015, July 2015, August 2016, May 2017 and May 2018. CARRA-CTRL lost slightly more energy to the atmosphere through longwave radiation than ERA5-CTRL. The latent turbulent heat flux was higher in CARRA-CTRL than in ERA5-CTRL. However, the highest difference in the energy balances of both reanalyses was present in the sensible heat flux. Sensible heat fluxes of ERA5-CTRL were higher in summer than for CARRA-CTRL.

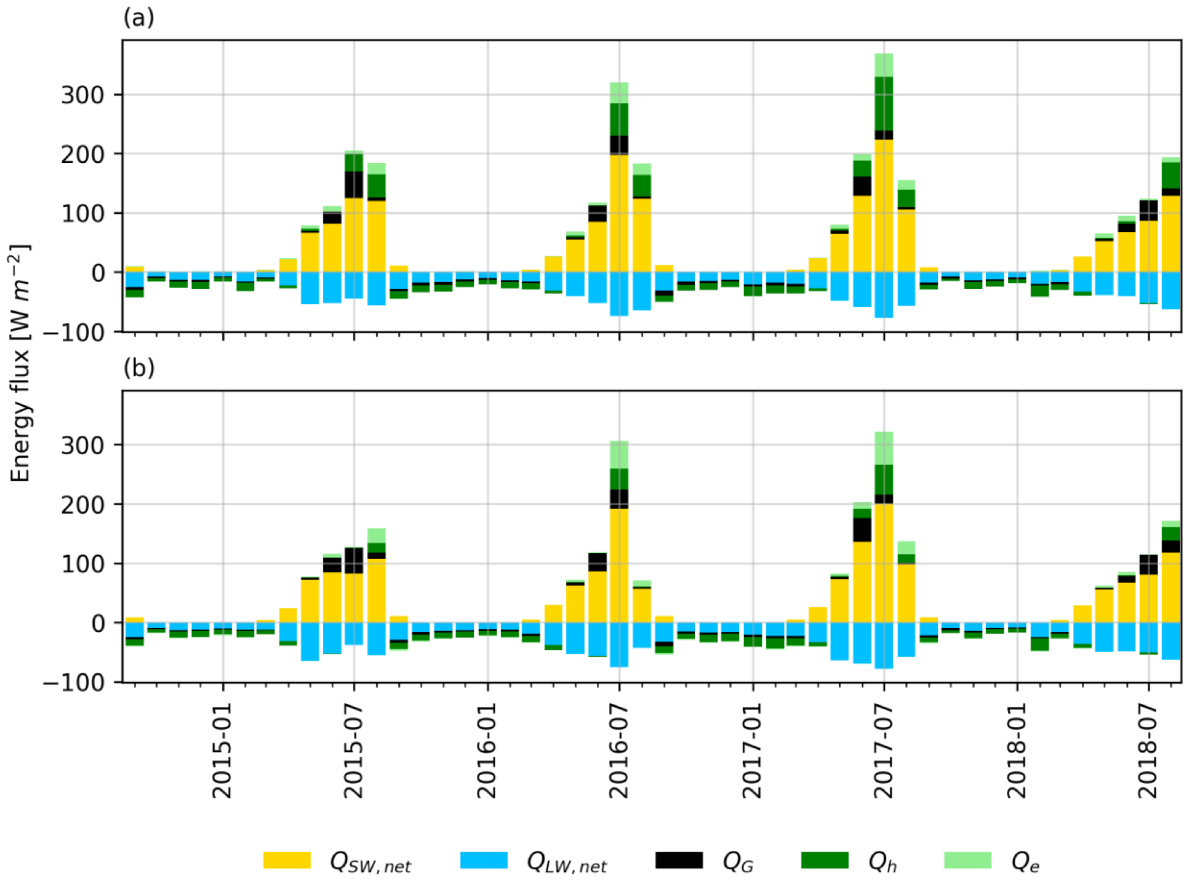

Figure 7.10: Monthly energy balance simulated with (a) ERA5-CTRL and (b) CARRA-CTRL. $Q_{SW,net}$: net shortwave radiation, $Q_{LW,net}$: net longwave radiation, Q_G: ground heat flux, Q_h: sensible turbulent heat flux, Q_e: latent turbulent heat flux. Note that heat flux from rain is missing because it is negligible.

CARRA forced simulations showed over a snow season cumulated negative latent heat fluxes due to deposition instead of sublimation in all years considered, while ERA5 forced simulations showed positive heat fluxes. Instead of snow changing its aggregation state from solid to gas, moisture from the air became solid over long periods in CARRA forced simulations and a mass gain instead of a mass lost is present approximately until May (Figure C.8 to Figure C.11 in the Appendix). Furthermore, instead of an energy surplus by sublimation for CARRA-CTRL there was an energy loss from the surface towards the atmosphere due to negative sublimation.

7.4 Discussion

7.4.1 Performance of atmospheric high and medium resolution reanalyses

As CARRA is a rather new atmospheric reanalyses released in 2021, not many studies are published yet using or evaluating the performance of CARRA. One study by Duyck et al. (2022) applied CARRA-West for analysing wind driven fresh water export in Greenland while Køltzow et al. (2022) evaluated the performance of near-surface air temperatures and wind speed of CARRA-East in the surrounding of Norway.

For CARRA-West covering the surrounding of Greenland and analysed at VRS, I find a better agreement between in-situ 2 m temperature than with ERA5. This is in line with findings of Køltzow et al. (2022) for CARRA-East and with Copernicus Climate Change Service (2020) who analysed 2 m temperature of CARRA taking into account several four months long periods over several seasons and over several hundred stations (varying between 303 – 703 stations).

I attribute the higher agreement of near-surface air temperatures of CARRA with measurements to the finer resolution of CARRA and therefore to the higher resolution of topography. ERA5 resolution being a medium-horizontal reanalysis is relatively coarse. Thus, the reanalysis is not able to reproduce complex topography and coastlines adequately (Krampe et al., 2021; Køltzow et al., 2022). This is, e.g., visible in the overestimation of surface altitude of ERA5 resulting in erroneous air temperature and air pressure.

CARRA has as well some advantages over ERA5 because it includes additional observational data in the assimilation process and comprises improvements in the handling of cold surfaces (Yang et al., 2018; Copernicus Climate Change Service, 2020; Køltzow et al., 2022). Note that, even if CARRA would have used the same set of observations as ERA5, differences in the utilised atmospheric model and the assimilation scheme would generate biases between both products (Køltzow et al., 2022).

While some variables such as surface air temperature are assimilated in the reanalyses, others such as wind speed profiles are not assimilated in both reanalyses (Køltzow et al., 2022). For mean wind speed, I find a better agreement between CARRA and in-situ wind speed than between ERA5 and in-situ wind speed. However, biases vary over the year. The amount of the mean wind speed biases over the entire study period is about the same for CARRA and ERA5. This is in line with findings for CARRA-East by Køltzow et al. (2022).

I find that maximum wind speeds are represented better by CARRA than by ERA5 but are still underestimated. In general, maximum wind speeds are higher in CARRA than in ERA5. This corresponds well to the findings of Copernicus Climate Change Service (2020) which found higher wind speeds and a better representation of higher wind speed events in CARRA than in ERA5.

However, biases in wind speed representation remain. Models with resolutions higher than 15 km can reduce the wind speed bias but are still not able to capture all wind features (Moore et al., 2016). Furthermore, biases are not reduced because assimilation of wind speed observations is not present in ERA5 and CARRA.

As CARRA resolves topography better than ERA5, CARRA is also superior in representing surface air pressure. Also, spatial and temporal variability is better resolved by CARRA than using ERA5 (see Køltzow et al., 2022 for CARRA-East).

However, even if CARRA's resolution is higher than ERA5, both reanalyses have low correlation with snowfall measurements and tend to overestimate snowfall in autumn but underestimate snowfall in spring clearly. Thus, it seems that there are still fundamental issues in simulating correctly precipitation in medium and higher resolution horizontal reanalyses.

7.4.2 Model simulations

For the CTRL-simulations snow density in the upper snow layers, especially in surface snow is distinctly underestimated. This leads to deviations of measured and simulated snow depth. Several reasons are responsible for this behaviour, some are discussed below. The impacts of the discussed reasons should be analysed in more depth in follow up studies.

(1) Underestimation of snowfall amount: An underestimation of the snowfall amount would lead to lower snow mass. However, the weight of the snow is crucial for the compaction of the underlying layers. Since measured snow density in the middle layers agree well with simulated density and density in the bottom layers is overestimated, I conclude that this is probably not the main reason for the underestimation of upper snow densities.

(2) Underestimation of new snow density: As the snow model was originally developed for the European Alps (Brun et al., 1992; Vionnet et al., 2014) the parameterisation of new snow was developed for snow falling in regions with warmer temperatures and lower wind speeds than in the Arctic. Thus, for temperatures warmer than -10°C and no wind or warmer than -20°C and 10 m s^{-1} of wind speed a fixed density of 50 kg m^{-3} is assumed. Furthermore, atmospheric humidity is not included in the new snow density parameterisation. Thus, I suspect that simulated new snow density is underestimated, which is in line with other studies (Sauter and Obleitner, 2015; Essery et al., 2016).

(3) Biases in snow density due to underestimation of wind speed: As the evaluation of ERA5 and CARRA has shown, both reanalyses underestimate high wind speeds and thus the effect of high wind speed on snow density. Crocus has implemented enhanced compaction of the upper snow layers when a wind speed threshold is reached. However, if the forcing underestimates large wind speed, this threshold may not be reached as often as would be necessary. Therefore, the formulation of enhanced compaction at high wind speeds in Crocus should be evaluated for the Arctic.

(4) Overestimation of snow compaction: As can be seen from the comparison of snow depth and SWE time series, the formulation of snow compaction in the model could lead to an overestimation of compaction. As already described in the results, the shapes of SWE and measured snow depth correspond well, indicating that at least parts of the too early snow depth decrease during spring is caused by overestimation of compaction and not by too early melting, as the snow mass seems to be simulated correctly. Note that simulated SWE stays high until the observed snow depth drops due to intense melting, which shows that the too early drop in the simulated snow depths is due to internal changes in the stratification of the snow and is probably not caused by external drivers. As no SWE measurements were carried out, this hypothesis cannot be verified. However, Brun et al. (2013) also found indications of an overestimation of the simulated compaction in the presence of liquid water, as it is the case during the melt season for simulations for northern Eurasia.

(5) Missing vertical water vapour transport: The model does not include any parameterisation of the vertical water vapour transport. This transport is important for the simulation of depth hoar, which is common in the Arctic bottom snow layers. Vertical water vapour transport leads to a transport of water vapour directed from the bottom to the top of the snowpack due to high temperature gradients that often occur in the Arctic. As a result, snow density decreases in the bottom snowpack while it increases in the upper snowpack. Other studies also suggested that this is problematic in reliably simulating Arctic snow properties (Barrere et al., 2017; Domine et al., 2019).

(6) The underestimation of SSA in the deeper snowpack in the simulations indicates that the model overestimates the decrease of SSA with time. This could be due to biases in the forcing data, biases in the simulation of other variables used to calculate simulated SSA, or in the formulation of the SSA evolution with time, e.g. the metamorphism. Note that the rate of metamorphism is temperature depending and the dependence in Crocus might be not adequate for the Arctic's cold snowpack in winter.

Further discrepancies in snow depth between measurements and simulations could be caused by weaknesses in the formulation of enhanced sublimation during snowdrift, as simulations without enhanced snow sublimation decrease later in spring. Nevertheless, the results of the simulated snow depth of the CTRL-simulations and the noENSUBL-simulations show that for this Arctic site it is essential to consider enhance sublimation during wind drift. This is particularly evident in the superior performance of CARRA-CTRL over the entire study period compared to CARRA-noENSUBL. ERA5-CTRL performs only slightly better over the entire study period than ERA5-noENSUBL. However, in 2014/15 ERA5-CTRL is clearly superior to ERA5-noENSUBL, while in 2017/18 it is the other way

around. This evens out and leads to similar performance of both ERA5 simulations if the entire study period is considered. A better performance of the simulations when enhanced sublimation during wind drift is included is consistent with results of Brun et al. (2013) who found considerable improvements in snow depth and SWE with that parameterisation. Thereby, the importance varies due to interannual variability of blowing snow events. Consideration of blowing snow sublimation is also important for Alpine sites. Vionnet et al. (2014) found three times higher sublimation fluxes when not only surface sublimation but also blowing snow sublimation is considered. In their simulations for the Alps, sublimation of suspended snow particles accounted for a reduction of deposited snow mass of about 5 %.

However, weaknesses in the forcing data, especially the poor skill of snowfall from both reanalyses, also lead to differences in snow depth. The reliability, including biases, of simulated snow properties depends considerably on the quality of the atmospheric forcing data. Thereby, not only in-situ measurements but also reanalyses data are subject to various uncertainties. These include the quality of the assimilated observational data, the way measurements are assimilated, the model physics and temporal discontinuities in the data (Liston and Hiemstra, 2011 and references therein). Further, not only the amount of precipitation is important but also the timing, as air and ground temperature as well as incoming solar radiation also strongly influence snow accumulation (Liston and Hiemstra, 2011). Krampe et al. (2021) found that not only the amount but also the timing of precipitation of ERA5 has weaknesses (see also Chapter 6).

In terms of cumulated daily latent heat due to sublimation, there is a difference between ERA5-CTRL and CARRA-CTRL of about 35,000 kJ m^{-2} at the beginning of May in 2014/15 and 2017/18, the years with the largest differences in snow depth between ERA5-CTRL and CARRA-CTRL. Assuming a snow density of 300 kg m^{-3} and the latent heat of fusion required to melt 1 kg of snow at 0°C of 335 kJ kg^{-1}, this difference results in a snow depth contrast of about 0.3 m already at the beginning of the melt season. In other words, a large proportion of the snow depth contrast can be attributed to the difference in latent heat due to sublimation, which is caused by differences in humidity between the reanalyses. While CARRA overestimates humidity in winter/spring, ERA5 underestimates humidity in winter/spring. Thus, while in CARRA there is a gain in mass, there is sublimation in ERA5.

Latent heat and sensible heat fluxes both depend on wind speed and snow surface temperature. The latent heat flux also depends on humidity while the sensible heat flux depends in addition on surface air pressure and air temperature. However, differences in sensible heat fluxes are especially connected to differences in snow covered and snow free dates between both simulations. Deviations between simulated sensible heat fluxes during the time snow is present on the ground in both simulations are rather small. The differences in sublimation latent heat flux as well as the latent heat flux between ERA5 and CARRA are connected to differences in humidity. Therefore, the energy terms depend strongly on the forcing datasets used. The comparison of the simulated energy balances of the CTRL-simulations shows once again how important reliable forcing data are.

7.5 Conclusion

Atmospheric reanalyses are a good way to obtain continuous time series required to drive a snow model also for remote regions like the Arctic. Here, I analyse differences between the medium horizontal reanalysis ERA5 and the high horizontal resolution reanalysis CARRA to investigate if a reanalysis with a higher resolution also better represents atmospheric conditions in the Arctic using exemplary a site in northeast Greenland.

Not surprisingly, CARRA resolves local topography more reliably and is superior to ERA5's resolved topography. This affects many atmospheric variables such as surface pressure, air temperature and wind speed. However, while CARRA has a better representation of surface air pressure, both reanalyses show biases in air temperature, ERA5 underestimates air temperature in summer while CARRA overestimates air temperatures in winter. Further, CARRA has a higher correlation of daily mean wind speed than

ERA5 with in-situ measurements. However, both reanalyses clearly underestimate daily maximum wind speed but CARRA maximum wind speeds are higher than that of ERA5 and correlation with in-situ measurements is slightly higher.

Differences between both reanalyses are largest in near surface humidity as ERA5 has a clear seasonal cycle, which is not present in the CARRA or in-situ data. Snowfall between both reanalyses has a high correlation but poorly represents measurements. Snowfall is underestimated in both reanalyses in spring but overestimated in autumn.

Driving the detailed snow model Crocus with both reanalyses to simulate prevailing snow properties at VRS in northeast Greenland I find varying performance for individual simulation years. While ERA5 is superior in 2014/2015, CARRA is superior in 2017/18 in simulating snow depth evolution. In general, small scale events are better represented in CARRA than in ERA5. Unlike simulations driven with CARRA, simulations with ERA5 are not able to simulate, e.g., small peaks in snow depth before the actual start of snow accumulation. In both simulations, decreasing of snow depth starts too early, which I suspect is due to for the Arctic inadequate process parameterisations in the model, which are not valid for the cold temperatures prevailing in high latitudes. The differences in humidity between both reanalyses are reflected in the snow depth simulations especially in 2014/15 and 2017/18 as it influences latent heat and sublimation. Simulations in the Arctic should use enhanced sublimation formulation as snow depth biases are reduced remarkable. Without that option, snow does not melt completely in some years in the simulations with Crocus.

8 Improvements of Arctic snow modelling by adapting the new snow density parameterisation

Parts of this chapter are published in a preprint in The Cryosphere Discussion as

Krampe, D.[1], Kauker, F.[1,2], Dumont, M.[3], and Herber, A.[1]: **On the performance of the snow model Crocus driven by in situ and reanalysis data at Villum Research Station in northeast Greenland**, The Cryosphere Discuss. [preprint], https://doi.org/10.5194/tc-2021-100, 2021.

[1] Alfred-Wegener-Institut Helmholtz-Zentrum für Polar- und Meeresforschung, Department of Climate Science, Bremerhaven, Germany
[2] Ocean Atmosphere Systems GmbH, Hamburg, Germany
[3] Univ. Grenoble Alpes, Université de Toulouse, Météo-France, CNRS, CNRM, Centre d'Études de la Neige, 38000 Grenoble, France

Author contributions

DK carried out the analysis, performed the model simulations, drafted the manuscript and prepared the figures. FK helped with fruitful discussions of the analysis. All authors contributed to the editing of the manuscript. AH helped with the observational design of the study. FK and MD assisted with the numerical design. AH was leading the PAMARCMiP campaign.

Abstract

Cold and windy conditions lead to different snow conditions in the Arctic than in the warmer European Alps. Thus, when applying a snow model developed for the European Alps in the Arctic, adaptations in the parameterisations are necessary.

Here, I present new snow density parameterisations adapted to the cold and windy conditions of the Arctic and evaluate the parameterisation of post-depositional effects of wind on upper snow layers. The aim is to improve simulations of snow evolution.

The adaptations result in a better agreement between snow depth evolution and snow density simulation. Higher mean and maximum densities are reached and the variability of snow density agrees better with the measurements. Simulations achieve the highest agreement with measurements using a new snow density parameterisation adapted to cold temperatures and the effects of wind on new snow density using a gust factor.

The proposed adaptations provide a more reliable simulation of snow depth evolution and snow density and are an important step towards more reliable simulation of snow properties in the Arctic. However, there are other processes that differ between Arctic and Alpine snow that should be analysed in future studies.

8.1 Introduction

Weather conditions during and after snow deposition lead to various layering of the snowpack. Important weather factors are wind, temperature, snowfall rate and solar radiation, whereby wind drift plays a major role (Sturm and Benson, 2004). In the Arctic, annual mean air temperature is usually below the freezing point and precipitation is generally low. However, melting or rain on snow events can still occur at the beginning and end of the snow season and have impacts on existing snow layers (Domine et al., 2018a). In addition, strong winds lasting several days are common in the Arctic (Gearheard et al., 2010; Derksen et al., 2014), often accompanied by warmer air temperatures due to mixing with higher and warmer atmospheric layers (Cabanes et al., 2002; Dominé et al., 2002).

Wind speed influences, e.g., snow distribution through local redistribution during blowing snow events as well as through enhanced sublimation and compaction of snow (Sturm and Benson, 2004). Inuit consider wind as one of the key variables determining their lives. In recent years, many Inuit observed changes in wind speed towards stronger and longer lasting winter winds (Gearheard et al., 2010). Strong winds lead to wind-packed snow, which can be too hard to build igloos as shelter from bad weather conditions during their hunting activities (Gearheard et al., 2010).

Wind packed snow also called wind slabs are hard and dense snow layers forming during strong wind events (Dominé et al., 2002; Sturm and Benson, 2004; Sommer et al., 2016; Domine et al., 2018b). These layers form as snowflakes break during the collision with each other and the snow surface, and are blown away until they are deposited having a higher density as under calm conditions (Colbeck, 1982; Dominé et al., 2002; Sato et al., 2008). During this process, snow particles change their shape towards more spherical shapes (Schmidt, 1982; Cabanes et al., 2002; Dominé et al., 2002; Bormann et al., 2013) and thus, they can be packed closer together increasing their density (Colbeck, 1982; Bormann et al., 2013). Hard, wind-packed layers at the top of snowpacks are typically for the Arctic (Sturm and Holmgren, 1994; Dominé et al., 2002; Sturm and Benson, 2004; Domine et al., 2018b). Densities for hard wind-packed layers on land range from about 350 kg m^{-3} to 520 kg m^{-3} (Dominé et al., 2002; Domine et al., 2018b), often exceeding 450 kg m^{-3} (Derksen et al., 2014).

Mean annual air temperatures in the Arctic are clearly below zero but vary considerable between -18°C and -4°C (Eckerstorfer and Christiansen, 2011). The cold air temperatures and the absence of direct radiation in winter lead to huge temperature gradients that determine the stratigraphy of Arctic snowpacks (Sauter and Obleitner, 2015) as it causes a strong vertical water vapour transport in the

snowpack and thus a mass transfer from the bottom to the top (Domine et al., 2007; Domine et al., 2019). Due to the relatively high thermal conductivity of the upper snow layers, temperature variations are transmitted quickly towards the ground (Domine et al., 2019).

As reliable and detailed snow measurements in the Arctic are limited, detailed multilayer models like the snow models Crocus (Vionnet et al., 2012), SNOWPACK (Bartelt and Lehning, 2002) or snow evolution model SnowModel (Liston and Elder, 2006) are used to simulate Arctic snowpacks (e.g., Barrere et al. (2017), Pedersen et al. (2016b) and Domine et al. (2019)). In this study I concentrate on the snow model Crocus developed for applications in the European Alps, which is embedded into the surface scheme SURFEX and fully coupled to the land surface model ISBA-DF (Boone et al., 2000). Challenges arise from the different atmospheric conditions causing considerably different snow characteristics for the Arctic and the European Alps. Snowpacks in the European Alps are warmer and deeper than in the Arctic. In addition, Alpine snow is close to its melting point and melting occurs frequently (Jacobi et al., 2010; Essery et al., 2016).

Several studies showed lower simulated near surface snow densities than measured using Crocus in the Arctic (Sauter and Obleitner, 2015; Essery et al., 2016; Domine et al., 2019). The model has several weaknesses that cause this underestimation of near surface snow densities, such as the lack of the parameterisation of the vertical water vapour transport, which in reality leads to lower basal densities and higher densities in the upper layers (Barrere et al., 2017; Domine et al., 2019). Further, the newly fallen snow (hereafter: new snow) density parameterisation was formulated for snow of the European Alps having a warmer climate than the Arctic (Vionnet et al., 2012). Regarding strong wind, a parameterisation for enhanced compaction of near surface snow layers after deposition exists, but may need to be adapted for the Arctic as an underestimation of settling and compaction in the upper layers were found (Sauter and Obleitner, 2015; Royer et al., 2021).

Thus, to account for differences between Alpine and Arctic regions several processes and parameterisations have to be revised (Chapter 3.2.1, Table 5.4, Gouttevin et al. (2018)). One important factor is to simulate realistic new snow densities as new snow density affects the density of underlying layers (e.g., through thermal conductivity) and becomes deeper layers themselves after the next snowfall event. Further, compaction of surface snow during wind events leads to high surface snow densities common in the Arctic. Thus, in this study, I focus on

(1) the development and evaluation of a new snow density parameterisation suitable for Arctic temperature and wind conditions.

(2) the evaluation of post-depositional effects of high wind speeds on upper snow density

8.2 Data and methods

The underestimation of new snow density in Crocus is caused by the use of Crocus' default parameterisation defined for the European Alps for air temperatures above -15°C for the calculation of new snow density from air temperature and wind speed and not for the colder and harsher conditions of the Arctic. Sommer et al. (2016) found that wind packing can already occur within minutes. As usually mean wind speeds over a time period are used to drive snow models, the influence of higher gust wind speeds occurring at smaller than the temporal resolution of the forcing on new snow density over shorter time periods is not considered. Wind packing does not only influence new snow density but also surface snow density as it compacts the upper snow layers.

In-situ snow measurements from an Arctic site in northeast Greenland called Villum Research Station (VRS) were exemplary used to evaluate Crocus. Snow depth was measured continuously from 1 September 2014 to 31 August 2018. Additionally, from an expedition called PAMARCMIP 2018 (Polar Airborne Measurements and Arctic Regional Climate Model Simulation Project) snow density

profiles (3 April 2018) and surface snow density measurements (21 March to 3 April 2018) using a density cutter (60x30x56 mm) were considered for evaluations.

To drive the snow model, I used the reanalyses CARRA-West (Copernicus Arctic Regional Reanalysis; hereafter CARRA). Previous analyses have shown that CARRA forced simulations agrees best with in-situ snow depth measurements for the entire study period (and especially for the snow season 2017/18 in which the observed snow density data are gathered) compared to simulations where atmospheric in-situ data or ERA5 reanalysis are forcing the model (Chapter 6, Chapter 7). I evaluated the performance of the default formulation to various adaptations regarding simulated snow depth and snow density.

Details about the model set up with default parameterisations (hereafter called CARRA-CTRL), the snow measurements and atmospheric conditions during the measurements are available in Krampe et al. (2021), and Chapter 5. The following list gives an overview of the measures carried out. The parameterisations used are described in detail in the next subchapters.

Adaptation (1) Simulation CARRA-K22

Revised formulation of the new snow density parameterisation (hereafter K22) adapted for the cold temperatures, enhanced wind compaction for wind speeds ≥5 m s^{-1}, and inclusion of humidity

Adaptation (2)

i. Simulation CARRA-K22gf1.3
ii. Simulation CARRA-K22gf1.6

Introduction of a gust factor in the new snow density parameterisation K22 to account for the effects of gust wind speeds (not resolved by the temporal resolution of the forcing data – 3 h in the case of CARRA) and the underestimation of the reanalysis' wind speeds

Adaptation (3)

i. Simulation CARRA-V12wind
ii. Simulation CARRA-K22wind

Enhancement of the wind effect of drifting snow on surface snow (Royer et al., 2021)

Adaptation (4)

i. Simulation CARRA-V12max
ii. Simulation CARRA-K22max

Increase of maximum snow density where influence of wind on snow compaction takes place from 350 kg m^{-3} to 600 kg m^{-3}

8.2.1 New snow density parameterisation

8.2.1.1 Default parameterisation V12

Crocus' default parameterisation for the density of new (freshly fallen) snow ρ_{new} (hereafter V12) formulated for the European Alps reads

$$\rho_{new} = a_\rho + b_\rho\left(T_a - T_{fus}\right) + c_\rho\, U^{1/2} \tag{8.1}$$

where T_a is the air temperature [°C], T_{fus} the melting point temperature for water [°C], U the wind speed [m s^{-1}] and a_ρ = 109 kg m^{-3}, b_ρ = 6 kg m^{-3} K^{-1}, and c_ρ = 26 $m^{-7/2}$ $s^{-1/2}$ (Vionnet et al., 2012). Figure 8.1 (a) shows the dependency of the new snow density using V12 on wind speed and air temperature. With this

linear dependence on temperature the new snow density becomes negative for temperatures below -30°C. To avoid negative and unrealistic small new snow densities, the minimum new snow density is set to 50 kg m^{-3} in V12. However, this parameterisation was deduced from measurements at Col de Porte, French Alps, where temperatures below -20°C occur seldom (Vionnet et al., 2012).

For the Arctic, where temperatures below -20°C are frequent, this parameterisation leads to numerous new snow densities with the minimum density (50 kg m^{-3}), which is deemed unrealistic for Arctic conditions. The lowest measured snow density during PAMARCMiP, for instance, was 117 kg m^{-3}.

8.2.1.2 Adaptation (1) K22

I aimed to find a new snow density parameterisation suitable for the cold temperatures in the Arctic and enhanced wind compaction. I compared the performance of Crocus for alternative new snow density parameterisations from Anderson (1976), Liston et al. (2007), Sauter and Obleitner (2015), and Van Kampenhout et al. (2017) and used in addition different minimum values for new snow density and various adaptations of these parameterisations. I decided against an "unphysical" ad hoc fixed minimum new snow density parameterisation. Also, I decided against a constant new snow density independent on temperature, wind speed and humidity because it has been clearly shown that these variables are impacting the new snow density (Liston et al., 2007; Sauter and Obleitner, 2015; Van Kampenhout et al., 2017).

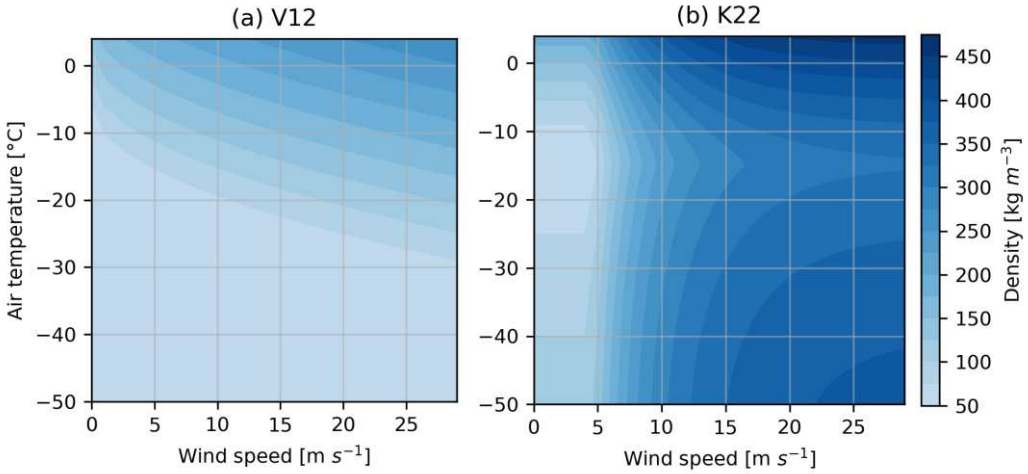

Figure 8.1: New snow density dependence on wind speed and air temperature for the parameterisation of (a) V12 (default) and (b) K22.

The parameterisation of Anderson (1976) does not account for wind influence on new snow density, Liston et al. (2007) is only defined for temperatures above -16°C, while Sauter and Obleitner (2015) adapted the constants for a_ρ, b_ρ and c_ρ of Eq. (8.1), which are only valid for Svalbard. Van Kampenhout et al. (2017) used the same equation to obtain temperature related new snow density for temperatures from -15°C to 2°C as Liston et al. (2007).

Based on that, I use a combination of Liston et al. (2007) and Van Kampenhout et al. (2017) as it represents best our observations and needs. The new snow density parameterisation by Liston et al. (2007) is defined for $T_{wb} \geq 258.16$ K and is given as

$$\rho_{new_{T_{wb}} \geq -15°C} = 50 + 1.7(T_{wb} - 258.16)^{1.5} \tag{8.2}$$

for wind speed below 5 m s^{-1}, where T_{wb} is the wet-bulb air temperature [K]. For wind speeds ≥ 5 m s^{-1} the new snow density is defined as

$$\rho_S = \rho_{new_{T_{wb} \geq -15°C}} + \rho_U \tag{8.3}$$

with

$$\rho_U = D_1 + D_2\{1 - exp[-D_3(W_t - 5)]\} \tag{8.4}$$

where D_1 is the density offset of 25 kg m^{-3} for a 5 m s^{-1} wind, D_2 the maximum density increase of 250 kg m^{-3} caused by wind and D_3 sets the progression from low to high wind speed and is 0.2 m s^{-1}. W_t is the terrain-modified wind speed at 2 m above the surface [m s^{-1}].

To simplify Eq. (8.4) I used directly measured wind speed for in-situ and given CARRA wind speed without any terrain modifications. CARRA wind speed is given for 10 m height. I tested the log law and the power law approach to downscale wind speed to 2 m with almost identical results in snow density and snow specific surface area (SSA) for both approaches. Therefore, I present only results for 10 m wind speeds.

For temperatures below -15°C, I extend the parameterisation by the new snow density parameterisation from Van Kampenhout et al. (2017) but kept the wind depended part from Liston et al. (2007)

$$\rho_{S_{T_{wb}<15°C}} = \rho_{new_{T \leftarrow 15°C}} + \rho_W \tag{8.5}$$

with

$$\rho_{new_{T_{wb}<15°C}} = -3.8328(T - T_{frz}) - 0.0333(T - T_{frz})^2 \tag{8.6}$$

where T is the near-surface air temperature [K] and T_{frz} the freezing temperature of water of 273.15 K.

The parameterisation for temperatures below -15°C from Van Kampenhout et al. (2017) does not consider any dependence on humidity. However, the influence of humidity below -15°C should be negligible, as absolute humidity at temperatures below -15°C is low. Density inversions at temperatures below -15°C as observed by Van Kampenhout et al. (2017) are taken into account with this parameterisation. Figure 8.1 visualises the new snow densities obtained with the default parameterisation and the adapted parameterisation (hereafter K22).

8.2.1.3 Adaptation (2) K22gf

I extended K22 by a gust factor gf in the wind depended term ρ_U to account for maximum wind speeds that are not resolved in the reanalysis data (delivered every three hours) because already high wind speeds over a time period of a few minutes can lead to the densification of new snow and surface snow (Sommer et al., 2016)

$$\rho_U = D_1 + D_2\{1.0 - \exp[-D_3((U \times \boldsymbol{gf}) - 5.0)]\} \tag{8.7}$$

I used two different gust factors for scaling of the wind speed

(a) A gust factor of 1.6 from the literature after Yu and Gan Chowdhury (2009)

(b) A gust factor of 1.3 calculated from the measured wind speeds at Villum Research Station every five minutes between 25 April 2017 and 8 August 2018. The calculated gust factor gf_c

$$gf_c = \frac{\max(U)_{hr}}{mean(U)_{hr}} \tag{8.8}$$

is the mean quotient of the maximum wind speed within an hour divided by the mean wind speed within that hour. Figure 8.2 gives a summary of the distribution of the calculated gust factor over the entire period where 5 min data were available.

The three different new snow density parameterisations used in this paper are summarised in Table 8.1.

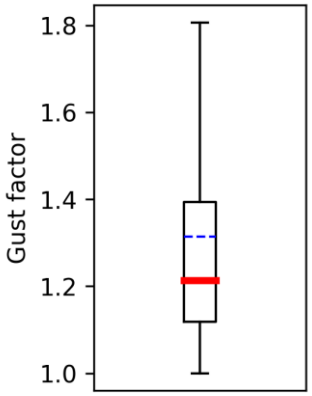

Figure 8.2: Mean in-situ wind speed calculated for 5 min data between 25 April 2017 and 8 August 2018 for in-situ wind speed from Villum Research Station. Red line: median, blue dashed line: mean.

While without the implementation of the gust factor in K22 mean wind speeds have to be ≥5 m s^{-1} to have impacts on the new snow density, with a gust factor this value declines to 3.1 m s^{-1} for a gust factor of 1.6, and to 3.8 m s^{-1} for a gust factor of 1.3. Using a gust factor instead of adapting the minimum wind speed for wind drift effects allows for calculating a gust factor for a specific site taking into account the individual local wind effects of a site. The use of the gust factor also reduces the underestimation of high wind speeds occurring in reanalyses (Chapter 6, Chapter 7), which holds as well for CARRA (Figure 8.3). While in CARRA, delivered with a temporal resolution of 3 h, 14.5 % of the wind speed is ≥5 m s^{-1}, it is 20.2 % and 26.7 % for 3 h measured mean and maximum wind speed, respectively.

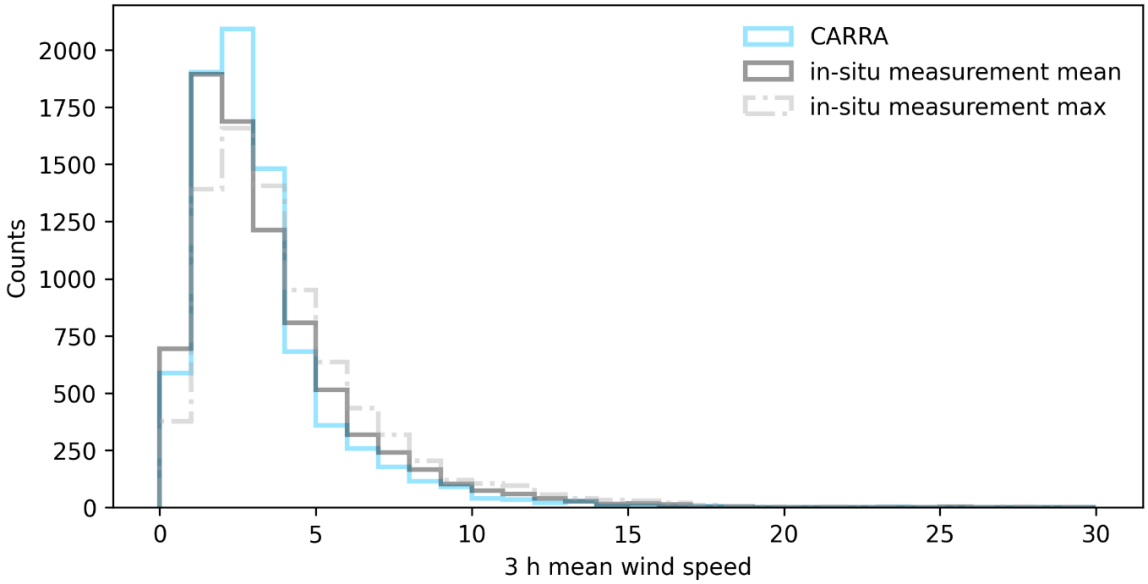

Figure 8.3: Histogram of 3 h wind speed of CARRA, 3 h mean measured wind speed and 3 h measured maximum wind speed.

8.2.2 Further adaptations

8.2.2.1 Adaptation (3) Wind effect

Crocus accounts for enhanced post depositional changes of snow density due to wind effects. For this, the density ρ_i for every layer compacted by wind due to drifting snow is calculated as (Vionnet et al., 2012)

$$\frac{\partial \rho_i}{\partial t} = \frac{\rho_{\max} - \rho_i}{\tau_i} \tag{8.9}$$

with τ_i being the characteristic time to change snow grains due to wind drift calculated as (Vionnet et al., 2012; Royer et al., 2021)

$$\tau_i = \frac{\tau}{W_E \, \tau_{i,drift}} \tag{8.10}$$

and t being time in hours, $\rho_{\max}$ the maximum density caused by wind effects (default: 350 kg m^{-3}), τ is a constant set to 48 h, $\tau_{i,drift}$ is the grain driftability and W_E is the effect of wind on snow density change. In the default version of Crocus, the W_E is set to one. Here, I follow Royer et al. (2021), who set this effect to three to account for enhanced compaction in the Arctic.

8.2.2.2 Adaptation (4) Maximum density effected by wind compaction

I increased the maximum density caused by wind effects $\rho_{\max}$ from 350 kg m^{-3} to 600 kg m^{-3} as suggested by Barrere et al. (2017) as they observed snow densities of 450 kg m^{-3} and Sturm et al. (1997) reported densities for wind slab of up to 600 kg m^{-3}. The increase of $\rho_{\max}$ can lead to denser snow layers which in turn can also limit the driftability of snow layers.

8.3 Results

8.3.1 Impacts on snow depth

All introduced adaptations on the parameterisation of new snow density, the enhanced wind effect on snow density change and the increased maximum density caused by wind effects showed improvements in the snow depth simulation compared to the CTRL-simulation (Table 8.2 and Figure 8.4). All simulations with adapted parameterisations were superior to the CTRL-simulation when compared to measured snow depth using the metrics root mean square difference (RMSD), Pearson correlation coefficient r, and the coefficient of determination R^2 (see Chapter 7 for an explanation of R^2). In addition, all simulations with adapted parameterisations but CARRA-K22gf1.6 had a smaller mean bias (simulated snow depth – measured snow depth) than the CTRL-simulation.

Table 8.1: Overview about newly fallen snow density parameterisations used in this paper.

default	
$\rho_{new} = a_\rho + \rho_T + \rho_U$ Lowest density is fixed 50 kg m^{-3} → appears for cold temperatures	
Temperature dependent part	$\rho_T = b_\rho (T_a - T_{fus})$
Wind dependent part	$\rho_U = c_\rho U^{0.5}$
References	Vionnet et al., 2012

modified for Arctic conditions
$\rho_{new\ T \geq -15°C} = \rho_{T \geq -15°C} + \rho_U$ $\rho_{new\ T < -15°C} = \rho_{T < -15°C} + \rho_U$

(a) modified to cold temperatures enhanced compaction by wind speeds from 5 m s^{-1} and humidity	
Temperature dependent part	$\rho\ T_{wb \geq -15°C} = 50 + 1.7\ (T_{wb} - 258.16)^{1.5}$ $\rho\ T_{wb < -15°C} = -3.8328\ (T - T_{frz}) - 0.0333\ (T - T_{frz})^2$
Wind dependent part (for wind speed ≥ 5 m s^{-1})	$\rho_U = D_1 + D_2\ \{\ 1 - exp\ [\ -D_3\ (U - 5)\ ]\ \}$
References	Liston et al. (2007) Van Kampenhout et al. (2017) This paper

(b) modified as (a) but accounting for effects of gust wind speeds	
Temperature dependent part	same as (a)
Wind dependent part (for wind speed ≥ 5 m s^{-1})	$\rho_U = D_1 + D_2\ \{\ 1 - exp\ [\ -D_3\ (g_f U - 5)\ ]\ \}$
References	Liston et al. (2007) Van Kampenhout et al. (2017) This paper

Variables	a_ρ: 109 kg m^{-3} b_ρ: 6 kg m^{-3} K^{-1} c_ρ: 26 m$^{-3.5}$ s$^{-0.5}$ T_a: air temperature T_{fus}: melting point temperature for water U: wind speed D_1: density offset 25 kg m^{-3} for a 5 m s^{-1} wind D_2: maximum density increase 250 kg m^{-3} caused by wind D_3: progression from low to high wind speed 0.2 m s^{-1} g_f: gust factor

CARRA-K22gf1.6 had the highest agreement with measured snow depth in all metrics but in bias. The RMSD was 0.05 m lower for CARRA-K22gf1.6 (RMSD: 0.20 m) than for CARRA-V12 (RMSD: 0.25 m). Furthermore, the correlation with measured snow depth was increased from 0.86 for CARRA-V12 to 0.92 for CARRA-K22gf1.6. This is reflected in R^2, which was clearly higher for CARRA-K22gf1.6 (R^2: 0.82) than for CARRA-V12 (R^2: 0.71), i.e. about 10 % more variance could be explained by CARRA-K22gf1.6. However, the snow simulated by CARRA-K22gf1.6 did not melt completely at the end of the snow season 2017/18. The same was true for CARRA-K22gf1.3. This explains the higher mean bias for both simulations compared to CARRA-CTRL.

Table 8.2: Descriptive statistics of metrics for different snow depth simulations compared to snow depth measurements (September 2014 to August 2018). Bias (simulated snow depth - measured snow depth), RMSD: root mean square difference, r: Pearson correlation coefficient, and R2: coefficient of determination. The values showing the highest and the lowest agreements between simulation and measurements are highlighted in bold.

Simulation	**Bias** [m]	**RMSD** [m]	**r** [-]	**R^2** [-]
CARRA-CTRL	0.025	**0.25**	**0.86**	**0.71**
CARRA-K22	**0.015**	0.24	0.87	0.74
CARRA-K22gf1.3	0.047	0.21	0.90	0.80
CARRA-K22gf1.6	**0.066**	**0.20**	**0.92**	**0.82**
CARRA-V12wind	0.046	0.23	0.89	0.76
CARRA-K22wind	0.038	0.21	0.90	0.79
CARRA-V12max	0.042	0.23	0.88	0.75
CARRA-K22max	0.025	0.22	0.89	0.78

In general, CARRA-K22gf1.6 snow depth was lower during the snow accumulation period but higher during the melting period than CARRA-CTRL (Figure 8.4 (b)). Snow depth simulated with CARRA-K22gf1.3 was between CARRA-K22gf1.6 and CARRA-CTRL. Both K22gf-simulations showed a clear improvement in the simulation of snow depth during the melting period, which was more pronounced for CARRA-K22gf1.6 than for CARRA-K22gf1.3. In the snow season 2015/16 CARRA-K22gf1.6 was able to simulate the correct timing of the melt onset and followed the snow depth measurements while CARRA-CTRL snow depth started to decrease too early and too quickly. In addition, in 2017/18 there was a clear improvement during the melting period. The superior performance of the K22gf-simulations is also shown in Figure D.1 in the Appendix.

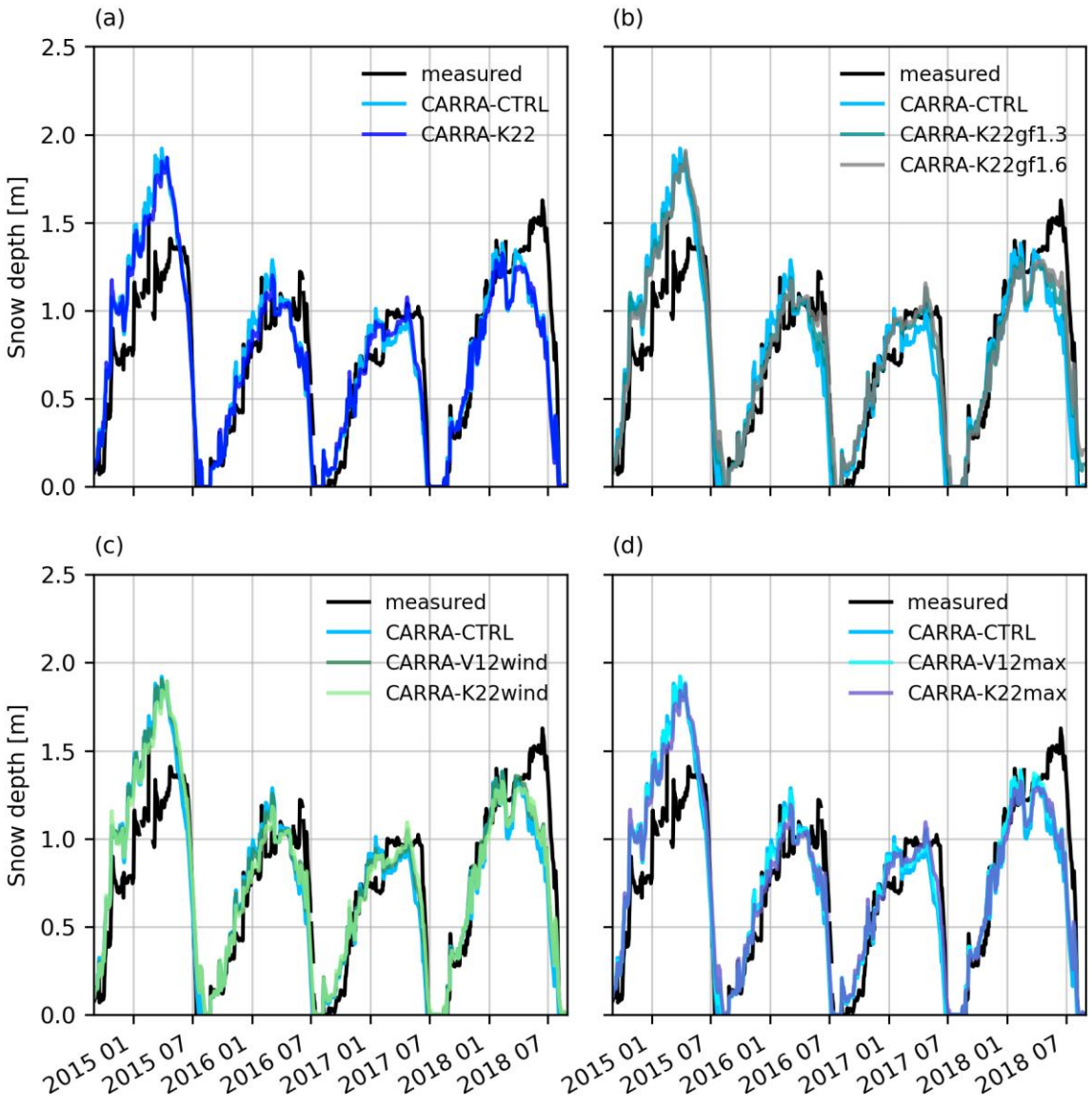

Figure 8.4: Time series of measured and simulated snow depth from September 2014 to August 2018. Simulations include the default new snow density parameterisation V12 (CTRL – shown in all subplots) and the (a) adapted new snow density parameterisation K22 (b) introduced new snow density parameterisations K22gf1.3 and K22gf1.6 (c) enhanced effect of wind on snow density (set W_E = 3, (default W_E= 1), see Eq. (8.10)) for the new snow density parameterisation V12 and K22 and (d) increased maximum density caused by wind effects to 600 kg m^{-3} (default: 350 kg m^{-3}) for the new snow density parameterisation V12 and K22.

The wind-simulations (Figure 8.4 (c)) and the max-simulations (Figure 8.4 (d)) showed a small improvement in the melting season, having slightly higher values than the CTRL-simulation. Thereby, snow depth for simulations using the K22 parameterisation were higher than for the V12 parameterisation. During the accumulation phase, wind-simulations and max-simulations were lower than the CTRL-simulation. This is more pronounced in the K22-simulations than in the V12-simulations. The performance of CARRA-V12wind compared to CARRA-V12max and of CARRA-K22wind compared to CARRA-K22max is similar.

8.3.2 Impacts on the vertical snow density profile on 3 April 2018 and the snowyear 2016/17

When applying simulations using the K22 parameterisation (CARRA-K22, CARRA-K22gf1.3, CARRA-K22gf1.6, CARRA-K22wind, CARRA-K22max), simulated density reached occasionally the measurement ranges in the upper snow layers (0.9 to 0.7 normalised snow depth) especially when the sample uncertainty was taken into account for the vertical snow density profile measured on 3 April 2018 (Figure 8.5). All simulations were able to simulate measured snow density in the middle part of the snow profile (0.6 to 0.15 normalised snow depth). Simulations with adapted parameterisation all showed a higher variability with several distinct density peaks, which was most pronounced for simulations using the K22 parameterisation. Thus, in contrast to the V12-CTRL simulation the snow density did not increase only monotony with depth for the adapted simulations. Rather, layers of higher density, i.e. more heterogeneous profiles, were simulated, which roughly match the observations.

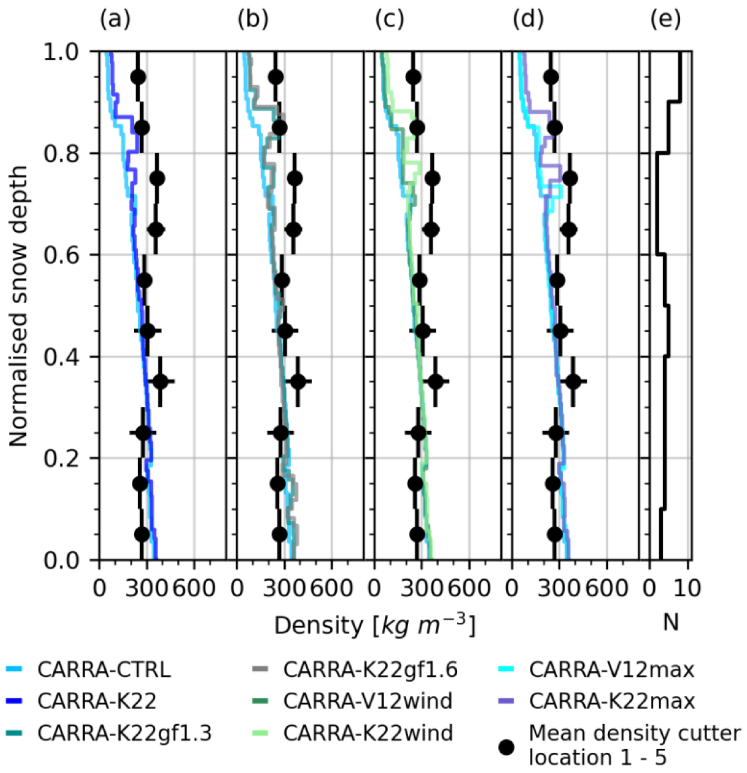

Figure 8.5: (a) – (d) Simulated and measured snow density on 3 April 2018 using different parameterisations described in Chapter 8.2. (e) shows the sample frequency of density cutter measurements. Black vertical lines represent the normalised snow depth range where measurements had been averaged and black horizontal lines represent the sample variability (± one standard deviation).

Simulations using the K22-parameterisation were closer to the measurements than simulations using the V12-parameterisation (CARRA-CTRL, CARRA-V12wind, CARRA-V12max) as the simulations using the K22-parameterisation showed an additional increase in density from 0.9 to 0.8 normalised snow depth not visible in the simulations using the V12- parameterisation. Simulated bottom snow density (0.02 to 0 normalised snow depth) was similar for all simulations but for CARRA-K22gf1.3 and CARRA-K22gf1.6, which both simulated higher densities and thus overestimated measured bottom snow density more than the other simulations.

All adapted simulations achieved a higher mean snow density for the vertical profile from 3 April 2018 compared to the CTRL-simulation (Table 8.3). Thereby, the lowest increase in mean density was +16 kg m^{-3} for CARRA-V12wind (226 kg m^{-3}) and the highest increase was +40 kg m^{-3} for CARRA-K22gf1.6. In general, mean densities were higher for simulations using the K22-parameterisation than

for those using the V12-parameterisation. The minimum snow density for all simulations using the V12-parameterisation was 50 kg m^{-3} while it was 78 kg m^{-3} for all simulations using the K22-simulation. Apart from CARRA-K22gf1.6, maximum density was in the range of the CTRL-simulation (359 kg m^{-3} to 364 kg m^{-3}). The maximum density of CARRA-K22gf1.6 was 25 kg m^{-3} higher than the CTRL-simulation.

Table 8.3: Descriptive statistics of metrics for different snow density simulations described in Chapter 8.2 and the measurements for the vertical density profile from 3 April 2018. Std: standard deviation. The values showing the highest and the lowest values in the simulations are highlighted in bold.

	Mean [kg m^{-3}]	**Minimum [kg m^{-3}]**	**Maximum [kg m^{-3}]**	**Std [kg m^{-3}]**
Measurements	302	246	388	50
CARRA-CTRL	**209**	50	**359**	100
CARRA-K22	235	78	360	87
CARRA-K22gf1.3	239	78	364	85
CARRA-K22gf1.6	**249**	78	**384**	89
CARRA-V12wind	226	50	363	100
CARRA-K22wind	245	78	361	82
CARRA-V12max	225	50	362	101
CARRA-K22max	242	78	360	86

Figure 8.6 shows the proportions of simulated and measured snow density for the vertical snow profile from 3 April 2018. It is clearly visible that the highest density categories 400 kg m^{-3} – 449 kg m^{-3} and >450 kg m^{-3} present in the measurements could not be reproduced by any simulation. Further, the lowest density categories found in all simulations with densities <100 kg m^{-3} and 100 kg m^{-3} – 149 kg m^{-3} were not present in the measurements. However, note that the simulations had a considerably higher resolution than the measurements.

The proportion of densities between 350 kg m^{-3} – 399 kg m^{-3} (highest simulated densities) was highest for CARRA-K22gf1.3 and CARRA-K22gf1.6. Simulations with higher wind effects (CARRA-V12wind and CARRA-K22wind) and CARRA-K22max had the lowest proportion in the density range 100 kg m^{-3} – 149 kg m^{-3} combined with <100 kg m^{-3} (density ranges not present in the measurements).

To analyse changes in the vertical density profiles throughout the year between the different parameterisations, I choose exemplarily the snowyear 2016/17 as snow depth agreed well with measurements in this year and show all simulated vertical density profiles of one day (15^{th}) every month where snow was covering the ground (Figure 8.7). Only the gross differences are described, as no measurements for comparison are available.

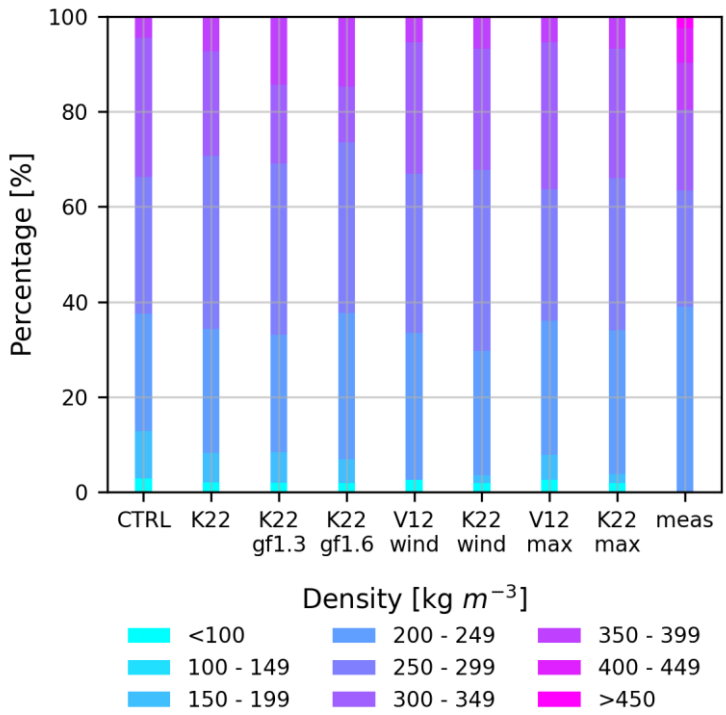

Figure 8.6: Snow density simulated with various adaptations on the parameterisations described in Chapter 8.2 and from density cutter measurements on the 3 April 2018 in percentage. Shown is the occupation of density classes given below the plot in percentage. The measurements comprises five profiles at different locations with a total of 41 measurements. CTRL: CARRA-CTRL, K22: CARRA-K22, K22gf1.3: CARRA-K22gf1.3, K22gf1.6: CARRA-K22gf1.6, V12wind: CARRA-V12wind, K22wind: CARRA-K22wind, V12 max: CARRA-V12max, K22 max: CARRA-K22max, meas: measured snow density.

In the beginning of the snow season (September), snow density profiles showed a huge variability between the simulations, as the snowpack was thin and only consisted of few snow layers. As time progressed, snowpacks got thicker and more snow layers were occupied. Gradually until May, simulated snow density in the lower snow layers got more and more similar for all simulations. In June variability was high again because the snowpack got thinner accompanied by lowering the number of active layers in the model (up to 50 vertical layers are possible) and the increase of surface variability starts to dominate the deeper layers again. Peaks in the simulations using the K22-parameterisation were more distinct than simulations using the V12-parameterisation due to higher surface densities with K22.

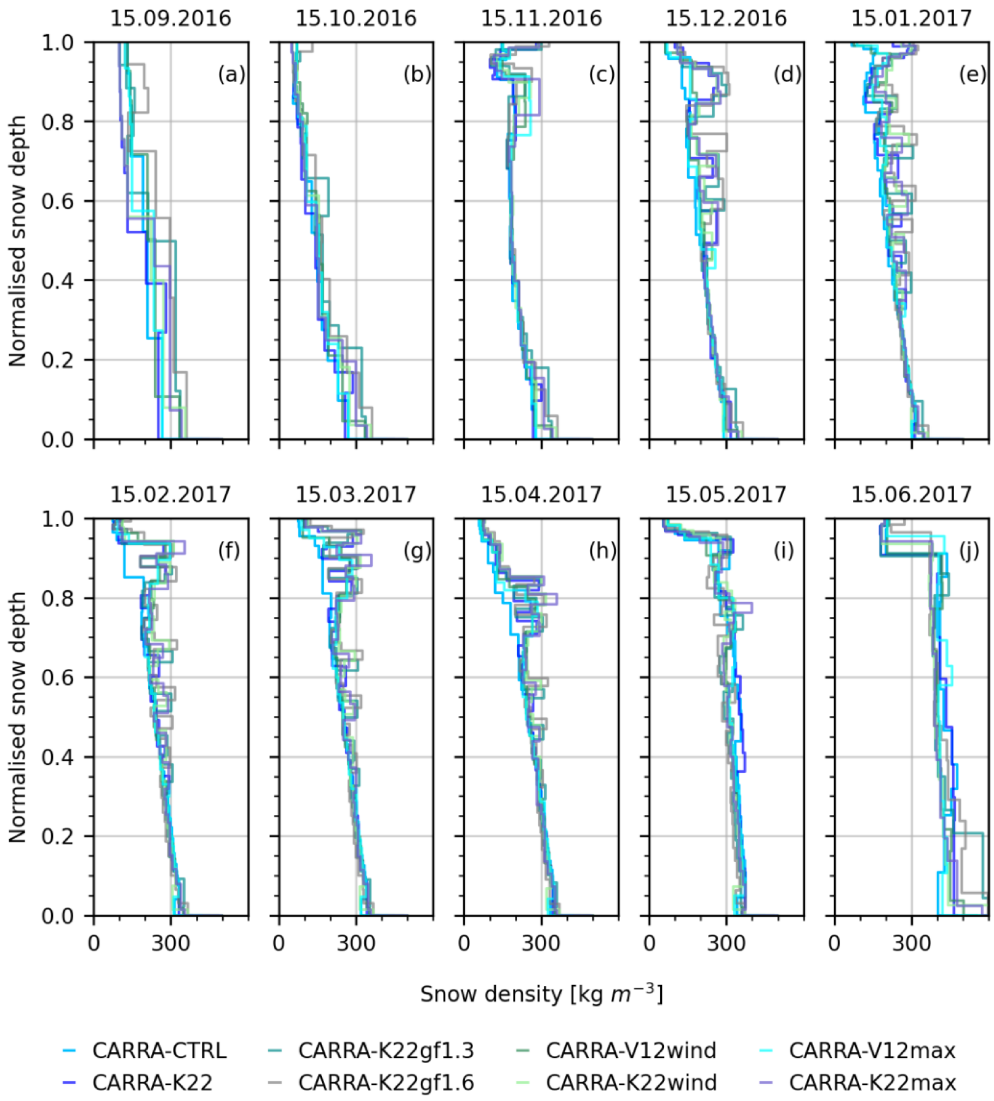

Figure 8.7: Simulated snow density using different parameterisations described in Chapter 8.2 for the snow season 2016/17 for every 15th day of a month. Note, that there was no snow on 15.07.2017 and 15.08.2017.

8.3.3 Impacts on surface snow density

During the PAMARCMiP campaign, also surface snow density (upper 3 cm) was measured between 21 March and 3 April 2018 at the same five locations as the vertical density profile on 3 April 2018. The time series of surface density measurements together with simulated surface snow densities for the upper 3 cm for the simulations described in Chapter 8.2 are displayed in Figure 8.8. The measurements showed no distinct trends but a high spatial variability ranging from 156 kg m^{-3} to 325 kg m^{-3} with a mean of 224 kg m^{-3}. More details about the surface snow density measurements can be found in Chapter 9.

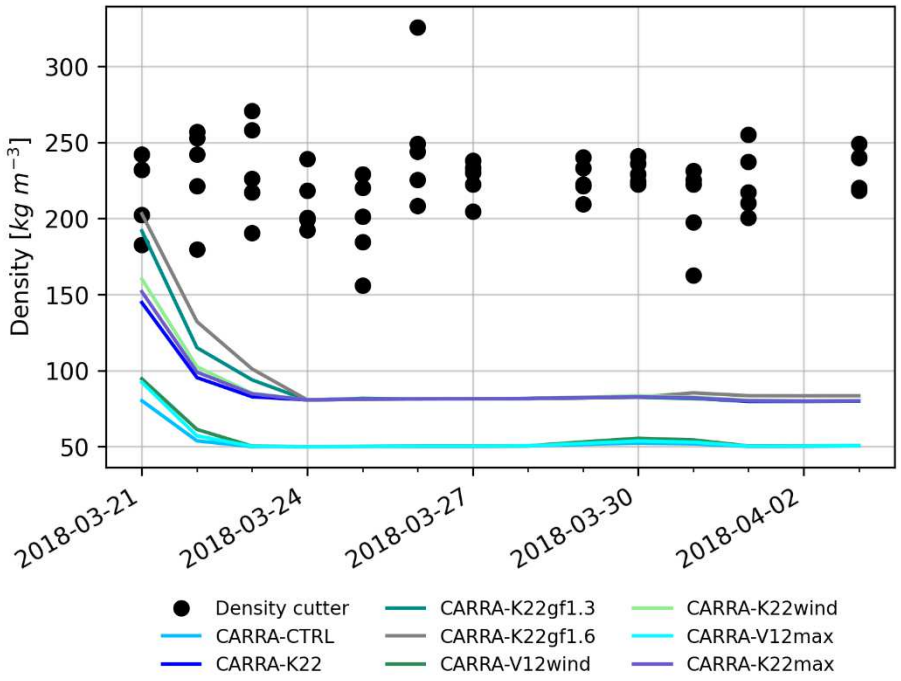

Figure 8.8: Bulk surface density of the first 3 cm. Simulated with different parameterisations described in Chapter 8.2 and measured with the density cutter at different locations from 21 March to 3 April 2018.

All model simulations decreased from 21 March to 23/24 March and were clearly below the measurements most of the time. Lowest densities were reached for CARRA-CTRL ranging from 50 kg m^{-3} to 80 kg m^{-3}. CARRA-V12wind and CARRA-V12max were slightly higher in the beginning (CARRA-V12wind: 95 kg m^{-3}, CARRA-V12max: 92 kg m^{-3}) but dropped quickly to about 50 kg m^{-3} similar to the CARRA-CTRL simulation. Simulations using the K22-parameterisation had considerably higher surface snow densities than the simulations using the V12-parameterisation. CARRA-K22gf1.3 and CARRA-K22gf1.6 were able to reproduce the surface density on 21 March (CARRA-K22gf1.3: 192 kg m^{-3}, CARRA-K22gf1.6: 203 kg m^{-3}) but all simulations using the K22-parameterisation dropped as well afterwards due to new snowfall on 21 March to 23 March in CARRA. Snow surface density from simulations using the K22-parameterisation were similar (around 80 kg m^{-3}) from 24 March onwards.

Figure 8.9 shows the seasonal cycle (upper panel) for the upper snow density (upper 10 cm) and differences between CARRA-CTRL and the adapted simulations (lower panel). Further, Figure D.3 in the Appendix shows the time series over all four snowyears for the upper snow density (upper 10 cm).

Surface density clearly increased from December to March/April before it dropped again to the same level as before for all simulations. Thereby, variability was highest in April and highest for the K22gf-simulations. Overall, differences to the CARRA-CTRL were highest for CARRA-K22gf1.6, especially in April, May and August. In addition, CARRA-K22gf1.3, CARRA-K22max and CARRA-K22 showed distinct deviations from CARRA-CTRL. Most of the year upper snow densities were higher for the adapted simulations than for CARRA-CTRL. However, especially in January to March, densities could also be lower than for CARRA-CTRL.

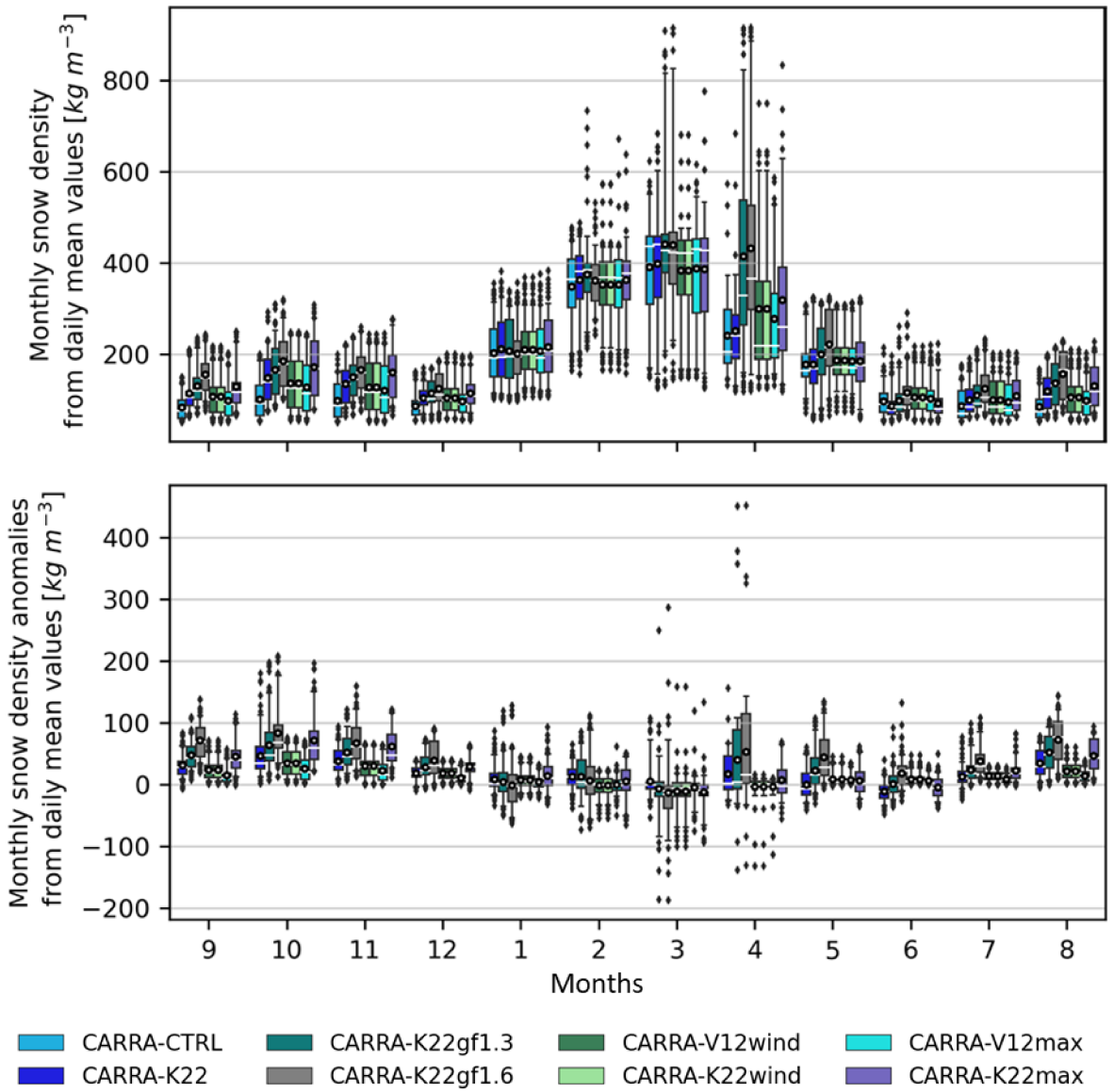

Figure 8.9: Boxplots of simulated monthly upper snow density (upper 10 cm) from different parameterisations described in Chapter 8.2 (September to August) averaged from daily mean values from September 2014 to August 2018. White dot: mean, white line: median. Top: absolute snow densities. Bottom: Difference between CARRA-CTRL and other simulation. Note: The order of the boxplots is the same as in the legend (Top: CARRA-CTRL, CARRA-K22, CARRA-K22gf1.3, CARRA-K22gf1.6 and so on, Bottom: CARRA-K22, CARRA-K22gf1.3, CARRA-K22gf1.6 and so on).

Throughout the year, mean upper snow densities (upper 10 cm) were between +64 kg m^{-3} (CARRA-K22gf1.6) and 14 kg m^{-3} (CARRA-V12max) higher than for CARRA-CTRL (Table 8.4). Minimum densities for all simulations were similar, ranging from 51 kg m^{-3} (CARRA-CTRL and CARRA-K22) to 57 kg m^{-3} (CARRA-K22gf1.6). In contrast, maximum upper snow densities showed huge variability ranging from 624 kg m^{-3} (CARRA-CTRL) to above 900 kg m^{-3} (CARRA-K22gf1.3 and CARRA-K22gf1.6), thus being rather ice than snow. Standard deviations were similar ranging from 110 kg m^{-3} (CARRA-CTRL) to 119 kg m^{-3} (CARRA-K22wind) for all simulations but CARRA-K22gf1.3 (142 kg m^{-3}) and CARRA-K22gf1.6 (137 kg m^{-3}).

Table 8.4: Descriptive statistics of metrics for different upper snow density (upper 10 cm) simulations described in Chapter 8.2 (September 2014 to August 2018). Std: standard deviation. The values showing the highest and the lowest values in the simulations are highlighted in bold.

Simulation	Mean [kg m^{-3}]	Minimum [kg m^{-3}]	Maximum [kg m^{-3}]	Std [kg m^{-3}]
CARRA-CTRL	**152**	51	**624**	**110**
CARRA-K22	172	51	684	111
CARRA-K22gf1.3	202	55	914	**142**
CARRA-K22gf1.6	**216**	**57**	**916**	137
CARRA-V12wind	173	52	749	113
CARRA-K22wind	191	53	897	119
CARRA-V12max	166	52	671	112
CARRRA-K22max	187	52	833	117

8.4 Discussion

8.4.1 Simulated snow densities using the default model formulation

I found an underestimation of new snow density in Crocus, which confirms the results from former studies in the Arctic (Lefebre et al., 2005; Sauter and Obleitner, 2015; Essery et al., 2016). In the new snow density parameterisation currently used in Crocus, new snow density is set to 50 kg m^{-3} for temperatures below -30°C, which are common in Arctic winter, and a linear relationship between temperature and density is applied (Vionnet et al., 2012). In contrast, Meister (1985) found increasing new snow densities for temperatures below -15°C, which I considered in the implemented new snow density parameterisation K22. Crystallization at low temperatures and breaking through wind impacts are reasons for a higher new snow density in the Arctic than in the warmer and more sheltered European Alps (Jordan et al., 1999). This results, for instance, in densities for new and recent snow layers of 172 kg m^{-3} in the High-Arctic and 239 kg cm^{-3} for the Sub-Arctic (Derksen et al., 2014).

Further, only when the strongest wind events (including gust winds) are taken into account, drifting snow frequency and magnitude as well as density changes due to drifting snow processes can be simulated adequately (Keenan et al., 2021). This is often not the case when working with mean wind speeds over a period as is often done for simulations. Especially short time gust wind speeds, which can still lead to considerable changes of the surface snow properties, are not considered when forcing with wind speeds averaged for some hours. But already low wind speeds can change the snow density. During wind tunnel experiments Sato et al. (2008) found partly breaking snowflakes for wind speeds between 2 m s^{-1} and 3 m s^{-1}. For wind speeds higher 5 m s^{-1}, they found completely broken snowflakes. Liston and Hiemstra (2011) assume that densification by blowing snow cause snow densities in nonforested areas of the Arctic to be about 50 kg m^{-3} higher than without taking blowing snow densification into account. Thus, by implementing a gust factor in the new snow density parameterisation, I account for the effects of higher wind speeds found in the Arctic and lower the wind speed threshold required to have effects on the new snow density.

Reliable new snow densities are as well important because too low causes too strong insulation of lower snow layers from the surface snow layers due to too low heat conduction through the snow. In the consequence, the temperatures of deeper snow layers are too high, subsurface melt may occur (Van Kampenhout et al., 2017), and the temperature dependent metamorphism of the snowpack (towards lower SSA) might be overestimated (see Table 5.3).

Another factor that is beyond the scope of this work, but should nevertheless be mentioned, is the redistribution of snow by wind. Snow transport by wind reveils in a snow surface that is older and can be denser than the underlying snow layer. The redistribution process is not parameterised in the model while the compaction of the snow surface by wind processes is taken into account.

8.4.2 Performance of individual parameterisations

Simulations using the K22-parameterisation are clearly superior compared to the simulations using the V12-parameterisation. V12 was developed for warmer temperatures than prevalent in the Arctic. In addition, K22 takes impacts of wind speeds ≥5 m s^{-1} strongly into account, while new snow density in V12 depends on the square root of wind speed. The superior performance of simulations using the K22-parameterisation are apparent for snow depth evolution, vertical density profiles and surface snow densities. However, more density measurements (vertical profiles and surface/ upper snow density measurements) are required to perform a more solid validation of the presented parameterisations, as the measurements presented here are limited to one site and one short time period.

But already using the available measurements, this study shows that the wind effect on snow density is clearly underestimated in the default simulation and in the simulations using the V12-parameterisation. However, for snow depth evolution the performance of CARRA-V12wind compared to CARRA-V12max and the performance for CARRA-K22wind compared to CARRA-K22max are similar. Regarding the density, CARRA-K22wind and CARRA-K22max result in higher densities and seems to be closer to the measurements than CARRA-V12wind and CARRA-V12max, respectively.

Especially applying any K22-parameterisation results in a denser new snow density and thus higher maximum and mean snow densities for the upper snow layers than with the default formulation. I address this to much higher surface densities earlier in time in the K22-simulations that were visible in greater depth when the time progress. Further, the simulated snow densities showed a much higher variability with several distinct density peaks compared to simulations using the default parameterisations. This peaks and variability were also visible in the density cutter profiles. Thus, using simulations with the K22-parameterisation, snow density is not only increasing monotony with depth as for the CARRA-CTRL-simulation, which would be typical for the European Alps but not for the Arctic.

There are different ways to improve the model performance in simulating snow depth evolution and density. Thereby, from the here tested parameterisations, changes in new snow density parameterisation have higher effects than changes in the enhanced wind effect on surface density or the maximum density affected by wind. Further, the selection of the effect wind has on snow density from one or three appears random without any scientific judgement. Changing the maximum density caused by wind effects is based on field observations of wind slabs reaching higher densities (Sturm et al., 1997; Barrere et al., 2017). However, it is preferable that an increase in wind slab densities is caused by a physical based parameterisations rather than by setting a threshold. In contrast, the formulation using the gust factor can easily be calculated from the prevailing wind conditions at a site and thus is physically based. Overall, the smallest improvement for CARRA-K22 in most of the metrics for snow depth evolution and a weaker performance in snow density simulations than other adaptations using the K22-parameterisation in addition to other adaptations shows, that wind induced effects on the snow density are still underestimated using the K22-parameterisation without any further adaptations. However, as shown in the Appendix (Chapter D.2), improvements using the K22-parameterisation is not only achieved when using CARRA to force the model but also when forcing the model with ERA5 and in-situ measurements.

The calculated gust factor of 1.3 used in this study was calculated for a station close to the ocean. High winds are higher at coastal stations than in stations located in the inland area (Kislov and Matveeva, 2016; Minola et al., 2020). Thus, the prescribed gust factor of 1.3 might be overestimated for inland areas but could fit well to stations on sea ice as both ocean and sea ice have rather low roughnesses and should be tested at other stations. However, as proposed before, the calculation of a site specific gust

factor can easily be done when wind speed data are available. Further, wind speeds are also higher during daytime than during nighttime whereby the amplitude is lowest at coastal locations (Minola et al., 2020). In addition, wind speeds in the Arctic differ with seasons as circulation patterns in the cold and warm season are different (Kislov and Matveeva, 2016; Minola et al., 2020). This was also observed by Inuit (Gearheard et al., 2010). The here used gust factor of 1.3 does not change with season or daytime. However, it is questionable whether a seasonal or time-of-day implementation of a gust factor would lead to serious improvements rather than just pretending a non-existent accuracy. The gust factor of 1.3 was calculated using hourly mean and maximum values of 5-minutes measured wind speed data. When calculated for 3-hourly mean and maximum values (as the temporal resolution of CARRA is 3 h), the calculated gust factor is 1.5 and thus closer to the used 1.6 gust factor.

Applying a gust factor in the new snow density parameterisation only affects the new snow density. Densification of the surface snow is not taken into account with this parameterisation but were analysed in this study by changing the enhanced wind effect on surface density and the maximum density affected by wind. However, both effects should be combined in a future study, preferably in a more physical way than the here proposed post-depositional effects on upper snow density.

Simulated snow density in the lower snow layers is higher than measured snow density (and higher than for the other simulations), while upper snow density is still underestimated, also when using the adapted parameterisations. However, I assume that the higher than observed values are an artefact of the missing vertical water vapour transport that would redistribute the mass flux from the bottom to higher layers in the snowpack (Barrere et al., 2017; Domine et al., 2019; Lackner et al., 2022b).

In addition to the here analysed too low new snow density parameterisation in the default model parameterisation and post-depositional wind effects, there are also other processes that lead to deviations in measured and simulated snow density (Barrere et al., 2017; Domine et al., 2019; Krampe et al., 2021), Chapter 6 and Chapter 7. There is a lack of important processes in the model for Arctic applications as the vertical water vapour transfer and redistribution of snow by wind (Barrere et al., 2017; Domine et al., 2019). Further, settling and compaction as well as the formulation of SSA evaluation seems to be unrealistic for Arctic applications (Chapter 7) (Brun et al., 2013). However, analysing and improving these effects is beyond the scope of this study. The here proposed parameterisations are already a step forward to achieve reliable snow simulations with Crocus in the Arctic.

8.5 Conclusion

Arctic snow deviates from snow in other regions as, e.g., the European Alps. Thus, when applying snow models developed for warmer and less windy snow conditions such as the detailed snow model Crocus, adaptations have to be made to allow representative simulation of snow properties. This paper focuses on the introduction of a new snow density parameterisation suitable for Arctic temperature and wind conditions. Further, the effect enhanced wind has on surface snow density is evaluated. The overall aim is to improve snow depth and density simulations for the Arctic.

The proposed new snow density parameterisations and changes on post-depositional effects caused by wind all reveal a better agreement between measured and simulated snow depth evolution than using the default parameterisations. Thereby, adaptations using a parameterisation adapted to the cold temperatures in the Arctic and wind effects on new snow density for higher wind speeds than 5 m s^{-1} in combination with further adaptations for wind speed effects on snow density show the highest agreement with snow depth evolution and density measurements. Thereby, the most promising adaptation is a combination of this parameterisation together with a gust factor to receive new snow density. Further measurements from different seasons and locations would be beneficial to achieve more robust result.

9 Measured and simulated black carbon concentrations in spring at a site in Greenland

Abstract

Black carbon (BC) particles in Arctic snow contribute to rapid climate change in the Arctic by lowering surface albedo and triggering positive feedback mechanisms. So far, however, longer measured time series of BC in snow are lacking, and thus little is known about processes and effects associated with BC in snow. This includes BC deposition rates, the development of BC concentrations in snow over the course of the year especially in remote regions, trends, associated changes in snow properties and post-depositional processes. Quantifying the effects of BC in snow is therefore subject to large uncertainties.

Detailed snow models that are able to simulate the effects of BC on related snow properties and take into account post-depositional effects, such as the snow model Crocus, can help to better understand and quantify the effects of BC in snow. In this study, Crocus is applied to approximate prevailing BC deposition rates through inverse modelling using BC concentrations measured in snow profiles during a campaign in spring 2018 before the melt onset. Furthermore, the prevailing measured conditions of BC concentrations in surface snow and snow profiles are presented. In a sensitivity study, the impacts of different BC concentrations on snow properties including surface albedo are investigated.

Deduced from inverse modelling experiments it is shown that deposition rates are low compared to deposition rates in the European Alps and measured deposition rates for a high deposition event in Greenland. The prevailing measured BC concentrations are consistent with previous studies on Greenland.

The largest effects of higher BC deposition rates is the shortening of the snow season caused by lower surface albedo during the melting period. As the ground has a lower albedo than the snow surface, more heat is absorbed due to the longer snow free period, leading to warmer ground temperatures of up to 13°C. This in turn results in tiny lower snow thicknesses in the beginning of the following snow season – an indirect effect of the accelerated melting in spring/early summer due to higher BC deposition rates.

Limits are set by using constant deposition rates throughout the year. In addition, there are discrepancies between the simulated and measured surface albedo in spring, which are probably caused by model deficiencies in the formulation of snow metamorphism to account for the colder conditions and therefore slower snow ageing in the Arctic compared to the European Alps.

In conclusion, the study provides an approximation of prevailing deposition rates in Arctic Greenland and contributes to the understanding of the impacts of BC in snow on different snow properties. Furthermore, limitations of the snow model Crocus in simulating BC concentrations in the Arctic are discussed. Overall, the snow model Crocus is a valuable tool to understand processes and effects related to BC in snow.

9.1 Introduction

Black carbon (BC) is assumed to be a driving factor behind rapid Arctic climate change. BC is the atmospheric aerosol that most efficiently absorbs sunlight (Flanner et al., 2007; Bond et al., 2013; AMAP, 2015). BC is produced by incomplete combustion and originates from natural sources such as forest fires, but also from anthropogenic sources such as diesel engines and industry (Warren, 1984; Bond et al., 2013; Thomas et al., 2017). From the atmosphere, BC is deposited on the snow surface via wet and dry deposition and incorporated into the snowpack (Bond et al., 2013). Wet deposition refers to the deposition of particles during precipitation and dry deposition takes place due to gravity processes (World Meteorological Organization, 2019).

The presence of BC in snow causes positive albedo feedbacks: BC reduces the surface snow albedo, which results in more absorption of sunlight and thus warming of the snowpack, the underlying layers and the near surface air. This leads to additional melting. During melting BC accumulates at the surface as BC is hydrophobic and only a small fraction of BC particles is transported through the snowpack with meltwater or rain. Thus, melt redistribution of BC is low (Flanner et al., 2007; Doherty et al., 2013; Bertò et al., 2021). In addition, the BC concentration at the surface increases even more due to enhanced sublimation caused by the warming of the upper snow induced by the additional absorption by BC particles and associated feedbacks. Melting accelerates metamorphism, and thus the growth of snow grains, i.e., snow grain size increases. Thereby, albedo reduction due to BC particles is more efficient in coarse-grained than in fine-grained snow (Warren, 1984; Flanner et al., 2007; Bond et al., 2013; Doherty et al., 2013; Tedesco et al., 2016). Thus, the snow properties are affected by the initial snow albedo reduction caused by BC and by a cascade of adjoined feedbacks, which results in higher radiative forcing than the initial albedo effect of BC alone. These rapid adjustments after the initial snow albedo decrease are responsible for a substantial part of the large climate impact of BC in snow. The overall snow effective forcing due to BC is estimated to be +0.08 [0.00 to 0.18] W m^{-2}, whereby uncertainties are high (Bond et al., 2013; Lin et al., 2014; Arias et al., 2021).

Consequently, it is of great importance to be able to quantify the concentration of BC in the snowpack as well as its scavenging ratio and post-depositional effects (Gogoi et al., 2018). In addition, an increase in forest fires (burned area and fire intensity) as projected (Flannigan et al., 2000; Abatzoglou et al., 2021; Canadell et al., 2021) could result in higher deposition rates of BC. Furthermore, due to the reduction of sea ice extent in the Arctic, new shipping routes will bring more ships into the Arctic and will likely enhance BC concentrations in Arctic snow. Simulations for West-Greenland show that local shipping (without fishery) caused 6 % - 8 % of deposited BC in 2004 and may increase to 10 % - 15 % by 2050 (Browse et al., 2013). Accordingly, knowledge about BC emissions, their origin, pathways and concentrations in the snowpack are crucial for making reliable predictions of the future climate (Thomas et al., 2017).

In general, median BC concentrations in dry snow increase in west Arctic from north to south from ~5 ng g^{-1} to ~10 ng g^{-1} and from ~8 ng g^{-1} in Alaska/Canada to 14 ng g^{-1} for sub-Arctic Canada. BC concentrations in the east Arctic (Tromsø, Norway, Russia) are about twice as high as for the Canadian Arctic located on the same latitude. For Greenland, a median BC concentration of 3 ng g^{-1} was found (Doherty et al., 2010).

However, most analyses for Greenland were conducted at the Greenland ice sheet. On the Greenland ice sheet snow is present year-round for most areas (Doherty et al., 2010; Polashenski et al., 2015; Tedesco et al., 2016). Furthermore, the ice sheet is located at an altitude of ~2600 m a.s.l., representing BC concentrations from the free troposphere with “the cleanest snow of the Arctic” (Doherty et al., 2010). In-situ measurements of BC concentrations in snow in Greenland are rare and long and homogenious time series are missing. Therefore, it is difficult to calculate any trends (Tedesco et al., 2016).

Additionally, there is a lack of knowledge on BC deposition (Sinha et al., 2018; Mori et al., 2020). For example, there are rarely field data allowing to estimate the amount of dry deposition on snow (Bertò et al., 2021). However, it is generally agreed that wet deposition is the predominant form of deposition for BC (e.g.,Flanner et al., 2007; Sinha et al., 2018; Yang et al., 2019; Mori et al., 2020)

Scenario calculations show a further decrease of the surface albedo of the entire Greenland ice sheet of about 0.08 from 2000 to 2100, whereby BC and other light absorbing impurities are not included in the simulations and melting and thus grain size growth is likely underestimated in the model (Tedesco et al., 2016). Thus, also impacts of enhanced BC concentrations in Greenlandic snow on the surface snow albedo are of great importance to predict reliably future surface snow albedo and climate warming.

First, I present vertical BC profiles in snow from 3 April 2018 as well as measurements of BC concentrations in surface snow from 21 March to 3 April 2018 for Villum Research Station (VRS), located close to the coast in northeast Greenland. Second, I present simulations with the detailed snow model Crocus to study the impact of BC on snow properties. I used inverse modelling to estimate the unknown BC deposition rates that fit best the measurements of BC concentration. With these analyses, I aim to answer the following research questions

(1) How high were the longterm mean BC deposition rates consistent with the spring 2018 BC concentrations at VRS, northeast Greenland?

(2) What are impacts of different BC deposition rates on snow properties and surface albedo?

In general, BC particles found in the vicinity of VRS typically do not originate from local sources, but are transported over long distances (Donth et al., 2020). The frequency of fires norths of 50°N begins to increase from March onwards. This suggests that open biomass burning occurring around 45°N – 60°N causes the increase in atmospheric BC concentrations in Arctic spring (Ohata et al., 2021). However, Ohata et al. (2021) suspected that atmospheric BC particles observed during the PAMARCMiP (Polar Airborne Measurements and Arctic Regional Climate Model Simulation Project) campaign originated mainly from anthropogenic sources (82 % – 98 %). Also other studies found that BC particles deposited in Greenland originates, e.g., from forest fires in Canada and that biomass burning seems to be the main source of BC particles in spring, whereas pollution seems to be the main source of BC particles during summer (Doherty et al., 2010; Thomas et al., 2017).

9.2 Data and methods

9.2.1 Black carbon (BC) sampling and physical snow measurements

Snow samples and physical measurements were taken 2018 during the PAMARCMiP field campaign at VRS (81°34’ N, 16°38’ W) nearby the military base Station Nord. A small team operates Station Nord all year-round. VRS can be reached only by small planes from Longyearbyen, Svalbard, or with a military aircraft directly from Denmark. The station is only used for research purposes. The site is far away from the next towns (Longyearbyen, Svalbard: 720 km east; Ittoqqortoormiit, Greenland: 1250 km south). Thus, the station is the only local source for BC particles and the surrounding area is rather “clean” due to missing industrial and shipping activity.

I used vertical snow profiles taken close to VRS on 3 April 2018 that had been sampled for BC concentration every 10 cm and 24 surface snow samples taken between 21 March and 3 April 2018 together with physical measurements of the snowpack, like snow density and snow specific surface area (SSA) (see Krampe et al. (2021) and Chapter 6 herein for more details). The snowpits were located facing upwind (prevailing wind direction south-west) from the stations. Figure 9.1 shows a sample site and its surrounding.

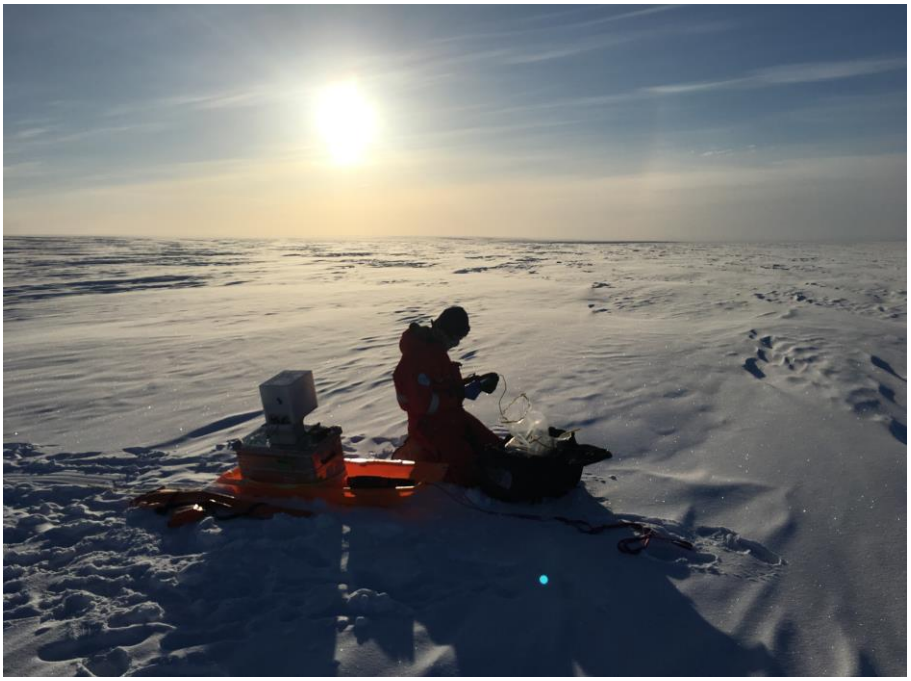

Figure 9.1: A photo of the snow sampling site close to Villum Research Station, northeast Greenland, spring 2018 (Photo: Andreas Herber).

Surface snow samples contain snow from the first 3 cm of the snowpack. Snow samples were collected with 50 mL volume in polypropylene vials and stored frozen at -20°C until they were analysed in the laboratory. A 50 mL snow sample typically corresponds to 20 g to 30 g water content (Zanatta et al., 2021). Figure 9.2 shows a photo of taking a surface snow sample.

Figure 9.2: Sampling of surface snow for later analysis of black carbon (BC) concentration during PAMARCMiP (Polar Airborne Measurements and Arctic Regional Climate Model Simulation Project) 2018 (Photo: Andreas Herber).

The snow samples were analysed in the laboratory of the Alfred Wegener Institute to determine the refractory black carbon (rBC; refers to the applied measurement technique of laser-induced incandescence) content with the single particle soot photometer (SP2, Droplet Measurement Technologies, Lonmont, USA). The detailed methods for measuring BC concentration with the SP2 are described, e.g., by Schwarz et al. (2010), Lim et al. (2014) and in Chapter 4.5. In brief, samples were injected at a constant flow rate into a nebulizer (Marine-5, Teledyne Technologies, Omaha, NE, USA) directly after the snow samples were melted. From here, the samples went into a SP2 where they were heated by a laser until evaporation temperature was reached and the light absorption was measured giving the BC mass concentration and size distribution.

Further information about the study site, atmospheric reanalyses and atmospheric in-situ measurements and the performance of the snow model Crocus in simulating prevailing snow conditions can be found in Krampe et al. (2021) and in Chapter 6, Chapter 7 and Chapter 8.

Incoming and outgoing shortwave radiation was measured using a Kipp & Zonen CNR4 device (Kipp & Zonen). Daily surface albedo was calculated from the ratio between incoming and outgoing radiation from daily sums. This allows to circumvent the issue of low radiation conditions by weighting maximum radiation more than low radiation (Stroeve et al., 2013; Carmagnola et al., 2014). As the measurement area is located on a relatively flat terrain (Figure 4.7), possible slope effects as proposed in Picard et al. (2020) were not taken into account. When the solar zenith angle is high, the accuracy of measured radiation declines substantially (Kipp & Zonen). Thus, albedo measurements in the Arctic are of limited use when the sun is close to the horizon. For comparison of measured and simulated albedo, I distinguish between measurements taken during solar zenith angles larger or smaller 70° as proposed by Stroeve et al. (1997). See Figure E.2 (in the Appendix) for the daily zenith angle for the position of the atmospheric in-situ measurements of VRS.

In addition, during a flight campaign of PAMARCMiP, atmospheric vertical profiles of BC concentration were measured in the surrounding of VRS (Donth et al., 2020; Ohata et al., 2021). Thereby, median concentrations from 7 ng m^{-3} to 18 ng m^{-3} were measured below 4.5 km altitude but at altitudes of about 5 km concentrations of up to 250 ng m^{-3} were detected (Ohata et al., 2021).

9.2.2 Model set-up and simulations

I used the detailed snow model Crocus to simulate the impacts of BC on snow properties, analyse the sensitivity of the model to different BC deposition rates and I used inverse modelling to estimate the unknown deposition rates, assumed to be constant over time, that fits best to the field measurements. Details of the model and its performance for simulating Arctic snow conditions are described, e.g. by Brun et al. (1992), Vionnet et al. (2012), Barrere et al. (2017), Tuzet et al. (2017) and in Chapter 6 to Chapter 8.

To drive the snow model, I used the reanalyses CARRA-West (Copernicus Arctic Regional Reanalysis; hereafter CARRA). I used the model configuration described in Krampe et al. (2021) and Chapter 8 adapted for Arctic conditions by using the introduced new snow density parameterisation CARRA-K22gf1.3. This simulation is hereafter denoted as CARRA-BC. I chose this parameterisation as the performance of Crocus is considerably improved and snow depth overestimation at the end of 2018 is lower than using CARRA-K22gf1.6, although that setup performed best when considering the entire time period, where snow depth was observed (see Chapter 8 for details).

The direct and indirect radiative impacts of BC in snow are implemented in the model using the two-stream analytical radiative transfer in snow model TARTES (Libois et al., 2013). The model is able to account for amplification of BC in surface snow when melting occurs. For this purpose, a scavenging efficiency can be given. Details about the implementation of BC radiative effects can be found in Tuzet et al. (2017) and in Chapter 5.

Simulations were performed for September 2014 to August 2018 after a spin-up time of more than 14 years. Simulations used constant dry and wet deposition rates for BC. As no measured BC deposition rates were available, the rates were approximated by inverse modelling: the deposition rates of BC were varied until a good fit to measured vertical BC concentrations during the PAMARCMiP campaign was found. An overview about the conducted simulations and corresponding deposition rates are given in Table 9.1.

In addition, simulations with different scavenging efficiency were performed. Thereby, a scavenging efficiency of 0 corresponds to no redistribution of BC due to meltwater and all BC remains at the surface. This set up consequently results in an overestimation of melt. According to Doherty et al. (2013) scavenging efficiencies are in the range of 10 – 30 %. Table 9.1 gives an overview about the conducted simulations.

Table 9.1: Overview of all conducted model simulations to backtrack prevailing black carbon deposition rates.

Name of simulation (acronym)	Deposition rate wet/dry [g m^{-2} s^{-1}]		Scavenging rate [%]
CARRA-BC	6.67 x 10^{-11}	3.33 x 10^{-11}	0
CARRA-BC8	8.33 x 10^{-12}	4.17 x 10^{-12}	0
CARRA-BC9	7.41 x 10^{-12}	3.70 x 10^{-12}	0
CARRA-BC10	6.67 x 10^{-12}	3.33 x 10^{-12}	0
CARRA-BC11	6.06 x 10^{-12}	3.03 x 10^{-12}	0
CARRA-BC12	5.56 x 10^{-12}	2.78 x 10^{-12}	0
CARRA-BC13	5.13 x 10^{-12}	2.56 x 10^{-12}	0
CARRA-BC13sca10	5.13 x 10^{-12}	2.56 x 10^{-12}	10
CARRA-BC13 sca20	5.13 x 10^{-12}	2.56 x 10^{-12}	20
CARRA-BC13 sca30	5.13 x 10^{-12}	2.56 x 10^{-12}	30
CARRA-BC14	4.76 x 10^{-12}	2.38 x 10^{-12}	0
CARRA-BC15	4.44 x 10^{-12}	2.22 x 10^{-12}	0
CARRA-BC20	3.33 x 10^{-12}	1.67 x 10^{-12}	0

Based on the results of the inverse modelling of BC deposition rates, different setups mimicking different air pollution scenarios were tested by increasing the “optimal” BC deposition rate. I increased deposition by multiplying deposition rates with a constant to investigate the impact of increasing BC deposition rates on snow albedo and related snow properties. The simulations used for this analysis are presented in Table 9.2.

Table 9.2: Overview of all conducted model simulations to mimic the effects of increasing BC deposition rates. The factor x by which the deposition rates of the CARRA-BC13 simulation described in Table 9.1 are multiplied is written as part of the acronym (e.g., CARRA-BC13-2: deposition rates of CARRA-BC13 multiplied by 2).

Name of simulation (acronym)	Deposition rate wet/dry [g/m2/s]	
CARRA-BCno	0	0
CARRA-BC13	5.13 x 10^{-12}	2.56 x 10^{-12}
CARRA-BC13-2	1.03 x 10^{-11}	5.13 x 10^{-12}
CARRA-BC13-5	2.56 x 10^{-11}	1.28 x 10^{-11}
CARRA-BC13-10	5.13 x 10^{-11}	2.56 x 10^{-11}
CARRA-BC13-20	1.03 x 10^{-10}	5.13 x 10^{-11}
CARRA-BC13-50	2.56 x 10^{-10}	1.28 x 10^{-10}
CARRA-BC13-100	5.13 x 10^{-10}	2.56 x 10^{-10}

9.2.3 Statistical metrics used to evaluate the model performance

A cost function is used to quantify the fit of simulated BC concentrations to measured BC concentrations. This is a common method to determine the model-data misfit (Koldunov et al., 2017; Sumata et al., 2019; Zampieri et al., 2021). Thereby, the cost function $J\ (x)$ given by

$$J(x) = 1/2 \sum_{i=0}^{n} \frac{(m\ (x_i) - d_i)^2}{\sigma_i^2} \tag{9.1}$$

where $m\ (x_i)$ denotes the simulated concentration, d_i the measured (expected) concentration, σ_i the standard deviation and n the number of points to compare. If the quotient of the sum is smaller than one, the simulations are within the measurement uncertainty. The advantage of this metric is that it takes observation uncertainty into account. A disadvantage is that the cost function is not easy to interpret. Therefore, I used the mean difference in sigma units to rate the performance of the simulations. The mean difference in sigma units is calculated as

$$\overline{\left(\frac{m-d}{\sigma}\right)} = \sqrt{\frac{2}{n}\ J(x)} \tag{9.2}$$

The simulations are adequate if the "bulk" of simulated data are within the measurement uncertainty meaning that the mean difference in sigma units is ≤1. Other metrics used to quantify model performance was the mean bias (simulation – measurement) and the root mean square deviation (RMSD).

9.3 Results

9.3.1 In-situ measured surface snow measurements (21 March 2018 to 3 April 2018)

Figure 9.3 presents the results of the snow surface measurements taken from 21 March to 3 April and Table 9.3 provides a summary (mean, standard deviation, maximum and minimum) of the measurements. To analyse these results prevailing atmospheric conditions during this period are visualised in Figure 9.4.

SSA

Surface SSA was highest at the beginning of the observation period on 22 March due to newly fallen snow (about 60 $m^2\ kg^{-1}$). Overall, SSA decreased thereafter. Snow metamorphism could be a reason for this decrease. However, snowfall was measured on all days except 23 March and 1 April, which potentially increased the SSA. Thereby, the highest snowfall recorded was on 27 March (5.4 mm). In CARRA, snowfall occurred on all days except 2 April and 3 April. Thereby, maximum snowfall was on 22 March (4.3 mm).

Temperature

Another process leading to the decline of SSA is melting. However, snow surface temperatures and air temperatures stayed well below the melting point during the period under consideration. Mean snow surface temperatures on the measurement days were -28.6°C (standard deviation: 4.1°C) with minimum values of -38.4°C (29 March) and maximum values of -18.8°C (3 April). Furthermore, daily mean measured air temperature was -30.0°C (standard deviation 2.2°C) with maximum temperature of -28.0°C (30 March) and minimum temperature of -34.1°C (28 March). CARRA daily mean air temperature was -27.5°C (standard deviation: 2.2°C) with a minimum daily air temperature of -31.1°C (28 March) and a maximum daily air temperature of -23.1°C (21 March).

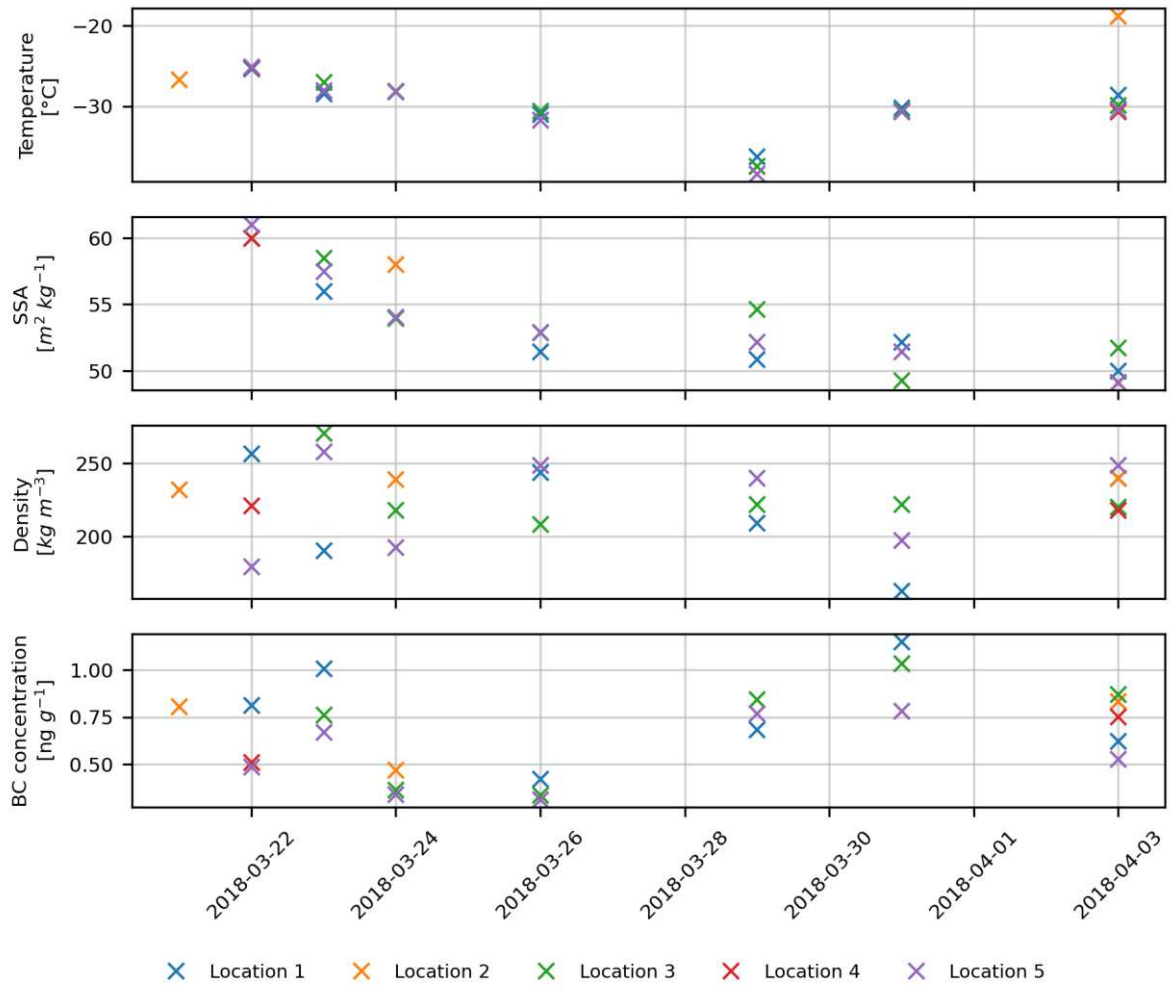

Figure 9.3: Surface snow measurements of temperature, specific surface area (SSA), density and black carbon (BC) concentration during PAMARCMiP (Polar Airborne Measurements and Arctic Regional Climate Model Simulation Project) campaign (21 March 2018 to 3 April 2018) at five different locations.

Table 9.3: Overview of snow surface measurements: Mean, standard deviation, maximum and minimum. The sample period is 21 March 2018 to 3 April 2018.

Variable	Mean	Standard deviation	Maximum	Minimum
BC mass concentration	0.67 ng g^{-1}	0.23 ng g^{-1}	1.15 ng g^{-1} 31 March 2018 Location 1	0.31 ng g^{-1} 26 March 2018 Location 5
Specific surface area	53.7 m^2 kg^{-1}	3.8 m^2 kg^{-1}	61.0 m^2 kg^{-1} 22 March 2018 Location 5	49.1 m^2 kg^{-1} 3 April 2018 Location 2, 4, 5
Density	224.2 kg m^{-3}	26.6 kg m^{-3}	270.8 kg m^{-3} 23 March 2018 Location 3	162.7 kg m^{-3} 31 March 2018 Location 1
Temperature	-29.4°C	4.1°C	-18.8°C 3 April 2018 Location 2	-38.4°C 29 March 2018 Location 5

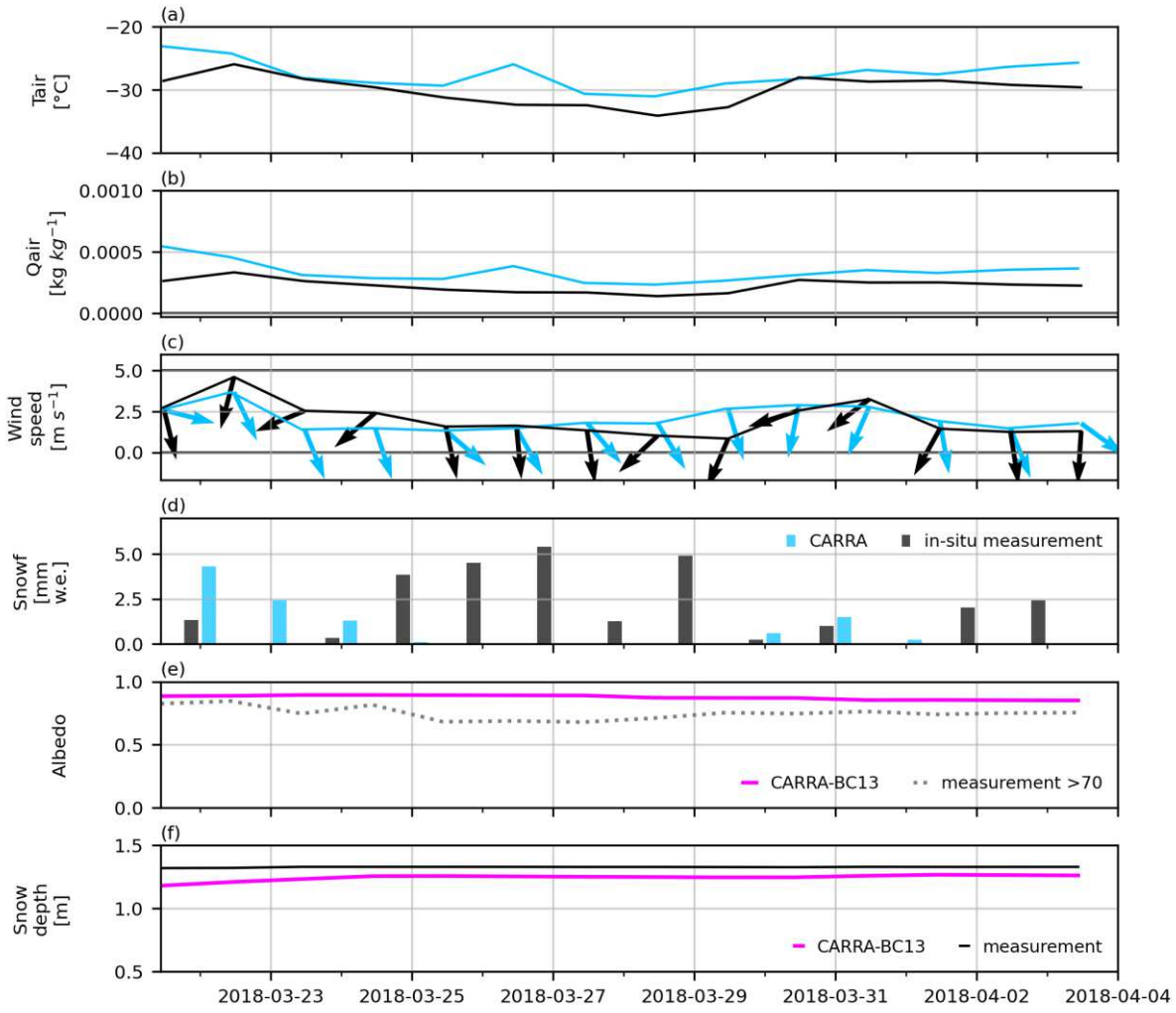

Figure 9.4: Daily in-situ measurements and CARRA atmospheric conditions during the surface snow measurements of PAMARCMiP (Polar Airborne Measurements and Arctic Regional Climate Model Simulation Project) campaign (21 March 2018 – 4 April 2018). (a) air temperatures, (b) specific humidity, (c) wind speed and wind direction shown by the arrows, (d) snowfall, (e) measured and simulated albedo taken from CARRA-BC13, and (f) simulated snow depth taken from CARRA-BC13 in addition to the measurements. Note that the measured albedo for zenith angles above 70°C is subject to high uncertainties and simulated surface albedo is plotted at midday for CARRA-BC13.

Density

Overall, surface snow density was stable over the period but showed spatial variability. Several snowfall events might be the reason why the snow density almost did not change. However, the density was rather high for newly fallen snow. I suspect that the prevailing cold air temperatures, together with high wind speeds (see below) led to the formation of snow layers with high densities.

Wind speed

Daily maximum measured wind speed was 4.6 m s^{-1} (22 March) and mean daily wind speed was 2.0 m s^{-1} (standard deviation 1.0 m s^{-1}). Maximum daily wind speed of CARRA was 3.7 m s^{-1} (22 March) and mean daily wind speed was 2.1 m s^{-1} (standard deviation: 0.7 m s^{-1}). Thus, daily mean wind speed did not reach the wind drift threshold of about 5 m s^{-1} during this period.

However, hourly maximum measured wind speed was 7.5 m s^{-1} (22 March) and the occurrence of wind drift was documented during the campaign at that day. Altogether, there had been 16 hours when wind speed exceeded 5 m s^{-1}, during the campaign of which 11 hours occurred on 22 March. CARRA's wind speed was generally lower. Three hourly wind speed of CARRA had a maximum at 5.9 m s^{-1} (22 March). There were 9 hours where wind speed exceeded 5 m s^{-1} (22 March).

BC concentration

Surface snow BC concentrations were generally low, presumably due to relative low atmospheric BC concentration and low deposition rates. Dry deposition played a minor role in the snow samples, as several new snow events resulted in layers of new snow that masked a possible accumulation of BC by dry deposition. Mean BC concentration of all 24 samples was 0.67 ng g^{-1} (standard deviation: 0.23 ng g^{-1}) with a minimum concentration of 0.31 ng g^{-1} (26 March, location 5) and a maximum concentration of 1.15 ng g^{-1} (31 March, location 1). The surface snow median BC concentration was 0.72 ng g^{-1}.

BC surface snow concentrations decreased after 23 March and increased again after 26 March. The higher surface BC concentrations at location 1 on 23 March could be due to snowdrift, which led to snow redistribution and enhanced sublimation, both possible causes of higher concentrations at the snow surface. Afterwards, wind speeds were low. The shift from higher to lower concentrations after 23 March coincided with a shift of the wind direction from southward to south-westward. Neither in-situ measurements nor CARRA showed any rainfall or melting during this period. Therefore, during the campaign there was no scavenging of surface BC particles by meltwater or rain and thus, no accumulation of BC at the surface due to such events. Changes in wind direction bring air masses from different source regions, which may be cleaner or more polluted, leading to different BC concentrations (see Figure E.3 in the Appendix). Overall, BC concentration seemed to follow the wind pattern with higher surface concentrations occurring at higher wind speeds caused by snow redistribution, and changes in concentration with changes in wind direction.

Surface snow albedo

The dependence of albedo on variations in surface snow BC was low during the surface measurements period due to the low BC quantity and the associated small differences in BC concentration. However, the measurements were taken (about three months) before the melting season and thus before BC accumulated on the snow surface. During the melting season, the impact of BC in the upper snow layers might have a more pronounced impact on snow albedo.

9.3.2 Black carbon observations: Profile 3 April 2018

BC concentrations in vertical snow profiles taken at five locations on 3 April 2018 are shown in Figure 9.5 (Figure E.1 in the Appendix shows the vertical measured BC concentration for the individual profiles). All measurements have been sampled in a radius of <200 m. Snow depths varied between the different locations. Therefore, results for the vertical profile are normalised and plotted relative to the fraction of total snow depth within a given profile.

The gross vertical BC pattern showed an increase in mean BC concentration from 0.63±19 ng g^{-1} at the snow-air interface to 1.55±1.86 ng g^{-1} at the base of the snowpack. The median concentrations of the profiles ranged between 0.42 ng g^{-1} and 1.11 ng g^{-1}. Over the entire vertical snow profile, the maximum concentration was 3.70 ng g^{-1}, measured 10 cm above the ground at location 4. The lowest concentration was 0.27 ng g^{-1} from a sample 30 cm above the ground at location 2.

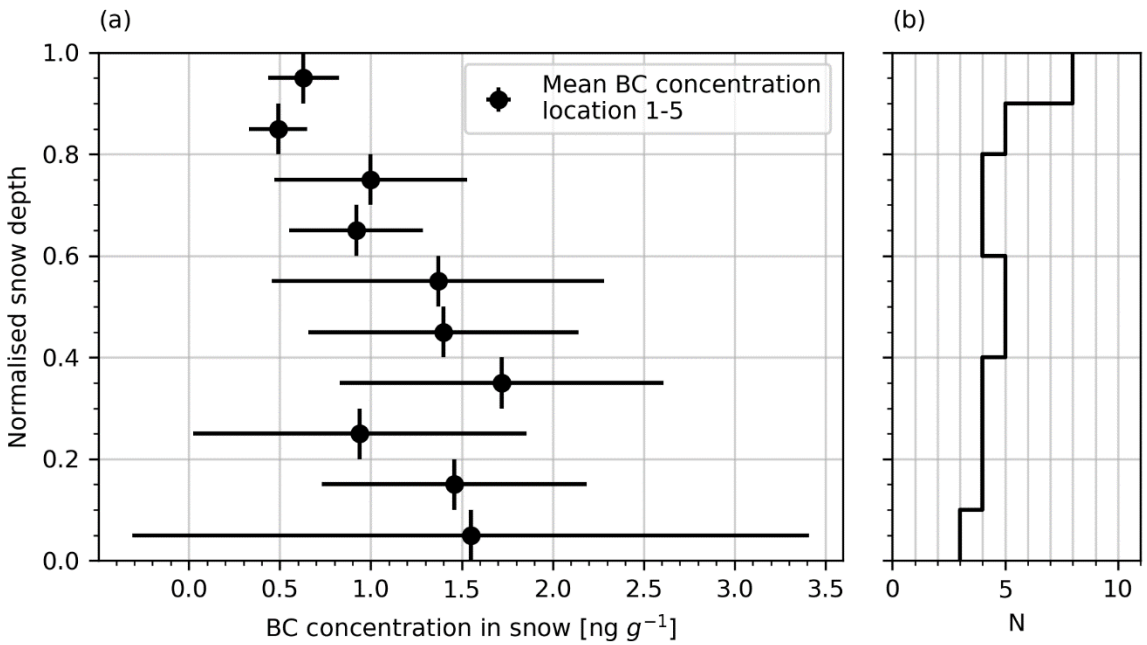

Figure 9.5: (a) Vertical profile of observed black carbon (BC) concentration in snow on 3 April 2018. Visualised is the mean concentration and the standard deviation of five different measurement locations. (b) shows the sample frequency of BC concentration measurements.

No melting and thus only accumulation due to dry deposition at the snow surface and no scavenging of BC particles were observed in the entire snowpack on 3 April, which explains the lower concentrations in the upper snow pack. On 3 April, the vertical snow temperatures ranged between -10.2°C and -30°C (mean: -21.5°C). Thereby, temperatures increased from the surface to the bottom of the snowpack. In addition, measured air temperatures (Figure 9.4) as well as the measured snow surface temperatures (Figure 9.3) in the days before the measurements confirm that there was no melting within the snowpack between 21 March and 3 April. There were several small snowfall events but with probably low wet deposition rates.

The higher concentrations in the underlying snow layers were the results of earlier events. For instance, freezing rain fell on 25 March 2018 (0.91 mm). After this event, there had been no rain on snow event before sampling took place anymore. Furthermore, a warm air intrusion event accompanied by exceptionally strong north-westward winds end of February (Moore et al., 2018; Ludwig et al., 2019; Chapter 6) possibly caused melting (hourly air temperature above 0°C) and enhanced sublimation. These events are possible reasons for the increase in BC concentration with depth.

I suspect as well that these events led to scavenging and accumulation of BC on the snow surface. Also, higher temperatures and associated melting together with rain on snow events at the beginning of the snow season could have led to an accumulation of BC and scavenging on the former snow surface, which resides later in larger depth. Furthermore, changes in wind direction probably caused differences in deposition rates leading to different BC concentrations in the snowlayers like the warm air intrusion event end of February that brought air masses from the south-east into the region. This would explain the high BC concentrations near the ground.

The inter-profile variability of BC concentration of the five different measurement locations increased with depth. In the lower layers BC concentrations ranged from 0.47 ng g^{-1} to 3.70 ng g^{-1}, while the upper layers had concentrations between 0.35 ng g^{-1} and 0.87 ng g^{-1}. Post-depositional processes including snow redistribution possibly caused these differences in snow concentrations for the various locations.

9.3.3 Simulated surface snow BC concentration

Simulated BC concentrations at the surface of CARRA-BC between 21 March and 3 April 2018 failed to reach the measurement range most of the time (Figure 9.6 (a)). Instead, the BC concentrations at the surface (upper ~3 cm) were overestimated by an order of magnitude. Note that for all simulations conducted within this study constant deposition rates were used.

Simulated BC surface concentration using reduced BC deposition rates were in the range of measured BC surface concentrations (Figure 9.6 (b)). Here, simulations with different simulation rates were close to each other from 21 March to 24 March. From 25 March to 29 March, simulated surface BC concentration increased with different slopes so that the range of simulated BC concentrations with different deposition rates on 29 March was much wider than before. From 29 March to 31 March, concentration decreased again and the simulated range narrowed again. From 31 March onwards, concentrations increased again and the simulated range of BC concentrations with different deposition rates became larger.

During the increase in BC concentration at the snow surface between 25 March and 29 March, there was no snowfall in CARRA. Thus, no new snow with a low, constant BC concentration was deposited and covered the old snow. Instead, the BC concentration increased due to the constant amount of dry deposition added to the BC already present in the surface snow. Afterwards, simulated BC concentration in surface snow decreased again due to the snowfall on 30 March to 1 April, before the dry deposition without snowfall led to accumulation.

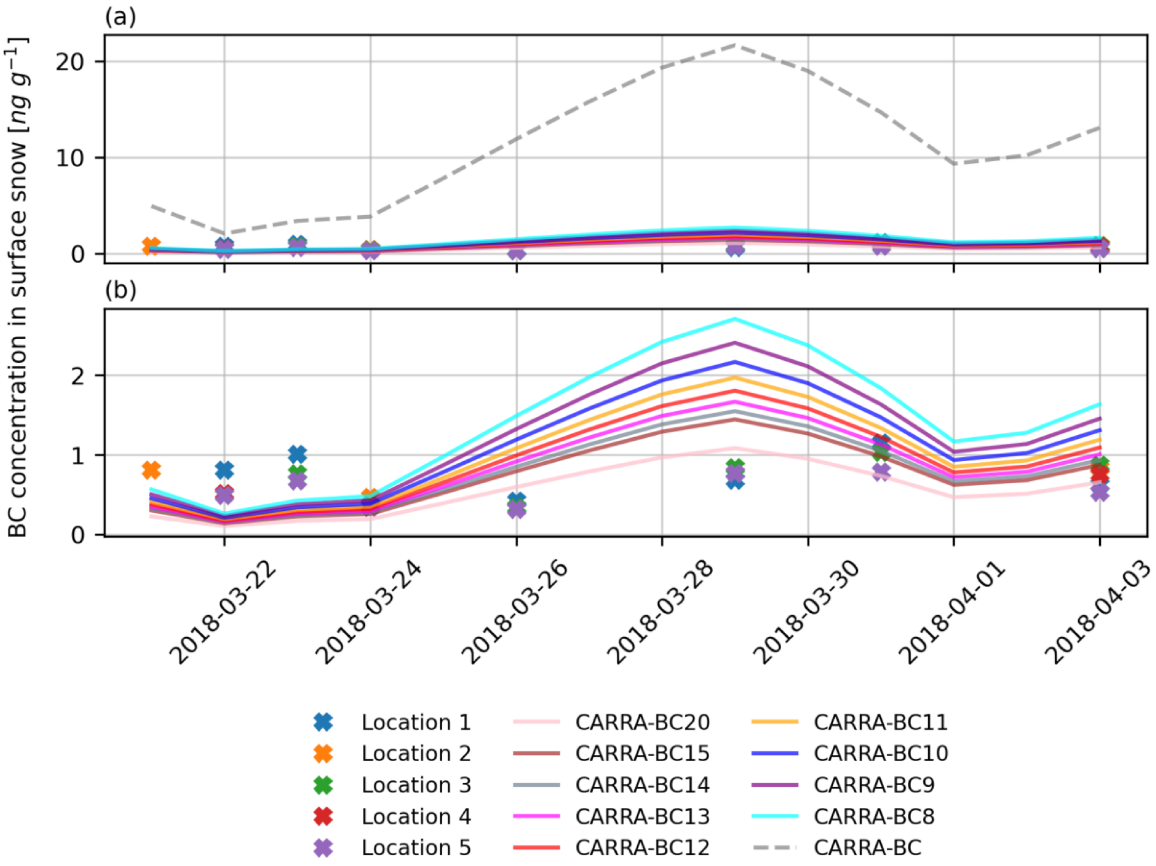

Figure 9.6: Simulated and measured black carbon (BC) concentration in surface snow (3 cm) from 21 March 2018 to 3 April 2018. Measurements were taken at five different locations denoted as Location 1 to Location 5. (a) includes all simulations (b) is a zoom in of (a) and does not show CARRA-BC.

CARRA-BC had a poor mean difference in sigma units of 188.10 (see Eq. (9.2) and Table 9.5), i.e. the BC concentration in the simulation was far outside the observational range. Note, that the mean difference in sigma units should be <1 for a "perfect" simulation – then all simulated BC concentration would be inside of the measurement uncertainty range. However, this is very unlikely to be reached for any simulation given the imperfections in the process formulations of the model and because of the unknown deposition rates, which are assumed to be constant in time. Reducing the BC deposition rate by one order of magnitude gave a much better result of 12.53, but still far from the desired value around one. Of all the simulations carried out, the simulated surface concentration of CARRA-BC20 achieved the highest agreement with the measurements with a mean difference in sigma of 4.30. Of course, there might be simulations (e.g., CARRA-BC30) that fit much better but were not conducted during this study for reasons that will become clear below.

Figure 9.6 shows that all simulations (except CARRA-BC) were close to the measurements as long as new snowfall occurred. During the time when there was no new snowfall, the surface concentrations of all simulations increased strongly. Here, the simulation with the lowest dry deposition rate had the smallest increase in simulated BC surface concentration and the highest agreement with the measurements. A slight increase in the BC concentration at the surface was also visible in the measurements during this period, but the increase in measurements continued until 31 March, while the simulations decreased again from 29 March on. Furthermore, there was no new snowfall during the increase in the CARRA-simulations, while the measurements showed snowfall.

During PAMARCMiP, there was no rain on snow event or melting. Therefore, using a scavenging rate of 10 %, 20 % and 30 % for the CARRA-BC13 simulation resulted in almost identical BC surface concentrations during PAMARCMiP with changes in the order of 10^{-4} ng g^{-1} or smaller.

Table 9.4: Metrics for different black carbon (BC) snow surface concentration simulations compared to measurements (22 March 2018 – 3 April 2018). Mean bias (simulated BC concentration - measured BC concentration), RMSD: root mean square difference. The values showing the highest and the lowest agreements between simulations and measurements are highlighted in bold.

Name of simulation (acronym)	Mean bias [ng g^{-1}]	RMSD [ng g^{-1}]	J(x) [-]	Mean difference in sigma units [-]
CARRA-BC	**9.41**	**11.52**	**123834.60**	**188.10**
CARRA-BC20	-0.16	**0.37**	**64.67**	**4.30**
CARRA-BC15	**0.00**	0.44	151.92	6.59
CARRA-BC14	0.05	0.45	190.52	7.38
CARRA-BC13	0.11	0.50	242.60	8.33
CARRA-BC12	0.17	0.55	313.60	9.47
CARRA-BC11	0.25	0.63	411.70	10.85
CARRA-BC10	0.34	0.72	549.72	12.53
CARRA-BC9	0.45	0.84	748.51	14.62
CARRA-BC8	0.59	0.99	1043.51	17.27

9.3.4 Black carbon simulation: Profile 3 April 2018

BC concentrations of the vertical snow profile were considerably overestimated in the CARRA-BC simulation for most parts of the profile (Figure 9.7 (a)), with a mean bias of 4.79 ng g^{-1}. However, for the lower snowpack (0 to 0.2 normalised snow depth), the BC concentrations simulated with CARRA-BC and measured BC concentrations agreed well with a bias of -0.08 ng g^{-1} and -0.61 ng g^{-1},

respectively, while the maximum bias was 13.17 ng g^{-1} at 0.7 – 0.8 normalised snow depth. Overall, the simulated vertical BC concentrations for CARRA-BC on 3 April 2018 were far off from the measurement uncertainties, as the mean difference in sigma units was 30.76.

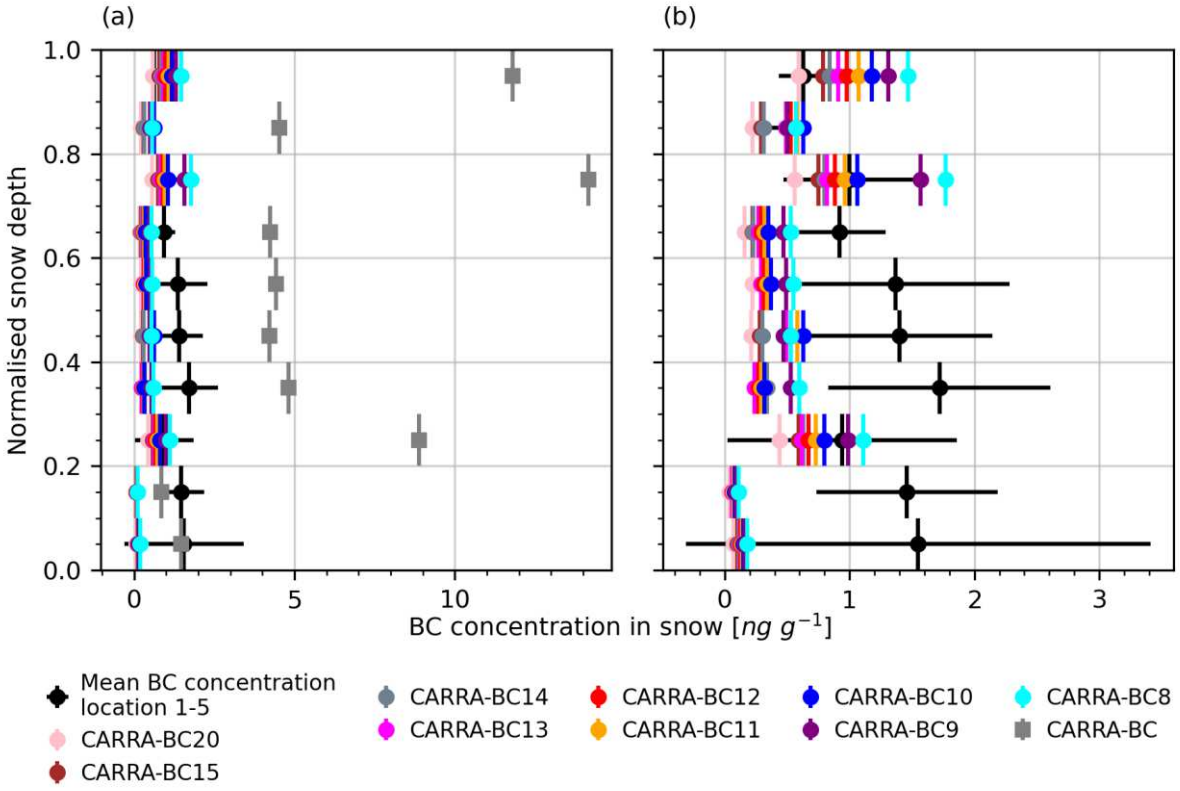

Figure 9.7: Simulated and measured black carbon (BC) concentration in the vertical profile on 3 April 2018 using different BC deposition rates described in Chapter 9.2.2. Vertical lines represent the normalised snow depth range where simulations and measurements had been averaged and black horizontal lines represent the sample variability (± one standard deviation). (a) includes all simulations (b) is a zoom in of (a) and does not show CARRA-BC.

The simulations performed with lower BC deposition rates than CARRA-BC all showed a negative mean bias (simulated BC concentration - measured BC concentration). The lower the deposition rates the larger the amount of the bias (CARRA-BC8: -0.41 ng g^{-1} to CARRA-BC20: -0.87 ng g^{-1}, Table 9.5). However, when considering the measurement uncertainties by calculating the cost function, it turned out that CARRA-BC13 agreed best with the measurements (Figure 9.7). CARRA-BC13 had a mean difference in sigma units of 1.75. Changes when using scavenging rates of 10 %, 20 % and 30 % in the CARRA-BC13 simulation for the vertical snow profile of BC concentration on the 3 April 2018 were marginal.

Table 9.5: Metrics for simulated black carbon (BC) concentration simulations varied with deposition rates compared to measurements (vertical profile, 3 April 2018). Mean bias (simulated BC concentration - measured BC concentration), RMSD: root mean square difference. The values showing the highest and the lowest agreements between simulation and measurements are highlighted in bold.

Name of simulation (acronym)	Mean bias [ng g^{-1}]	RMSD [ng g^{-1}]	J(x) [-]	Mean difference in sigma units [-]
CARRA-BC	**4.79**	**6.45**	**4731.69**	**30.76**
CARRA-BC20	-0.87	1.01	19.31	1.97
CARRA-BC15	-0.78	0.96	16.52	1.82
CARRA-BC14	-0.75	0.95	16.25	1.80
CARRA-BC13	-0.72	0.94	**15.27**	**1.75**
CARRA-BC12	-0.68	0.93	15.96	1.79
CARRA-BC11	-0.64	0.91	17.39	1.87
CARRA-BC10	-0.59	0.90	20.01	2.00
CARRA-BC9	-0.59	**0.88**	23.15	2.15
CARRA-BC8	**-0.41**	0.89	29.98	2.45

9.3.5 Simulated effect of enhanced deposition rates

Because CARRA-BC13 fits best the observations of the profile, I selected this simulation as the baseline experiment to study the effect of increased BC deposition rates. Wet and dry BC deposition rates were increased by factors of 2, 5, 10, 20, 50 and 100, respectively. The resulting deposition rates are shown in Table 9.2. The simulated BC concentration in the upper 3 cm for CARRA-BC13 was 3 ng g^{-1}. Increasing deposition rates resulted in an increase of mean surface snow concentration with mean surface concentrations between 7 ng g^{-1} and 231 ng g^{-1} over the entire study period (Table 9.6). Additionally, I performed a simulation without any BC deposition (pure snow).

Table 9.6: Mean surface conditions (upper 3 cm) of BC concentration, snow specific surface area (SSA) and snow density simulated for pure snow (CARRA-BCno), CARRA-BC13, and increased deposition rates as described in Table 9.2 for September 2014 to August 2018.

Name of simulation (acronym)	BC concentration [ng g^{-1}]	SSA [m^2 kg^{-1}]	Density [kg m^{-3}]
CARRA-BCno	0	35.1	168.4
CARRA-BC13	3	35.1	168.0
CARRA-BC13-2	7	35.1	167.9
CARRA-BC13-5	16	35.1	166.4
CARRA-BC13-10	32	35.3	164.8
CARRA-BC13-20	62	36.0	160.2
CARRA-BC13-50	161	36.4	155.1
CARRA-BC13-100	231	36.9	151.2

Increasing the deposition rates not only increased BC content in the snowpack, but changed related snow properties. Figure 9.8 shows the time series of measured and simulated albedo and simulated surface SSA for the CARRA-BC13 simulation. The measured shortwave radiation at high zenith angles is subject to large uncertainties. Therefore, the figure distinguishes between measured albedo at zenith angles above 70° and below. Simulated surface albedo decreased faster and earlier than measured albedo in all years. Furthermore, minimum measured albedo is lower than simulated minimum albedo. The bare ground albedo in the model is set to 0.2 while the measured albedo decreased to about 0.1.

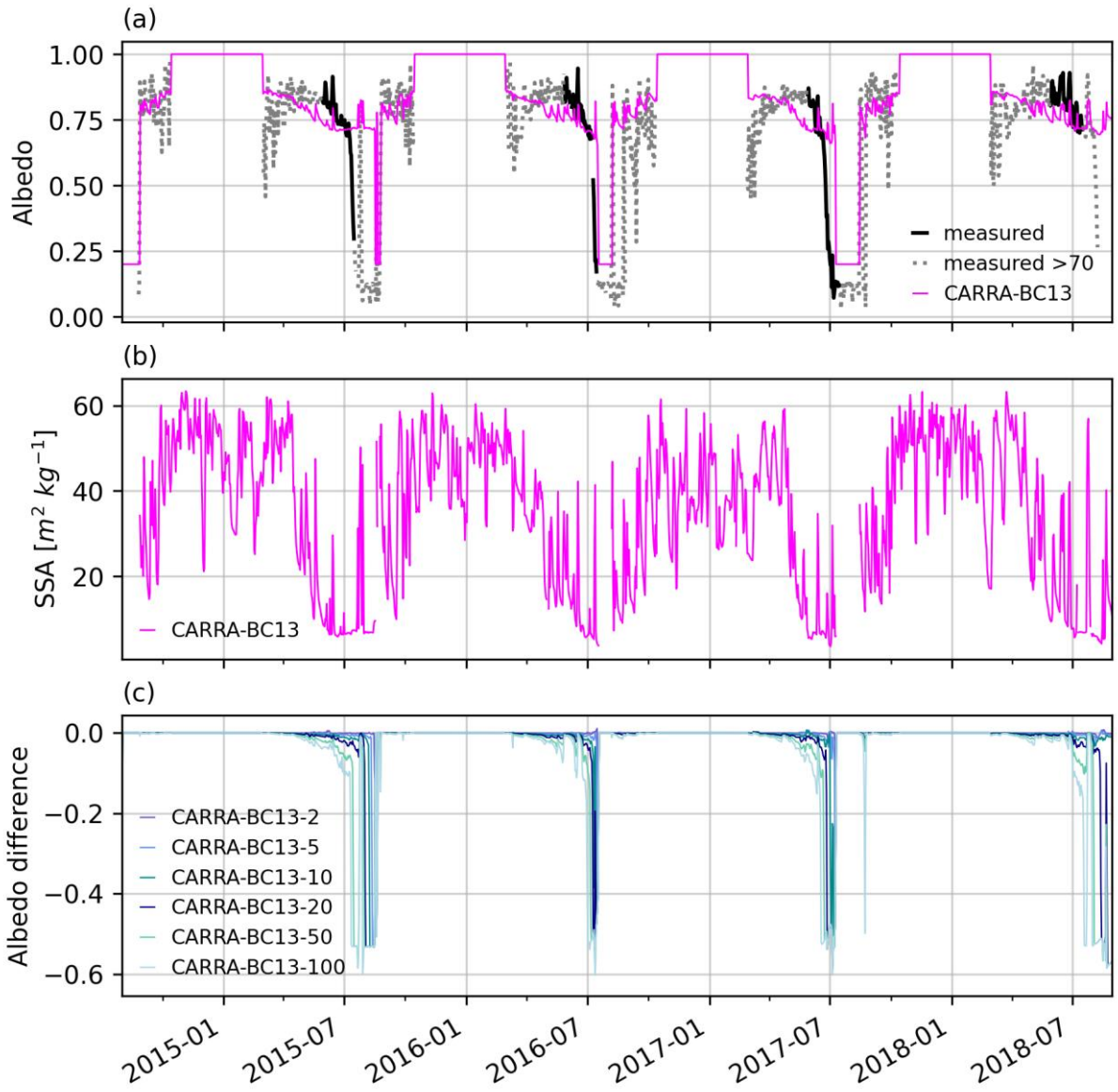

Figure 9.8: (a) Time series of measured and simulated surface albedo from September 2014 to August 2018. Since shortwave radiation measurements at high zenith angle are subject to large uncertainties, measured albedo for zenith angles above 70° are plotted in dashed grey lines. (b) simulated surface snow albedo (upper 3 cm) with CARRA-BC13 (c) time series of anomalies between snow surface albedo of CARRA-BC13 and simulations using enhanced deposition rates as described in Table 9.2 (scenario simulation - CARRA-BC13). Note that for (a) and (b) only the results for CARRA-BC13 are shown. This allows a better comparison between measured and simulated albedo and changes in surface SSA are generally small.

Surface albedo of CARRA-BC13 was on average 0.0012 lower than that of pure snow, with a maximum difference of 0.3966, due to the earlier exposure of bare ground. Increasing the BC deposition rates resulted in a decrease in the surface albedo (Figure 9.8). An increase of deposition rates of CARRA-BC13 by factor 20 led to a mean increase of 0.0237 with a maximum difference of 0.600 (bare ground) compared to CARRA-BC13 simulation (Table 9.7). An increase by a factor of 100 resulted in a mean albedo decrease of 0.0502 and a maximum decrease of 0.602 compared to CARRA-BC13 simulation. Albedo for increased BC deposition simulations was especially reduced during the melting period, when BC particles accumulated on the snow surface and during the time when there was no snow on the ground in the enhanced simulations while there was still snow in the CARRA-BC13 simulation (Figure 9.8).

Changes in mean surface snow SSA over the entire study period were small, ranging from 35.1 m^2 kg^{-1} for pure snow and low surface concentrations to more than 36 m^2 kg^{-1} for the highest deposition rates used in this study (Table 9.6). Figure 9.8 shows that surface albedo decreased with decreasing surface SSA. However, the currently implemented BC parameterisation has only low impacts on surface SSA. Mean surface snow density over the entire study period decreased with increasing BC surface content from 168.4 kg m^{-3} for pure snow to 151.2 kg m^{-3} for increased deposition rates of a factor 100 compared to CARRA-BC13.

Snow depth decreased with increasing BC content over the entire study period (Figure 9.9). While for a doubling of BC deposition rates the mean decrease in snow depth over the entire study period was 0.003 m, the maximum decrease in snow depth was 0.032 m. Note, that there is no snow in the scenario simulations for the time of the maximum snow depth differences (Table 9.7). For a simulation with deposition rates 100 times higher than CARRA-BC13, the mean decrease in snow depth was 0.061 m and the maximum decrease was 0.549 m during the study period. Note that the mean snow depth decrease for CARRA-BC13 simulation compared to pure snow was 0.002 m with a maximum difference of 0.025 m.

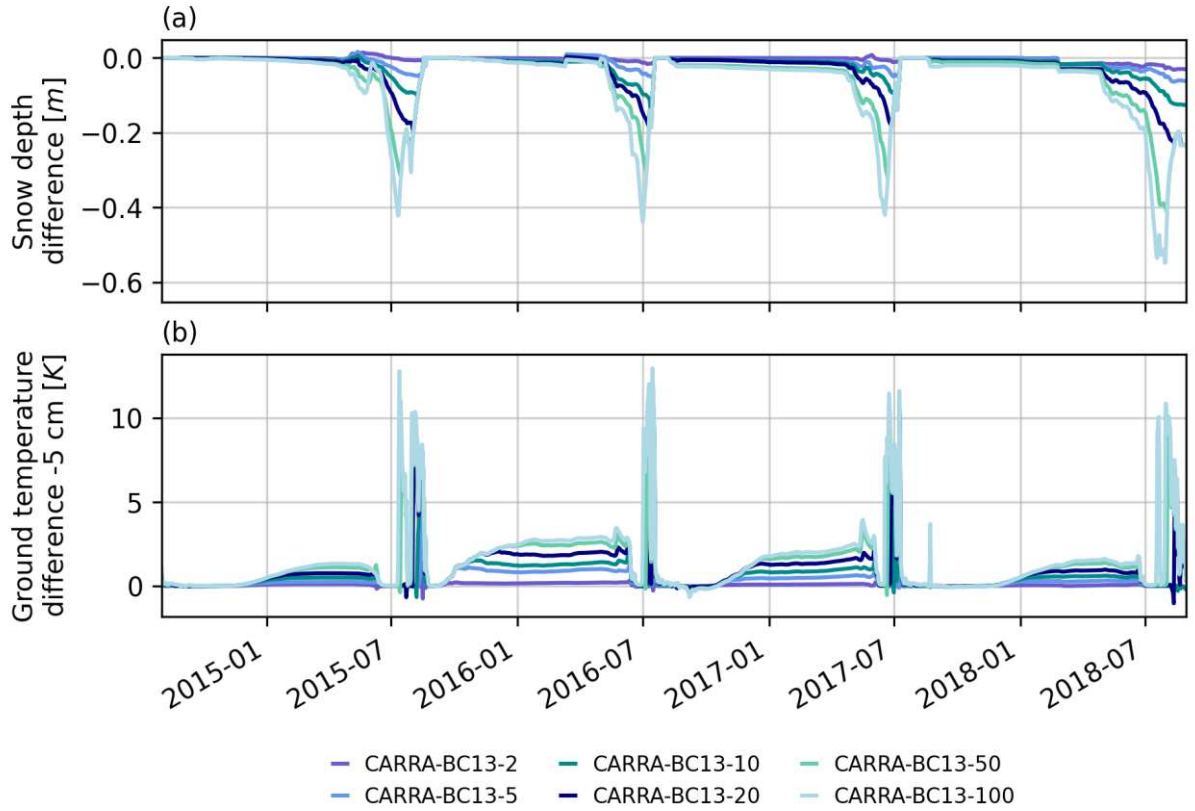

Figure 9.9: Difference between (a) snow depth and (b) ground temperature at -5 cm from 1 September 2014 to 30 August 2018 simulated with CARRA-BC13 (scenario simulation - CARRA-BC13) and increase deposition rates as described in Table 9.2 from September 2014 to August 2018.

Table 9.7: Differences in simulated snow depth and surface albedo of simulations using enhanced deposition rates as described in Table 9.2 in comparison to CARRA-BC13 from September 2014 to August 2018.

Name of simulation (acronym)	Max snow depth difference to CARRA-BC13 [m]	Mean snow depth difference to CARRA-BC13 [m]	Max albedo difference to CARRA-BC13 [-]	Mean albedo difference to CARRA-BC13 [-]
CARRA-BC13-2	0.032 (2018-08-13)	0.003	0.191 (2017-07-10)	0.0007
CARRA-BC13-5	0.064 (2018-08-12)	0.010	0.534 2015-08-15)	0.0042
CARRA-BC13-10	0.146 (2016-07-13)	0.019	0.534 (2015-08-15)	0.0097
CARRA-BC13-20	0.234 (2018-08-30)	0.030	0.600 (2017-07-05)	0.0237
CARRA-BC13-50	0.412 (2018-08-02)	0.048	0.602 (2016-07-13)	0.0380
CARRA-BC13-100	0.549 (2018-07-30)	0.061	0.602 (2016-07-13)	0.0502

As the BC concentration in snow increased, the time the ground was covered with snow shortened. For the snow seasons 2014/15, 2015/16, 2016/17, the time snow covered the ground (snow depth ≥0.05 m) was one day shorter for CARRA-BC13 simulations compared to a pure snow simulation. Increasing the BC deposition rates from CARRA-BC13 by a factor of ten resulted in six to nine days shorter snow seasons compared to CARRA-BC13 simulations (Table 9.8). When increased by a factor of 20 or higher, after the first snowfree day in July 2014/15 a thin snow cover reestablished that melts within a few days. An increase in BC deposition rates of a factor 100 led to 16 to 35 days shorter snow seasons compared to CARRA-BC13.

Table 9.8: First day when daily mean snow depth falls below 0.05 m and related shortening of the snow season (in brackets in days) between simulations using enhanced deposition rates as described in Table 9.2 compared to CARRA-BC13 from September 2014 to August 2018.

Name of simulation (acronym)	2014/15	2015/16	2016/17	2017/18
CARRA-BC13	2015-08-15	2016-07-17	2017-07-09	-
CARRA-BC13-2	2015-08-13 (2 days)	2016-07-17 (0 days)	2017-07-09 (0 days)	-
CARRA-BC13-5	2015-08-10 (5 days)	2016-07-16 (1 day)	2017-07-07 (2 days)	-
CARRA-BC13-10	2015-08-06 (9 days)	2016-07-11 (6 days)	2017-07-01 (8 days)	-
CARRA-BC13-20	2015-07-21 (25 days)	2016-07-09 (8 days)	2017-06-26 (12 days)	2018-08-09
CARRA-BC13-50	2015-07-14 (32 days)	2016-07-05 (12 days)	2017-06-21 (17 days)	2018-08-02
CARRA-BC13-100	2015-07-11 (35 days)	2016-07-01 (16 days)	2017-06-17 (21 days)	2018-07-18

The shortening of the snow season also affected the ground temperature (Figure 9.9). More heat was absorbed by the ground due to the longer snow free period. Thereby, ground temperature increased with increasing BC deposition rates. Raising the BC deposition rates from CARRA-BC13 by a factor of five resulted in about 0.5°C warmer ground temperatures at -5 cm almost over the entire snow season. A higher deposition rate of a factor of 100 led to about 2°C warmer ground temperatures. The effect of the warmer ground temperature can be detected in autumn when the snow cover built up. The energy stored in the ground hampered the build up of the snow layer because part of the energy was used to melt snow.

9.4 Discussion

9.4.1 Black carbon (BC) concentrations and deposition rates

Measured BC snow surface concentrations during PAMARCMiP are low with a median BC mass concentration of 0.72 ng g^{-1}. The vertical profiles from 3 April 2018 have median concentrations between 0.42 ng g^{-1} and 1.11 ng g^{-1} with highest concentration of 3.70 ng g^{-1}. The instrument used to measure the BC concentrations, the SP2, is known to one of the most adequate instruments for detecting low BC concentrations in snow with in accuracy of about 10 % (Laborde et al., 2012; Lim et al., 2014; Sedlacek, 2017). The detection limit for BC concentration measured with the SP2 is ~0.02 ng g^{-1}. Caution is required when processing the samples to avoid contamination of, e.g., the pump with BC residues from higher concentrated samples. In addition, even relatively clean equipment may already show a background contamination of 0.05 – 0.5 ng g^{-1} (McConnell et al., 2007; Schwarz et al., 2012; Keegan et al., 2014).

Measurements on the Greenland Ice Sheet corresponds well with measurements during PAMARCMiP. Measured concentrations at Dye-2 of newly fallen snow had concentrations from 0 ng g^{-1} of 2 ng g^{-1}. A vertical snow profile (July 2008) showed measured concentrations from ~1 ng g^{-1} to 2 ng g^{-1} except for a melt layer with concentrations up to 20 ng g^{-1} (Doherty et al., 2013). The measurements during PAMARCMiP taken in spring also correspond well with proposed annual mean values usually between 1.5 ng g^{-1} and 3 ng g^{-1} and higher values during events of about 5 ng g^{-1} to 10 ng g^{-1} or even higher (Polashenski et al., 2015).

As the measurements were taken before the actual snow melt started, no accumulation effect on the snow surface was found. In addition, the vertical profiles do not reflect any outstanding events that caused higher BC concentrations in the snow. For instance, biomass burning events can lead to outstanding high BC concentrations in snow (on the Greenland ice sheet up to 43 ng g^{-1} were measured) building a huge fraction from annual accumulated BC concentrations (about 60 % in the Greenland ice sheet example) (Thomas et al., 2017).

Redistribution of snow and the BC particles contained in a snow layer can make it difficult to assign layers of BC particles to individual deposition and snow events and thus to interpret the data (Thomas et al., 2017). However, the prevailing wind direction and precipitation events seem to be the major determinant for the measured BC concentrations during PAMARCMiP. As snow accumulates over time, snow deeper in the snowpack corresponds to snowfall events that could happened months before. BC particles in deeper snow layers orginate from snowfall during winter and possibly early spring. The lower BC concentrations in the upper snowpack and the higher concentrations in the lower snowpack reflect a shift from one source of BC to another source of BC. The higher BC concentrations around the normalised snow depth of 0.8 might be related to northward winds and short time melting prevailing in February 2018 leading to possible higher concentrations and accumulation of BC at the former snow surface.

As Crocus does not account for wind redistribution and I use no scavenging for most of the simulations, only wet and dry deposition or sublimation can drive BC concentrations. Note that using a scavenging efficiency of 0 % results in the maximum possible amplification of BC at the snow surface and therefore in a maximum impact on radiative forcing (Doherty et al., 2013). As the BC concentrations during

PAMARCMiP were low, simulations using scavenging of 10 % to 30 % resulted in similar results of snow properties as simulations without scavenging.

In general, it is assumed that most of the BC concentration in snow results from wet deposition (Flanner et al., 2007; Doherty et al., 2013; Sinha et al., 2018; Mori et al., 2020). However, no deposition rates were measured at Villum Research Station. Thus, I approximated the rates by inverse modelling. The simulation CARRA-BC13 gives a good fit to measured vertical BC concentrations during the PAMARCMiP campaign with a constant over time wet deposition rate of 5.13 x 10^{-12} g m^{-2} s^{-1} and a dry deposition rate of 2.56 x 10^{-12} g m^{-2} s^{-1}. As there is a lack of knowledge about BC deposition rates (Sinha et al., 2018; Mori et al., 2020), it is difficult to assess the value of this resulting deposition rate, especially because the assumption of constant over time deposition rates is questionable. Measurements of high BC deposition events on the Greenland Ice Sheet in summer 2013 yielded BC deposition rates of 7.9 x 10^{-5} g m^{-2} s^{-1} to 1.17 x 10^{-3} g m^{-2} s^{-1} resulting in BC concentrations between 2.8 ng g^{-1} and 43 ng g^{-1} (Thomas et al., 2017). Deposition rates from a climate model used for simulations over one snow season in the French Alps were between 1 x 10^{-8} g m^{-2} s^{-1} and 1 x 10^{-10} g m^{-2} s^{-1} for wet and dry deposition, respectively. As snow in Greenland is in the mean cleaner than in the European Alps and no high BC deposition event is apparent in the vertical snow profile measurements, the lower deposition rates obtained by inverse modelling seems to be plausible.

Crocus is able to reproduce the order of magnitude of measured BC concentrations in surface snow and in the vertical snow profiles using the prescribed constant deposition rates. However, using constant deposition rates does not reflect reality as events from, e.g. biomass burning, or changing wind directions bringing air from different source regions, change deposition rates over the year. Furthermore, in this study prescribed deposition rates leading to a good fit with measured vertical BC concentrations overestimate surface BC measurements. This can be related to the constant deposition fluxes. However, the same behaviour of Crocus is described in Tuzet et al. (2017) who used varying deposition rates from a climate model. They suspect that weaknesses in simulated deposition rates from the climate model are responsible. The proportion of wet and dry deposition rate is as well a source of uncertainty. Studies agree that wet deposition is the main source of BC in snow but still little is known about the exact ratio between wet and dry deposition (Flanner et al., 2007; Sinha et al., 2018; Yang et al., 2019; Mori et al., 2020). While wet deposition occurs only in combination with precipitation events, dry deposition, which seems to be of low importance for the measurements, is added constantly to the surface. This leads to continuous increase of BC concentration in surface snow until the next precipitation event. A too high and constant dry deposition rate might be a cause of the overestimation of simulated surface BC concentrations during PAMARCMiP. Also, the amount and timing of precipitation events impact the surface BC concentration, which we showed are not always perfectly met by CARRA.

9.4.2 Related snow properties

Since CARRA daily mean air temperature was -27.5°C (standard deviation: 2.2°C) with a minimum daily air temperature of -31.1°C (28 March) and a maximum daily air temperature of -23.1°C (21 March) during the time of the measurement period, I assume that these cold temperatures led to the formation of snowflakes having the shape of plates and columns. These formed snow layers with higher density and lower SSA than dendritic snow. Since the total amount of newly fallen snow during the considered period was 2.9 mm and the samples were measured over the first 3 cm of the snowpack, the sample contained a mixture of older (fallen before the considered period) and younger snow.

My assumption that the decreasing SSA of new snow could be caused by different shapes of snow particles is supported by measurements of Legagneux et al. (2002). They found mean SSA for newly fallen snow of dendritic shape of 96.2 m^2 kg^{-1} (standard deviation 31 m^2 kg^{-1}), for columns, bullet combinations at temperatures below -25°C of 95.3 m^2 kg^{-1} (standard deviation: 34.0 m^2 kg^{-1}) and for plates, needles and columns of 62.9 m^2 kg^{-1} (standard deviation: 24.0 m^2 kg^{-1}). In addition, there might also be a contribution of metamorphism, depending on when the measurement was conducted with respect to the snowfall.

BC in snow has impacts on related snow properties such as snow depth, SSA, and snow albedo with consequences on the length of the snow season. The BC concentrations found for Villum Research Station are small compared to concentrations found for other Arctic places (e.g., Svalbard, Arctic Canada). However, already those small BC concentrations (mean surface concentration of 3 ng g^{-1} over the entire study period) lead to a maximum reduction of snow depth of 0.025 m and a one day shorter snow season compared to pure snow. The snow model Crocus is used to simulate the effect of increasing BC deposition rates, showing in particular the impact on the length of the snow season and allowing quantification. The higher the BC deposition rate, the shorter the snow season. This is in line with the findings of Tuzet et al. (2017) but for European Alps, where considerably higher BC concentrations prevail. However, I can show that already rather small changes in the concentration lead to quantifiable reductions in snow season length.

A comparison of measured and simulated surface albedo shows that simulated albedo decreases faster in spring than measured even if only the times are considered when the zenith angle is below 70° and the measured surface albedo can be regarded as trustworthy. Snow albedo depends on several variables, for instance the solar zenith angle, the frequency of snowfall events, the amount of direct and diffuse solar radiation and snow grain size related to SSA and snow aging (Doherty et al., 2010; Bond et al., 2013). As previous studies with Crocus showed (Chapter 6 and Chapter 7), also the simulated SSA is underestimated, meaning that snow aging is simulated faster than observed. Because lower SSA is related to lower albedo surface melting sets in too early and too strongly in the simulations. As Crocus was developed for warmer regions where snow metamorphism is faster and vertical temperature gradients are lower (Sommerfeld and LaChapelle, 1970) their might be adaptations of the metamorphism scheme necessary for applications in the Arctic.

The way BC is parametrised in Crocus, increasing BC deposition rates and thus increasing BC concentrations only have small effects on SSA. This is in line with findings from Tuzet et al. (2017) for studies in the European Alps. During the melting phase and the accumulation of BC particles on the snow surface, surface albedo is reduced clearly. Already a doubling of the deposition rates of CARRA-BC13 with mean surface BC concentrations of 3 ng g^{-1} leads to a reduction of mean surface albedo of 0.0042, while mean BC surface concentrations of 16 ng g^{-1} lead to a mean reduction of 0.0042 over the entire study period. BC in snow on the Greenland ice sheet reduced the albedo on average by 0.0016 to 0.005 during 2012 and 2013. Events like forest fires can lead to higher deposition of BC in snow, which leads in simulations for summer 2013 to albedo reduction of 0.01 - 0.02 (Polashenski et al., 2015).

The effects of BC on snow properties in this study are calculated for the entire study period. When calculated for events or for the melting season, effects would probably be more announced. This is beyond the scope of this study as no high deposition events could be identified in the measured vertical snow profiles and no seasonal depended deposition rates were applied.

The scenario simulations presented do not consider scavenging. This results in maximum BC particle accumulation on the snow surface. Therefore, the impact on snow properties may be slightly overestimated. As BC concentrations increase with higher BC deposition rates, the effect of scavenging could have larger impacts than in the tested CARRA-BC13 simulation. The parameterisation of scavenging and the implementation of liquid water content are subject to large uncertainties (Tuzet et al., 2017). In addition, no prevailing scavenging rate is known. In a follow up study, the sensitivity of the simulated snow properties to different scavenging proportions should be investigated.

The here proposed simulation results are a sensitivity study of the effects of different deposition rates on the basis of approximated deposition rates of the spring 2018 conditions. However, important relation between BC deposition rates, BC concentration in snow and related effects on snow properties could be studied. Here, the focus is on the effects of BC particles on snow properties. However, BC is not the only light absorbing impurity found in Arctic snow. Twenty percent to 50 % of light-absorption is done by other particles, for instance, by dust particles (Doherty et al., 2010; Bond et al., 2013). Thus, albedo

changes due to all light absorbing impurities add up (not linearly) and have a higher impact than BC particles alone.

The interpretation of BC concentration in snow is difficult. The knowledge about several variables, including deposition rates and post-depositional processes are important (Doherty et al., 2010). The in-situ measurements presented are a snapshot of the snowpack at a point in time. Snow models including deposition rates and post-depositional processes (like Crocus) may help to better analyse the evolution and timing of these processes and thus the measured BC concentration in snow. This study is a first step in the application of the snow model Crocus for analysing BC concentration in snow and related effects in the Arctic. The evolution of post-depositional processes is behind the scope of this manuscript but may be covered in future research.

9.5 Conclusion

BC in snow leads to positive albedo feedbacks as it reduces the surface albedo and affects snow properties. To analyse these effects, snow samples were collected during a campaign in spring 2018 at a site in northeast Greenland before the onset of melt and BC concentrations in the snow were determined. Using the snow model Crocus, BC deposition rates could be approximated by inverse modelling. The resulting deposition rates are low compared to the simulated deposition rates for the European Alps and the measured deposition rates for a high deposition event in Greenland. In addition, measured BC concentrations (surface and profiles) are in agreement with measurements on the Greenland ice sheet. The main factor for the variations of the measured BC concentration seem to be precipitation events and wind direction.

To analyse the effects of higher BC concentrations on surface albedo and related snow properties, a sensitivity study was performed with increased deposition rates. The main effect was found in the shortening of the time, during which snow covers the ground due to decreased albedo of melting snow. Higher BC concentrations also alter snow depth and snow density. Simulated effects on snow SSA were small.

The study shows that simulated surface albedo in spring decreases too quickly in Crocus compared to measurements also for simulations without BC content in snow. This might be related to too fast ageing of the snow in the simulation, which leads to an underestimation of the SSA. Future studies should evaluate the performance of the metamorphism scheme implemented in the snow model Crocus, which might have to be adapted to account for the colder conditions and therefore slower snow ageing in the Arctic compared to the European Alps.

Measurements can only provide a snapshot of the snowpack. Moreover, a variety of variables is required to analyse BC concentrations in snow and its impacts. Therefore, the snow model Crocus, which simulates BC concentrations in snow using prescribed wet and dry deposition rates and can simulate post-depositional processes, is a valuable tool to study the effects of BC in snow on snow properties especially in remote regions, as the Arctic.

10 Conclusions

The **key findings** of this dissertation are

(1) Atmospheric reanalyses are overall sufficient to simulate reliably Arctic snowpack evolution, but weaknesses prevail in representing precipitation and high wind speeds. This holds as well for high resolution regional reanalyses.

(2) In general, the snow model Crocus simulates sufficiently well snow depth evolution but has weaknesses in reliably simulating vertical profiles of snow SSA and snow density.

(3) Crocus simulates a too early and too fast decrease in snow depth in spring, possibly due to a combination of overestimation of snow compaction and inadequate formulation of snow metamorphism for cold snow temperatures. This leads to a too fast decrease in SSA, which in turn affects surface snow albedo and thus sets limits to simulate adequately effects of BC in snow.

(4) More work needs to be done to improve the modelling of Arctic snow. Due to the complexity of detailed snow models, adaptations are time consuming, but already small modifications can contribute to a more representative simulation of Arctic snowpacks.

This dissertation aims to improve detailed modelling of snowpack evolution in the Arctic to enable eventually impact studies of light absorbing impurities on snow properties and snow surface albedo. For reliable Arctic snow model simulations, the model parameterisation needs to be fit for Arctic conditions, e.g., cold temperatures and strong winds. This holds as well for the atmospheric forcing used to drive the model. Therefore, the fitness of different atmospheric forcing datasets (in-situ measurements and reanalyses) are assessed as part of this dissertation, as reliable and long time series of in-situ measurement are not available for many locations in the Arctic.

The atmospheric data required to drive the snow model Crocus from two reanalyses with different spatial resolutions (global: ERA5 and regional: CARRA) were compared with available atmospheric measurements (**Chapter 6** (addressing research question R1) and **Chapter 7** (addressing research question R2)). Overall, reanalyses and measurements show a good agreement. Weaknesses are found in particular for precipitation and high wind speeds, which are both important variables for the correct simulation of snowpack evolution. In addition, the measured precipitation has large measurement gaps (in total 35.2 % of the measurements are missing). This demonstrates why reanalyses as continuous datasets are essential as forcing data for simulations, also and in particular for the poorly observed Arctic. Despite the weakness in precipitation, the comparison between simulated and measured snow depth shows overall good agreement when forced by both reanalyses. Furthermore, quite a surprising result was the worse agreement of simulated snow depth evolution with the measured snow depth when the model was forced with in-situ atmospheric measurements compared to the simulations when forced with reanalyses (CARRA and ERA5), which highlights how important accurate forcing data are for driving snow models.

In general, Crocus has never been quantitatively evaluated against detailed vertical snow property profile measurements. Instead, evaluation has been based primarily on bulk and surface properties of snow (Viallon-Galinier et al., 2020). Variables assessed include snow depth (Brun et al., 1989), surface temperature (Brun et al., 2012), SWE, bulk snow density and albedo (Lafaysse et al., 2017). Even though several studies have examined measured and simulated profiles of, e.g., thermal conductivity, snow density, SSA among others (e.g., Jacobi et al., 2010; Domine et al., 2013; Carmagnola et al., 2014; Barrere et al., 2017), these evaluations were mostly qualitative (Viallon-Galinier et al., 2020).

In addition, the snow model applied in this dissertation was originally developed for applications in the European Alps. The prevailing atmospheric conditions in the Arctic and the European Alps, however, cause different processes to be important for the snowpack evolution. In particular, I find deviations between the measured and simulated snow depth evolution in spring and in the vertical profiles of snow density and SSA. Even though the model is regularly used to simulate Arctic (and Antarctic) snowpacks (e.g., Carmagnola et al., 2014: e.g.; Libois et al., 2014; Domine et al., 2016b; Essery et al., 2016; Barrere et al., 2017; Lackner et al., 2022a), the model parameterisations have been built and optimised in particular based on measurements conducted in the European Alps (Brun et al., 1989; Lafaysse et al., 2017) and thus need to be adapted for Arctic conditions.

To achieve more reliable snow simulations under harsh Arctic conditions (e.g. cold air temperatures accompanied by strong winds), **Chapter 8** (addressing research question R3**)** introduces and evaluates new parameterisations for (1) density of newly fallen snow and (2) modifications on the parameterisation of the effect of strong wind speeds on upper snow density. With the default parameterisation simulated new snow densities and densities of the upper snow layers are too low compared to measurements (Sauter and Obleitner, 2015; Essery et al., 2016). The largest improvements in the snow depth simulations are achieved with a new snow density parameterisation adapted to the cold temperatures of the Arctic and by including a gust factor of 1.6 to account better for wind induced effects on snow density. For the snow density simulations, I achieve improvements with the snow density parameterisation adapted for cold temperatures in combination with modifications to the effect of high wind speeds on density, whereby different combinations of adaptations result in similar improvements with respect to the (limited) available measurements.

In all simulations, I find deviations in snow depth compared to measured snow depth from spring onwards. However, the simulated SWE time series has roughly the same shape as the measured snow depth time series - SWE does not show too early decrease in spring. Therefore, I hypothesise that this erroneously simulated snow depth decrease in spring is to some extent caused by an overestimation of compaction in the model, especially in spring. Brun et al. (2013) suspect as well an overestimation of simulated compaction when liquid water is present. However, because no SWE measurements were carried out during PAMARCMiP 2018, I cannot verify this hypothesis.

Another reason for the too early decrease of snow depth might be the formulation of snow metamorphism that does not fully reflect the processes and rate of snow ageing in the Arctic (in general, snow metamorphism is slower in cold snow than close to its melting point (Sommerfeld and LaChapelle, 1970)). The comparison between simulated and measured vertical profiles of SSA shows that simulated SSA is considerably lower than measured SSA. In general, simulated SSA cannot exceed 65 $m^2 kg^{-1}$, while measurements show SSA of newly fallen snow of up to 105 $m^2 kg^{-1}$ and SSA of surface hoar or rime of 65 to 75 $m^2 kg^{-1}$ has also been measured (Carmagnola et al., 2014; Tuzet et al., 2020). In addition, I observe a faster decrease in surface albedo in spring than measured (**Chapter 9** (addressing research question R4)) and a too early and too strong decrease in snow depth in spring, which I partly attribute to an overestimation of compaction. Moreover, I hypothesise that in the model snow aging, which decreases SSA, is too fast for Arctic conditions, at least in spring. Libois et al. (2015) delayed metamorphosis in Crocus for simulations at Dome C in Antarctica. This approach should also be tested for the Arctic. Since snow albedo is strongly controlled by SSA, biases in simulated SSA have a large impact on simulated albedo. Thus, to improve albedo simulations, modifications of the SSA parameterisation would be necessary (Tuzet et al., 2017). Due to the limitations in simulating Arctic surface albedo, simulated effects of BC on snow properties are subject to high uncertainties.

Two important processes for Arctic snowpack evolution, which are not parametrised in Crocus, cause a major limitation for applications in the Arctic. These are the redistribution of snow and the vertical water vapour transport (Domine et al., 2019; Lackner et al., 2022b). So far, it is difficult to implement these processes in the model but there are first attempts to do so (Touzeau et al., 2018; Jafari et al., 2020; Simson et al., 2021; Jafari et al., 2022; Lackner et al., 2022b; Schürholt et al., 2022).

A caveat of this dissertation is the validation of the model simulations and the reanalyses data only at one site in the Arctic. For the validation of the snow depth simulations and reanalyses, only point measurements were available over a longer time period, whereas the reanalyses and consequently the simulations forced by them have a spatial resolution of several kilometres. This makes the validation of data with a high spatial heterogeneity difficult. Additionally, with the exception of snow depth, the snow simulations could be only validated against data from one short time period and one season.

I also find that snow depth measurements are of limited value for model validation, as the reason of decreasing snow depth is not clearly and unambiguously interpretable without additional measurements. SWE measurements are of utmost importance to distinguish whether snow depth decrease is due to melting/sublimation or compaction.

From the perspective of snow modelling, there is still much work to be done to adapt a “European snow model” for the harsh conditions in the Arctic. For example, it seems that the wide range of cold temperatures in the Arctic is not taken into account in some parameterisations. This is evident in the default new snow density parameterisation, and I assume this is also the case for the parameterisation of metamorphism of dry snow. Even small changes in the parameterisations can yield large improvements in the model performance. However, as the used snow model is highly complex (as is reality), many processes interact. Changes in one parameterisation can affect several other variables, which is why analyses have to be carried out carefully and investigations are time consuming. Ultimately, the sum of several model modifications will lead to significant improvements in snow modelling in the Arctic.

The dissertation provides an improved understanding of the reasons for deviations between measured and simulated snow properties caused by the forcing data and model parameterisations. Finally, the application of a fit-for-the-Arctic snow model can lead to knowledge gain in the understanding of various processes related to snow evolution, for instance, of the effects of BC on radiative forcing and can enrich our understanding of Arctic Amplification and therefore climate change. The analyses presented in this dissertation are important pieces in the puzzle of reliable snow simulations in the Arctic.

11 Outlook

The dissertation provides a good basis for the design of future research studies and field campaigns. Some of these are already planned. The following list provides a roadmap towards more complete Arctic but also Antarctic snow research.

- All analyses in this dissertation were conducted for a single site in northeast Greenland using available data between 2014 and 2018. As a next logical step, the transferability of the results and the introduced new snow density parameterisations to other sites in the Arctic should be evaluated. Thereby, the formulation of the introduced new snow density parameterisations is not restricted to the Arctic domain, but can also be applied to sites in the European Alps and in Antarctica due to their universal physical formulation. Furthermore, with the exception of snow depth, the snow measurements that could be used for the validation of the simulations were quite short in time and limited to one season. On that account, the validation should be extended to longer time series if possible. As the studies of this dissertation have shown, the quality of the in-situ validation data and in-situ forcing data is of great importance, since the snow model reacts sensitively to biases, e.g. in humidity, in the forcing data.

- One recurring result was the too early decrease of simulated snow depths in spring compared to measurements. The analyses show that this could be related to an overestimation of snow compaction. Thus, SWE simulations should be compared to SWE measurements to examine the validity of this hypothesis. If the hypothesis is correct, a first attempt could intend to increase the snow viscosity and thus to reduce snow compaction.

- I found indications for a too strong compaction but also for inadequate model formulations of snow metamorphism when used for sites in the Arctic - simulated SSA and albedo (in spring) decreases too fast. This hypothesis has to be validated against longer time series. If the hypothesis is correct, modifications to the dry snow metamorphism parameterisation has to be conducted. I suggest the following strategy to tackle this problem.

  I assume that the snow metamorphism for warmer snow temperatures prevailing in the European Alps is well calibrated against measurements but that for colder snow temperatures typical for the Arctic, the parameterisation is not as well validated against measurements as those colder snow temperatures are not occurring often in the European Alps. Thus, in a first attempt a sensitivity survey was conducted, in which modifications on the term T_{decay} used in the dry snow metamorphism parameterisation of Crocus were applied (see Table 5.3). Preliminary results presented below show a possible direction for future efforts of improving the snow model Crocus for Arctic applications. Careful validation with measurements especially SSA and albedo are necessary to investigate whether the proposed attempt is reasonable.

  The formulation of T_{decay} is defined as

$$T_{decay} = e^{-6000\ K\ /\ T_{st}} \tag{11.1}$$

where T_{st} is the snow temperature [K]. For the sensitivity study, T_{decay} was modified to

$$T_{decay} = e^{-6000\,K\,/\,T_{fus}-x^{p_c}} \tag{11.2}$$

where x is defined as $T_{fus} - T_{st}$, T_{fus} as temperature of the melting point of water, and for p_c the values p_c = 1.1 and p_c = 1.2 were tested. With this change, the dependence of metamorphism for colder snow temperatures is changed strongly, while the dependence for warmer temperatures is only changed slightly (Figure 11.1).

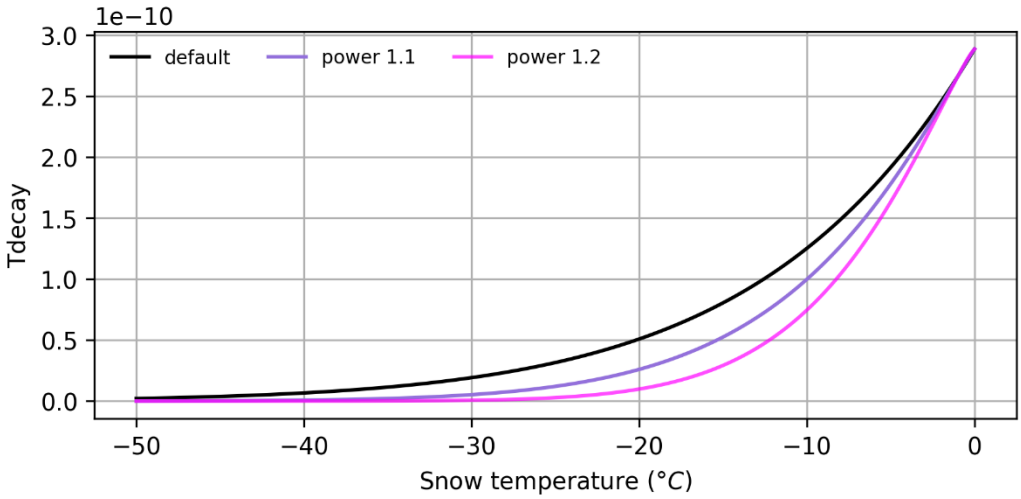

Figure 11.1: Metamorphism dependence on snow temperature. T_{decay} (Eq.(11.1) and Eq. (11.2)) is used in the dry snow metamorphism laws described in Table 5.3.

The results show that especially SSA is sensitive to changes in the formulation of T_{decay} with higher SSA values suggesting slower snow aging (Figure 11.2). This also affects simulated snow depth, SWE and snow surface albedo evolution (Figure 11.3), whereby the snow is not melting in the adapted simulations in all years. Differences are especially visible in the snowyears 2015/16 and 2017/18 compared to the CARRA-K22gf1.3 simulation. In addition, snow depth simulated with the adapted simulations decrease later in spring, and thus are closer to the measurements. Thereby, SWE is slightly higher than for the CARRA-K22gf1.3 simulation and snow surface albedo of the adapted simulations decreases slower as well in better agreement with the observations (see Figure 11.3).

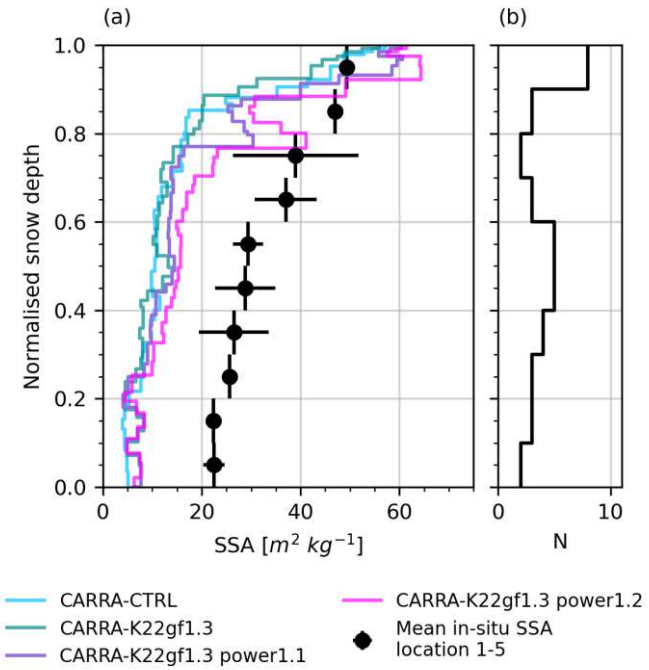

Figure 11.2: (a) Simulated and measured snow specific surface area (SSA) on 3 April 2018 using the default new snow density parameterisation (V12) and the introduced new snow density parameterisation K22gf1.3 (see Chapter 8 for definition) as well as the K22gf1.3 parameterisation in combination with changes in the term T_{decay} (Eq. (11.1) and Eq. (11.2)) (b) shows the sample frequency of IceCube measurements. Black vertical lines represent the normalised snow depth range where measurements had been averaged and black horizontal lines represent the sample variability (± one standard deviation).

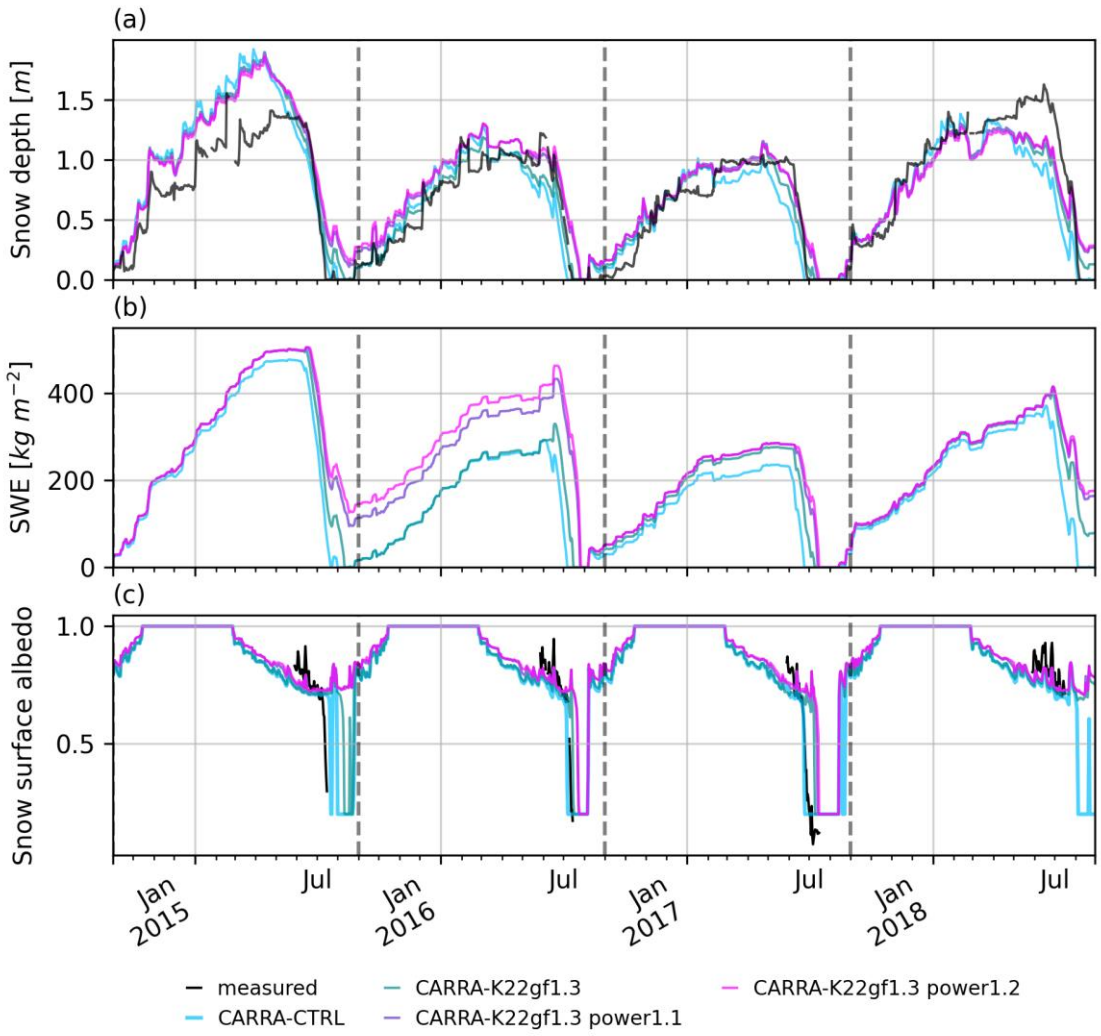

Figure 11.3: Time series for (a) snow depth, (b) snow water equivalent (SWE) and (c) snow surface albedo from 1 September 2014 to 30 August 2018. (a) measured and simulated using the default new snow density parameterisation (V12) and the introduced new snow density parameterisation K22gf1.3 (see Chapter 8 for definition) as well as the K22gf1.3 parameterisation in combination with changes in the term T_{decay} (Eq. (11.1) and Eq. (11.2)). (b) shows only simulation results. Vertical dashed lines denote 1 September of each simulation year.

- Reliable information about snow properties and their evolution are important on land but also on sea ice. For instance, (1) to retrieve sea ice thickness from satellite altimeter data, (2) to improve cryosphere-atmosphere coupling in reanalyses products or numerical weather prediction systems and (3) to simulate sea ice evolution (Hunke et al., 2010; Stroeve and Notz, 2018; Arduini et al., 2022; Jutila et al., 2022). However, regarding (1) even the most recent products use outdated snow climatologies (e.g., Warren et al., 1999) for snow on multi-year sea ice and regarding (2) and (3) relatively simple snow models are used to represent snow on sea ice (Hunke et al., 2010; Stroeve and Notz, 2018; Arduini et al., 2022; Jutila et al., 2022). Thus, coupling the snow model Crocus with an state-of-the-art sea ice model (e.g., Icepack (Hunke and Dukowicz, 1997; Roberts et al., 2018; Hunke et al., 2022)) has the potential for major improvements with respect to sea ice research but also for climate change simulations.

- During the Multidisciplinary drifting Observatory for the Study of Arctic Climate (MOSAiC) expedition from October 2019 to September 2020 in the central Arctic, in which I participated, a unique dataset including year-round atmospheric, sea-ice and snow measurements was collected. First publications, some of which I co-authored, show the great potential arising from the outcome of this expedition. For instance, Nicolaus et al. (2022) provide an overview about the expedition and of measurements related to physical sea ice and snow properties and processes. Stroeve et al. (2020) present first results of a surface-based radar system together with detailed snow and ice measurements. Wagner et al. (2022) compared snowfall retrieval from various instruments during the winter and spring season, which allows to select the most reliable snowfall measurements for driving snow models in the future. In addition, there are various data products available on PANGAEA, some of which I co-authored, that will be beneficially used in future.

  Various snow properties at numerous locations were measured (e.g., snowfall, snow depth, snow density, snow SSA). In addition, we collected year-round more than 600 samples for analysing BC in snow. Thus, the data allow to validate and develop (new) snow model parameterisations through year-round measurements from different locations. The datasets are extremely valuable for the validation of the snow model Crocus including the introduced new snow density parameterisations with respect to various snow properties but also for the development of new parameterisations better suited for higher latitudes. Furthermore, the BC dataset allows investigation of the seasonal cycle of BC in snow and in combination with Crocus investigation of the impact on related snow properties and radiative forcing.

- For spring 2023, collaborative fieldwork is planned at Villum Research Station (VRS), Greenland, together with the Department of Environmental Sciences, Western Washington University, allowing for a continuation of the measurements of PAMARCMiP campaign 2018. The planning takes into account the results of this dissertation - more regular vertical snow profile measurements as well as SWE measurements and atmospheric BC concentrations measurements onsite are planned. These additional measurements will be beneficial for the further development of the parameterisation of compaction and SSA in Crocus and will also contribute to a better understanding of the vertical redistribution of BC concentration during melting, which is still an open question (Doherty et al., 2010).

- As this dissertation suggests, future fieldwork should pay special attention to measuring SWE together with snow depth to allow for a distinction of snow depth decrease due to melting/sublimation or compaction of snow. Otherwise, it is difficult to link the profiles with other measurements and model simulations. In addition, for model simulations it is valuable to have data from several days (e.g., vertical profiles) repeated at several locations to obtain more robust validation results.

A Appendix: Reanalyses data

The measurements of snow properties described in the previous subchapter are point measurements. These provide information for a limited period of time and for a small spatial extent. To study the evolution of snow properties over the annual cycle and over several years, snow models are often used to simulate snow properties (see Chapter 5) (Liston et al., 2016; Pedersen et al., 2016b; Royer et al., 2021). Continuous atmospheric data are needed to drive these snow models. However, observational data in the Arctic are limited in time and space and have gaps in their time series (Goosse et al., 2018; Przybylak and Wyszyński, 2020). To reliable obtain continuous atmospheric data over a long period of time, also for distant locations, atmospheric reanalyses are often used (Barrere et al., 2017; Domine et al., 2019). Here, reanalyses are introduced generally, before the specific reanalyses used in this dissertation are discussed in more detail.

Reanalyses are used when a comprehensive picture of the atmospheric state is needed. Examples for applications range from mass balance and runoff modelling of glaciers (Azam and Srivastava, 2020) and atmospheric phenomena as cyclonic characteristics (Zahn et al., 2018) to aerosol-cloud-radiation studies (Bender et al., 2019).

Reanalyses provide time dependent spatial fields by combining in a physical consistent way observations and models via data assimilation (Parker, 2016; Hersbach et al., 2020). Talagrand (1997) describes data assimilation as "[…] process through which all available [meteorological] information is used in order to estimate as accurately as possible the state of the atmospheric […] flow". For atmospheric data assimilation observational data and forecasts from numerical weather prediction models, are used (Talagrand, 1997; Parker, 2016; Hersbach et al., 2020). Observational data include satellite observations and aircraft measurements, station measurements including radar observations, radiosonde and dropsonde data as well as buoy data and ship measurements (Hersbach et al., 2020).

An estimation of the initial atmospheric conditions of past periods is provided by forecasts from numerical weather prediction models updated from observations. By assimilating the data an estimation of a complete gridded state of the atmosphere can be obtained (Parker, 2016). The strength of reanalyses are homogeneous global or regional datasets of climate variables over a long time period, continuous available at regular intervals (Parker, 2016; Bell et al., 2021).

For the here presented work, two reanalyses (see for short comparison) have been used:

- **ERA5** from the European Centre for Medium-Range Weather Forecast (ECMWF)
  The acronym ERA5 stands for ECMWF ReAnalysis-5th Generation (ERA5) atmospheric reanalyses data set.

- **CARRA** from the EU Copernicus program
  The acronym CARRA stands for Copernicus Arctic Regional Reanalysis.

Table A.1: Short comparison of the used reanalyses ERA5 and CARRA.

	ERA5	**CARRA**
Producer	ECMWF	EU Copernicus program MET Norway (contractor)
Region	global	regional (Greenland, Iceland)
Spatial resolution (at study location)	5 km x 31 km	2.5 km x 2.5 km
Temporal resolution	1 h	3 h

A.1 ERA5

The global reanalysis ERA5 is expected to be produced for the next 5 to 10 years (Bell et al., 2021). ERA5 is available from 1950 onwards and has a horizontal resolution of 31 km at the equator on a longitude-latitude grid (Hersbach et al., 2020; Bell et al., 2021). The data are delivered for the state of the global atmosphere, the land surface and for ocean waves (Bell et al., 2021).

The basis of ERA5 is the Integrated Forecasting System (IFS), cycle Cy41r2, whereby a 4D-Var data assimilation for "observations sensitive to surface and upper-air atmospheric quantities" is employed (Bell et al., 2021) and hourly model output is delivered. The model is initialised daily at 06 and 18 UTC (European Centre for Medium-Range Weather Forecasts, 2018; Hersbach et al., 2020; Copernicus Climate Change Service, 2021c).

Surface elevation data used are products of the Shuttle Radar Topography Mission 30´´ (30 min) version (SRTM30) for latitudes between 60°N and 60°S. For areas north of 60°N Greenland Global Land One-kilometre Base Elevation (GLOBE) data and Byrd Polar Research Center (BPRC) data are used. All elevation datasets are projected on the global 30´´ grid (European Centre for Medium-Range Weather Forecasts, 2016). As input, apart from satellite data, data from buoys, ships and aircrafts, land stations from surface synoptic observations (SYNOP) and METeorological Aerodrome Report (METAR) are employed in ERA5. Variables used from SYNOP and METAR are surface pressure, temperature, wind and humidity (Copernicus Climate Change Service, 2021c). In ERA5, point observation data on snow depth are directly assimilated, which affects, e.g., ERA5 air temperatures (Mortimer et al., 2020). In general, the number of assimilated data increases in time, i.e., 53 000 observations per day in 1950, 570 000 in 1978 and 24 million per day in 2018, which means that the quality of ERA5 increases with time (Hersbach et al., 2019; Bell et al., 2021).

According to Bell et al. (2021) there are shortcomings that shall be improved in future reanalyses: "[…] [T]he assimilation of tropical cyclone data, the spin-up of soil moisture and stratospheric humidity, and the representation of surface temperatures over Australia." In addition, ECMWF has found further issues in their reanalyses for applications in Polar Regions due to large errors in modelling, limited availability of in-situ measurements and challenges using satellite data (e.g., uncertainties due to snow and sea ice). Furthermore, the data assimilation was optimised for mid-latitudes and not for Polar Regions. For Polar Regions, little is known about how to handle systematic errors and how accurate estimates of model uncertainty are. These factors are crucial because they determine the weighting of observations versus model results (European Centre for Medium-Range Weather Forecasts, 2018).

Additional components that have to be improved include "[…] the representation of stable boundary layers, mixed-phase clouds, snow and sea ice, plus the coupling of these different elements of the Earth system. Currently, erroneous fluxes of heat, momentum and radiation at the interfaces can occur […]" (European Centre for Medium-Range Weather Forecasts, 2018). Biases in ERA5 but also in other reanalyses (e.g., Japanese 55-yr Reanalysis (JRA-55), Modern Era Retrospective analysis for Research and Modern Era Retrospective analysis for Research and Applications-version 2 (MERRA-2), Arctic System Reanalysis version2 (ASRv2)) are especially large over sea ice in, e.g., near surface temperature and net longwave radiation (Graham et al., 2019a; Wang et al., 2019; Heinemann et al., 2021). Furthermore, especially in the Arctic the planetary boundary layer can be thin – only a few tens of metres – and therefore processes within this layer are difficult to parametrise. This sets additional limits on the performance of ERA5 at high latitudes near the surface (Dethloff et al., 2001; Beljaars, 2002).

Nevertheless, ERA5 shows strengths compared to other modern reanalyses used for Arctic applications (Graham et al., 2019a; Graham et al., 2019b). For example, according to Graham et al. (2019a) ERA5 has a better representation of spring and summer surface radiative fluxes over sea ice than other reanalyses, e.g. JRA-55 and MERRA-2, thus indicating a better prediction of arctic cloud covers. Further, Seo et al. (2020) found promising results for ERA5 for surface net radiation in the Arctic (Seo et al., 2020). Moreover, comparison with radiosonde measurements in the Fram Strait shows the best performance of ERA5 in representing temperature, wind speed and specific humidity compared to, e.g., JRA-55 and MERRA-2. This good performance also affects the representation of moisture transport within the Arctic, which is likely improved compared to the precursor ERA-Interim because of a higher vertical resolution (Graham et al., 2019b). In addition, comparisons with buoy measurements show improved representation of Arctic precipitation in comparison to ERA-Interim (Wang et al., 2019). Because of the presented advantages of ERA5 compared to other reanalyses, I choose ERA5 data for the studies presented within this dissertation.

The output of ERA5 is available hourly (Hersbach et al., 2020) and 5 days behind real time (Bell et al., 2021). ERA5 data is freely available and can be downloaded from the C3S Climate Data Store (https://cds.climate.copernicus.eu/cdsapp#!/dataset/reanalysis-era5-single-levels?tab=form or via the Climate Data Store API).

A.2 CARRA

The reanalysis CARRA is available with a 2.5 km grid resolution on a Lambert conformal conic grid for two regions called CARRA-West, covering Greenland and Iceland and CARRA-East, covering Svalbard and Northern Scandinavia (Copernicus Climate Change Service, 2020, 2021b). For this dissertation, CARRA-West is used as it includes the study area of the PAMARCMiP campaign 2018 in northeast Greenland, and I denote CARRA-West shortly CARRA hereafter.

CARRA is employing the regional Numerical Weather Prediction system AROME[5]-Arctic (Norwegian Meteorological Institute, 2019). The model system is based on the HARMONIE[6]-AROME configuration of the ALADIN[7]-HIRLAM[8] numerical weather prediction system (Bengtsson et al., 2017).

Adaptations include, e.g., the usage of higher resolution topography and corrections of the northeastern fjords and major glacier area in the land-sea mask for Greenland. Thereby, the glacier extents for the whole CARRA period 1997-2021 are fixed to the area during the middle of the reanalysis period. The assimilation window for CARRA is 3 h. Lateral boundary conditions are taken from ERA5 (Copernicus Climate Change Service, 2020).

Within the domain of CARRA, observational data is sparse. In addition to the observational data used for ERA5, for CARRA also data from the networks of the Programme for Monitoring of the Greenland Ice Sheet (PROMICE), ASIAQ Greenland Survey, and the Greenland Climate Network (GC-NET) are used for assimilation and verification (Copernicus Climate Change Service, 2020). A major improvement relative to ERA5 is the use of satellite-derived glacier albedo data (Copernicus Climate Change Service, 2021a). Due to its high resolution, CARRA is expected to represent especially clouds and precipitation more reliable than global reanalyses (Copernicus Climate Change Service, 2021b).

The temporal resolution of CARRA output is 3 h. The data is freely available and can be downloaded from the C3S Climate Data Store (https://cds.climate.copernicus.eu/cdsapp#!/dataset/reanalysis-carra-single-levels?tab=form or via the Climate Data Store API).

[5] AROME: Application of Research to Operations at Mesoscale
[6] HARMONIE: HIRLAM-ALADIN Research towards Mesoscale Operational Numerical weather prediction In Euromed
[7] ALADIN: Aire Limitée Adaptation dynamique Développement InterNational
[8] HIRLAM: High Resolution Limited Area Model

B Appendix to Chapter 6

B.1 Preparation of forcing data

VRS provided meteorological measurements that we compared with ERA5 data. We removed the annual cycle from the time series by subtracting the observed monthly mean "climatology" from 27 November 2015 to 8 August 2018 from both, the in situ data and the ERA5 reanalysis. By analysing these anomalies, we identified the mean biases, RMSD and correlations between the in situ data and the reanalysis.

For all simulations, we set the absorption enhancement parameter B0 to 1.6, which is used to calculate the shape parameter B to describe the effects of the ice matric shape in the radiation theory, in agreement with other studies (Libois et al., 2013; Tuzet et al., 2020). As we had no measurements for wet and dry black carbon deposition rates, we used results from Tuzet et al. (2020) for the French Alps as indication, but assumed lower rates for northeast Greenland. Therefore, we set wet and dry constant deposition rates to 6.67 x 10^{-11} g m^{-2} s^{-1} and 3.33 x 10^{-11} g m^{-2} s^{-1}, respectively.

ERA5

Several data conversions were needed to drive Crocus: (i) ERA5 provides the variables snowfall and precipitation. However, model tests showed a better agreement between simulated and observed snow depths when splitting ERA5's total precipitation rate into liquid and solid precipitation rates after Jennings et al. (2018). Therefore, precipitation at temperatures of +1°C or warmer is handled as liquid precipitation and the residual as snowfall. (ii) Incident shortwave radiation was split into diffuse and direct shortwave radiation using the zenith angle depending on the solar declination, the local time and latitude. (iii) Wind speed and wind direction were calculated from the wind vector and (iv) specific humidity from surface air pressure, temperature and dew point temperature according to Willett et al. (2008).

In situ

Most of the surface input variables required by Crocus were measured directly. However, some conversions had to be carried out to get all required forcing variables in the appropriate form: (i) Precipitation was split in liquid and solid phase after Jennings et al. (2018), as it was done for the ERA5 precipitation. (ii) The zenith angle depending on the solar declination, the local time and latitude is used to separate incident shortwave radiation into diffuse and direct shortwave radiation. (iii) The Magnus-equation (Magnus, 1844) is applied to calculate specific humidity from the measured surface air pressure, air temperature, and relative humidity.

B.2 Visualisation of SnowMicroPen (SMP) data

We compared the snow density profiles obtained from the SMP after Calonne et al. (2020) on 23 March 2018 with the simulations (Fig. 8a). Since we do not have measurements of the total snow depth of the SMP data, we cannot compare the results of the SMP measurements and the simulations for the depth directly. Instead, a constant snow depth (the maximum snow depth of all simulations and observations during PAMARCMiP: 2.4 m) was assumed as the total snow depth for all profiles. The penetration depth of the SMP measurements as well as the simulated profiles were thus displayed up to the last measurement point or to the absolute simulated snow depth from the snow surface down from the somewhat arbitrary maximal snow depth of 2.4 m.

B.3 Additional figures and tables

Table B.1: Time periods analysed and used for simulations.

27 Nov 2015 – 8 Aug 2018	in situ measured atmospheric forcing
26 Aug 2014 – 30 Sep 2018	in situ measured snow depth
10 March 2018 – 8 Apr 2018	PAMARCMiP campaign
Jan 2010 – Dec 2019	spin-up run for ERA5 simulations
Jan 2010 – Dec 2019 + Jan 2010 – 26 Nov 2015	spin-up run for in situ simulations
Jan 2010 – Aug 2020	time period used to calculate more reliable standard deviation for sensitivity simulation

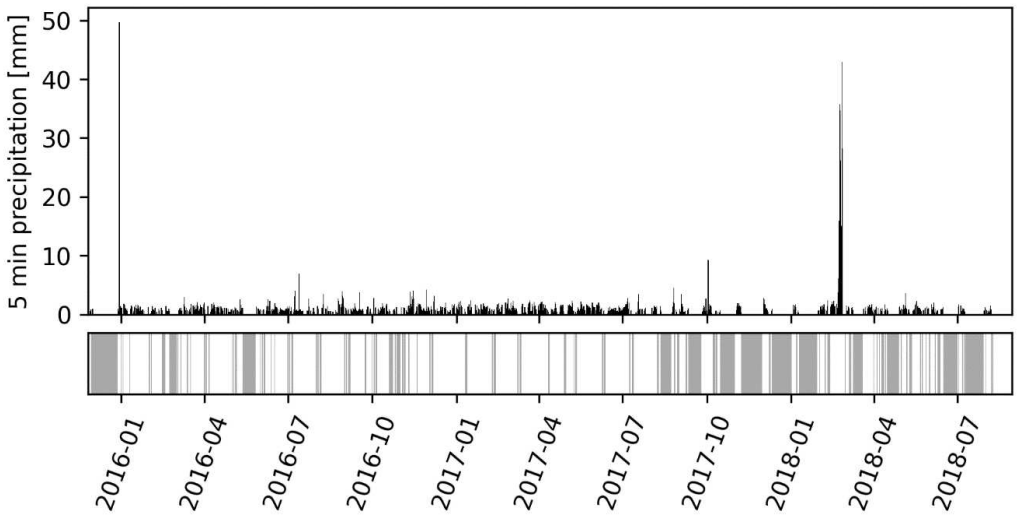

Figure B.1: Upper panel: Every five minutes measured precipitation at Villum Research Station. Lower panel: Data gaps in grey, data in white shaded areas. Note the strong precipitation event in late February 2018 caused by the extreme intrusion of warm air masses from the southwest.

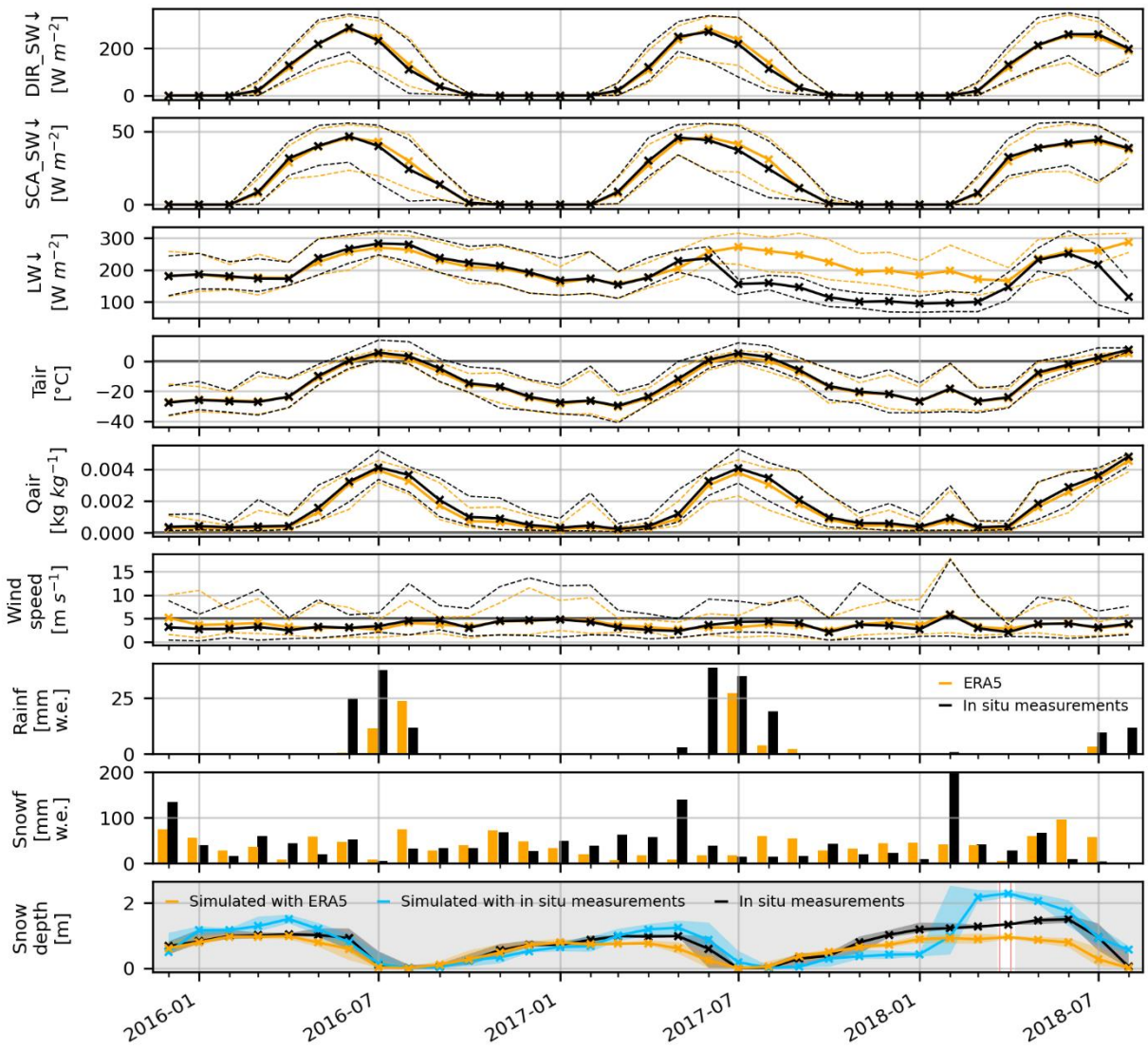

Figure B.2: Measured and ERA5 atmospheric variables. The solid lines show the monthly mean, the dashed lines the monthly minimum and maximum values, respectively. Note the measuring failures in the longwave radiation from June 2017 to April 2018 and again after June 2018. In the lowest panel, monthly minimum and maximum values are represented by the filled areas. The white area in the lowest panel represents the time of the PAMARCMiP campaign 2018 and the vertical red lines the dates of the snowpits. DIR_SW: Direct incoming shortwave radiation, SCA_SW: Diffuse incoming shortwave radiation, LW: Incoming longwave radiation, Tair: Air temperature, Qair: Specific humidity, Rainf: Rainfall, and Snowf: Snowfall in water equivalent (w.e.).

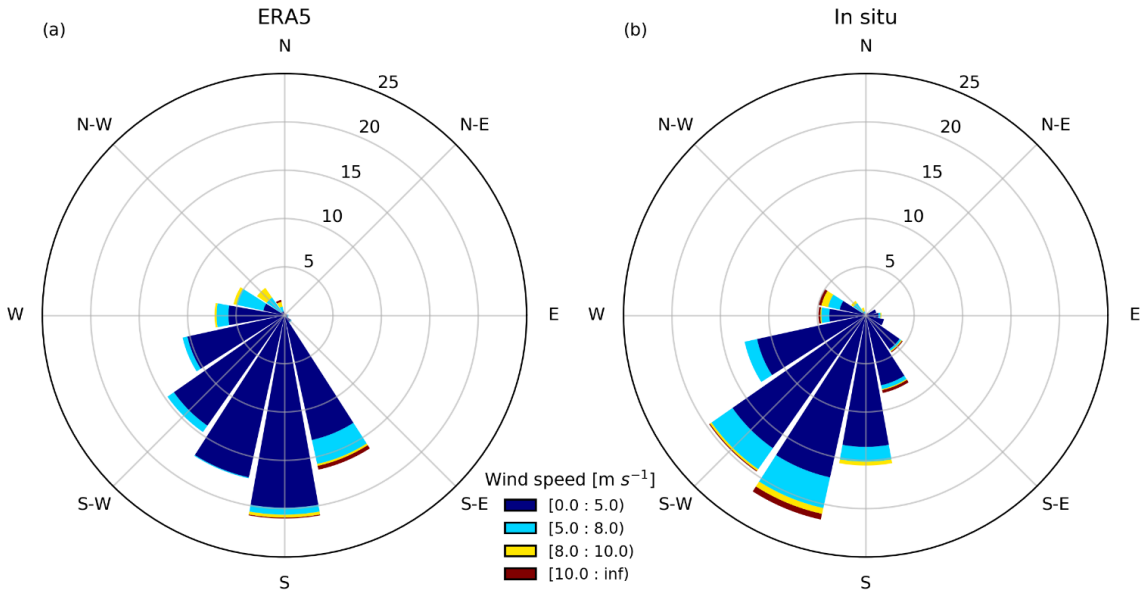

Figure B.3: Daily mean wind speed and wind direction for (a) ERA5 data and (b) in situ data. Wind speed is indicated by colour, numbers represent the frequency of wind direction occurrence in percent.

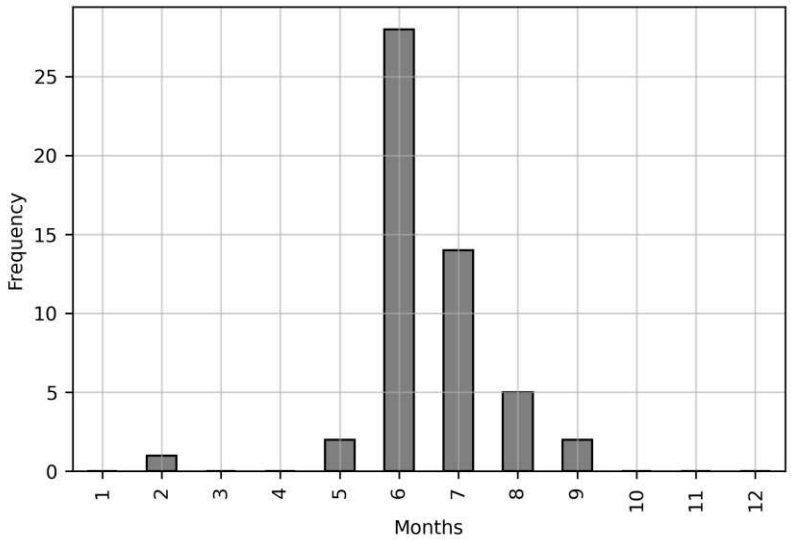

Figure B.4: Timing and frequency of rain on snow events during available precipitation measurements from 26 November 2015 to 8 August 2018, i.e. on the 987 days.

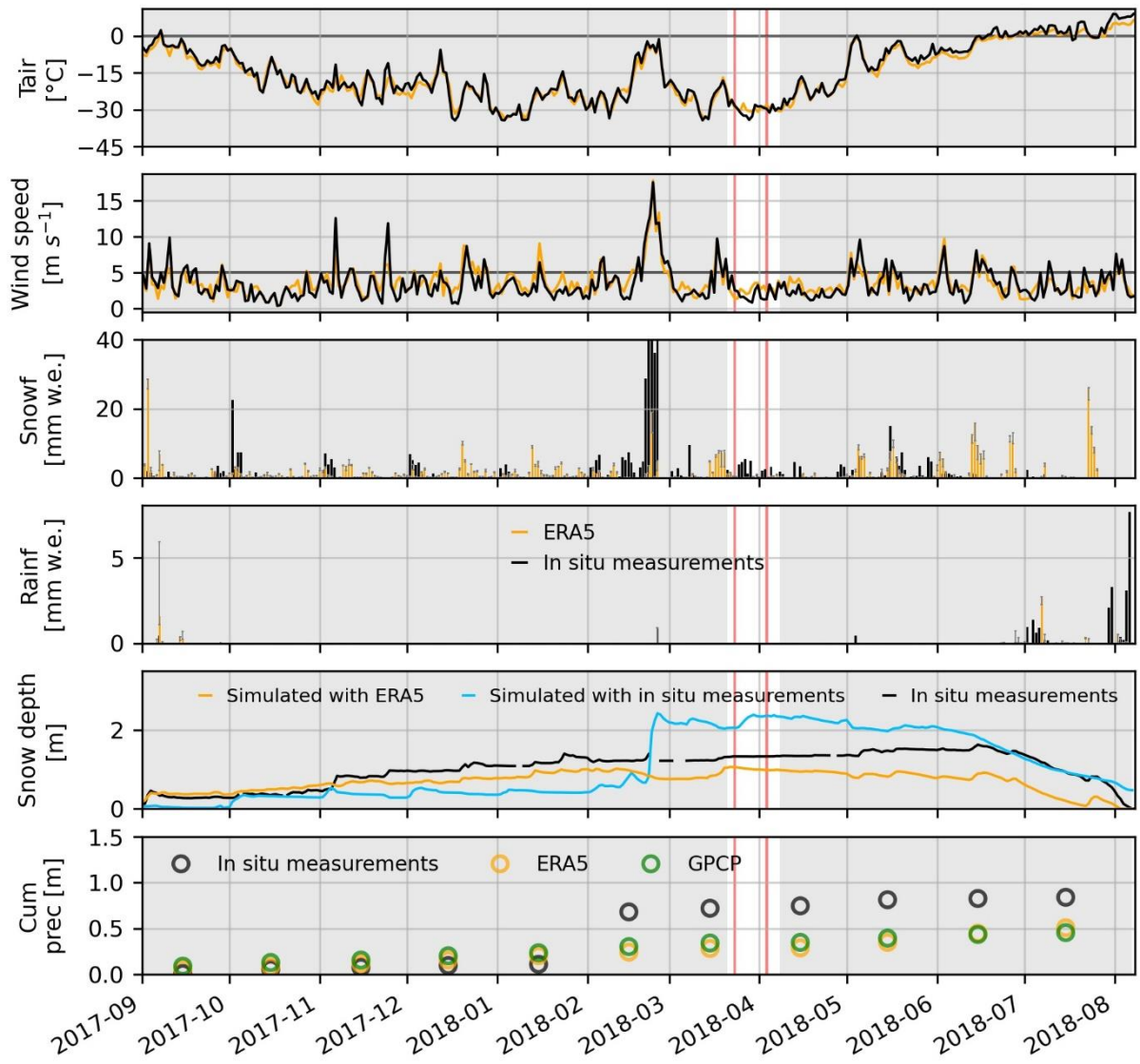

Figure B.5: Atmospheric development from 01 September 2017 to 07 August 2018. PAMARCMiP time is shown as the white and red area, whereby the red area is the time of the snowpit measurements. All variables are daily except cumulative total precipitation, which is monthly. Note the high snowfall at the end of February 2018. The range of the abscissa is cut off. Figure 6.6 provides a detailed visualisation of this period.

C Appendix to Chapter 7

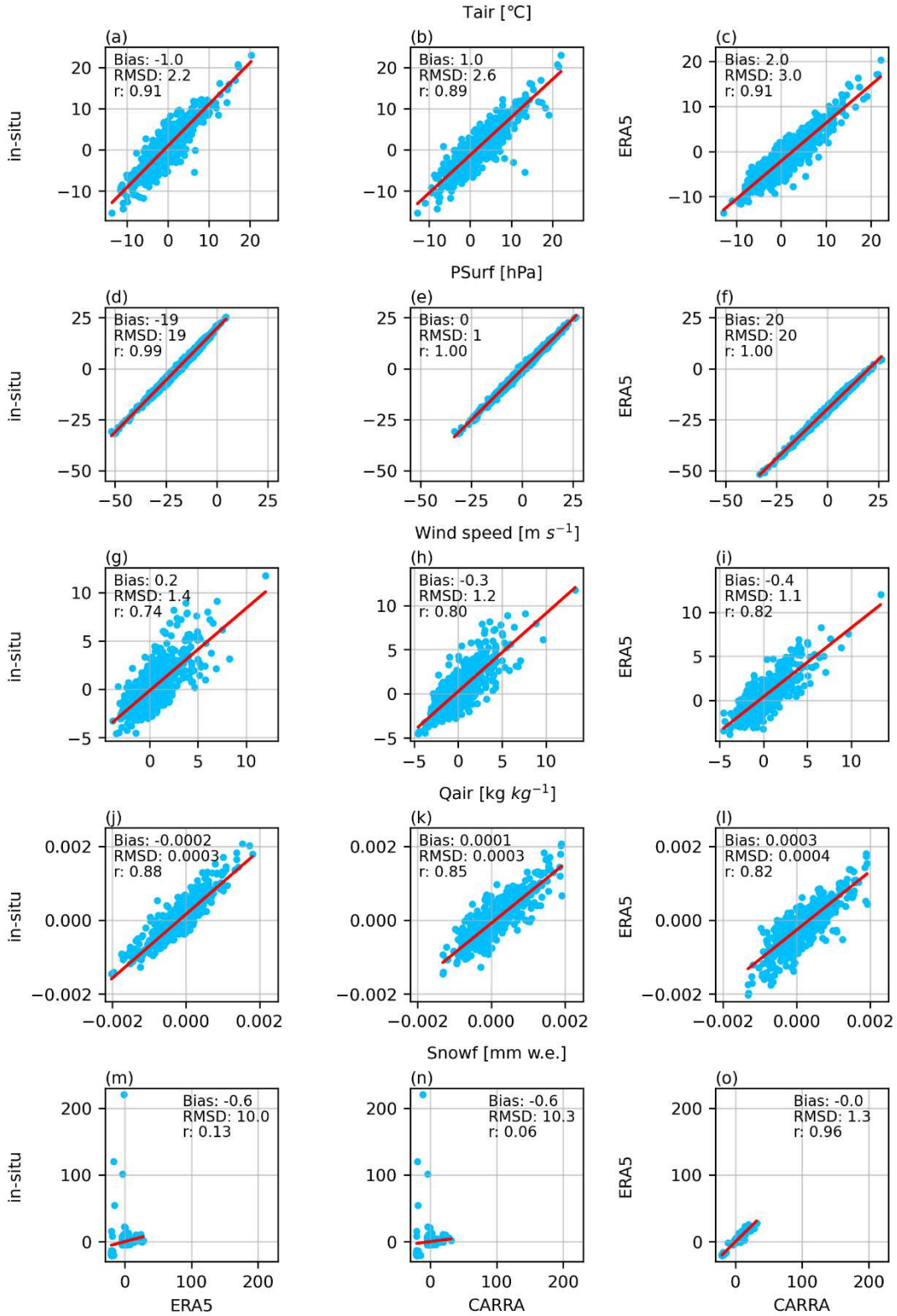

Figure C.1: Scatter plots of daily anomalies (reanalyses – measurements). 1st column: ERA5 and in-situ, 2nd column: CARRA and in-situ and 3rd column: CARRA and ERA5. Metrics inserted into each panel are the mean bias calculated as reanalyses – measurements and CARRA – ERA5, respectively, root mean square difference (RMSD) and correlation coefficient (r). The red line depicts the regression line. Mean biases are defined for the three columns as ERA5 – in-situ, CARRA – in-situ and CARRA – ERA5, respectively. w.e. refers to water equivalent.

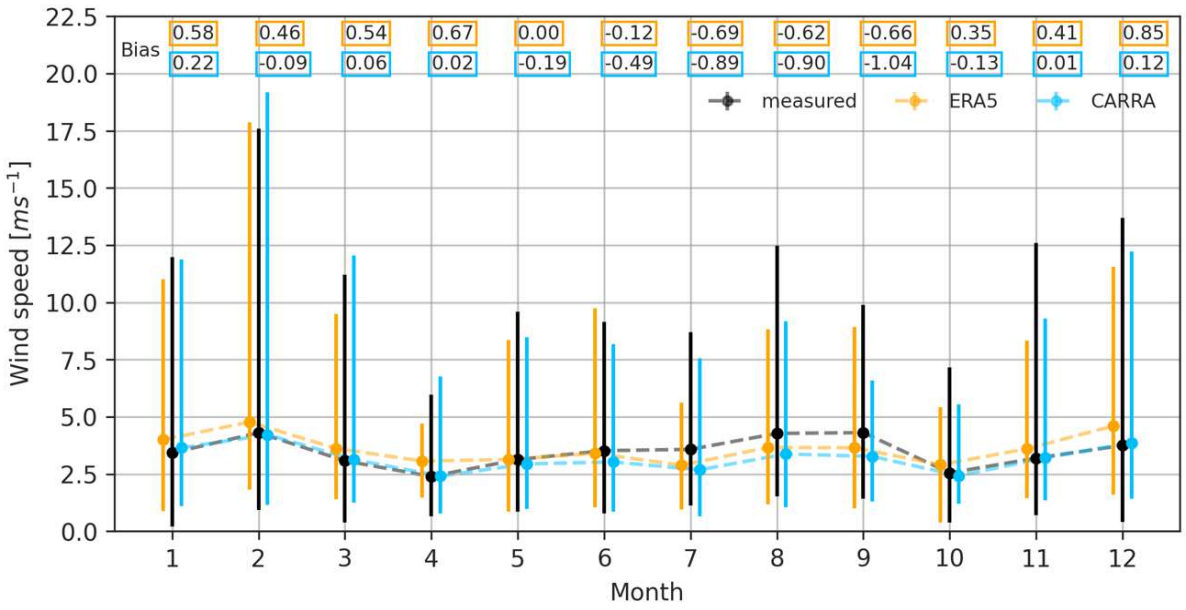

Figure C.2: Yearly mean monthly wind speed calculated from daily mean values from 27 November 2015 to 8 August 2018 from CARRA, ERA5 and measurements. The dots represent mean while the bars represent minimal and maximum values.

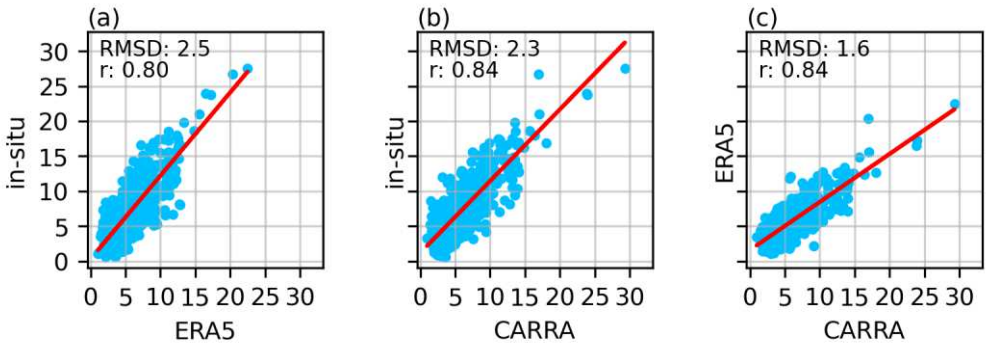

Figure C.3: Scatter plots and metrics of daily maximum wind speed. For (a) in-situ vs. ERA5, (b) in-situ vs. CARRA, and (c) ERA5 vs. CARRA. Metrics inserted into each panel are the root mean square difference (RMSD) and correlation coefficient (r). The red line depicts the regression line.

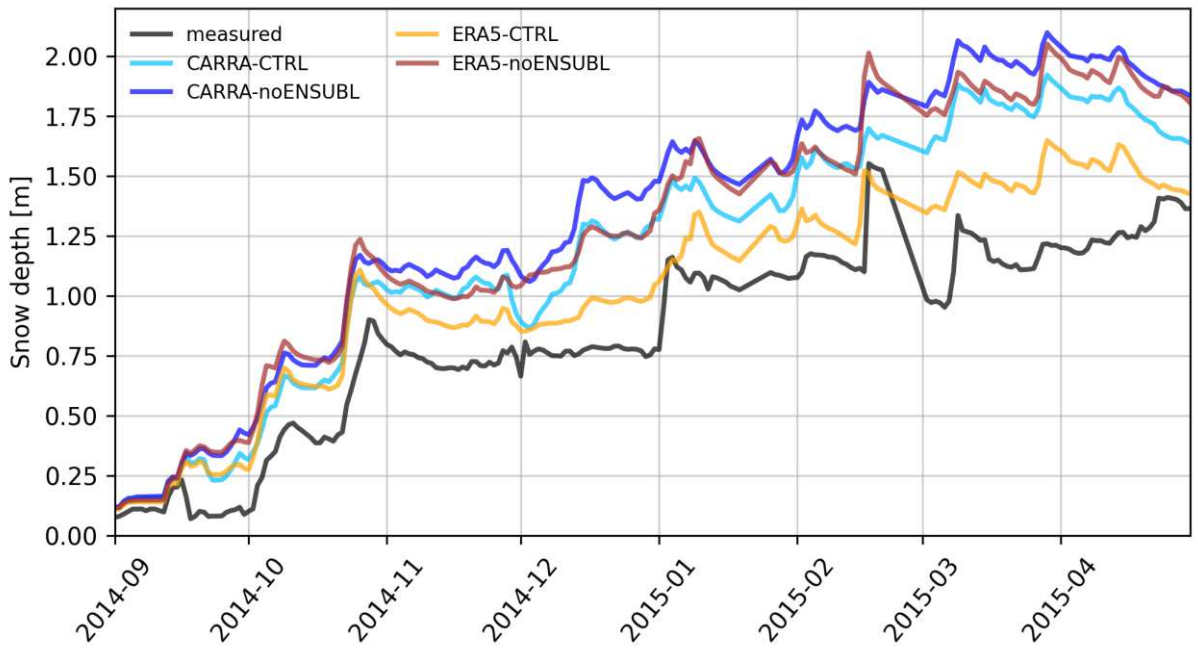

Figure C.4: Time series for snow depth from 1 September 2014 to 30 April 2015. Simulated with ERA5 forcing and CARRA forcing with and without enhanced sublimation during wind drift. The black line depicts the measured snow depth.

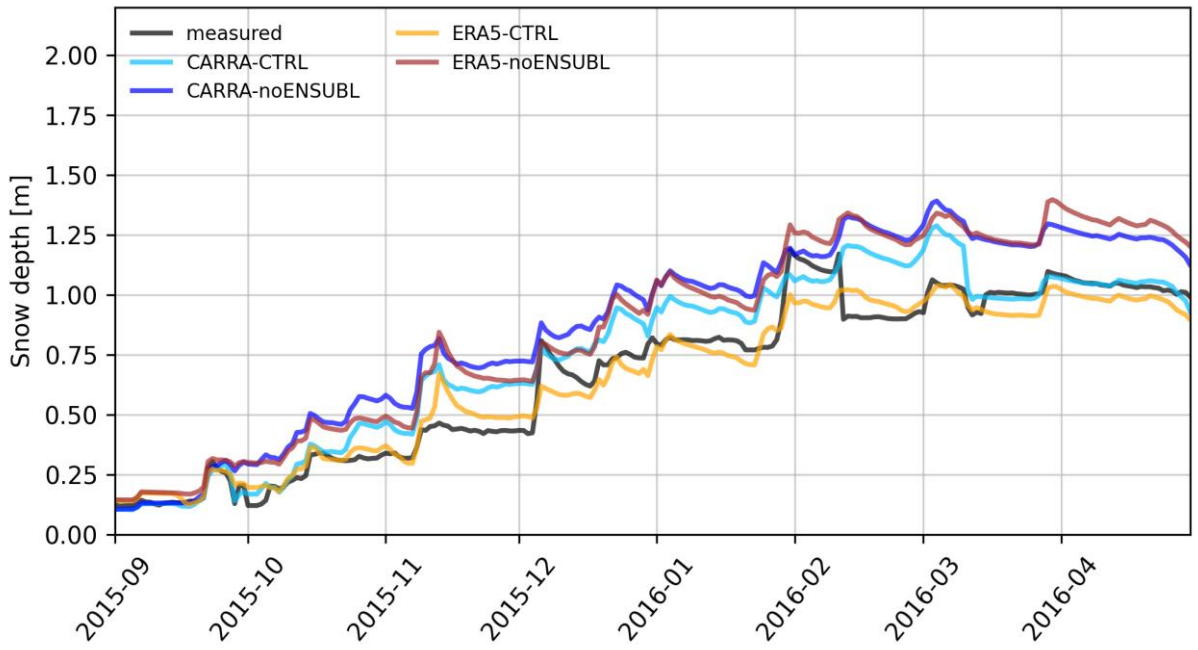

Figure C.5: Time series for snow depth from 1 September 2015 to 30 April 2016. Simulated with ERA5 forcing and CARRA forcing with and without enhanced sublimation during wind drift. The black line depicts the measured snow depth.

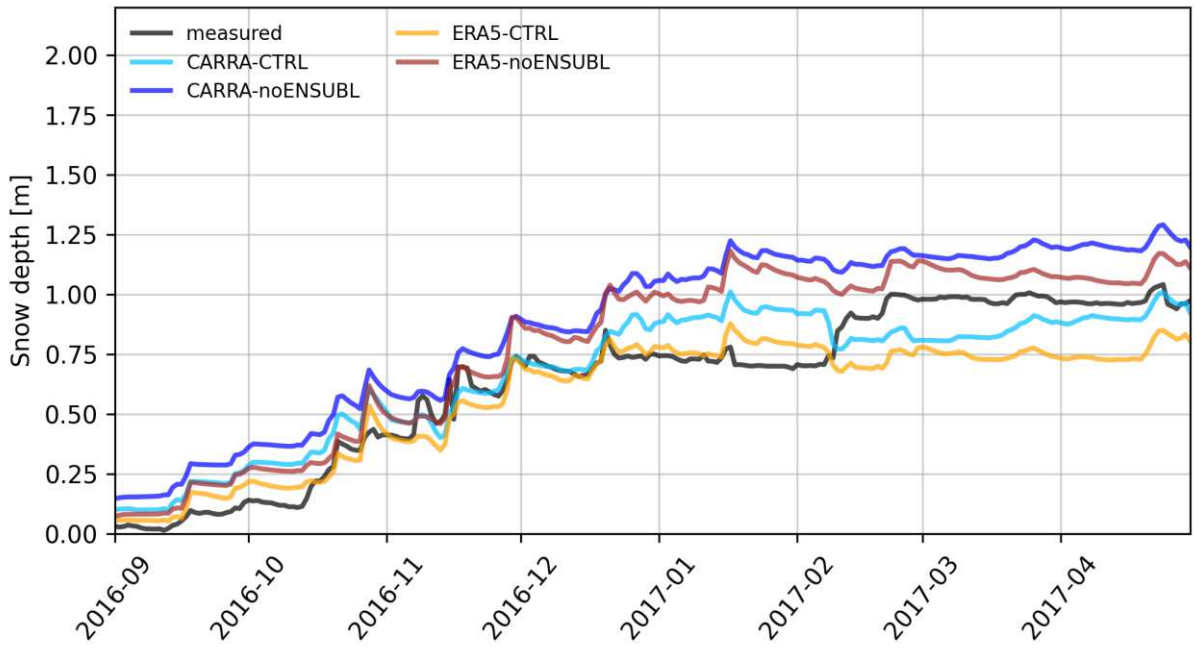

Figure C.6: Time series for snow depth from 1 September 2016 to 30 April 2017. Simulated with ERA5 forcing and CARRA forcing with and without enhanced sublimation during wind drift. The black line depicts the measured snow depth.

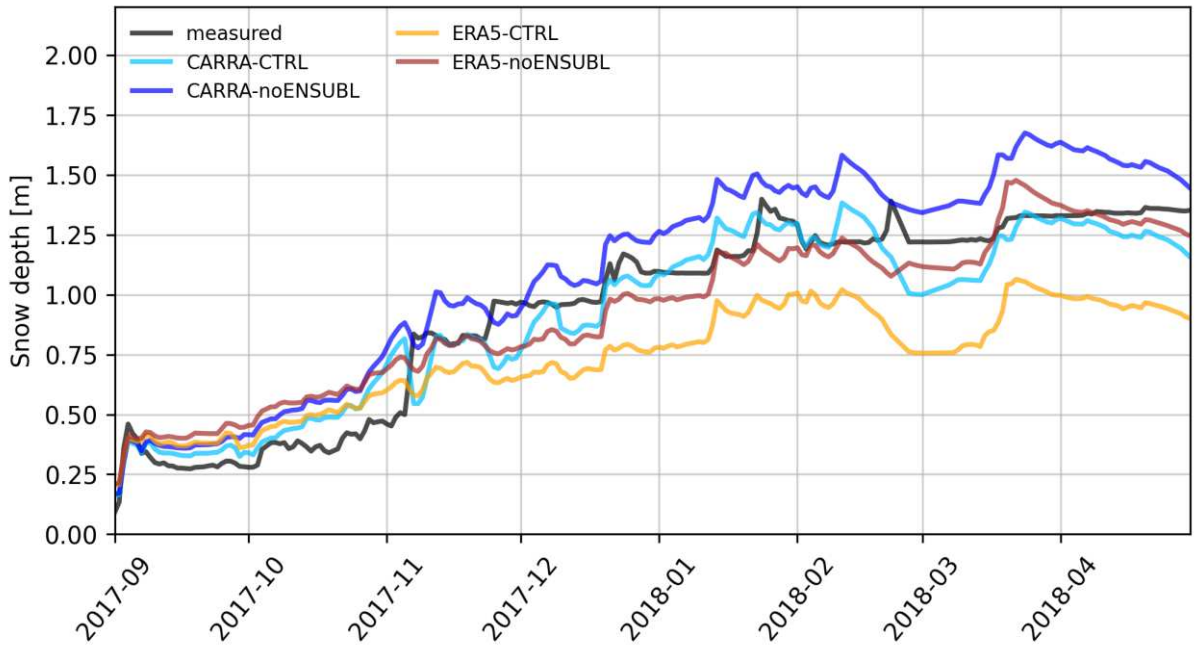

Figure C.7: Time series for snow depth from 1 September 2017 to 30 April 2018. Simulated with ERA5 forcing and CARRA forcing with and without enhanced sublimation during wind drift. The black line depicts the measured snow depth.

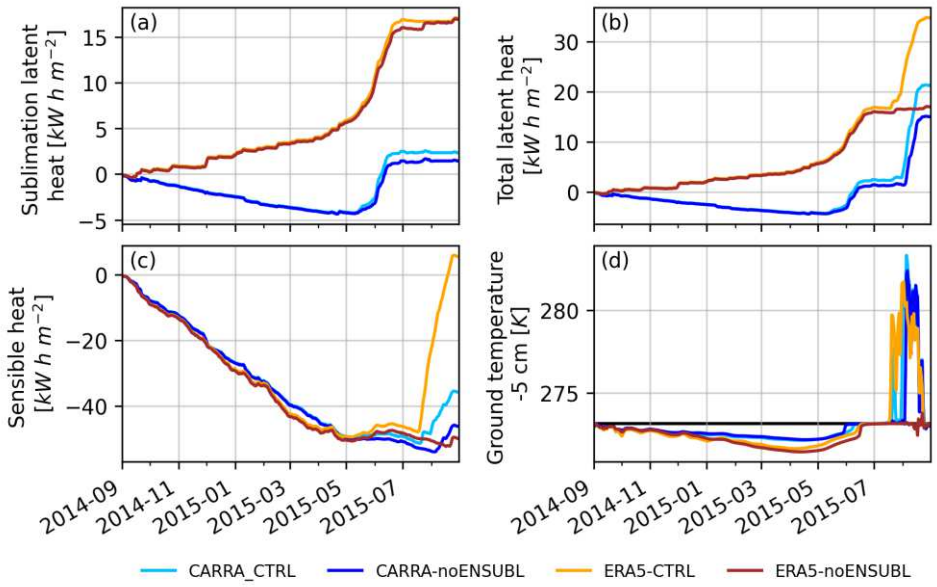

Figure C.8: Cumulated heat. Simulated (a) latent heat due to sublimation, (b) total latent heat, (c) sensible heat and (d) ground temperature 5 cm into the soil for 2014/15. Note that the direct effects of enhanced sublimation during strong winds are not considered in (a). Indirect effects due to changed surface properties cause the differences in (a) between noENSUBL and CTRL simulations.

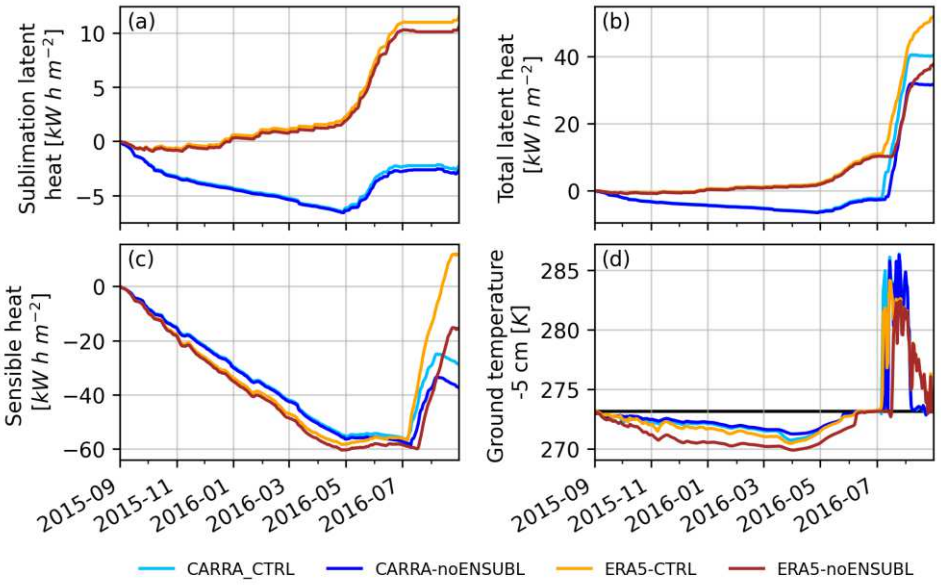

Figure C.9: Cumulated heat. Simulated (a) latent heat due to sublimation, (b) total latent heat, (c) sensible heat and (d) ground temperature 5 cm into the soil for 2015/16. Note that the direct effects of enhanced sublimation during strong winds are not considered in (a). Indirect effects due to changed surface properties cause the differences in (a) between noENSUBL and CTRL simulations.

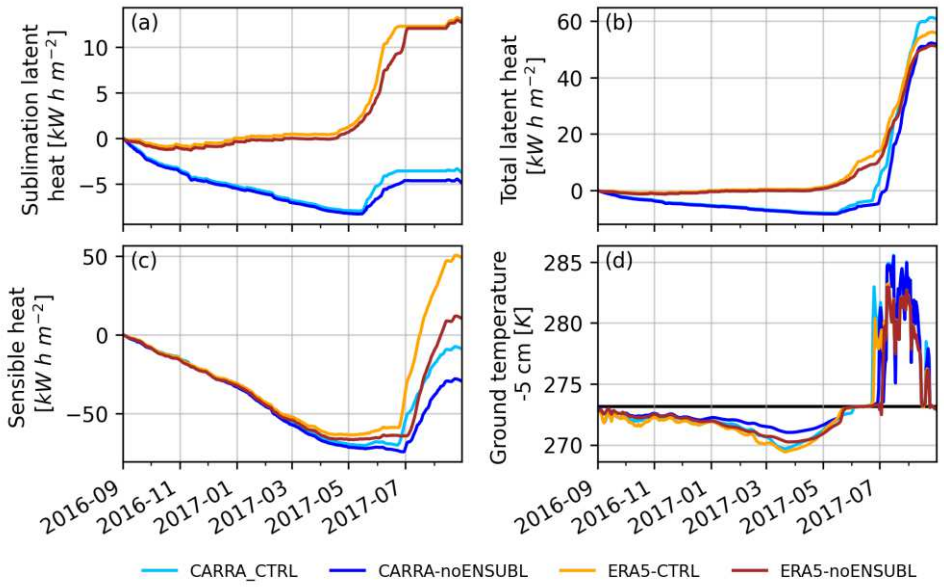

Figure C.10: Cumulated heat. Simulated (a) latent heat due to sublimation, (b) total latent heat, (c) sensible heat and (d) ground temperature 5 cm into the soil for 2016/17. Note that the direct effects of enhanced sublimation during strong winds are not considered in (a). Indirect effects due to changed surface properties cause the differences in (a) between noENSUBL and CTRL simulations.

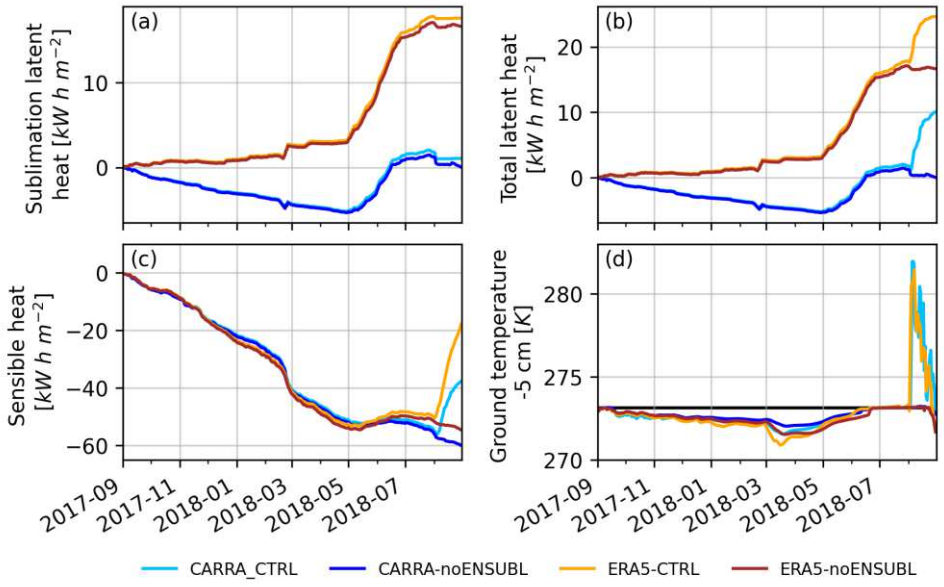

Figure C.11: Cumulated heat. Simulated (a) latent heat due to sublimation, (b) total latent heat, (c) sensible heat and (d) ground temperature 5 cm into the soil for 2017/18. Note that the direct effects of enhanced sublimation during strong winds are not considered in (a). Indirect effects due to changed surface properties cause the differences in (a) between noENSUBL and CTRL simulations.

D Appendix to Chapter 8

D.1 Additional figures

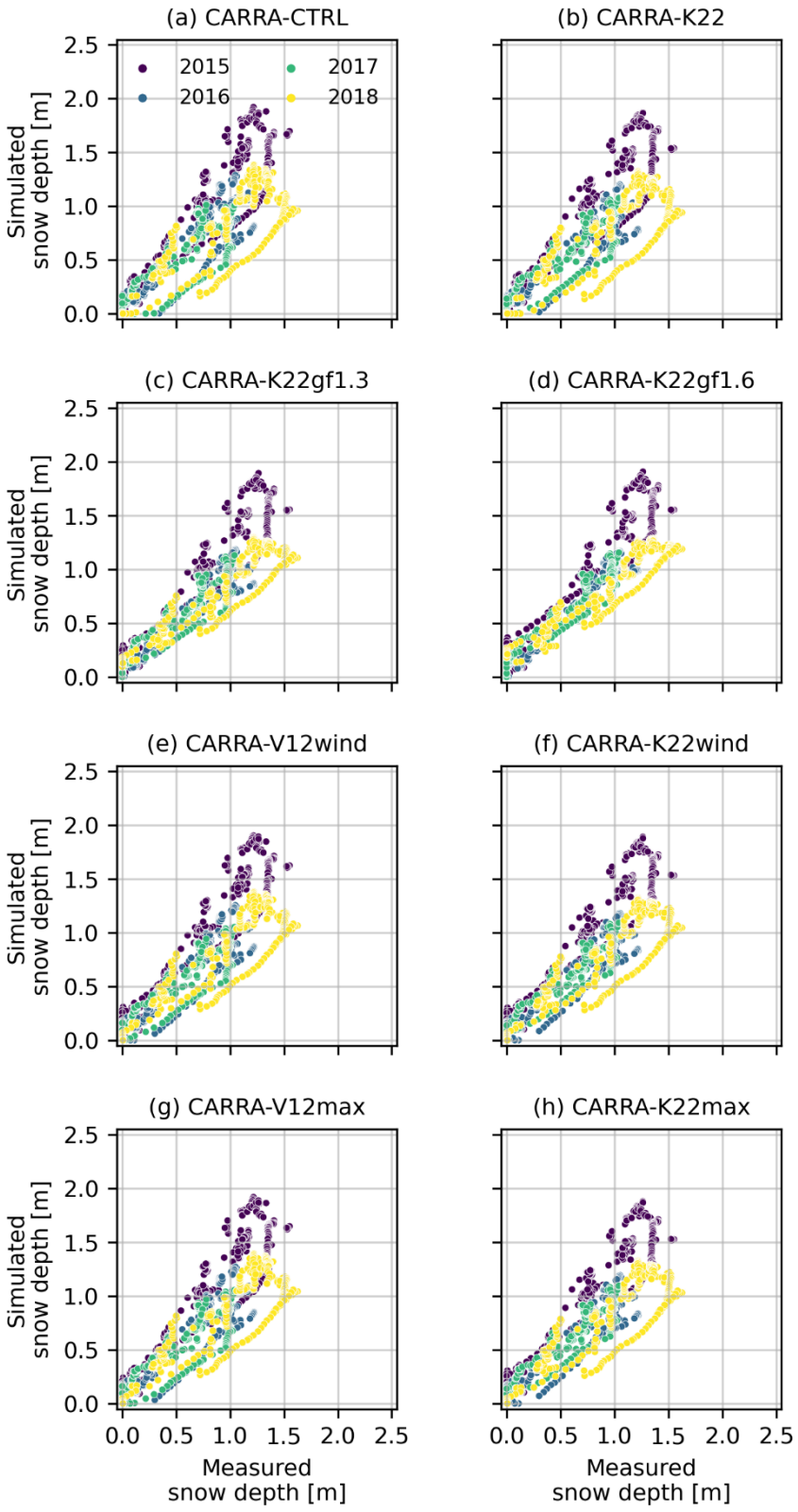

Figure D.1: Scatter diagram of measured and simulated daily snow depth between September 2014 and August 2018 using the different parameterisations described in Chapter 8.2. The different colours visualise different years, whereby 2015 denotes to the snow season 2014/2015 and so on.

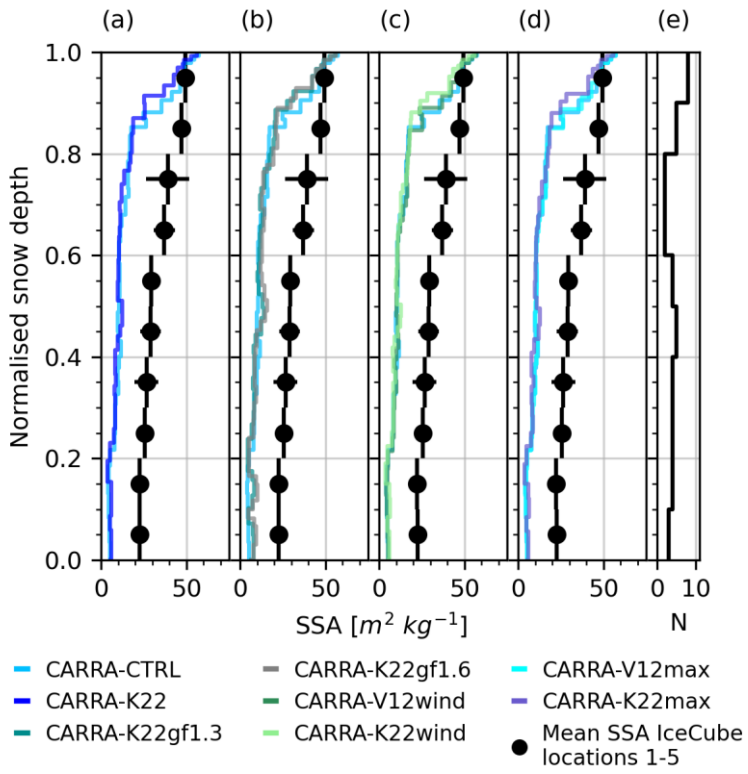

Figure D.2: (a) – (d): Simulated and measured snow specific surface area (SSA) from 3 April 2018 using different parameterisations described in Chapter 8.2. (e) shows the sample frequency of IceCube measurements.

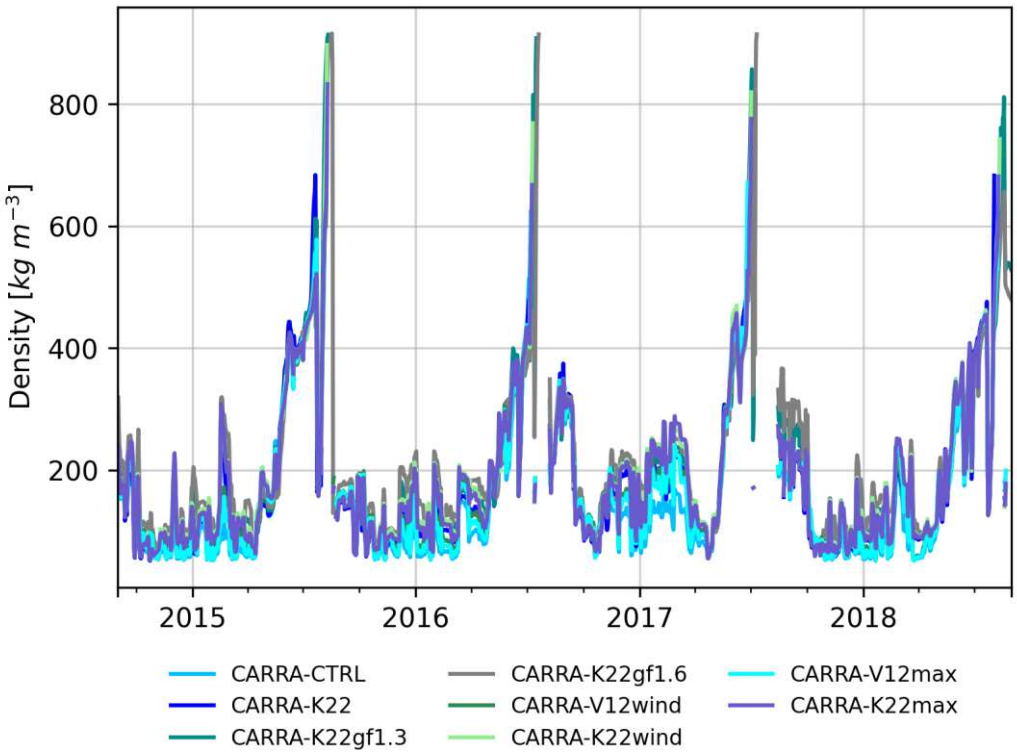

Figure D.3: Time series of upper snow density (upper 10 cm) simulated with different parameterisations described in Chapter 8.2 from September 2014 to August 2018.

D.2 Additional analyses with ERA5 and atmospheric in-situ measurements

In addition to the application of the new snow parameterisation K22 with CARRA forcing, I also tested its performance using ERA5 and atmospheric in-situ measurements as forcing (see Chapter 6 for description of the forcing and the set-up of the model simulations). The time series of measured snow depth and simulated snow depth using the default parameterisation (V12, CTRL-simulations) and the introduced parameterisation (K22, NSD-simulations) for new snow density is shown in Figure D.4 using ERA5 and atmospheric in-situ measurements as forcing, respectively.

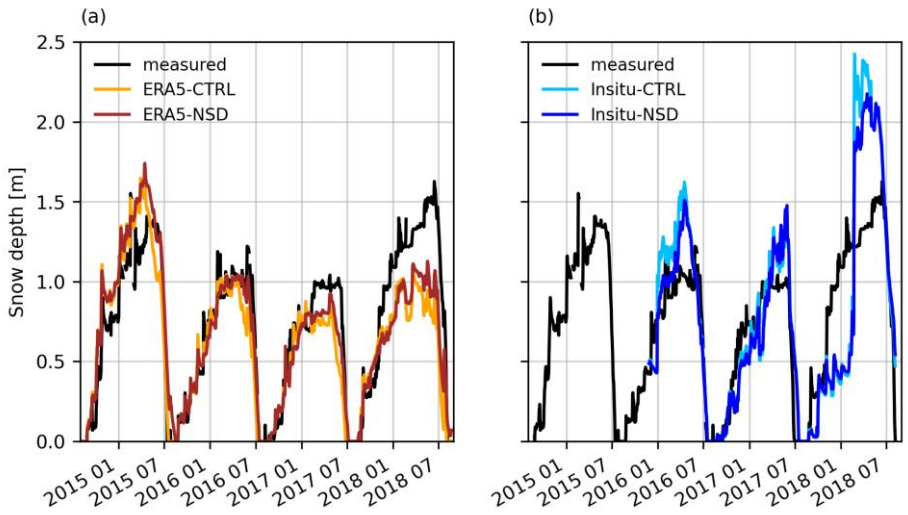

Figure D.4: The measured and with the new snow density parameterisation V12 (CTRL) and the introduced K22 parameterisation (NSD) simulated snow depth. (a) ERA5 simulations from August 2014 to August 2018 and (b) in-situ simulations from 27 November 2015 to August 2018.

ERA5-NSD's snow depths were higher and more in correspondence to the measurements towards the end of the snow season than ERA5-CTRL's. Especially in 2016/17, the differences in snow depth during the melting phase were improved considerably. Insitu-NSD showed clearly lower snow depths than Insitu-CTRL for 2015/16 and 2017/18 leading to a better agreement with measured snow depth.

With the introduced new snow density parameterisation K22, I could reduce mean bias and RMSD of ERA5 forced simulated snow depth by 0.04 m and 0.07 m, respectively (see ERA5-NSD, Figure D.5). Furthermore, the explained variance increased by 11 % to 84 %. The Insitu-NSD's snow depth mean bias and RMSD could be improved by 0.04 m and 0.05 m, respectively. The explained variance increased by 17 % to 40 %.

In addition to the density cutter measurements and the IceCube measurements from 3 April 2018 used for validation of the CARRA-simulations, here I also used SMP measurements conducted on 23 March 2018, further described in Chapter 6. The measurements are not used for the validations of CARRA-simulations, as they do not cover the entire snow profile.

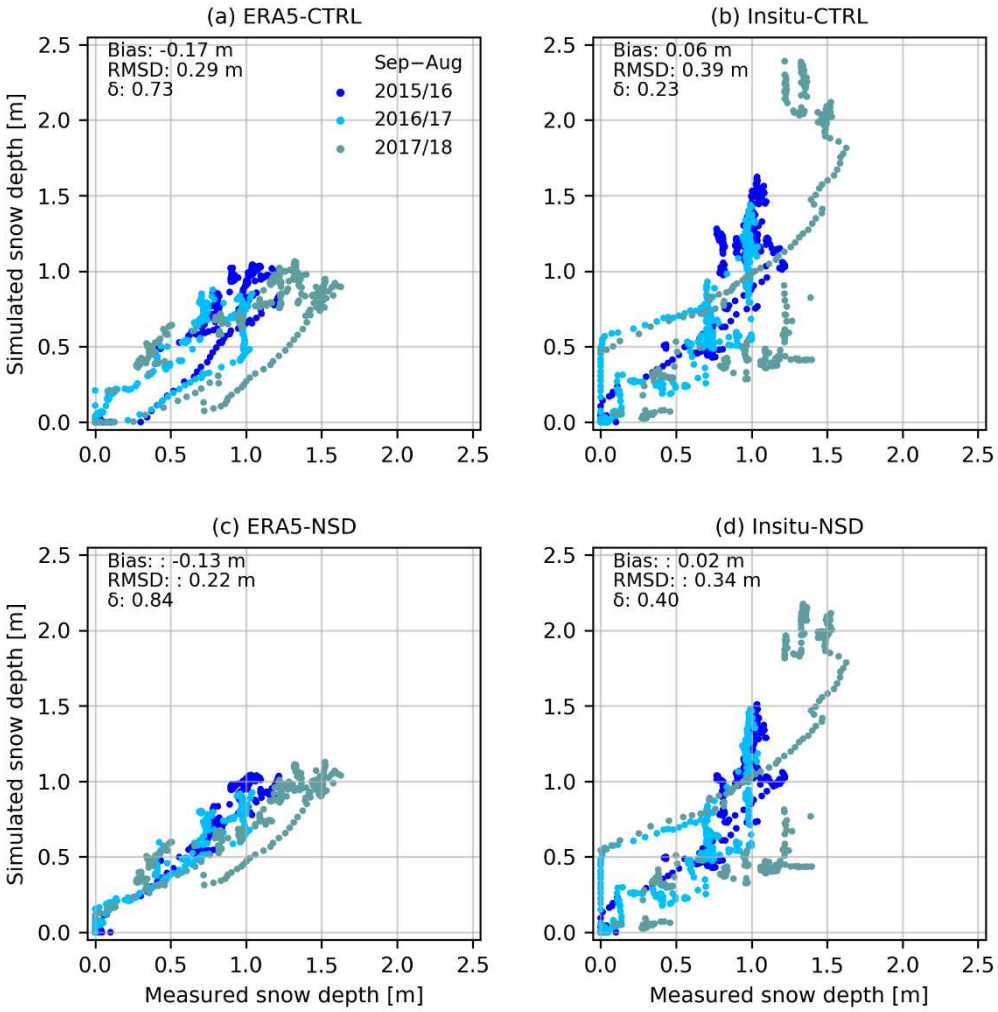

Figure D.5: Scatter diagram of measured and simulated daily snow depth between 27 November 2015 and 8 August 2018. The different colours visualise different years (a) and (b): ERA5-CTRL and Insitu-CTRL results with original parameterisation of new snow density V12 (c) and (d) ERA5-NSD and Insitu-NSD with the adapted new snow density parameterisation K22. Metrics displayed are the mean bias, root mean squared difference (RMSD) and explained variance δ.

Applying K22, I obtained more reliable density profile simulations than using the default parameterisation V12. The simulated snow densities showed a much higher variability with several distinct density peaks, which were also visible in the SMP profiles and the density cutter profiles (Figure D.6 and Figure D.7). The densities simulated with K22 were also considerably higher than simulated with V12. In ERA5-NSD, the vertical mean density on 23 March 2018 increased by 36 kg m^{-3} and on 3 April 2018 by 15 kg m^{-3}. In Insitu-NSD the vertical mean density increased by 51 kg m^{-3} and by 66 kg m^{-3} on the same dates, respectively (see also Table D.1) . Furthermore, the snow density not only increased with depth when applying K22, but also showed more pronounced variability.

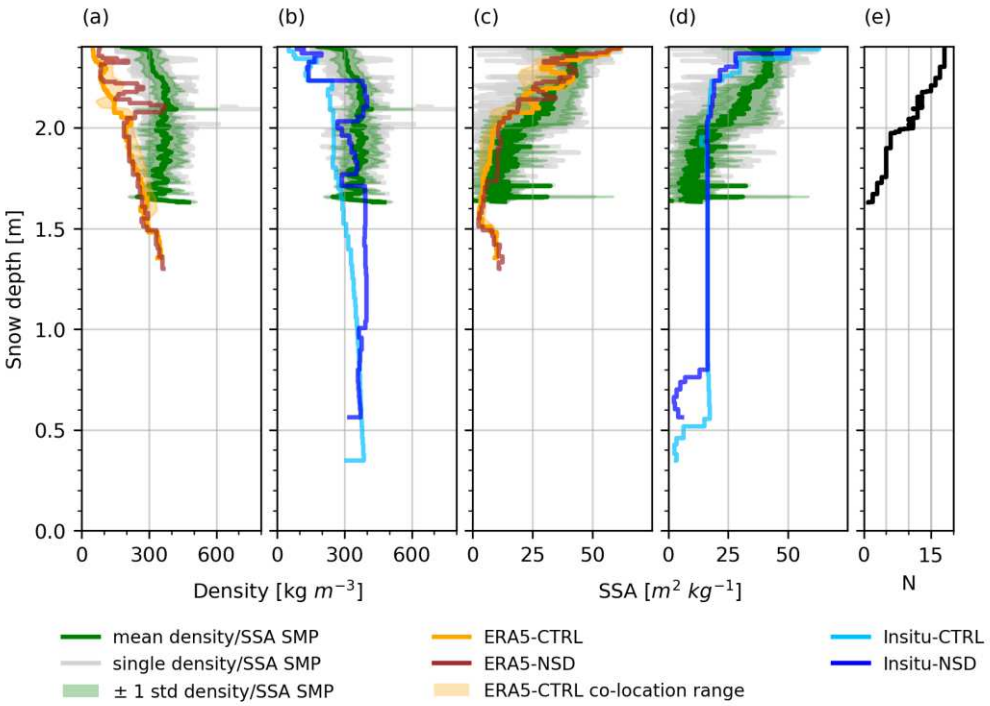

Figure D.6: Simulated and measured snow density and specific surface area (SSA) on 23 March 2018. Measured density and SSA are derived after Calonne et al. (2020) from the SnowMicroPen (SMP). (a) and (b) display snow density, (c) and (d) SSA and (e) the sampling frequency of SMP measurements. "CTRL" use the new snow density parameterisation V12 and "NSD" use K22. Snow depth baseline is the maximum snow depth during PAMARCMiP (Polar Airborne Measurements and Arctic Regional Climate Model Simulation Project) campaign of all measurements and simulations (2.4 m) (see explanation in the Appendix). Single density/SSA SMP shows measured single SMP profiles. The meaning of the colours are expressed in the legend. SMP did not penetrate the entire snowpack.

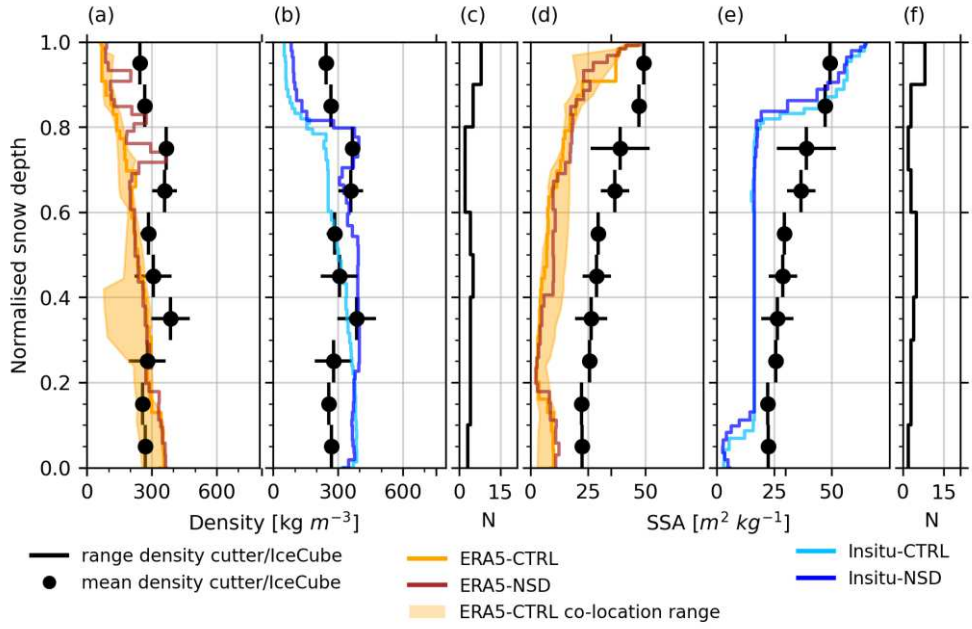

Figure D.7: Simulated and measured snow density from density cutter and specific surface area (SSA) from IceCube on 3 April 2018. (a) and (b) snow density, (d) and (e) SSA and (c) and (f) the sampling frequency of density cutter measurements and IceCube measurements, respectively. "CTRL" use the new snow density parameterisation V12 and "NSD" use K22.

K22 affected the simulated SSA to a smaller extent than the snow density. Overall, on 23 March 2018 the SSA profile of ERA5-NSD was similar to ERA5-CTRL (Figure D.6) with a small increase in mean vertical averaged SSA of +0.8 m^2 kg^{-1} (see Table D.1). SSA in Insitu-NSD changed mainly in the upper and in the lower part of the profile: After a decrease of SSA to 20 m^2 kg^{-1}, SSA remained constant as in Insitu-CTRL. The difference in mean SSA over the entire profile on 23 March 2018 for the in-situ simulations was -1.4 m^2 kg^{-1}. Similar changes as on 23 March 2018 between the use of K22 instead of V12 are also visible on 3 April 2018 (Figure D.7) with differences in mean SSA of +2.5 m^2 kg^{-1} for ERA5 simulations and -2.8 m^2 kg^{-1} for in-situ simulations.

Table D.1: Snow SSA and density obtained using the CTRL-simulations compared to the NSD-simulations. Std: Standard deviation.

Variable	Date	Simulation	Minimum	Maximum	Mean	Std
Snow SSA [m^2 kg^{-1}]	23 March 2018	ERA5-CTRL	2.7	62.0	22.3	17.0
		ERA5-NSD	2.3	61.1	23.1	16.0
		Insitu-CTRL	2.5	63.1	19.3	11.6
		Insitu-NSD	2.3	50.7	17.9	10.1
	3 April 2018	ERA5-CTRL	2.7	46.6	13.7	11.8
		ERA5-NSD	2.3	47.5	16.2	11.1
		Insitu-CTRL	3.0	65.0	25.0	18.0
		Insitu-NSD	2.6	64.8	22.2	17.0
Snow density [kg m^{-3}]	23 March 2018	ERA5-CTRL	50.1	353.2	176.9	93.6
		ERA5-NSD	74.7	371.0	212.6	95.4
		Insitu-CTRL	51.7	386.6	279.4	96.0
		Insitu-NSD	87.3	399.7	329.7	92.1
	3 April 2018	ERA5-CTRL	65.4	356.7	216.4	89.6
		ERA5-NSD	85.0	368.6	230.8	89.5
		Insitu-CTRL	50.0	386.4	248.2	120.3
		Insitu-NSD	82.3	399.1	311.7	114.7

The additional comparison of the performance of simulations using the V12-parameterisation and K22-parameterisation for new snow density shows, that the proposed parameterisation does not only show improvements using CARRA to force the snow model but also when forcing the model with other forcing datasets as ERA5 and atmospheric in-situ measurements.

E Appendix to Chapter 9

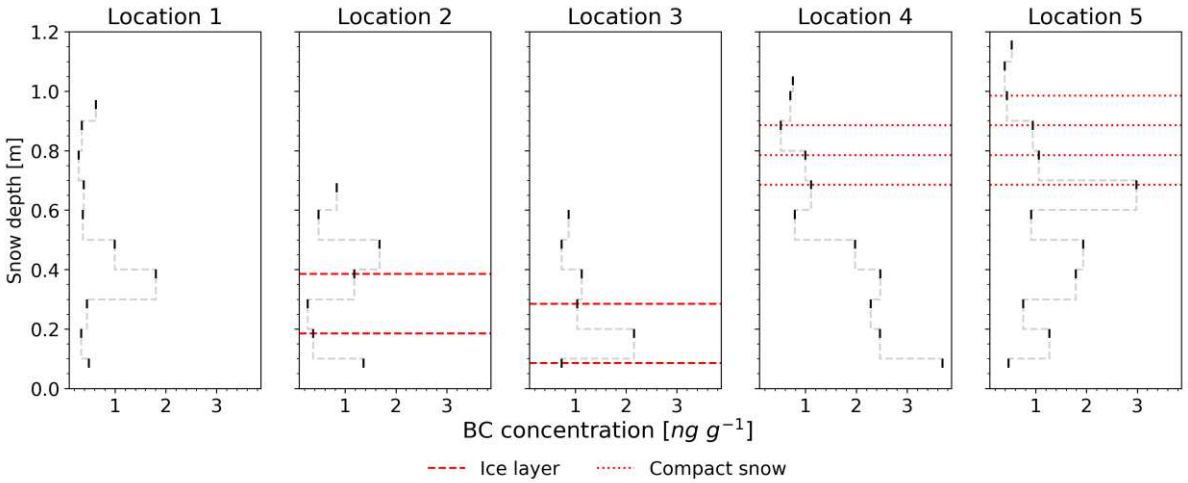

Figure E.1: Observed black carbon (BC) concentrations in black. Measurements from 3 April 2018. Note the difference snow depth of the five profiles.

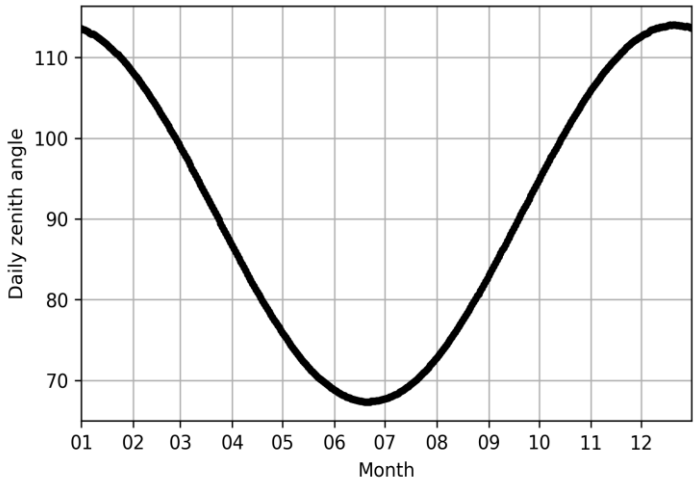

Figure E.2: Daily zenith angle for the position of the atmospheric in-situ measurements of Villum research Station (81.6°N, 16.67°E). Note that a zenith angle of ≥90° means that the sun is below the horizon while a zenith angle of 0°C would mean the sun is in zenith and therefore directly overhead.

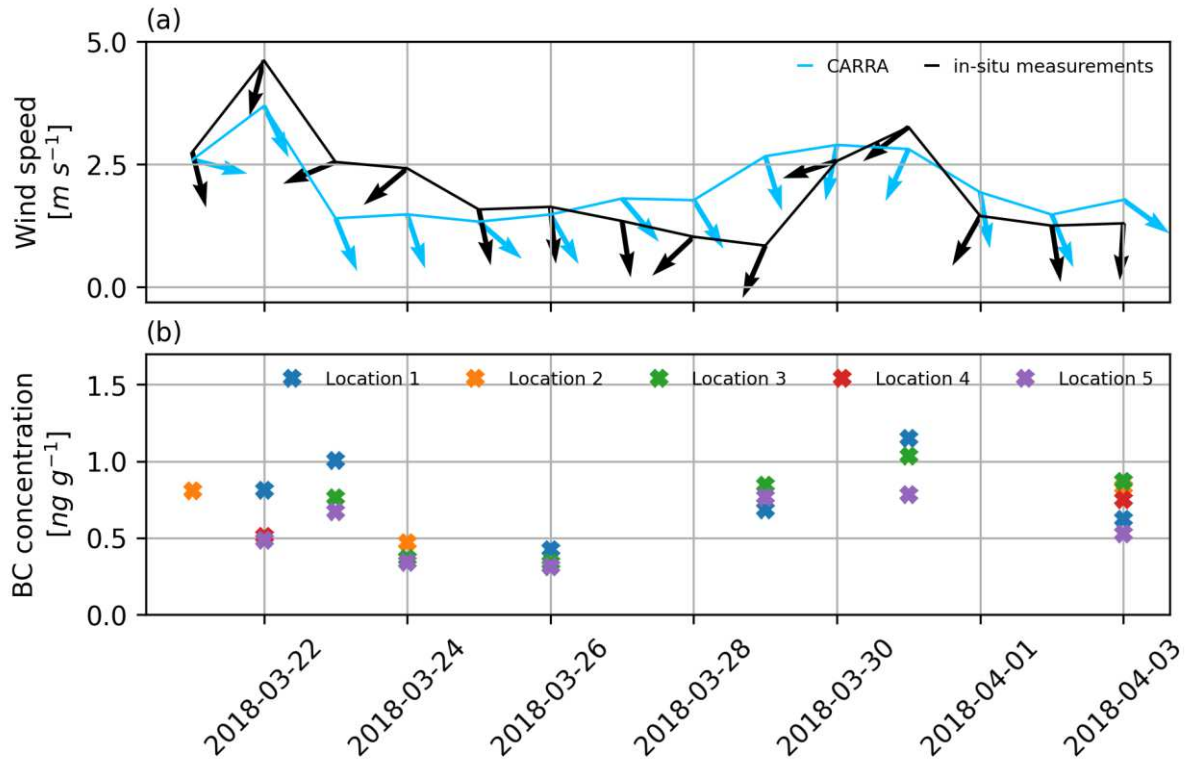

Figure E.3: (a) Daily in-situ measurements and CARRA atmospheric conditions of wind speed and wnd direction during the surface snow measurements of PAMARCMiP (Polar Airborne Measurements and Arctic Regional Climate Model Simulation Project). (b) Surface snow measurements of black carbon (BC) concentration (21 March 2018 to 3 April 2018) at five different locations.

F Co-authorship of related publications

In this Chapter, the abstracts of publications that I co-authored related to this dissertation are provided. The publications utilised data I collected during the MOSAiC expedition or are collaborative work of the PAMARCMiP campaign 2018 and are further steps to reach the goal to understand better the role of Arctic snow in the climate system. The order is chronology with the first paper listed being the last that was submitted.

Paper 1

Nandan, V., Willatt, R., Mallett, R., Stroeve, J., Geldsetzer, T., Scharien, R., Tonboe, R., Landy, J., Clemens-Sewall, D., Jutila, A., Wagner, D. N., **Krampe**, D., Huntemann, M., Yackel, J., Mahmud, M., Jensen, D., Newman, T., Hendricks, S., Spreen, G., Macfarlane, A., Schneebeli, M., Mead, J., Ricker, R., Gallagher, M., Duguay, C., Raphael, I., Polashenski, C., Tsamados, M., Matero, I., and Hoppman, M.: Wind Transport of Snow Impacts Ka- and Ku-band Radar Signatures on Arctic Sea Ice, The Cryosphere Discuss. [preprint], https://doi.org/10.5194/tc-2022-116, in review, 2022.

Abstract

Wind transport alters the snow topography and microstructure on sea ice through snow redistribution controlled by deposition and erosion. The impact of these processes on radar signatures is poorly understood. Here, we examine the effects of snow redistribution on Arctic sea ice from Ka- and Ku-band radar signatures. Measurements were obtained during two wind events in November 2019 during the MOSAiC expedition. During both events, changes in Ka- and Ku-band radar waveforms and backscatter coincident with surface height changes measured from a terrestrial laser scanner are observed. At both frequencies, snow redistribution events increased the dominance of the air/snow interface at nadir as the dominant radar scattering surface, due to wind densifying the snow surface and uppermost layers. The radar waveform data also detect the presence of previous air/snow interfaces, buried beneath newly deposited snow. The additional scattering from previous air/snow interfaces could therefore affect the range retrieved from Ka- and Ku-band satellite radar altimeters. The relative scattering contribution of the air/snow interface decreases, and the snow/sea ice interface increases with increasing incidence angles. Relative to pre-wind conditions, azimuthally averaged backscatter at nadir during the wind events increases by up to 8 dB (Ka-band) and 5 dB (Ku-band). Binned backscatter within 5° azimuth bins reveals substantial backscatter variability in the radar footprint at all incidence angles and polarizations. The sensitivity of the co-polarized phase difference is linked to changes in snow settling and temperature-gradient induced grain metamorphism, demonstrating the potential of the radar to discriminate between newly deposited and older snow on sea ice. Our results reveal the importance of wind, through its geophysical impact on Ka- and Ku-band radar signatures of snow on sea ice and has implications for reliable interpretation of airborne and satellite radar measurements of snow-covered sea ice.

Paper 2

Wendisch, M., Brückner, M., Crewell, S., [et al., including **Krampe**, D.]: Atmospheric and Surface Processes, and Feedback Mechanisms Determining Arctic Amplification: A Review of First Results and Prospects of the (AC)3 Project, Bulletin of the American Meteorological Society, https://doi.org/10.1175/BAMS-D-21-0218.1, 2022.

Abstract

Mechanisms behind the phenomenon of Arctic amplification are widely discussed. To contribute to this debate, the (AC)3 project has been established in 2016 (http://www.ac3-tr.de/). It comprises modeling and data analysis efforts as well as observational elements. The project has assembled a wealth of ground-based, airborne, ship-borne, and satellite data of physical, chemical, and meteorological properties of the Arctic atmosphere, cryosphere, and upper ocean that are available for the Arctic climate research community. Short-term changes and indications of long-term trends in Arctic climate parameters have been detected using existing and new data. For example, a distinct atmospheric moistening, an increase of regional storm activities, an amplified winter warming in the Svalbard and North Pole regions, and a decrease of sea ice thickness in the Fram Strait and of snow depth on sea ice have been identified. A positive trend of tropospheric bromine monoxide (BrO) column densities during polar spring was verified. Local marine/biogenic sources for cloud condensation nuclei and ice nucleating particles were found. Atmospheric/ocean and radiative transfer models were advanced by applying new parameterizations of surface albedo, cloud droplet activation, convective plumes and related processes over leads, and turbulent transfer coefficients for stable surface layers. Four modes of the surface radiative energy budget were explored and reproduced by simulations. To advance the future synthesis of the results, cross cutting activities are being developed aiming to answer key questions in four focus areas: lapse rate feedback, surface processes, Arctic mixed-phase clouds, and air mass transport and transformation.

Paper 3

Wagner, D. N., Shupe, M. D., Cox, C., Persson, O. G., Uttal, T., Frey, M. M., Kirchgaessner, A., Schneebeli, M., Jaggi, M., Macfarlane, A. R., Itkin, P., Arndt, S., Hendricks, S., **Krampe**, D., Nicolaus, M., Ricker, R., Regnery, J., Kolabutin, N., Shimanshuck, E., Oggier, M., Raphael, I., Stroeve, J., and Lehning, M.: Snowfall and snow accumulation during the MOSAiC winter and spring seasons, The Cryosphere, 16, 2373–2402, https://doi.org/10.5194/tc-16-2373-2022, 2022.

Abstract

Data from the Multidisciplinary drifting Observatory for the Study of Arctic Climate (MOSAiC) expedition allowed us to investigate the temporal dynamics of snowfall, snow accumulation and erosion in great detail for almost the whole accumulation season (November 2019 to May 2020). We computed cumulative snow water equivalent (SWE) over the sea ice based on snow depth and density retrievals from a SnowMicroPen and approximately weekly measured snow depths along fixed transect paths. We used the derived SWE from the snow cover to compare with precipitation sensors installed during MOSAiC. The data were also compared with ERA5 reanalysis snowfall rates for the drift track. We found an accumulated snow mass of 38 mm SWE between the end of October 2019 and end of April 2020. The initial SWE over first-year ice relative to second-year ice increased from 50 % to 90 % by end of the investigation period. Further, we found that the Vaisala Present Weather Detector 22, an optical precipitation sensor, and installed on a railing on the top deck of research vessel Polarstern, was least affected by blowing snow and showed good agreements with SWE retrievals along the transect. On the contrary, the OTT Pluvio2 pluviometer and the OTT Parsivel2 laser disdrometer were largely affected by wind and blowing snow, leading to too high measured precipitation rates. These are largely reduced when eliminating drifting snow periods in the

comparison. ERA5 reveals good timing of the snowfall events and good agreement with ground measurements with an overestimation tendency. Retrieved snowfall from the ship-based Ka-band ARM zenith radar shows good agreements with SWE of the snow cover and differences comparable to those of ERA5. Based on the results, we suggest the Ka-band radar-derived snowfall as an upper limit and the present weather detector on RV Polarstern as a lower limit of a cumulative snowfall range. Based on these findings, we suggest a cumulative snowfall of 72 to 107 mm and a precipitation mass loss of the snow cover due to erosion and sublimation as between 47 % and 68 %, for the time period between 31 October 2019 and 26 April 2020. Extending this period beyond available snow cover measurements, we suggest a cumulative snowfall of 98–114 mm.

Paper 4

Nicolaus, M., Perovich, D. K., Spreen, G., [et al., including **Krampe**, D.]: Overview of the MOSAiC expedition, Elementa: Science of the Anthropocene, 10, https://doi.org/10.1525/elementa.2021.000046, 2022.

Abstract

Year-round observations of the physical snow and ice properties and processes that govern the ice pack evolution and its interaction with the atmosphere and the ocean were conducted during the Multidisciplinary drifting Observatory for the Study of Arctic Climate (MOSAiC) expedition of the research vessel Polarstern in the Arctic Ocean from October 2019 to September 2020. This work was embedded into the interdisciplinary design of the 5 MOSAiC teams, studying the atmosphere, the sea ice, the ocean, the ecosystem, and biogeochemical processes. The overall aim of the snow and sea ice observations during MOSAiC was to characterize the physical properties of the snow and ice cover comprehensively in the central Arctic over an entire annual cycle. This objective was achieved by detailed observations of physical properties and of energy and mass balance of snow and ice. By studying snow and sea ice dynamics over nested spatial scales from centimeters to tens of kilometers, the variability across scales can be considered. On-ice observations of in situ and remote sensing properties of the different surface types over all seasons will help to improve numerical process and climate models and to establish and validate novel satellite remote sensing methods; the linkages to accompanying airborne measurements, satellite observations, and results of numerical models are discussed. We found large spatial variabilities of snow metamorphism and thermal regimes impacting sea ice growth. We conclude that the highly variable snow cover needs to be considered in more detail (in observations, remote sensing, and models) to better understand snow-related feedback processes. The ice pack revealed rapid transformations and motions along the drift in all seasons. The number of coupled ice–ocean interface processes observed in detail are expected to guide upcoming research with respect to the changing Arctic sea ice.

Paper 5

Stroeve, J., Nandan, V., Willatt, R., Tonboe, R., Hendricks, S., Ricker, R., Mead, J., Mallett, R., Huntemann, M., Itkin, P., Schneebeli, M., **Krampe**, D., Spreen, G., Wilkinson, J., Matero, I., Hoppmann, M., and Tsamados, M.: Surface-based Ku- and Ka-band polarimetric radar for sea ice studies , The Cryosphere, 14, 4405–4426, https://doi.org/10.5194/tc-14-4405-2020, 2020.

Abstract

To improve our understanding of how snow properties influence sea ice thickness retrievals from presently operational and upcoming satellite radar altimeter missions, as well as to investigate the potential for combining dual frequencies to simultaneously map snow depth and sea ice thickness, a new, surface-based, fully polarimetric Ku- and Ka-band radar (KuKa radar) was built and deployed

during the 2019–2020 year-long MOSAiC international Arctic drift expedition. This instrument, built to operate both as an altimeter (stare mode) and as a scatterometer (scan mode), provided the first in situ Ku- and Ka-band dual-frequency radar observations from autumn freeze-up through midwinter and covering newly formed ice in leads and first-year and second-year ice floes. Data gathered in the altimeter mode will be used to investigate the potential for estimating snow depth as the difference between dominant radar scattering horizons in the Ka- and Ku-band data. In the scatterometer mode, the Ku- and Ka-band radars operated under a wide range of azimuth and incidence angles, continuously assessing changes in the polarimetric radar backscatter and derived polarimetric parameters, as snow properties varied under varying atmospheric conditions. These observations allow for characterizing radar backscatter responses to changes in atmospheric and surface geophysical conditions. In this paper, we describe the KuKa radar, illustrate examples of its data and demonstrate their potential for these investigations.

Paper 6

Katlein, C., Mohrholz, V.,Sheikin, I., Itkin, P., Divine, D. V., Stroeve, J., Jutila, A., **Krampe**, D., Shimanchuk, E., Raphael, I., Rabe, B., Kuznetov, I., Mallet, M., Liu, H., Hoppmann, M., Fang, Y. C., Dumitrascu, A., Arndt, S., Anhaus, P., Nicolaus, M., Matero, I., Haas, C., Platelet Ice under Arctic Pack Ice in Winter. Geophysical Research Letters,47, https://doi.org/10.1029/2020GL088898, 2020.

Abstract

The formation of platelet ice is well known to occur under Antarctic sea ice, where subice platelet layers form from supercooled ice shelf water. In the Arctic, however, platelet ice formation has not been extensively observed, and its formation and morphology currently remain enigmatic. Here, we present the first comprehensive, long-term in situ observations of a decimeter thick subice platelet layer under free-drifting pack ice of the Central Arctic in winter. Observations carried out with a remotely operated underwater vehicle (ROV) during the midwinter leg of the MOSAiC drift expedition provide clear evidence of the growth of platelet ice layers from supercooled water present in the ocean mixed layer. This platelet formation takes place under all ice types present during the surveys. Oceanographic data from autonomous observing platforms lead us to the conclusion that platelet ice formation is a widespread but yet overlooked feature of Arctic winter sea ice growth.

Nomenclature

Abbreviations

AART	Asymptotic analytical radiative transfer theory
AC^3	ArctiC Amplification: Climate Relevant Atmospheric and SurfaCe Processes, and Feedback Mechanisms
ALADIN	Aire Limitée Adaptation dynamique Développement InterNational
AROME	Application of Research to Operations at Mesoscale
ASRv2	Arctic System Reanalysis version2
BC	Black carbon
BPRC	Byrd Polar Research Center
CARRA	Copernicus Arctic Regional Reanalysis
CH_4	Methane
CMIP5	Coupled Model Intercomparison Project 5
CO_2	Carbon Dioxide
ECMWF	European Centre for Medium-Range Weather Forecast
ERA5	ECMWF ReAnalysis-5th Generation (ERA5) atmospheric reanalyses data set
GC-NET	Greenland Climate Network
GLOBE	Greenland Global Land One-kilometre Base Elevation
HARMONIE	HIRLAM-ALADIN Research towards Mesoscale Operational Numerical weather prediction In Euromed
HIRLAM	High Resolution Limited Area Model
IFS	Integrated Forecasting System
ISBA	Interactions between Soil, Biosphere, and Atmosphere, Interactions between Soil, Biosphere, and Atmosphere
JRA-55	Japanese 55-yr Reanalysis
LAI	Light absorbing impurities
MERRA-2	Modern Era Retrospective analysis for Research and Modern Era Retrospective analysis for Research and Applications-version 2
METAR	METeorological Aerodrome Report
micro-CT	Micro computed tomography
MMLE	Multi-Model Large Ensemble
MOSAiC	Multidisciplinary drifting Observatory for the Study of Arctic Climate
N_2O	Nitrous Oxide
Nd:YAG	Neodymium-doped Yttrium Aluminum Garnet; $Nd:Y_3Al_5O_{12}$
NSIDC	National Snow and Ice Data Center
PAMARCMiP	Polar Airborne Measurements and Arctic Regional Climate Model Simulation Project
PROMICE	Programme for Monitoring of the Greenland Ice Sheet, Denmark
r	correlation

rBC	Refractory black carbon
RCP	Representative concentration pathway
RMSD	Root mean square difference
SMP	SnowMicroPen
SnowModel	Snow-Evolution MODELing System
SRTM30	Shuttle Radar Topography Mission 30
SSA	Specific surface area
SSP	Shared Socio-economic Pathway
SWE	Snow water equivalent
SYNOP	Surface synoptic observations
TARTES	Two-stream Analytical Radiative TranfEr in Snow model
WMO	World Meteorological Organisation

Symbols

Symbol	Unit	Description
A	[-]	Blowing sublimation parameter (default: 0.0018)
B	[-]	Absorption enhancement parameter
B_0	[-]	Enhancement parameter
C_H	[-]	Turbulent exchange coefficient
C_p	[J K^{-1} kg^{-1}]	Air specific heat
C_{pd}	[kJ kg^{-1} K^{-1}]	Specific heat capacity for the surface and the atmosphere
D	[g m^{-2} s^{-1}]	Dry deposition flux
D_{bs}	[kg m^{-2}]	Blowing snow transport
E	[kg m^{-2}]	Evaporation and condensation
E_S	[-]	Blowing sublimation parameter (default: 3.6)
E_{bs}	[kg m^{-2}]	Sublimation rate of blowing snow transport
F	[N]	Penetration resistance force
G	[K m^{-1}]	Temperature gradient
H	[W m^{-2}]	Internal energy of the snowpack
I_c^{SMP}	[mm]	Slope of the correlation function at the origin
L	[mm]	Length of the microstructure
L_f	[J kg^{-1}]	Latent heat of fusion for ice
L_v	[J kg^{-1}]	Latent heat of vaporisation
M	[kg m^{-2}]	Snow mass per unit area
M_a	[kg]	Mass
M_{ob}	[-]	Snow mobility index
M_p	[g m^{-2}]	Mass content due to wet deposition
$M_{t+\Delta t,l}$	[g m^{-2}]	Mass content due to dry deposition
$Melt$	[m s^{-1}]	Energy required to melt the snow
N	[-]	Number of snow layers
P	[kg m^{-2}]	Precipitation rate
Q_h	[W m^{-2}]	Sensitive turbulent heat flux
Q_G	[W m^{-2}]	Ground heat flux
$Q_{LW,in}$	[W m^{-2}]	Incoming longwave radiation
$Q_{LW,net}$	[W m^{-2}]	Net shortwave radiation
$Q_{LW,out}$	[W m^{-2}]	Outgoing shortwave radiation
Q_M	[W m^{-2}]	Latent heat of the snowpack
$Q_{SW,in}$	[W m^{-2}]	Incoming shortwave radiation
$Q_{SW,net}$	[W m^{-2}]	Net shortwave radiation
$Q_{SW,out}$	[W m^{-2}]	Outgoing shortwave radiation
Q_{Sub}	[kg m^{-2} s^{-1}]	Sublimation rate
Q_a	[W m^{-2}]	Advective energy flux: Heat flux due to precipitation and blowing snow
Q_e	[W m^{-2}]	Latent turbulent heat flux
Q_{net}	[W m^{-2}]	Net radiation
R	[kg m^{-2}]	Runoff rate
R_G	[]	Specific gas constant
Rh	[-]	Relative humidity with respect to water
Rh$_i$	[-]	Relative humidity with respect to ice

Symbol	Unit	Description
R_i	[-]	Richardson number
S	[m^2]	Surface area
S_I	[-]	Snow driftability index
SSA	[$m^2\ kg^{-1}$], [$m^2\ m^{-3}$]	Specific surface area
SSA_{SMP_C}	[$m^2\ kg^{-1}$]	SSA derived after Calonne et al. (2020)
SSA_{SMP_P}	[mm^{-1}]	SSA derived after Proksch et al. (2015)
T	[K]	Temperature
T_0	[K]	Triple point temperature (273.15 K)
T_a	[K]	Surface air temperature
T_{fus}	[K]	Temperature of the melting point of water
T_s	[K]	Snow surface temperature
T_{st}	[K]	Snow temperature
U	[m s^{-1}]	Wind speed
U_t	[m s^{-1}]	Threshold wind speed for wind drift
V	[m^3]	Volume
W	[g $m^{-2}\ s^{-1}$]	Wet deposition flux
W_E	[-]	Parameter for calculation τ_i (default: 1)
Z	[m]	Layer thickness
a_1	[kg m^{-3}]	Parameter for calculation density from SMP (ρ_{SMP}) Proksch et al. (2015): 420.47 kg m^{-3}, Calonne et al. (2020): 295.8 kg m^{-3}, King et al. (2020): 312.54 kg m^{-3}
a_2	[N^{-1}]	Parameter for calculation density from SMP (ρ_{SMP}) Proksch et al. (2015): 102.47 N^{-1}, Calonne et al. (2020): 65.1 N^{-1}, King et al. (2020): 50.27 N^{-1}
a_3	[$N^{-1}\ mm^{-1}$]	Parameter for calculation density from SMP (ρ_{SMP}) Proksch et al. (2015): -121.15 $N^{-1}\ mm^{-1}$, Calonne et al. (2020): -43.2 $N^{-1}\ mm^{-1}$, King et al. (2020): -50.26 $N^{-1}\ mm^{-1}$
a_4	[mm^{-1}]	Parameter for calculation density from SMP (ρ_{SMP}) Proksch et al. (2015): -169.96 mm^{-1}, Calonne et al. (2020): 47.1 mm^{-1}, King et al. (2020): -85.35 mm^{-1}
a_ρ	[kg m^{-3}]	Empirical constant for calculation of newly fallen snow density (109 kg m^{-3})
b_1	[$m^2\ kg^{-1}$]	Parameter for calculation SSA from SMP ($Calonne\ SSA_{SMP}$) (0.57 $m^2\ kg^{-1}$)
b_2	[mm^{-1}]	Parameter for calculation SSA from SMP ($Calonne\ SSA_{SMP}$) (-18.56 mm^{-1})
b_3	[N^{-1}]	Parameter for calculation SSA from SMP ($Calonne\ SSA_{SMP}$) (-3.66 N^{-1})
b_ρ	[kg $m^{-3}\ K^{-1}$]	Empirical constant for calculation of newly fallen snow density (6 kg $m^{-3}\ K^{-1}$)
c_1	[mm]	Parameter for calculation I_c^{SMP} (0.131 mm)
c_2	[mm^{-1}]	Parameter for calculation I_c^{SMP} (0.355 mm^{-1})

Symbol	Unit	Description
c_3	[N^{-1}]	Parameter for calculation I_c^{SMP} (0.0291 N^{-1})
c_ρ	[$m^{-7/2}$ $s^{-1/2}$]	Empirical constant for calculation of newly fallen snow density (26 $m^{-7/2}$ $s^{-1/2}$)
d_i	[-]	Typical disturbance used to calculate forcing variable sensitivity
d_{opt}	[m]	Optical grain size
f	[-]	Empirical function to predict depth hoar growth rates
g	[-]	Asymmetry factor
g^G	[-]	Geometric asymmetry factor
g_0	[-]	Asymmetry factor
gf	[-]	gust factor
gf_c	[-]	calculated gust factor
g_s	[m]	Grain size
h	[-]	Empirical function to predict depth hoar growth rates
h_e	[mm]	E-folding depth
l	[-]	Near-surface layers
p	[Pa]	Surface air pressure
p_c	[-]	Constant to calculate the adapted T_{decay}
p_0	[Pa]	Reference atmospheric pressure
q_a	[kg kg^{-1}]	Air specific humidity
$q_{sat}(T_s)$	[kg kg^{-1}]	Saturation specific humidity over a flat ice surface at the snow surface temperature T_s
q_{si}	[kg kg^{-1}]	Saturation specific humidity with respect to ice
r	[µm]	Grain size radius
r_i	[-]	Real part of ice refractive index
s	[-]	Sphericity
s_{fall}	[-]	Sphericity of falling snow particles
t	[s], [hours], [days]	Time
Δt	[s], [hours], [days]	Time step
v	[-]	Equivalent volume of snow grain
v_0'	[-]	Empirical constant
v_1'	[-]	Empirical constant
w	[-]	Empirical function to predict depth hoar growth rates
x_i	[-]	Forcing variables
z_k	[m]	Thickness of the kth layer
z_l	[m]	Layer depth
$\Gamma_{i,drift}$	[-]	Grain driftability
π_a	[-]	Exner function for the atmosphere
π_s	[-]	Exner function for the surface
τ	[h]	Constant for calculation τ_i (48 h)
τ_i	[h]	Time characteristic for snow grain change under wind transport
ϕ	[-]	Empirical function to predict depth hoar growth rates
ϕ_i^{SMP}	[-]	Volume fraction of ice

Symbol	Unit	Description
Ƙ	[-]	Ratio of solid and liquid phase of the turbulent mass exchange between snow surface and atmosphere
X	[-]	Imaginary part of the ice refractive index
α	[-]	Snow albedo
β	[m]	Empirical constant (10^{-4} m)
γ	[-]	Blowing sublimation parameter (default: 4)
δ	[-]	Dendricity
δ_{fall}	[-]	Dendricity of falling snow particles
η	[kg s^{-1} m^{-1}]	Snow viscosity
θ	[%]	Percentage of mass liquid water content
λ	[m]	Wavelength
ξ	[m^{-1}]	Wavelength dependent ice absorption coefficient
ρ_{SMP}	[kg m^{-3}]	Snow density derived after Proksch et al. (2015)
ρ_W	[kg m^{-3}]	Density of water
ρ_a	[kg m^{-3}]	Air density
ρ_i	[kg m^{-3}]	Ice density
ρ_{ice}	[kg m^{-1}]	Density of ice (917 kg m^{-1} at 0°C)
ρ_{max}	[kg m^{-3}]	Maximal snow density for which an impact due to snowdrift occurs (default: 350 kg m^{-3})
ρ_{new}	[kg m^{-3}]	Density of newly fallen snow
σ	[N m^{-2}]	Vertical stress
ω	[-]	Single scattering albedo

List of Figures

List of Tables

12 References

A2 Photonic Sensors: IceCube: Innovative optical system for measurement of the specific surface area (SSA) of snow, available at: http://www.a2photonicsensors.com/medias/A2PS_IceCube_EN.pdf, 2016.

Abatzoglou, J. T., Battisti, D. S., Williams, A. P., Hansen, W. D., Harvey, B. J., and Kolden, C. A.: Projected increases in western US forest fire despite growing fuel constraints, Commun Earth Environ, 2, 1–8, https://doi.org/10.1038/s43247-021-00299-0, 2021.

Adler, R., Wang, J.-J., Sapiano, M., Huffman, G., Chiu, L., Xie, P. P., Ferraro, R., Schneider, U., Becker, A., Bolvin, D., Nelkin, E., Gu, G., and NOAA CDR Program: Global Precipitation Climatology Project (GPCP) Climate Data Record (CDR), Version 2.3 (Monthly), 2016.

Adler, S., Chimani, B., Drechsel, S., Hasliner, K., Hiebl, J., Meyer, V., Resch, G., Rudolph, J., Vergeiner, J., and Zingerle, C.: Das Klima von Tirol-Südtirol-Belluno: 1981–2010, Vergangenheit-Gegenwart-Zukunft, Report in German]. Zentralanstalt für Meteorologie und Geodynamik, Südtirol Abteilung Brand-und Zivilschutz, Bozen, 2015.

Alekseev, G. V., Glok, N. I., Vyazilova, A. E., and Kharlanenkova, N. E.: Climate change in the Arctic: causes and mechanisms, IOP Conf. Ser.: Earth Environ. Sci., 606, 12002, https://doi.org/10.1088/1755-1315/606/1/012002, 2020.

AMAP (Ed.): AMAP Assessment 2015: Black carbon and ozone as Arctic climate forcers: Arctic Monitoring and Assessment Programme (AMAP), Oslo, 116 pp., 2015.

Anderson, E. A.: A point energy and mass balance model of a snow cover, NOAA technical report, NWS 19, U.S. Dept. of Commerce, National Oceanic and Atmospheric Administration, National Weather Service, Office of Hydrology, Silver Spring, Md., 1976.

Arduini, G., Keeley, S., Day, J. J., Sandu, I., Zampieri, L., and Balsamo, G.: On the Importance of Representing Snow Over Sea-Ice for Simulating the Arctic Boundary Layer, J. Adv. Model. Earth Syst., 14, https://doi.org/10.1029/2021MS002777, 2022.

Arias, P. A., Bellouin, N., Coppola, E., Jones, R. G., Krinner, G., Marotzke, J., Naik, V., Palmer, M. D., Plattner, G.-K., Rogelj, J., Rojas, M., Sillmann, J., Storelvmo, T., Thorne, P. W., Trewin, B., Azhuta Rao, K., Adhikary, B., Allan, R. P., Armour, K., Bala, G., Barimalala, R., Berger, S., Canadell, J. G., Cassou, C., Cherchi, A., Collins, W., Collins, W. D., Connors, S. L., Corti, S., Cruz, F., Dentener, F. J., Dereczynski, C., Di Luca, A., Diongue Niang, A., Doblas-Reyes, F. J., Dosio, A., Douville, H., Engelbrecht, F., Eyring, V., Fischer, E., Forster, P., Fox-Kemper, B., Fuglestvedt, J. S., Fyfe, J. C., Gillett, N. P., Goldfarb, L., Gorodetskaya, I., Gutierrez, Y. M., Hamdi, R., Hawkins, E., Hewitt, H. T., Hope, P., Islam, A. S., Jones, C., Kaufman, D. S., Kopp, R. E., Kosaka, Y., Kossin, J., Krakovska, S., Lee, J.-Y., Li, J., Mauritsen, T., Maycock, T. K., Meinshausen, M., Min, S.-K., Monteiro, P. M. S., Ngo-Duc, T., Otto, F., Pinto, I., Pirani, A., Raghavan, K., Ranasinghe, R., Ruane, A. C., Ruiz, L., Sallée, J.-B., Samset, B. H., Sathyendranath, S., Seneviratne, S. I., Sörensson, A. A., Szopa, S., Takayabu, I., Tréguier, A.-M., van den Hurk, B., Vautard, R., Schuckmann, K. von, Zaehle, S., Zhang, X., and Zickfeld, K.: Technical Summary, in: Climate Change 2021 – The Physical Science Basis: Contribution of Working Group I to the Sixth Assessment Report of the Intergovernmental Panel on Climate Change, edited by: Masson-Delmotte, V., Zhai, P., Pirani, A., Connors, S. L., Péan, C., Berger, S., Caud, N., Chen, Y., Goldfarb, L., Gomis, M. I., Huang, M., Leitzell, K., Lonnoy, E., Matthews, J. B. R., Maycock, T. K., Waterfield, T., Yelekçi, O., Yu, R., and Zhou, B., Cambridge University Press, Cambridge, United Kingdom and New York, NY, USA, 33–144, https://doi.org/10.1017/9781009157896.002, 2021.

Armstrong, R. L. and Brun, E. (Eds.): Snow and climate: Physical processes, surface energy exchange and modeling, Cambridge Univ. Press, Cambridge, 2008.

ASIAQ: Weather station at Station Nord Technical Documentation. Obtained by personal contact with Villum Research Station., 2014.

Auer, I., Böhm, R., Jurković, A., Orlik, A., Potzmann, R., Schöner, W., Ungersböck, M., Brunetti, M., Nanni, T., Maugeri, M., Briffa, K., Jones, P., Efthymiadis, D., Mestre, O., Moisselin, J.-M., Begert, M., Brazdil, R., Bochnicek, O., Cegnar, T., Gajić-Čapka, M., Zaninović, K., Majstorović, Ž., Szalai,

S., Szentimrey, T., and Mercalli, L.: A new instrumental precipitation dataset for the greater alpine region for the period 1800-2002, Int. J. Climatol., 25, 139–166, https://doi.org/10.1002/joc.1135, 2005.

Azam, M. F. and Srivastava, S.: Mass balance and runoff modelling of partially debris-covered Dokriani Glacier in monsoon-dominated Himalaya using ERA5 data since 1979, Journal of Hydrology, 590, 125432, https://doi.org/10.1016/j.jhydrol.2020.125432, 2020.

Ballinger, T. J., Overland, J. E., Wang, M., Walsh, J. E., Brettschneider, B., Thoman, R. L., Bhatt, U. S., Hanna, E., Hanssen-Bauer, I., and Kim, S.-J.: NOAA Arctic Report Card 2022: Surface Air Temperatures, NOAA, https://doi.org/10.25923/13qm-2576, 2022.

Barlow, J., Berenguer, E., Carmenta, R., and França, F.: Clarifying Amazonia's burning crisis, Global Change Biology, 26, 319–321, https://doi.org/10.1111/gcb.14872, 2020.

Barrere, M., Domine, F., Decharme, B., Morin, S., Vionnet, V., and Lafaysse, M.: Evaluating the performance of coupled snow–soil models in SURFEXv8 to simulate the permafrost thermal regime at a high Arctic site, Geosci. Model Dev., 10, 3461–3479, https://doi.org/10.5194/gmd-10-3461-2017, 2017.

Bartelt, P. and Lehning, M.: A physical SNOWPACK model for the Swiss avalanche warning, Cold Regions Science and Technology, 35, 123–145, https://doi.org/10.1016/S0165-232X(02)00074-5, 2002.

Bartlett, S. J., Rüedi, J.-D., Craig, A., and Fierz, C.: Assessment of techniques for analyzing snow crystals in two dimensions, Annals of Glaciology, 48, 103–112, https://doi.org/10.3189/172756408784700752, 2008.

Bednorz, E. and Wibig, J.: Spatial distribution and synoptic conditions of snow accumulation in the Russian Arctic, 1, 35, 25916, https://doi.org/10.3402/polar.v35.25916, 2016.

Bekryaev, R. V., Polyakov, I. V., and Alexeev, V. A.: Role of Polar Amplification in Long-Term Surface Air Temperature Variations and Modern Arctic Warming, Journal of Climate, 23, 3888–3906, https://doi.org/10.1175/2010JCLI3297.1, 2010.

Beljaars, A.: The parametrization of the planetary boundary layer: Meteorological Training Course Lecture Series, https://www.ecmwf.int/en/elibrary/16959-parametrization-planetary-boundary-layer, last access: 24 February 2021, 2002.

Bell, B., Hersbach, H., Simmons, A., Berrisford, P., Dahlgren, P., Horányi, A., Muñoz-Sabater, J., Nicolas, J., Radu, R., Schepers, D., Soci, C., Villaume, S., Bidlot, J.-R., Haimberger, L., Woollen, J., Buontempo, C., and Thépaut, J.-N.: The ERA5 Global Reanalysis: Preliminary Extension to 1950, Q.J.R. Meteorol. Soc., https://doi.org/10.1002/qj.4174, 2021.

Bender, F. A.-M., Frey, L., McCoy, D. T., Grosvenor, D. P., and Mohrmann, J. K.: Assessment of aerosol–cloud–radiation correlations in satellite observations, climate models and reanalysis, Clim Dyn, 52, 4371–4392, https://doi.org/10.1007/s00382-018-4384-z, 2019.

Bengtsson, L., Andrae, U., Aspelien, T., Batrak, Y., Calvo, J., Rooy, W. de, Gleeson, E., Hansen-Sass, B., Homleid, M., Hortal, M., Ivarsson, K.-I., Lenderink, G., Niemelä, S., Nielsen, K. P., Onvlee, J., Rontu, L., Samuelsson, P., Muñoz, D. S., Subias, A., Tijm, S., Toll, V., Yang, X., and Køltzow, M. Ø.: The HARMONIE–AROME Model Configuration in the ALADIN–HIRLAM NWP System, Monthly Weather Review, 145, 1919–1935, https://doi.org/10.1175/MWR-D-16-0417.1, 2017.

Beniston, M.: Mountain Weather and Climate: A General Overview and a Focus on Climatic Change in the Alps, Hydrobiologia, 562, 3–16, https://doi.org/10.1007/s10750-005-1802-0, 2006.

Beniston, M.: Mountain Climates and Climatic Change: An Overview of Processes Focusing on the European Alps, Pure appl. geophys., 162, 1587–1606, https://doi.org/10.1007/s00024-005-2684-9, 2005.

Bertò, M., Cappelletti, D., Barbaro, E., Varin, C., Gallet, J.-C., Markowicz, K., Rozwadowska, A., Mazzola, M., Crocchianti, S., Poto, L., Laj, P., Barbante, C., and Spolaor, A.: Variability in black carbon mass concentration in surface snow at Svalbard, Atmos. Chem. Phys., 21, 12479–12493, https://doi.org/10.5194/acp-21-12479-2021, 2021.

Betts, A. K., Chan, D. Z., and Desjardins, R. L.: Near-Surface Biases in ERA5 Over the Canadian Prairies, Front. Environ. Sci., 7, 129, https://doi.org/10.3389/fenvs.2019.00129, 2019.

Bintanja, R. and Andry, O.: Towards a rain-dominated Arctic, Nature Clim Change, 7, 263–267, https://doi.org/10.1038/nclimate3240, 2017.

Bintanja, R. and van der Linden, E. C.: The changing seasonal climate in the Arctic, Sci Rep, 3, 1556, https://doi.org/10.1038/srep01556, 2013.

Boelman, N. T., Liston, G. E., Gurarie, E., Meddens, A. J. H., Mahoney, P. J., Kirchner, P. B., Bohrer, G., Brinkman, T. J., Cosgrove, C. L., Eitel, J. U. H., Hebblewhite, M., Kimball, J. S., LaPoint, S., Nolin, A. W., Pedersen, S. H., Prugh, L. R., Reinking, A. K., and Vierling, L. A.: Integrating snow science and wildlife ecology in Arctic-boreal North America, Environ. Res. Lett., 14, 10401, https://doi.org/10.1088/1748-9326/aaeec1, 2019.

Böhm, R., Auer, I., Brunetti, M., Maugeri, M., Nanni, T., and Schöner, W.: Regional temperature variability in the European Alps: 1760-1998 from homogenized instrumental time series, Int. J. Climatol., 21, 1779–1801, https://doi.org/10.1002/joc.689, 2001.

Boike, J.: Seasonal snow cover on frozen ground: Energy balance calculations of a permafrost site near Ny-Ålesund, Spitsbergen, J. Geophys. Res., 108, ALT 4-1-ALT 4-11, https://doi.org/10.1029/2001JD000939, 2003.

Bond, T. C., Doherty, S. J., Fahey, D. W., Forster, P. M., Berntsen, T., DeAngelo, B. J., Flanner, M. G., Ghan, S., Kärcher, B., Koch, D., Kinne, S., Kondo, Y., Quinn, P. K., Sarofim, M. C., Schultz, M. G., Schulz, M., Venkataraman, C., Zhang, H., Zhang, S., Bellouin, N., Guttikunda, S. K., Hopke, P. K., Jacobson, M. Z., Kaiser, J. W., Klimont, Z., Lohmann, U., Schwarz, J. P., Shindell, D., Storelvmo, T., Warren, S. G., and Zender, C. S.: Bounding the role of black carbon in the climate system: A scientific assessment, J. Geophys. Res. Atmos., 118, 5380–5552, https://doi.org/10.1002/jgrd.50171, 2013.

Boone, A., Masson, V., Meyers, T., and Noilhan, J.: The Influence of the Inclusion of Soil Freezing on Simulations by a Soil–Vegetation–Atmosphere Transfer Scheme, Journal of Applied Meteorology and Climatology, 39, 1544–1569, https://doi.org/10.1175/1520-0450(2000)039<1544:TIOTIO>2.0.CO;2, 2000.

Bormann, K. J., Westra, S., Evans, J. P., and McCabe, M. F.: Spatial and temporal variability in seasonal snow density, Journal of Hydrology, 484, 63–73, https://doi.org/10.1016/j.jhydrol.2013.01.032, 2013.

Box, J. E., Fettweis, X., Stroeve, J. C., Tedesco, M., Hall, D. K., and Steffen, K.: Greenland ice sheet albedo feedback: thermodynamics and atmospheric drivers, The Cryosphere, 6, 821–839, https://doi.org/10.5194/TC-6-821-2012, 2012.

Box, J. E., Colgan, W. T., Christensen, T. R., Schmidt, N. M., Lund, M., Parmentier, F.-J. W., Brown, R., Bhatt, U. S., Euskirchen, E. S., Romanovsky, V. E., Walsh, J. E., Overland, J. E., Wang, M., Corell, R. W., Meier, W. N., Wouters, B., Mernild, S., Mård, J., Pawlak, J., and Olsen, M. S.: Key indicators of Arctic climate change: 1971–2017, Environ. Res. Lett., 14, 45010, https://doi.org/10.1088/1748-9326/aafc1b, 2019.

Brown, R., Marsh, P., Déry, S., and Yang, D.: Snow Cover—Observations, Processes, Changes, and Impacts on Northern Hydrology, in: Arctic Hydrology, Permafrost and Ecosystems, edited by: Yang, Daqing, and Douglas L. Kane, Springer, Cham, 61–99, https://doi.org/10.1007/978-3-030-50930-9_3, 2021.

Browse, J., Carslaw, K. S., Schmidt, A., and Corbett, J. J.: Impact of future Arctic shipping on high-latitude black carbon deposition, Geophys. Res. Lett., 40, 4459–4463, https://doi.org/10.1002/grl.50876, 2013.

Brun, E.: Investigation on Wet-Snow Metamorphism in Respect of Liquid-Water Content, Annals of Glaciology, 13, 22–26, https://doi.org/10.1017/s0260305500007576, 1989.

Brun, E., David, P., Sudul, M., and Brunot, G.: A numerical model to simulate snow-cover stratigraphy for operational avalanche forecasting, J. Glaciol., 38, 13–22, https://doi.org/10.3189/S0022143000009552, 1992.

Brun, E., Martin, E., Simon, V., Gendre, C., and Coleou, C.: An Energy and Mass Model of Snow Cover Suitable for Operational Avalanche Forecasting, J. Glaciol., 35, 333–342, https://doi.org/10.1017/S0022143000009254, 1989.

Brun, E., Vionnet, V., Boone, A., Decharme, B., Peings, Y., Valette, R., Karbou, F., and Morin, S.: Simulation of Northern Eurasian Local Snow Depth, Mass, and Density Using a Detailed Snowpack Model and Meteorological Reanalyses, J. Hydrometeor, 14, 203–219, https://doi.org/10.1175/JHM-D-12-012.1, 2013.

Brun, É., Vionnet, V., Morin, S., Boone, A., Martin, É., Faroux, S., Le Moigne, P., and Willemet, J.-M.: Le modèle de manteau neigeux Crocus et ses applications, Météorologie, 8, 44, https://doi.org/10.4267/2042/47245, 2012.

Budyko, M. I.: The effect of solar radiation variations on the climate of the Earth, Tellus, 21, 611–619, https://doi.org/10.3402/tellusa.v21i5.10109, 1969.

Cabanes, A., Legagneux, L., and Dominé, F.: Evolution of the specific surface area and of crystal morphology of Arctic fresh snow during the ALERT 2000 campaign, Atmospheric Environment, 36, 2767–2777, https://doi.org/10.1016/S1352-2310(02)00111-5, 2002.

Callaghan, T. V., Johansson, M., Brown, R. D., Groisman, P. Y., Labba, N., Radionov, V., Bradley, R. S., Blangy, S., Bulygina, O. N., Christensen, T. R., Colman, J. E., Essery, R. L. H., Forbes, B. C., Forchhammer, M. C., Golubev, V. N., Honrath, R. E., Juday, G. P., Meshcherskaya, A. V., Phoenix, G. K., Pomeroy, J., Rautio, A., Robinson, D. A., Schmidt, N. M., Serreze, M. C., Shevchenko, V. P., Shiklomanov, A. I., Shmakin, A. B., Sköld, P., Sturm, M., Woo, M., and Wood, E. F.: Multiple Effects of Changes in Arctic Snow Cover, AMBIO, 40, 32–45, https://doi.org/10.1007/S13280-011-0213-X, 2011.

Calonne, N., Richter, B., Löwe, H., Cetti, C., Schure, J. ter, van Herwijnen, A., Fierz, C., Jaggi, M., and Schneebeli, M.: The RHOSSA campaign: multi-resolution monitoring of the seasonal evolution of the structure and mechanical stability of an alpine snowpack, The Cryosphere, 14, 1829–1848, https://doi.org/10.5194/tc-14-1829-2020, 2020.

Canadell, J. G., Meyer, C. P. M., Cook, G. D., Dowdy, A., Briggs, P. R., Knauer, J., Pepler, A., and Haverd, V.: Multi-decadal increase of forest burned area in Australia is linked to climate change, Nat Commun, 12, 6921, https://doi.org/10.1038/s41467-021-27225-4, 2021.

Carmagnola, C. M., Morin, S., Lafaysse, M., Domine, F., Lesaffre, B., Lejeune, Y., Picard, G., and Arnaud, L.: Implementation and evaluation of prognostic representations of the optical diameter of snow in the SURFEX/ISBA-Crocus detailed snowpack model, The Cryosphere, 8, 417–437, https://doi.org/10.5194/tc-8-417-2014, 2014.

Carturan, L., Rastner, P., and Paul, F.: On the disequilibrium response and climate change vulnerability of the mass-balance glaciers in the Alps, J. Glaciol., 66, 1034–1050, https://doi.org/10.1017/jog.2020.71, 2020.

Casty, C., Wanner, H., Luterbacher, J., Esper, J., and Böhm, R.: Temperature and precipitation variability in the European Alps since 1500, Int. J. Climatol., 25, 1855–1880, https://doi.org/10.1002/joc.1216, 2005.

Chapin, F. S., Sturm, M., Serreze, M. C., McFadden, J. P., Key, J. R., Lloyd, A. H., McGuire, A. D., Rupp, T. S., Lynch, A. H., Schimel, J. P., Beringer, J., Chapman, W. L., Epstein, H. E., Euskirchen, E. S., Hinzman, L. D., Jia, G., Ping, C.-L., Tape, K. D., Thompson, C. D. C., Walker, D. A., and Welker, J. M.: Role of land-surface changes in arctic summer warming, Science, 310, 657–660, https://doi.org/10.1126/science.1117368, 2005.

Chen, Y., Sharma, S., Zhou, X., Yang, K., Li, X., Niu, X., Hu, X., and Khadka, N.: Spatial performance of multiple reanalysis precipitation datasets on the southern slope of central Himalaya, Atmospheric Research, 250, 105365, https://doi.org/10.1016/j.atmosres.2020.105365, 2021.

Cohen, J. and Rind, D.: The Effect of Snow Cover on the Climate, J. Climate, 4, 689–706, https://doi.org/10.1175/1520-0442(1991)004<0689:TEOSCO>2.0.CO;2, 1991.

Colbeck, S. C.: The layered character of snow covers, Rev. Geophys., 29, 81, https://doi.org/10.1029/90RG02351, 1991.

Colbeck, S. C.: Theory of metamorphism of dry snow, J. Geophys. ;Res., 88, 5475–5482, https://doi.org/10.1029/JC088iC09p05475, 1983.

Colbeck, S. C.: An overview of seasonal snow metamorphism, Rev. Geophys., 20, 45, https://doi.org/10.1029/RG020i001p00045, 1982.

Copernicus Climate Change Service: Copernicus Arctic Regional Reanalysis Service, https://climate.copernicus.eu/copernicus-arctic-regional-reanalysis-service, last access: 29 November 2021, 2021a.

Copernicus Climate Change Service: Arctic regional reanalysis on single levels from 1998 to 2019, https://cds.climate.copernicus.eu/cdsapp#!/dataset/reanalysis-carra-single-levels?tab=overview, last access: 20 October 2021, 2021b.

Copernicus Climate Change Service: ERA5: data documentation, https://confluence.ecmwf.int/display/CKB/ERA5%3A+data+documentation#ERA5:datadocumentation-Observations, last access: 16 July 2021, 2021c.

Copernicus Climate Change Service: C3S Arctic regional reanalysis - Full System Documentation, https://datastore.copernicus-climate.eu/documents/reanalysis-carra/CARRAFullSystemDocumentationFinal.pdf, last access: 14 July 2021, 2020.

Davesne, G., Domine, F., and Fortier, D.: Effects of meteorology and soil moisture on the spatio-temporal evolution of the depth hoar layer in the polar desert snowpack, J. Glaciol., 1–16, https://doi.org/10.1017/jog.2021.105, 2021.

Day, J. J., Arduini, G., Sandu, I., Magnusson, L., Beljaars, A., Balsamo, G., Rodwell, M., and Richardson, D.: Measuring the Impact of a New Snow Model Using Surface Energy Budget Process Relationships, J. Adv. Model. Earth Syst., 12, https://doi.org/10.1029/2020MS002144, 2020.

Delhasse, A., Kittel, C., Amory, C., Hofer, S., van As, D., S. Fausto, R., and Fettweis, X.: Brief communication: Evaluation of the near-surface climate in ERA5 over the Greenland Ice Sheet, The Cryosphere, 14, 957–965, https://doi.org/10.5194/tc-14-957-2020, 2020a.

Delhasse, A., Kittel, C., Amory, C., Hofer, S., van As, D., S. Fausto, R., and Fettweis, X.: Supplement of Brief communication: Evaluation of the near-surface climate in ERA5 over the Greenland Ice Sheet, The Cryosphere, 14, https://doi.org/10.5194/tc-14-957-2020-supplement, 2020b.

Derksen, C., Lemmetyinen, J., Toose, P., Silis, A., Pulliainen, J., and Sturm, M.: Physical properties of Arctic versus subarctic snow: Implications for high latitude passive microwave snow water equivalent retrievals, J. Geophys. Res. Atmos., 119, 7254–7270, https://doi.org/10.1002/2013JD021264, 2014.

Déry, S. J. and Brown, R. D.: Recent Northern Hemisphere snow cover extent trends and implications for the snow-albedo feedback, Geophys. Res. Lett., 34, https://doi.org/10.1029/2007GL031474, 2007.

Dethloff, K., Abegg, C., Rinke, A., Hebestadt, I., and Romanov, V. F.: Sensitivity of Arctic climate simulations to different boundary-layer parameterizations in a regional climate model, Tellus A: Dynamic Meteorology and Oceanography, 53, 1–26, https://doi.org/10.3402/tellusa.v53i1.12176, 2001.

Dlugokencky, E. and Tans, P.: Trends in atmospheric carbon dioxide, National Oceanic and Atmospheric Administration, Earth System Research Laboratory, https://gml.noaa.gov/ccgg/trends/global.html, last access: 17 May 2022, 2022.

Doherty, S. J., Warren, S. G., Grenfell, T. C., Clarke, A. D., and Brandt, R. E.: Light-absorbing impurities in Arctic snow, Atmos. Chem. Phys., 10, 11647–11680, https://doi.org/10.5194/acp-10-11647-2010, 2010.

Doherty, S. J., Dang, C., Hegg, D. A., Zhang, R., and Warren, S. G.: Black carbon and other light-absorbing particles in snow of central North America, J. Geophys. Res. Atmos., 119, 12,807-12,831, https://doi.org/10.1002/2014JD022350, 2014.

Doherty, S. J., Grenfell, T. C., Forsström, S., Hegg, D. L., Brandt, R. E., and Warren, S. G.: Observed vertical redistribution of black carbon and other insoluble light-absorbing particles in melting snow, J. Geophys. Res. Atmos., 118, 5553–5569, https://doi.org/10.1002/jgrd.50235, 2013.

Domine, F., Morin, S., Brun, E., Lafaysse, M., and Carmagnola, C. M.: Seasonal evolution of snow permeability under equi-temperature and temperature-gradient conditions, The Cryosphere, 7, 1915–1929, https://doi.org/10.5194/tc-7-1915-2013, 2013.

Domine, F., Albert, M., Huthwelker, T., Jacobi, H.-W., Kokhanovsky, A. A., Lehning, M., Picard, G., and Simpson, W. R.: Snow physics as relevant to snow photochemistry, Atmos. Chem. Phys., 8, 171–208, https://doi.org/10.5194/acp-8-171-2008, 2008.

Domine, F., Taillandier, A.-S., and Simpson, W. R.: A parameterization of the specific surface area of seasonal snow for field use and for models of snowpack evolution, J. Geophys. Res., 112, https://doi.org/10.1029/2006JF000512, 2007.

Domine, F., Picard, G., Morin, S., Barrere, M., Madore, J.-B., and Langlois, A.: Major Issues in Simulating Some Arctic Snowpack Properties Using Current Detailed Snow Physics Models: Consequences for the Thermal Regime and Water Budget of Permafrost, J. Adv. Model. Earth Syst., 11, 34–44, https://doi.org/10.1029/2018MS001445, 2019.

Domine, F., Gauthier, G., Vionnet, V., Fauteux, D., Dumont, M., and Barrere, M.: Snow physical properties may be a significant determinant of lemming population dynamics in the high Arctic, Arctic Science, 4, 813–826, https://doi.org/10.1139/as-2018-0008, 2018a.

Domine, F., Belke-Brea, M., Sarrazin, D., Arnaud, L., Barrere, M., and Poirier, M.: Soil moisture, wind speed and depth hoar formation in the Arctic snowpack, J. Glaciol., 64, 990–1002, https://doi.org/10.1017/jog.2018.89, 2018b.

Domine, F., Barrere, M., and Sarrazin, D.: Seasonal evolution of the effective thermal conductivity of the snow and the soil in high Arctic herb tundra at Bylot Island, Canada, The Cryosphere, 10, 2573–2588, https://doi.org/10.5194/tc-10-2573-2016, 2016a.

Domine, F., Barrere, M., and Morin, S.: The growth of shrubs on high Arctic tundra at Bylot Island: impact on snow physical properties and permafrost thermal regime, Biogeosciences, 13, 6471–6486, https://doi.org/10.5194/bg-13-6471-2016, 2016b.

Domine, F., Gallet, J.-C., Bock, J., and Morin, S.: Structure, specific surface area and thermal conductivity of the snowpack around Barrow, Alaska, J. Geophys. ;Res., 117, https://doi.org/10.1029/2011JD016647, 2012.

Domine, F., Salvatori, R., Legagneux, L., Salzano, R., Fily, M., and Casacchia, R.: Correlation between the specific surface area and the short wave infrared (SWIR) reflectance of snow, Cold Regions Science and Technology, 46, 60–68, https://doi.org/10.1016/j.coldregions.2006.06.002, 2006a.

Domine, F., Taillandier, A., Houdier, S., Parrenin, F., Simpson, W. R., and Douglas, T. A.: Interactions between snow metamorphism and climate: Physical and chemical aspects: special publication-royal society of chemistry, Special publication royal society of chemistry, 311, 27, 2006b.

Dominé, F., Cabanes, A., and Legagneux, L.: Structure, microphysics, and surface area of the Arctic snowpack near Alert during the ALERT 2000 campaign, Atmospheric Environment, 36, 2753–2765, https://doi.org/10.1016/S1352-2310(02)00108-5, 2002.

Donth, T., Jäkel, E., Ehrlich, A., Heinold, B., Schacht, J., Herber, A., Zanatta, M., and Wendisch, M.: Combining atmospheric and snow radiative transfer models to assess the solar radiative effects of black carbon in the Arctic, Atmos. Chem. Phys., 20, 8139–8156, https://doi.org/10.5194/acp-20-8139-2020, 2020.

Draper, Norman R. and Smith, Harry: Applied Regression Analysis, 3rd ed., Wiley Series in Probability and Statistics Ser, v.326, John Wiley & Sons Incorporated, Newy York, 738 pp., 1998.

Duyck, E., Gelderloos, R., and Jong, M. F. de: Wind-Driven Freshwater Export at Cape Farewell, JGR Oceans, 127, e2021JC018309, https://doi.org/10.1029/2021JC018309, 2022.

Eckerstorfer, M. and Christiansen, H. H.: The "High Arctic Maritime Snow Climate" in Central Svalbard, Arctic, Antarctic, and Alpine Research, 43, 11–21, https://doi.org/10.1657/1938-4246-43.1.11, 2011.

Ernakovich, J. G., Hopping, K. A., Berdanier, A. B., Simpson, R. T., Kachergis, E. J., Steltzer, H., and Wallenstein, M. D.: Predicted responses of arctic and alpine ecosystems to altered seasonality under climate change, Global Change Biology, 20, 3256–3269, https://doi.org/10.1111/gcb.12568, 2014.

Essery, R. and Pomeroy, J.: Implications of spatial distributions of snow mass and melt rate for snow-cover depletion: theoretical considerations, Ann. Glaciol., 38, 261–265, https://doi.org/10.3189/172756404781815275, 2004.

Essery, R., Kontu, A., Lemmetyinen, J., Dumont, M., and Ménard, C. B.: A 7-year dataset for driving and evaluating snow models at an Arctic site (Sodankylä, Finland), Geosci. Instrum. Method. Data Syst., 5, 219–227, https://doi.org/10.5194/gi-5-219-2016, 2016.

Essery, R., Li, L., and Pomeroy, J.: A distributed model of blowing snow over complex terrain, Hydrol. Process., 13, 2423–2438, https://doi.org/10.1002/(SICI)1099-1085(199910)13:14/15<2423:AID-HYP853>3.0.CO;2-U, 1999.

Essou, G. R. C., Sabarly, F., Lucas-Picher, P., Brissette, F., and Poulin, A.: Can Precipitation and Temperature from Meteorological Reanalyses Be Used for Hydrological Modeling?, Journal of Hydrometeorology, 17, 1929–1950, https://doi.org/10.1175/JHM-D-15-0138.1, 2016.

Estilow, T. W., Young, A. H., and Robinson, D. A.: A long-term Northern Hemisphere snow cover extent data record for climate studies and monitoring, Earth System Science Data, 7, 137–142, https://doi.org/10.5194/essd-7-137-2015, 2015.

European Centre for Medium-Range Weather Forecasts: Improving prediction and climate monitoring of polar regions – challenges and priorities, https://www.ecmwf.int/en/about/media-centre/science-blog/2018/improving-prediction-and-climate-monitoring-polar-regions, last access: 4 November 2021, 2018.

European Centre for Medium-Range Weather Forecasts: IFS Documentation CY45R2—Part IV: Physical processes. IFS doc., https://www.ecmwf.int/node/16648, last access: 21 December 2020, 2016.

Fetterer, F., Knowles K., Meier W., Savoie M., and Windnagel A.: Sea Ice Index, Version 3, 2017.

Fierz, C., Armstrong, R. L., Durand, Y., Etchevers, P., Greene, E., McClung, D. M., Nishimura, K., Satyawali, P. K., and Sokratov, S. A.: The international classification for seasonal snow on the ground, 2009.

Flanner, M. G., Zender, C. S., Randerson, J. T., and Rasch, P. J.: Present-day climate forcing and response from black carbon in snow, J. Geophys. Res., 112, https://doi.org/10.1029/2006JD008003, 2007.

Flannigan, M., Stocks, B., and Wotton, B.: Climate change and forest fires, Science of The Total Environment, 262, 221–229, https://doi.org/10.1016/S0048-9697(00)00524-6, 2000.

Flin, F. and Brzoska, J.-B.: The temperature-gradient metamorphism of snow: vapour diffusion model and application to tomographic images, Annals of Glaciology, 49, 17–21, https://doi.org/10.3189/172756408787814834, 2008.

Frei, C. and Schär, C.: A precipitation climatology of the Alps from high-resolution rain-gauge observations, Int. J. Climatol., 18, 873–900, https://doi.org/10.1002/(SICI)1097-0088(19980630)18:8<873:AID-JOC255>3.0.CO;2-9, 1998.

Gabbi, J., Huss, M., Bauder, A., Cao, F., and Schwikowski, M.: The impact of Saharan dust and black carbon on albedo and long-term mass balance of an Alpine glacier, The Cryosphere, 9, 1385–1400, https://doi.org/10.5194/tc-9-1385-2015, 2015.

Gallet, J.-C., Domine, F., and Dumont, M.: Measuring the specific surface area of wet snow using 1310 nm reflectance, The Cryosphere, 8, 1139–1148, https://doi.org/10.5194/tc-8-1139-2014, 2014a.

Gallet, J.-C., Domine, F., Savarino, J., Dumont, M., and Brun, E.: The growth of sublimation crystals and surface hoar on the Antarctic plateau, The Cryosphere, 8, 1205–1215, https://doi.org/10.5194/tc-8-1205-2014, 2014b.

Gallet, J.-C., Domine, F., Zender, C. S., and Picard, G.: Measurement of the specific surface area of snow using infrared reflectance in an integrating sphere at 1310 and 1550 nm, The Cryosphere, 3, 167–182, https://doi.org/10.5194/tc-3-167-2009, 2009.

Gardner, A. S. and Sharp, M. J.: A review of snow and ice albedo and the development of a new physically based broadband albedo parameterization, J. Geophys. ;Res., 115, https://doi.org/10.1029/2009JF001444, 2010.

Gascon, G., Sharp, M., Burgess, D., Bezeau, P., Bush, A. B., Morin, S., and Lafaysse, M.: How well is firn densification represented by a physically based multilayer model? Model evaluation for Devon Ice Cap, Nunavut, Canada, J. Glaciol., 60, 694–704, https://doi.org/10.3189/2014JoG13J209, 2014.

Gearheard, S., Pocernich, M., Stewart, R., Sanguya, J., and Huntington, H. P.: Linking Inuit knowledge and meteorological station observations to understand changing wind patterns at Clyde River, Nunavut, Climatic Change, 100, 267–294, https://doi.org/10.1007/s10584-009-9587-1, 2010.

Gebhardt, H., Glaser, R., Radtke, U., and Reuber, P. (Eds.): Physische Geographie und Humangeographie, 2nd ed., Spektrum Akademie, 2012.

Glantz, S. A. and Slinker, B. K.: Primer of applied regression and analysis of variance, McGraw-Hill, New York, 777 pp., 1990.

Glass, T. W., Breed, G. A., Liston, G. E., Reinking, A. K., Robards, M. D., and Kielland, K.: Spatiotemporally variable snow properties drive habitat use of an Arctic mesopredator, Oecologia, 195, 887–899, https://doi.org/10.1007/s00442-021-04890-2, 2021.

Gogoi, M. M., Babu, S. S., Pandey, S. K., Nair, V. S., Vaishya, A., Girach, I. A., and Koushik, N.: Scavenging ratio of black carbon in the Arctic and the Antarctic, Polar Science, 16, 10–22, https://doi.org/10.1016/j.polar.2018.03.002, 2018.

Goosse, H., Kay, J. E., Armour, K. C., Bodas-Salcedo, A., Chepfer, H., Docquier, D., Jonko, A., Kushner, P. J., Lecomte, O., Massonnet, F., Park, H.-S., Pithan, F., Svensson, G., and Vancoppenolle, M.: Quantifying climate feedbacks in polar regions, Nat Commun, 9, https://doi.org/10.1038/s41467-018-04173-0, 2018.

Gordon, M., Simon, K., and Taylor, P. A.: On snow depth predictions with the Canadian land surface scheme including a parametrization of blowing snow sublimation, Atmosphere-Ocean, 44, 239–255, https://doi.org/10.3137/ao.440303, 2006.

Gouttevin, I., Langer, M., Löwe, H., Boike, J., Proksch, M., and Schneebeli, M.: Observation and modelling of snow at a polygonal tundra permafrost site: spatial variability and thermal implications, The Cryosphere, 12, 3693–3717, https://doi.org/10.5194/tc-12-3693-2018, 2018.

Graham, R. M., Cohen, L., Ritzhaupt, N., Segger, B., Graversen, R. G., Rinke, A., Walden, V. P., Granskog, M. A., and Hudson, S. R.: Evaluation of Six Atmospheric Reanalyses over Arctic Sea Ice from Winter to Early Summer, Journal of Climate, 32, 4121–4143, https://doi.org/10.1175/JCLI-D-18-0643.1, 2019a.

Graham, R. M., Hudson, S. R., and Maturilli, M.: Improved Performance of ERA5 in Arctic Gateway Relative to Four Global Atmospheric Reanalyses, Geophys. Res. Lett., 46, 6138–6147, https://doi.org/10.1029/2019GL082781, 2019b.

Grenfell, T. C. and Warren, S. G.: Representation of a nonspherical ice particle by a collection of independent spheres for scattering and absorption of radiation, J. Geophys. Res., 104, 31697–31709, https://doi.org/10.1029/1999JD900496, 1999.

Gryning, S.-E., Batchvarova, E., Floors, R., Münkel, C., Skov, H., and Sørensen, L. L.: Observed and modelled cloud cover up to 6 km height at Station Nord in the high Arctic, Intl Journal of Climatology, 41, 1584–1598, https://doi.org/10.1002/joc.6894, 2021.

Gutjahr, O. and Heinemann, G.: A model-based comparison of extreme winds in the Arctic and around Greenland, Int J Climatol, 38, 5272–5292, https://doi.org/10.1002/joc.5729, 2018.

Hall, A.: The Role of Surface Albedo Feedback in Climate, J. Climate, 17, 1550–1568, https://doi.org/10.1175/1520-0442(2004)017<1550:TROSAF>2.0.CO;2, 2004.

Heinemann, G., Willmes, S., Schefczyk, L., Makshtas, A., Kustov, V., and Makhotina, I.: Observations and Simulations of Meteorological Conditions over Arctic Thick Sea Ice in Late Winter during the Transarktika 2019 Expedition, Atmosphere, 12, 174, https://doi.org/10.3390/atmos12020174, 2021.

Hernández-Henríquez, M. A., Déry, S. J., and Derksen, C.: Polar amplification and elevation-dependence in trends of Northern Hemisphere snow cover extent, 1971–2014, Environ. Res. Lett., 10, 44010, https://doi.org/10.1088/1748-9326/10/4/044010, 2015.

Hersbach, H., Bell, B., Berrisford, P., Hirahara, S., Horányi, A., Muñoz-Sabater, J., Nicolas, J., Peubey, C., Radu, R., Schepers, D., Simmons, A., Soci, C., Abdalla, S., Abellan, X., Balsamo, G., Bechtold, P., Biavati, G., Bidlot, J., Bonavita, M., Chiara, G., Dahlgren, P., Dee, D., Diamantakis, M., Dragani, R., Flemming, J., Forbes, R., Fuentes, M., Geer, A., Haimberger, L., Healy, S., Hogan, R. J., Hólm, E., Janisková, M., Keeley, S., Laloyaux, P., Lopez, P., Lupu, C., Radnoti, G., Rosnay, P., Rozum,

I., Vamborg, F., Villaume, S., and Thépaut, J.-N.: The ERA5 Global Reanalysis, Q J R Meteorol Soc, https://doi.org/10.1002/qj.3803, 2020.

Hersbach, H., Bell, B., Berrisford, P., Horányi, A., Sabater, J. M., Nicolas, J., Radu, R., Schepers, D., Simmons, A., Soci, C., and Dee, D.: Global reanalysis: goodbye ERA-Interim, hello ERA5, https://www.ecmwf.int/en/newsletter/159/meteorology/global-reanalysis-goodbye-era-interim-hello-era5, last access: 15 June 2022, 2019.

Holko, L., Gorbachova, L., and Kostka, Z.: Snow Hydrology in Central Europe, Geography Compass, 5, 200–218, https://doi.org/10.1111/j.1749-8198.2011.00412.x, 2011.

Homan, J. W. and Kane, D. L.: Arctic snow distribution patterns at the watershed scale, Hydrology Research, 46, 507–520, https://doi.org/10.2166/nh.2014.024, 2015.

Howat, I., Negrete, A., and Smith, B.: MEaSUREs Greenland Ice Mapping Project (GIMP) Digital Elevation Model, Version 1. gimpdem5_5_v01.1., NASA National Snow and Ice Data Center Distributed Active Archive Center., https://doi.org/10.5067/NV34YUIXLP9W, last access: 29 July 2020, 2015.

Howat, I. M., Negrete, A., and Smith, B. E.: The Greenland Ice Mapping Project (GIMP) land classification and surface elevation data sets, The Cryosphere, 8, 1509–1518, https://doi.org/10.5194/tc-8-1509-2014, 2014.

Hunke, E. C. and Dukowicz, J. K.: An Elastic–Viscous–Plastic Model for Sea Ice Dynamics, J. Phys. Oceanogr., 27, 1849–1867, https://doi.org/10.1175/1520-0485(1997)027<1849:AEVPMF>2.0.CO;2, 1997.

Hunke, E., Allard, R., Bailey, D. A., Blain, P., Craig, A., Dupont, F., DuVivier, A., Grumbine, R., Hebert, D., Holland, M., Jeffery, N., Lemieux, J.-F., Osinski, R., Rasmussen, T., Ribergaard, M., and Roberts, A.: CICE-Consortium/Icepack: Icepack 1.3.2, 2022.

Hunke, E. C., Lipscomb, W. H., and Turner, A. K.: Sea-ice models for climate study: retrospective and new directions, J. Glaciol., 56, 1162–1172, https://doi.org/10.3189/002214311796406095, 2010.

Intrieri, J. M. and Shupe, M. D.: Characteristics and Radiative Effects of Diamond Dust over the Western Arctic Ocean Region, Journal of Climate, 17, 2953–2960, https://doi.org/10.1175/1520-0442(2004)017<2953:CAREOD>2.0.CO;2, available at: https://journals.ametsoc.org/view/journals/clim/17/15/1520-0442_2004_017_2953_careod_2.0.co_2.xml, 2004.

IPCC: Climate change 2014: Synthesis report. Contribution of Working Groups I, II and III to the Fifth Assessment Report of the Intergovernmental Panel on Climate Change [Core Writing Team, Pachauri, R.K. and Meyer L.A. (eds.)], Intergovernmental Panel on Climate Change, Geneva, Switzerland, 151 pp., 2014.

Isotta, F. A., Frei, C., Weilguni, V., Perčec Tadić, M., Lassègues, P., Rudolf, B., Pavan, V., Cacciamani, C., Antolini, G., Ratto, S. M., Munari, M., Micheletti, S., Bonati, V., Lussana, C., Ronchi, C., Panettieri, E., Marigo, G., and Vertačnik, G.: The climate of daily precipitation in the Alps: development and analysis of a high-resolution grid dataset from pan-Alpine rain-gauge data, Int. J. Climatol., 34, 1657–1675, https://doi.org/10.1002/joc.3794, 2014.

Jacobi, H.-W., Domine, F., Simpson, W. R., Douglas, T. A., and Sturm, M.: Simulation of the specific surface area of snow using a one-dimensional physical snowpack model: implementation and evaluation for subarctic snow in Alaska, The Cryosphere, 4, 35–51, https://doi.org/10.5194/tc-4-35-2010, 2010.

Jacobi, H.-W., Obleitner, F., Da Costa, S., Ginot, P., Eleftheriadis, K., Aas, W., and Zanatta, M.: Deposition of ionic species and black carbon to the Arctic snowpack: combining snow pit observations with modeling, Atmos. Chem. Phys., 19, 10361–10377, https://doi.org/10.5194/acp-19-10361-2019, 2019.

Jafari, M., Sharma, V., and Lehning, M.: Convection of water vapour in snowpacks, J. Fluid Mech., 934, A38, https://doi.org/10.1017/jfm.2021.1146, available at: https://www.cambridge.org/core/journals/journal-of-fluid-mechanics/article/convection-of-water-vapour-in-snowpacks/9FFBA8DAE8DEBF41BE98E699115C66EB, 2022.

Jafari, M., Gouttevin, I., Couttet, M., Wever, N., Michel, A., Sharma, V., Rossmann, L., Maass, N., Nicolaus, M., and Lehning, M.: The Impact of Diffusive Water Vapor Transport on Snow Profiles in Deep and Shallow Snow Covers and on Sea Ice, Front. Earth Sci., 8, 249, https://doi.org/10.3389/feart.2020.00249, available at: https://www.frontiersin.org/articles/10.3389/feart.2020.00249/full, 2020.

Jennings, K. S., Winchell, T. S., Livneh, B., and Molotch, N. P.: Spatial variation of the rain-snow temperature threshold across the Northern Hemisphere, Nature communications, 9, 1148, https://doi.org/10.1038/s41467-018-03629-7, 2018.

Jiménez Aquino, J. I. and Varela, J. R.: Two stream approximation to radiative transfer equation: An alternative method of solution, Revista Mexicana de Fisica, 51, 2005.

Johnson, J. B. and Schneebeli, M.: Characterizing the microstructural and micromechanical properties of snow, Cold Regions Science and Technology, 30, 91–100, https://doi.org/10.1016/S0165-232X(99)00013-0, available at: https://www.sciencedirect.com/science/article/pii/S0165232X99000130, 1999.

Joos, F. and Spahni, R.: Rates of change in natural and anthropogenic radiative forcing over the past 20,000 years, Proceedings of the National Academy of Sciences of the United States of America, 105, 1425–1430, https://doi.org/10.1073/pnas.0707386105, 2008.

Jordan, R. E., Andreas, E. L., and Makshtas, A. P.: Heat budget of snow-covered sea ice at North Pole 4, J. Geophys. Res., 104, 7785–7806, https://doi.org/10.1029/1999JC900011, 1999.

Judson, A. and Doesken, N.: Density of Freshly Fallen Snow in the Central Rocky Mountains, Bull. Amer. Meteor. Soc., 81, 1577–1587, https://doi.org/10.1175/1520-0477(2000)081<1577:DOFFSI>2.3.CO;2, 2000.

Jutila, A., Hendricks, S., Ricker, R., Albedyll, L. von, Krumpen, T., and Haas, C.: Retrieval and parameterisation of sea-ice bulk density from airborne multi-sensor measurements, The Cryosphere, 16, 259–275, https://doi.org/10.5194/tc-16-259-2022, 2022.

Katich, J. M., Perring, A. E., and Schwarz, J. P.: Optimized detection of particulates from liquid samples in the aerosol phase: Focus on black carbon, Aerosol Science and Technology, 51, 543–553, https://doi.org/10.1080/02786826.2017.1280597, 2017.

Keegan, K. M., Albert, M. R., McConnell, J. R., and Baker, I.: Climate change and forest fires synergistically drive widespread melt events of the Greenland Ice Sheet, Proceedings of the National Academy of Sciences of the United States of America, 111, 7964–7967, https://doi.org/10.1073/pnas.1405397111, 2014.

Keenan, E., Wever, N., Dattler, M., Lenaerts, J. T. M., Medley, B., Kuipers Munneke, P., and Reijmer, C.: Physics-based SNOWPACK model improves representation of near-surface Antarctic snow and firn density, The Cryosphere, 15, 1065–1085, https://doi.org/10.5194/tc-15-1065-2021, 2021.

Kinar, N. J. and Pomeroy, J. W.: Measurement of the physical properties of the snowpack, Rev. Geophys., 53, 481–544, https://doi.org/10.1002/2015RG000481, 2015.

King, J., Howell, S., Brady, M., Toose, P., Derksen, C., Haas, C., and Beckers, J.: Local-scale variability of snow density on Arctic sea ice, The Cryosphere, 14, 4323–4339, https://doi.org/10.5194/tc-14-4323-2020, 2020.

Kipp & Zonen: CNR 4 Net Radiometer Instruction Manual, https://www.kippzonen.com/Download/354/Manual-CNR-4-Net-Radiometer-English-V2104, last access: 23 October 2022.

Kislov, A. V. and Matveeva, T. A.: Extreme wind speeds in the European sector of the Arctic, Russ. Meteorol. Hydrol., 41, 447–454, https://doi.org/10.3103/S1068373916070013, 2016.

Kokhanovsky, A. A. and Zege, E. P.: Scattering optics of snow, Appl. Opt., AO, 43, 1589–1602, https://doi.org/10.1364/AO.43.001589, 2004.

Koldunov, N. V., Köhl, A., Serra, N., and Stammer, D.: Sea ice assimilation into a coupled ocean–sea ice model using its adjoint, The Cryosphere, 11, 2265–2281, https://doi.org/10.5194/tc-11-2265-2017, 2017.

Køltzow, M., Schyberg, H., Støylen, E., and Yang, X.: Value of the Copernicus Arctic Regional Reanalysis (CARRA) in representing near-surface temperature and wind speed in the north-east European Arctic, 1, 41, https://doi.org/10.33265/polar.v41.8002, 2022.

Krampe, D., Kauker, F., Dumont, M., and Herber, A.: On the performance of the snow model Crocus driven by in situ and reanalysis data at Villum Research Station in northeast Greenland, The Cryosphere Discussions, https://doi.org/10.5194/tc-2021-100, 2021.

Laborde, M., Mertes, P., Zieger, P., Dommen, J., Baltensperger, U., and Gysel, M.: Sensitivity of the Single Particle Soot Photometer to different black carbon types, Atmos. Meas. Tech., 5, 1031–1043, https://doi.org/10.5194/amt-5-1031-2012, 2012.

Lackner, G., Domine, F., Nadeau, D. F., Parent, A.-C., Anctil, F., Lafaysse, M., and Dumont, M.: On the energy budget of a low-Arctic snowpack, The Cryosphere, 16, 127–142, https://doi.org/10.5194/tc-16-127-2022, 2022a.

Lackner, G., Domine, F., Nadeau, D. F., Lafaysse, M., and Dumont, M.: Snow properties at the forest–tundra ecotone: predominance of water vapor fluxes even in deep, moderately cold snowpacks, The Cryosphere, 16, 3357–3373, https://doi.org/10.5194/tc-16-3357-2022, 2022b.

Lafaysse, M., Cluzet, B., Dumont, M., Lejeune, Y., Vionnet, V., and Morin, S.: A multiphysical ensemble system of numerical snow modelling, The Cryosphere, 11, 1173–1198, https://doi.org/10.5194/tc-11-1173-2017, 2017.

Landrum, L. and Holland, M. M.: Extremes become routine in an emerging new Arctic, Nat. Clim. Chang., 10, 1108–1115, https://doi.org/10.1038/s41558-020-0892-z, 2020.

Langer, M., Westermann, S., Muster, S., Piel, K., and Boike, J.: The surface energy balance of a polygonal tundra site in northern Siberia – Part 1: Spring to fall, The Cryosphere, 5, 151–171, https://doi.org/10.5194/tc-5-151-2011, 2011a.

Langer, M., Westermann, S., Muster, S., Piel, K., and Boike, J.: The surface energy balance of a polygonal tundra site in northern Siberia – Part 2: Winter, The Cryosphere, 5, 509–524, https://doi.org/10.5194/tc-5-509-2011, 2011b.

Langlois, A., Kohn, J., Royer, A., Cliche, P., Brucker, L., Picard, G., Fily, M., Derksen, C., and Willemet, J. M.: Simulation of Snow Water Equivalent (SWE) Using Thermodynamic Snow Models in Québec, Canada, Journal of Hydrometeorology, 10, 1447–1463, https://doi.org/10.1175/2009JHM1154.1, 2009.

Lefebre, F., Fettweis, X., Gallee, H., van Ypersele, J.-P., Marbaix, P., Greuell, W., and Calanca, P.: Evaluation of a high-resolution regional climate simulation over Greenland, Clim Dyn, 25, 99–116, https://doi.org/10.1007/s00382-005-0005-8, 2005.

Lefebre, F., Gallée, H., van Ypersele, J.-P., and Greuell, W.: Modeling of snow and ice melt at ETH Camp (West Greenland): A study of surface albedo, J. Geophys. Res., 108, https://doi.org/10.1029/2001JD001160, 2003.

Legagneux, L., Cabanes, A., and Dominé, F.: Measurement of the specific surface area of 176 snow samples using methane adsorption at 77 K, J. Geophys. Res., 107, ACH 5-1-ACH 5-15, https://doi.org/10.1029/2001JD001016, 2002.

Lehning, M., Bartelt, P., Brown, B., Fierz, C., and Satyawali, P.: A physical SNOWPACK model for the Swiss avalanche warning, Cold Regions Science and Technology, 35, 147–167, https://doi.org/10.1016/S0165-232X(02)00073-3, 2002.

Leppänen, L. and Kontu, A.: Analysis of QualitySpec Trek Reflectance from Vertical Profiles of Taiga Snowpack, Geosciences, 8, 404, https://doi.org/10.3390/geosciences8110404, 2018.

Leppänen, L., Kontu, A., Hannula, H.-R., Sjöblom, H., and Pulliainen, J.: Sodankylä manual snow survey program, Geosci. Instrum. Method. Data Syst., 5, 163–179, https://doi.org/10.5194/gi-5-163-2016, 2016.

Libbrecht, K. G.: Toward a Comprehensive Model of Snow Crystal Growth Dynamics: 1. Overarching Features and Physical Origins, 2012.

Libois, Q.: Evolution des propriétés physiques de neige de surface sur le plateau Antarctique. Observations et modélisation du transfert radiatif et du métamorphisme, PhD thesis, Laboratoire de glaciologie et géophysique de l'environnement, Grenoble, 2014.

Libois, Q., Picard, G., Arnaud, L., Dumont, M., Lafaysse, M., Morin, S., and Lefebvre, E.: Summertime evolution of snow specific surface area close to the surface on the Antarctic Plateau, The Cryosphere, 9, 2383–2398, https://doi.org/10.5194/tc-9-2383-2015, 2015.

Libois, Q., Picard, G., France, J. L., Arnaud, L., Dumont, M., Carmagnola, C. M., and King, M. D.: Influence of grain shape on light penetration in snow, The Cryosphere, 7, 1803–1818, https://doi.org/10.5194/tc-7-1803-2013, 2013.

Libois, Q., Picard, G., Arnaud, L., Morin, S., and Brun, E.: Modeling the impact of snow drift on the decameter-scale variability of snow properties on the Antarctic Plateau, J. Geophys. Res. Atmos., 119, 11,662-11,681, https://doi.org/10.1002/2014JD022361, 2014.

Lim, S., Faïn, X., Zanatta, M., Cozic, J., Jaffrezo, J.-L., Ginot, P., and Laj, P.: Refractory black carbon mass concentrations in snow and ice: method evaluation and inter-comparison with elemental carbon measurement, Atmos. Meas. Tech., 7, 3307–3324, https://doi.org/10.5194/amt-7-3307-2014, 2014.

Lin, G., Penner, J. E., Flanner, M. G., Sillman, S., Xu, L., and Zhou, C.: Radiative forcing of organic aerosol in the atmosphere and on snow: Effects of SOA and brown carbon, J. Geophys. Res. Atmos., 119, 7453–7476, https://doi.org/10.1002/2013jd021186, 2014.

Liston, G. E. and Sturm, M.: The role of winter sublimation in the Arctic moisture budget, Hydrology Research, 35, 325–334, https://doi.org/10.2166/nh.2004.0024, 2004.

Liston, G. E. and Hiemstra, C. A.: The Changing Cryosphere: Pan-Arctic Snow Trends (1979–2009), Journal of Climate, 24, 5691–5712, https://doi.org/10.1175/JCLI-D-11-00081.1, 2011.

Liston, G. E. and Elder, K.: A Distributed Snow-Evolution Modeling System (SnowModel), J. Hydrometeor, 7, 1259–1276, https://doi.org/10.1175/JHM548.1, 2006.

Liston, G. E. and Sturm, M.: Winter Precipitation Patterns in Arctic Alaska Determined from a Blowing-Snow Model and Snow-Depth Observations, J. Hydrometeor, 3, 646–659, https://doi.org/10.1175/1525-7541(2002)003<0646:WPPIAA>2.0.CO;2, 2002.

Liston, G. E. and Sturm, M.: A snow-transport model for complex terrain, Journal of Glaciology, 44, 498–516, https://doi.org/10.1017/s0022143000002021, 1998.

Liston, G. E., Perham, C. J., Shideler, R. T., and Cheuvront, A. N.: Modeling snowdrift habitat for polar bear dens, Ecological Modelling, 320, 114–134, https://doi.org/10.1016/j.ecolmodel.2015.09.010, 2016.

Liston, G. E., Haehnel, R. B., Sturm, M., Hiemstra, C. A., Berezovskaya, S., and Tabler, R. D.: Simulating complex snow distributions in windy environments using SnowTran-3D, J. Glaciol., 53, 241–256, https://doi.org/10.3189/172756507782202865, 2007.

Loe, L. E., Liston, G. E., Pigeon, G., Barker, K., Horvitz, N., Stien, A., Forchhammer, M., Getz, W. M., Irvine, R. J., Lee, A., Movik, L. K., Mysterud, A., Pedersen, Å. Ø., Reinking, A. K., Ropstad, E., Trondrud, L. M., Tveraa, T., Veiberg, V., Hansen, B. B., and Albon, S. D.: The neglected season: Warmer autumns counteract harsher winters and promote population growth in Arctic reindeer, Global Change Biology, 27, 993–1002, https://doi.org/10.1111/gcb.15458, 2020.

Loew, A., Bell, W., Brocca, L., Bulgin, C. E., Burdanowitz, J., Calbet, X., Donner, R. V., Ghent, D., Gruber, A., Kaminski, T., Kinzel, J., Klepp, C., Lambert, J.-C., Schaepman-Strub, G., Schröder, M., and Verhoelst, T.: Validation practices for satellite-based Earth observation data across communities, Rev. Geophys., 55, 779–817, https://doi.org/10.1002/2017RG000562, 2017.

Ludwig, V., Spreen, G., Haas, C., Istomina, L., Kauker, F., and Murashkin, D.: The 2018 North Greenland polynya observed by a newly introduced merged optical and passive microwave sea-ice concentration dataset, The Cryosphere, 13, 2051–2073, https://doi.org/10.5194/tc-13-2051-2019, 2019.

Luijting, H., Vikhamar-Schuler, D., Aspelien, T., Bakketun, Å., and Homleid, M.: Forcing the SURFEX/Crocus snow model with combined hourly meteorological forecasts and gridded observations in southern Norway, The Cryosphere, 12, 2123–2145, https://doi.org/10.5194/tc-12-2123-2018, 2018.

Magnus, G.: Versuche über die Spannkräfte des Wasserdampfs, Annalen der Physik, 137, 225–247, 1844.

Martin, J. and Schneebeli, M.: Impact of the sampling procedure on the specific surface area of snow measurements with the IceCube, EGUsphere, 1–13, https://doi.org/10.5194/egusphere-2022-501, 2022.

Maslanik, J. and Stroeve, J.: Near-Real-Time DMSP SSMIS Daily Polar Gridded Sea Ice Concentrations, Version 1. 2018-03-15., https://doi.org/10.5067/U8C09DWVX9LM, https://nsidc.org/data/NSIDC-0081/versions/1, last access: 24 February 2021.

Matiu, M., Crespi, A., Bertoldi, G., Carmagnola, C. M., Marty, C., Morin, S., Schöner, W., Cat Berro, D., Chiogna, G., Gregorio, L. de, Kotlarski, S., Majone, B., Resch, G., Terzago, S., Valt, M., Beozzo, W., Cianfarra, P., Gouttevin, I., Marcolini, G., Notarnicola, C., Petitta, M., Scherrer, S. C., Strasser, U., Winkler, M., Zebisch, M., Cicogna, A., Cremonini, R., Debernardi, A., Faletto, M., Gaddo, M., Giovannini, L., Mercalli, L., Soubeyroux, J.-M., Sušnik, A., Trenti, A., Urbani, S., and Weilguni, V.: Observed snow depth trends in the European Alps: 1971 to 2019, The Cryosphere, 15, 1343–1382, https://doi.org/10.5194/tc-15-1343-2021, 2021.

McConnell, J. R., Edwards, R., Kok, G. L., Flanner, M. G., Zender, C. S., Saltzman, E. S., Banta, J. R., Pasteris, D. R., Carter, M. M., and Kahl, J. D. W.: 20th-century industrial black carbon emissions altered Arctic climate forcing, Science, 317, 1381–1384, https://doi.org/10.1126/science.1144856, 2007.

Mei, L., Rozanov, V., Jäkel, E., Cheng, X., Vountas, M., and Burrows, J. P.: The retrieval of snow properties from SLSTR Sentinel-3 – Part 2: Results and validation, The Cryosphere, 15, 2781–2802, https://doi.org/10.5194/tc-15-2781-2021, 2021.

Meister, R.: Density of New Snow and its Dependence on Air Temperature and Wind. Correction of Precipitation Measurements, Zürcher Geographische Schriften, 1985.

Minola, L., Zhang, F., Azorin-Molina, C., Pirooz, A. A. S., Flay, R. G. J., Hersbach, H., and Chen, D.: Near-surface mean and gust wind speeds in ERA5 across Sweden: towards an improved gust parametrization, Clim Dyn, 55, 887–907, https://doi.org/10.1007/s00382-020-05302-6, 2020.

Mohammadzadeh Khani, H., Kinnard, C., and Lévesque, E.: Historical Trends and Projections of Snow Cover over the High Arctic: A Review, Water, 14, 587, https://doi.org/10.3390/w14040587, 2022.

Moore, G. W. K., Schweiger, A., Zhang, J., and Steele, M.: What Caused the Remarkable February 2018 North Greenland Polynya?, Geophysical Research Letters, 45, 13,342-13,350, https://doi.org/10.1029/2018GL080902, 2018.

Moore, G. W. K., Bromwich, D. H., Wilson, A. B., Renfrew, I., and Bai, L.: Arctic System Reanalysis improvements in topographically forced winds near Greenland, Q.J.R. Meteorol. Soc., 142, 2033–2045, https://doi.org/10.1002/qj.2798, 2016.

Mori, T., Kondo, Y., Ohata, S., Zhao, Y., Sinha, P. R., Oshima, N., Matsui, H., Moteki, N., and Koike, M.: Seasonal Variation of Wet Deposition of Black Carbon in Arctic Alaska, Journal of Geophysical Research: Atmospheres, 125, https://doi.org/10.1029/2019JD032240, 2020.

Mori, T., Goto-Azuma, K., Kondo, Y., Ogawa-Tsukagawa, Y., Miura, K., Hirabayashi, M., Oshima, N., Koike, M., Kupiainen, K., Moteki, N., Ohata, S., Sinha, P. R., Sugiura, K., Aoki, T., Schneebeli, M., Steffen, K., Sato, A., Tsushima, A., Makarov, V., Omiya, S., Sugimoto, A., Takano, S., and Nagatsuka, N.: Black Carbon and Inorganic Aerosols in Arctic Snowpack, Journal of Geophysical Research: Atmospheres, 124, 13325–13356, https://doi.org/10.1029/2019JD030623, 2019.

Mori, T., Moteki, N., Ohata, S., Koike, M., Goto-Azuma, K., Miyazaki, Y., and Kondo, Y.: Improved technique for measuring the size distribution of black carbon particles in liquid water, Aerosol Science and Technology, 50, 242–254, https://doi.org/10.1080/02786826.2016.1147644, 2016.

Moriana-Armendariz, M., Nilsen, L., and Cooper, E. J.: Natural variation in snow depth and snow melt timing in the High Arctic have implications for soil and plant nutrient status and vegetation composition, Arctic Science, 1–19, https://doi.org/10.1139/as-2020-0025, 2022.

Morin, S., Horton, S., Techel, F., Bavay, M., Coléou, C., Fierz, C., Gobiet, A., Hagenmuller, P., Lafaysse, M., Ližar, M., Mitterer, C., Monti, F., Müller, K., Olefs, M., Snook, J. S., van Herwijnen, A., and Vionnet, V.: Application of physical snowpack models in support of operational avalanche hazard forecasting: A status report on current implementations and prospects for the future, 170, 2020.

Mortimer, C., Mudryk, L., Derksen, C., Luojus, K., Brown, R., Kelly, R., and Tedesco, M.: Evaluation of long-term Northern Hemisphere snow water equivalent products, The Cryosphere, 14, 1579–1594, https://doi.org/10.5194/tc-14-1579-2020, 2020.

Mott, R., Vionnet, V., and Grünewald, T.: The Seasonal Snow Cover Dynamics: Review on Wind-Driven Coupling Processes, Front. Earth Sci., 6, 197, https://doi.org/10.3389/feart.2018.00197, 2018.

Mudryk, L. R., Derksen, C., Howell, S., Laliberté, F., Thackeray, C., Sospedra-Alfonso, R., Vionnet, V., Kushner, P. J., and Brown, R.: Canadian snow and sea ice: historical trends and projections, The Cryosphere, 12, 1157–1176, https://doi.org/10.5194/tc-12-1157-2018, 2018.

Nakaya, U.: Snow Crystals: Natural and Artificial, Harvard University Press, 1954.

Nakoudi, K., Ritter, C., Böckmann, C., Kunkel, D., Eppers, O., Rozanov, V., Mei, L., Pefanis, V., Jäkel, E., Herber, A., Maturilli, M., and Neuber, R.: Does the Intra-Arctic Modification of Long-Range Transported Aerosol Affect the Local Radiative Budget? (A Case Study), Remote Sensing, 12, 2112, https://doi.org/10.3390/rs12132112, 2020.

National Snow and Ice Data Center: What is the Arctic, https://nsidc.org/cryosphere/arctic-meteorology/arctic.html, last access: 9 May 2022, 2020.

Nguyen, Q. T., Skov, H., Sørensen, L. L., Jensen, B. J., Grube, A. G., Massling, A., Glasius, M., and Nøjgaard, J. K.: Source apportionment of particles at Station Nord, North East Greenland during 2008–2010 using COPREM and PMF analysis, Atmos. Chem. Phys., 13, 35–49, https://doi.org/10.5194/acp-13-35-2013, 2013.

Nicolaus, M., Perovich, D. K., Spreen, G., Granskog, M. A., Albedyll, L. von, Angelopoulos, M., Anhaus, P., Arndt, S., Belter, H. J., Bessonov, V., Birnbaum, G., Brauchle, J., Calmer, R., Cardellach, E., Cheng, B., Clemens-Sewall, D., Dadic, R., Damm, E., Boer, G. de, Demir, O., Dethloff, K., Divine, D. V., Fong, A. A., Fons, S., Frey, M. M., Fuchs, N., Gabarró, C., Gerland, S., Goessling, H. F., Gradinger, R., Haapala, J., Haas, C., Hamilton, J., Hannula, H.-R., Hendricks, S., Herber, A., Heuzé, C., Hoppmann, M., Høyland, K. V., Huntemann, M., Hutchings, J. K., Hwang, B., Itkin, P., Jacobi, H.-W., Jaggi, M., Jutila, A., Kaleschke, L., Katlein, C., Kolabutin, N., Krampe, D., Kristensen, S. S., Krumpen, T., Kurtz, N., Lampert, A., Lange, B. A., Lei, R., Light, B., Linhardt, F., Liston, G. E., Loose, B., Macfarlane, A. R., Mahmud, M., Matero, I. O., Maus, S., Morgenstern, A., Naderpour, R., Nandan, V., Niubom, A., Oggier, M., Oppelt, N., Pätzold, F., Perron, C., Petrovsky, T., Pirazzini, R., Polashenski, C., Rabe, B., Raphael, I. A., Regnery, J., Rex, M., Ricker, R., Riemann-Campe, K., Rinke, A., Rohde, J., Salganik, E., Scharien, R. K., Schiller, M., Schneebeli, M., Semmling, M., Shimanchuk, E., Shupe, M. D., Smith, M. M., Smolyanitsky, V., Sokolov, V., Stanton, T., Stroeve, J., Thielke, L., Timofeeva, A., Tonboe, R. T., Tavri, A., Tsamados, M., Wagner, D. N., Watkins, D., Webster, M., and Wendisch, M.: Overview of the MOSAiC expedition, Elementa: Science of the Anthropocene, 10, https://doi.org/10.1525/elementa.2021.000046, 2022.

Nitu, R., Roulet, Y.-A., Wolff, M., Earle, M., A.Reverdin, Smith, C., S.Morin, Rasmussen, R., K.Wong, J.Alastruè, L.Arnold, Baker, B., Buisan, S., Collado Aceituno, J. L., Colli, M., B.Collins, Gaydos, A., Hannula, H.-R., J.Hoover, and Yamashita, K.: WMO Solid Precipitation Intercomparison Experiment (SPICE), 2018.

Niwano, M., Aoki, T., Kuchiki, K., Hosaka, M., and Kodama, Y.: Snow Metamorphism and Albedo Process (SMAP) model for climate studies: Model validation using meteorological and snow impurity data measured at Sapporo, Japan, J. Geophys. ;Res., 117, https://doi.org/10.1029/2011JF002239, 2012.

Norwegian Meteorological Institute: About AROME-Arctic, https://www.met.no/en/projects/The-weather-model-AROME-Arctic/about, last access: 14 June 2022, 2019.

Ohata, S., Koike, M., Yoshida, A., Moteki, N., Adachi, K., Oshima, N., Matsui, H., Eppers, O., Bozem, H., Zanatta, M., and Herber, A. B.: Arctic black carbon during PAMARCMiP 2018 and previous aircraft experiments in spring, Atmos. Chem. Phys., 21, 15861–15881, https://doi.org/10.5194/acp-21-15861-2021, 2021.

Overland, J., Dunlea, E., Box, J. E., Corell, R., Forsius, M., Kattsov, V., Olsen, M. S., Pawlak, J., Reiersen, L.-O., and Wang, M.: The urgency of Arctic change, Polar Science, 21, 6–13, https://doi.org/10.1016/j.polar.2018.11.008, 2019.

Overland, J. E., Wang, M., Walsh, J. E., and Stroeve, J. C.: Future Arctic climate changes: Adaptation and mitigation time scales, Earth's Future, 2, 68–74, https://doi.org/10.1002/2013EF000162, 2014.

Painter, T. H., Bryant, A. C., and Skiles, S. M.: Radiative forcing by light absorbing impurities in snow from MODIS surface reflectance data, Geophys. Res. Lett., 39, https://doi.org/10.1029/2012GL052457, 2012.

Parker, W. S.: Reanalyses and Observations: What's the Difference?, Bulletin of the American Meteorological Society, 97, 1565–1572, https://doi.org/10.1175/BAMS-D-14-00226.1, 2016.

Pedersen, S. H., Tamstorf, M. P., Abermann, J., Westergaard-Nielsen, A., Lund, M., Skov, K., Sigsgaard, C., Mylius, M. R., Hansen, B. U., and Liston, G. E.: Spatiotemporal characteristics of seasonal snow cover in Northeast Greenland from in situ observations, Arctic, Antarctic, and Alpine Research, 48, 653–671, https://doi.org/10.1657/AAAR0016-028, 2016a.

Pedersen, S. H., Tamstorf, M. P., Abermann, J., Westergaard-Nielsen, A., Lund, M., Skov, K., Sigsgaard, C., Mylius, M. R., Hansen, B. U., Liston, G. E., and Schmidt, N. M.: Spatiotemporal Characteristics of Seasonal Snow Cover in Northeast Greenland from in Situ Observations, Arctic, Antarctic, and Alpine Research, 48, 653–671, https://doi.org/10.1657/AAAR0016-028, 2016b.

Pedersen, S. H., Liston, G. E., Tamstorf, M. P., Westergaard-Nielsen, A., and Schmidt, N. M.: Quantifying Episodic Snowmelt Events in Arctic Ecosystems, Ecosystems, 18, 839–856, https://doi.org/10.1007/s10021-015-9867-8, 2015.

Perovich, D. K.: The optical properties of sea ice, Cold Regions Research and Engineering Laboratory (U.S.); Engineer Research and Development Center (U.S.), 1996.

Picard, G., Dumont, M., Lamare, M., Tuzet, F., Larue, F., Pirazzini, R., and Arnaud, L.: Spectral albedo measurements over snow-covered slopes: theory and slope effect corrections, The Cryosphere, 14, 1497–1517, https://doi.org/10.5194/tc-14-1497-2020, 2020.

Pithan, F. and Mauritsen, T.: Arctic amplification dominated by temperature feedbacks in contemporary climate models, Nature Geosci, 7, 181–184, https://doi.org/10.1038/ngeo2071, 2014.

Polashenski, C. M., Dibb, J. E., Flanner, M. G., Chen, J. Y., Courville, Z. R., Lai, A. M., Schauer, J. J., Shafer, M. M., and Bergin, M.: Neither dust nor black carbon causing apparent albedo decline in Greenland's dry snow zone: Implications for MODIS C5 surface reflectance, Geophys. Res. Lett., 42, 9319–9327, https://doi.org/10.1002/2015GL065912, 2015.

Pomeroy, J. W., Marsh, P., and Gray, D. M.: Application of a distributed blowing snow model to the Arctic, Hydrological Processes, 11, 1451–1464, https://doi.org/10.1002/(SICI)1099-1085(199709)11:11<1451:AID-HYP449>3.0.CO;2-Q, 1997.

Pomeroy, J., Essery, R., and Toth, B.: Implications of spatial distributions of snow mass and melt rate for snow-cover depletion: observations in a subarctic mountain catchment, Annals of Glaciology, 38, 195–201, https://doi.org/10.3189/172756404781814744, 2004.

Pomeroy, J. W. and Gray, D. M.: Snowcover accumulation, relocation and management, National Hydrology Research Institute Saskatoon, Sask., Canada, 1995.

Proksch, M., Rutter, N., Fierz, C., and Schneebeli, M.: Intercomparison of snow density measurements: bias, precision, and vertical resolution, The Cryosphere, 10, 371–384, https://doi.org/10.5194/tc-10-371-2016, 2016.

Proksch, M., Löwe, H., and Schneebeli, M.: Density, specific surface area, and correlation length of snow measured by high-resolution penetrometry, J. Geophys. Res. Earth Surf., 120, 346–362, https://doi.org/10.1002/2014JF003266, 2015.

Przybylak, R. and Wyszyński, P.: Air temperature changes in the Arctic in the period 1951–2015 in the light of observational and reanalysis data, Theor Appl Climatol, 139, 75–94, https://doi.org/10.1007/s00704-019-02952-3, 2020.

Pulliainen, J., Luojus, K., Derksen, C., Mudryk, L., Lemmetyinen, J., Salminen, M., Ikonen, J., Takala, M., Cohen, J., Smolander, T., and Norberg, J.: Patterns and trends of Northern Hemisphere snow mass from 1980 to 2018, Nature, 581, 294–298, https://doi.org/10.1038/s41586-020-2258-0, 2020.

Rantanen, M., Karpechko, A. Y., Lipponen, A., Nordling, K., Hyvärinen, O., Ruosteenoja, K., Vihma, T., and Laaksonen, A.: The Arctic has warmed nearly four times faster than the globe since 1979, Commun Earth Environ, 3, 1–10, https://doi.org/10.1038/s43247-022-00498-3, available at: https://www.nature.com/articles/s43247-022-00498-3, 2022.

Rasch, M., Frandsen, E. R., Skov, H., and Hansen, J. L.: Site Manual. Villum Research Station. Station Nord. Greenland, https://villumresearchstation.dk/fileadmin/villumresearchstation/Generelle/SITE_MANUAL.pdf, last access: 28 May 2020, 2016.

Rauthe, M., Steiner, H., Riediger, U., Mazurkiewicz, A., and Gratzki, A.: A Central European precipitation climatology – Part I: Generation and validation of a high-resolution gridded daily data set (HYRAS), metz, 22, 235–256, https://doi.org/10.1127/0941-2948/2013/0436, 2013.

Rissanen, T., Niittynen, P., Soininen, J., and Luoto, M.: Snow information is required in subcontinental scale predictions of mountain plant distributions, Global Ecol. Biogeogr., 30, 1502–1513, https://doi.org/10.1111/geb.13315, 2021.

Roberts, A. F., Hunke, E. C., Allard, R., Bailey, D. A., Craig, A. P., Lemieux, J.-F., and Turner, M. D.: Quality control for community-based sea-ice model development, Philosophical transactions. Series A, Mathematical, physical, and engineering sciences, 376, https://doi.org/10.1098/rsta.2017.0344, 2018.

Royer, A., Picard, G., Vargel, C., Langlois, A., Gouttevin, I., and Dumont, M.: Improved Simulation of Arctic Circumpolar Land Area Snow Properties and Soil Temperatures, Front. Earth Sci., 9, 515, https://doi.org/10.3389/feart.2021.685140, 2021.

Sato, T., Kosugi, K., Mochizuki, S., and Nemoto, M.: Wind speed dependences of fracture and accumulation of snowflakes on snow surface, Cold Regions Science and Technology, 51, 229–239, https://doi.org/10.1016/j.coldregions.2007.05.004, 2008.

Sauter, T. and Obleitner, F.: Assessing the uncertainty of glacier mass-balance simulations in the European Arctic based on variance decomposition, Geoscientific Model Development, 8, 3911–3928, https://doi.org/10.5194/gmd-8-3911-2015, 2015.

Schmidt, N. M., Ims, R. A., Høye, T. T., Gilg, O., Hansen, L. H., Hansen, J., Lund, M., Fuglei, E., Forchhammer, M. C., and Sittler, B.: Response of an arctic predator guild to collapsing lemming cycles, Proceedings. Biological sciences, 279, 4417–4422, https://doi.org/10.1098/rspb.2012.1490, 2012.

Schmidt, R. A.: Properties of blowing snow, Rev. Geophys., 20, 39, https://doi.org/10.1029/RG020i001p00039, 1982.

Schneebeli, M., Pielmeier, C., and Johnson, J. B.: Measuring snow microstructure and hardness using a high resolution penetrometer, Cold Regions Science and Technology, 30, 101–114, https://doi.org/10.1016/S0165-232X(99)00030-0, 1999.

Schulz, H., Zanatta, M., Bozem, H., Leaitch, W. R., Herber, A. B., Burkart, J., Willis, M. D., Kunkel, D., Hoor, P. M., Abbatt, J. P. D., and Gerdes, R.: High Arctic aircraft measurements characterising black carbon vertical variability in spring and summer, Atmos. Chem. Phys., 19, 2361–2384, https://doi.org/10.5194/acp-19-2361-2019, 2019.

Schürholt, K., Kowalski, J., and Löwe, H.: Elements of future snowpack modeling – Part 1: A physical instability arising from the nonlinear coupling of transport and phase changes, The Cryosphere, 16, 903–923, https://doi.org/10.5194/tc-16-903-2022, 2022.

Schwarz, J. P., Doherty, S. J., Li, F., Ruggiero, S. T., Tanner, C. E., Perring, A. E., Gao, R. S., and Fahey, D. W.: Assessing Single Particle Soot Photometer and Integrating Sphere/Integrating Sandwich Spectrophotometer measurement techniques for quantifying black carbon concentration in snow, Atmos. Meas. Tech., 5, 2581–2592, https://doi.org/10.5194/amt-5-2581-2012, 2012.

Schwarz, J. P., Spackman, J. R., Gao, R. S., Perring, A. E., Cross, E., Onasch, T. B., Ahern, A., Wrobel, W., Davidovits, P., Olfert, J., Dubey, M. K., Mazzoleni, C., and Fahey, D. W.: The Detection Efficiency of the Single Particle Soot Photometer, Aerosol Science and Technology, 44, 612–628, https://doi.org/10.1080/02786826.2010.481298, 2010.

Sedlacek, A.: Single-Particle Soot Photometer (SP2) Instrument Handbook, ARM Climate Research Facility, Pacific Northwest National Laboratory, Richland, WA, DOE Office of Science Atmospheric Radiation Measurement (ARM) Program (United States), DOE/SC-ARM-TR-169, 2017.

Seo, M., Kim, H.-C., Lee, K.-S., Seong, N.-H., Lee, E., Kim, J., and Han, K.-S.: Characteristics of the Reanalysis and Satellite-Based Surface Net Radiation Data in the Arctic, Journal of Sensors, 2020, 1–13, https://doi.org/10.1155/2020/8825870, 2020.

Serreze, M. C., Box, J. E., Barry, R. G., and Walsh, J. E.: Characteristics of Arctic synoptic activity, 1952-1989, Meteorl. Atmos. Phys., 51, 147–164, https://doi.org/10.1007/BF01030491, 1993.

Sexstone, G. A., Clow, D. W., Stannard, D. I., and Fassnacht, S. R.: Comparison of methods for quantifying surface sublimation over seasonally snow-covered terrain, Hydrol. Process., 30, 3373–3389, https://doi.org/10.1002/hyp.10864, 2016.

Shapiro, L. H., Johnson, J. B., Sturm, M., and Blaisdell, G. L.: Snow mechanics review of the state of knowledge and applications, CRREL report 97-3, US Arcmy Corps Engineers, Hanover, 1997.

Simson, A., Löwe, H., and Kowalski, J.: Elements of future snowpack modeling – Part 2: A modular and extendable Eulerian–Lagrangian numerical scheme for coupled transport, phase changes and settling processes, The Cryosphere, 15, 5423–5445, https://doi.org/10.5194/tc-15-5423-2021, 2021.

Sinha, P. R., Kondo, Y., Goto-Azuma, K., Tsukagawa, Y., Fukuda, K., Koike, M., Ohata, S., Moteki, N., Mori, T., Oshima, N., Førland, E. J., Irwin, M., Gallet, J.-C., and Pedersen, C. A.: Seasonal Progression of the Deposition of Black Carbon by Snowfall at Ny-Ålesund, Spitsbergen, J. Geophys. Res. Atmos., 123, 997–1016, https://doi.org/10.1002/2017JD028027, 2018.

Sommer, C. G., Fierz, C., and Lehning, M. (Eds.): Wind slab formation: Will new experiments improve implementations in snow-cover models?, 2016.

Sommerfeld, R. A. and LaChapelle, E.: The Classification of Snow Metamorphism, Journal of Glaciology, 9, 3–18, https://doi.org/10.1017/s0022143000026757, 1970.

Spreen, G., Kaleschke, L., and Heygster, G.: Sea ice remote sensing using AMSR-E 89-GHz channels, J. Geophys. Res., 113, https://doi.org/10.1029/2005JC003384, 2008.

Steel, R. G. D. and Torrie, J. H.: Principles and Procedures of Statistics with Special Reference to Biological Sciences., McGraw-Hill, 1960.

Stiegler, C., Lund, M., Christensen, T. R., Mastepanov, M., and Lindroth, A.: Two years with extreme and little snowfall: effects on energy partitioning and surface energy exchange in a high-Arctic tundra ecosystem, The Cryosphere, 10, 1395–1413, https://doi.org/10.5194/tc-10-1395-2016, 2016.

Stohl, A.: Characteristics of atmospheric transport into the Arctic troposphere, J. Geophys. Res., 111, https://doi.org/10.1029/2005JD006888, 2006.

Stroeve, J. and Notz, D.: Changing state of Arctic sea ice across all seasons, Environ. Res. Lett., 13, 103001, https://doi.org/10.1088/1748-9326/aade56, 2018.

Stroeve, J., Nandan, V., Willatt, R., Tonboe, R., Hendricks, S., Ricker, R., Mead, J., Mallett, R., Huntemann, M., Itkin, P., Schneebeli, M., Krampe, D., Spreen, G., Wilkinson, J., Matero, I., Hoppmann, M., and Tsamados, M.: Surface-based Ku- and Ka-band polarimetric radar for sea ice studies, The Cryosphere, 14, 4405–4426, https://doi.org/10.5194/tc-14-4405-2020, 2020.

Stroeve, J., Box, J. E., Wang, Z., Schaaf, C., and Barrett, A.: Re-evaluation of MODIS MCD43 Greenland albedo accuracy and trends, Remote Sensing of Environment, 138, 199–214, https://doi.org/10.1016/j.rse.2013.07.023, 2013.

Stroeve, J., Nolin, A., and Steffen, K.: Comparison of AVHRR-derived and in situ surface albedo over the greenland ice sheet, Remote Sensing of Environment, 62, 262–276, https://doi.org/10.1016/S0034-4257(97)00107-7, 1997.

Sturm, M.: Changing snow and shrub conditions affect albedo with global implications, J. Geophys. Res., 110, https://doi.org/10.1029/2005JG000013, 2005.

Sturm, M. and Benson, C.: Scales of spatial heterogeneity for perennial and seasonal snow layers, Annals of Glaciology, 38, 253–260, https://doi.org/10.3189/172756404781815112, 2004.

Sturm, M. and Holmgren, J.: Differences in compaction behavior of three climate classes of snow, Annals of Glaciology, 26, 125–130, https://doi.org/10.1017/s0260305500014683, 1998.

Sturm, M. and Holmgren, J.: Effects of microtopography on texture, temperature and heat flow in Arctic and sub-Arctic snow, Ann. Glaciol., 19, 63–68, https://doi.org/10.3189/1994AoG19-1-63-68, 1994.

Sturm, M., Taras, B., Liston, G. E., Derksen, C., Jonas, T., and Lea, J.: Estimating Snow Water Equivalent Using Snow Depth Data and Climate Classes, Journal of Hydrometeorology, 11, 1380–1394, https://doi.org/10.1175/2010JHM1202.1, 2010.

Sturm, M., Holmgren, J., König, M., and Morris, K.: The thermal conductivity of seasonal snow, J. Glaciol., 43, 26–41, https://doi.org/10.3189/S0022143000002781, 1997.

Sumata, H., Kauker, F., Karcher, M., and Gerdes, R.: Covariance of Optimal Parameters of an Arctic Sea Ice–Ocean Model, Monthly Weather Review, 147, 2579–2602, https://doi.org/10.1175/MWR-D-18-0375.1, 2019.

Taillandier, A.-S., Domine, F., Simpson, W. R., Sturm, M., and Douglas, T. A.: Rate of decrease of the specific surface area of dry snow: Isothermal and temperature gradient conditions, J. Geophys. Res., 112, https://doi.org/10.1029/2006JF000514, 2007.

Talagrand, O.: Assimilation of Observations, an Introduction (gtSpecial IssueltData Assimilation in Meteology and Oceanography: Theory and Practice), Journal of the Meteorological Society of Japan, 75, 191–209, https://doi.org/10.2151/jmsj1965.75.1B_191, 1997.

Tedesco, M., Doherty, S., Fettweis, X., Alexander, P., Jeyaratnam, J., and Stroeve, J.: The darkening of the Greenland ice sheet: trends, drivers, and projections (1981–2100), The Cryosphere, 10, 477–496, https://doi.org/10.5194/tc-10-477-2016, 2016.

Thomas, J. L., Polashenski, C. M., Soja, A. J., Marelle, L., Casey, K. A., Choi, H. D., Raut, J.-C., Wiedinmyer, C., Emmons, L. K., Fast, J. D., Pelon, J., Law, K. S., Flanner, M. G., and Dibb, J. E.: Quantifying black carbon deposition over the Greenland ice sheet from forest fires in Canada, Geophysical Research Letters, 44, 7965–7974, https://doi.org/10.1002/2017GL073701, 2017.

Touzeau, A., Landais, A., Morin, S., Arnaud, L., and Picard, G.: Numerical experiments on vapor diffusion in polar snow and firn and its impact on isotopes using the multi-layer energy balance model Crocus in SURFEX v8.0, Geosci. Model Dev., 11, 2393–2418, https://doi.org/10.5194/gmd-11-2393-2018, 2018.

Tuzet, F., Dumont, M., Lafaysse, M., Picard, G., Arnaud, L., Voisin, D., Lejeune, Y., Charrois, L., Nabat, P., and Morin, S.: A multilayer physically based snowpack model simulating direct and indirect radiative impacts of light-absorbing impurities in snow, The Cryosphere, 11, 2633–2653, https://doi.org/10.5194/tc-11-2633-2017, 2017.

Tuzet, F., Dumont, M., Picard, G., Lamare, M., Voisin, D., Nabat, P., Lafaysse, M., Larue, F., Revuelto, J., and Arnaud, L.: Quantification of the radiative impact of light-absorbing particles during two contrasted snow seasons at Col du Lautaret (2058 m a.s.l., French Alps), The Cryosphere, 14, 4553–4579, https://doi.org/10.5194/tc-14-4553-2020, 2020.

Uotila, P., Goosse, H., Haines, K., Chevallier, M., Barthélemy, A., Bricaud, C., Carton, J., Fučkar, N., Garric, G., Iovino, D., Kauker, F., Korhonen, M., Lien, V. S., Marnela, M., Massonnet, F., Mignac, D., Peterson, K. A., Sadikni, R., Shi, L., Tietsche, S., Toyoda, T., Xie, J., and Zhang, Z.: An assessment of ten ocean reanalyses in the polar regions, Clim Dyn, 52, 1613–1650, https://doi.org/10.1007/s00382-018-4242-z, 2019.

Van Kampenhout, L., Lenaerts, J. T. M., Lipscomb, W. H., Sacks, W. J., Lawrence, D. M., Slater, A. G., and van den Broeke, M. R.: Improving the Representation of Polar Snow and Firn in the Community Earth System Model, J. Adv. Model. Earth Syst., 9, 2583–2600, https://doi.org/10.1002/2017MS000988, 2017.

Vavrus, S.: The role of terrestrial snow cover in the climate system, Clim Dyn, 29, 73–88, https://doi.org/10.1007/s00382-007-0226-0, 2007.

Viallon-Galinier, L., Hagenmuller, P., and Lafaysse, M.: Forcing and evaluating detailed snow cover models with stratigraphy observations, Cold Regions Science and Technology, 180, 103163, https://doi.org/10.1016/j.coldregions.2020.103163, 2020.

Villum Reserach Station: Meteorological Data, Asiaqmet, https://www2.dmu.dk/asiaqmet/Default.aspx, last access: 5 February 2021, 2021.

Vionnet, V., Martin, E., Masson, V., Guyomarc'h, G., Naaim-Bouvet, F., Prokop, A., Durand, Y., and Lac, C.: Simulation of wind-induced snow transport and sublimation in alpine terrain using a fully coupled snowpack/atmosphere model, The Cryosphere, 8, 395–415, https://doi.org/10.5194/tc-8-395-2014, 2014.

Vionnet, V., Guyomarc'h, G., Naaim Bouvet, F., Martin, E., Durand, Y., Bellot, H., Bel, C., and Puglièse, P.: Occurrence of blowing snow events at an alpine site over a 10-year period: Observations and modelling, Advances in Water Resources, 55, 53–63, https://doi.org/10.1016/j.advwatres.2012.05.004, 2013.

Vionnet, V., Brun, E., Morin, S., Boone, A., Faroux, S., Le Moigne, P., Martin, E., and Willemet, J.-M.: The detailed snowpack scheme Crocus and its implementation in SURFEX v7.2, Geosci. Model Dev., 5, 773–791, https://doi.org/10.5194/gmd-5-773-2012, 2012.

Wagner, D. N., Shupe, M. D., Cox, C., Persson, O. G., Uttal, T., Frey, M. M., Kirchgaessner, A., Schneebeli, M., Jaggi, M., Macfarlane, A. R., Itkin, P., Arndt, S., Hendricks, S., Krampe, D., Nicolaus, M., Ricker, R., Regnery, J., Kolabutin, N., Shimanshuck, E., Oggier, M., Raphael, I., Stroeve, J., and Lehning, M.: Snowfall and snow accumulation during the MOSAiC winter and spring seasons, The Cryosphere, 16, 2373–2402, https://doi.org/10.5194/tc-16-2373-2022, 2022.

Walden, V. P., Warren, S. G., and Tuttle, E.: Atmospheric Ice Crystals over the Antarctic Plateau in Winter, Journal of Applied Meteorology and Climatology, 42, 1391–1405, https://doi.org/10.1175/1520-0450(2003)042<1391:AICOTA>2.0.CO;2, available at: https://journals.ametsoc.org/view/journals/apme/42/10/1520-0450_2003_042_1391_aicota_2.0.co_2.xml, 2003.

Walsh, J. E.: Arctic Climate Change, Variability, and Extremes, in: Arctic Hydrology, Permafrost and Ecosystems, edited by: Yang, D., Springer International Publishing AG, Cham, 3–23, https://doi.org/10.1007/978-3-030-50930-9_1, 2021.

Wang, C., Graham, R. M., Wang, K., Gerland, S., and Granskog, M. A.: Comparison of ERA5 and ERA-Interim near-surface air temperature, snowfall and precipitation over Arctic sea ice: effects on sea ice thermodynamics and evolution, The Cryosphere, 13, 1661–1679, https://doi.org/10.5194/TC-13-1661-2019, 2019.

Wang, X., Doherty, S. J., and Huang, J.: Black carbon and other light-absorbing impurities in snow across Northern China, J. Geophys. Res. Atmos., 118, 1471–1492, https://doi.org/10.1029/2012JD018291, 2013.

Warren, S. G.: Impurities in Snow: Effects on Albedo and Snowmelt (Review), Ann. Glaciol., 5, 177–179, https://doi.org/10.3189/1984AoG5-1-177-179, 1984.

Warren, S. G.: Optical properties of snow, Rev. Geophys., 20, 67, https://doi.org/10.1029/RG020i001p00067, 1982.

Warren, S. G., Brandt, R. E., and Grenfell, T. C.: Visible and near-ultraviolet absorption spectrum of ice from transmission of solar radiation into snow, Appl. Opt., AO, 45, 5320–5334, https://doi.org/10.1364/AO.45.005320, 2006.

Warren, S. G., Rigor, I. G., Untersteiner, N., Radionov, V. F., Bryazgin, N. N., Aleksandrov, Y. I., and Colony, R.: Snow Depth on Arctic Sea Ice, J. Climate, 12, 1814–1829, https://doi.org/10.1175/1520-0442(1999)012<1814:SDOASI>2.0.CO;2, 1999.

Wendisch, M., Macke, A., Ehrlich, A., Lüpkes, C., Mech, M., Chechin, D., Dethloff, K., Velasco, C. B., Bozem, H., Brückner, M., Clemen, H.-C., Crewell, S., Donth, T., Dupuy, R., Ebell, K., Egerer, U., Engelmann, R., Engler, C., Eppers, O., Gehrmann, M., Gong, X., Gottschalk, M., Gourbeyre, C., Griesche, H., Hartmann, J., Hartmann, M., Heinold, B., Herber, A., Herrmann, H., Heygster, G., Hoor, P., Jafariserajehlou, S., Jäkel, E., Järvinen, E., Jourdan, O., Kästner, U., Kecorius, S., Knudsen, E. M., Köllner, F., Kretzschmar, J., Lelli, L., Leroy, D., Maturilli, M., Mei, L., Mertes, S., Mioche, G., Neuber, R., Nicolaus, M., Nomokonova, T., Notholt, J., Palm, M., van Pinxteren, M., Quaas, J., Richter, P., Ruiz-Donoso, E., Schäfer, M., Schmieder, K., Schnaiter, M., Schneider, J., Schwarzenböck, A., Seifert, P., Shupe, M. D., Siebert, H., Spreen, G., Stapf, J., Stratmann, F., Vogl, T., Welti, A., Wex, H., Wiedensohler, A., Zanatta, M., and Zeppenfeld, S.: The Arctic Cloud Puzzle: Using ACLOUD/PASCAL Multiplatform Observations to Unravel the Role of Clouds and Aerosol

Particles in Arctic Amplification, Bulletin of the American Meteorological Society, 100, 841–871, https://doi.org/10.1175/BAMS-D-18-0072.1, 2019.

Wendisch, M., Brückner, M., Burrows, J., Crewell, S., Dethloff, K., Ebell, K., Lüpkes, C., Macke, A., Notholt, J., Quaas, J., Rinke, A., and Tegen, I.: Understanding Causes and Effects of Rapid Warming in the Arctic, Eos, https://doi.org/10.1029/2017EO064803, 2017.

Westermann, S., Lüers, J., Langer, M., Piel, K., and Boike, J.: The annual surface energy budget of a high-arctic permafrost site on Svalbard, Norway, The Cryosphere, 3, 245–263, https://doi.org/10.5194/tc-3-245-2009, 2009.

Wever, N., Fierz, C., Mitterer, C., Hirashima, H., and Lehning, M.: Solving Richards Equation for snow improves snowpack meltwater runoff estimations in detailed multi-layer snowpack model, The Cryosphere, 8, 257–274, https://doi.org/10.5194/tc-8-257-2014, 2014.

Wever, N., Rossmann, L., Maaß, N., Leonard, K. C., Kaleschke, L., Nicolaus, M., and Lehning, M.: Version 1 of a sea ice module for the physics-based, detailed, multi-layer SNOWPACK model, Geosci. Model Dev., 13, 99–119, https://doi.org/10.5194/gmd-13-99-2020, 2020.

Willett, K. M., Jones, P. D., Gillett, N. P., and Thorne, P. W.: Recent Changes in Surface Humidity: Development of the HadCRUH Dataset, J. Climate, 21, 5364–5383, https://doi.org/10.1175/2008JCLI2274.1, 2008.

World Meteorological Organization: Blowing Snow, https://cloudatlas.wmo.int/en/blowing-snow.html, last access: 17 December 2021, 2021a.

World Meteorological Organization: Drifting Snow, https://cloudatlas.wmo.int/en/drifting-snow.html, last access: 17 December 2021, 2021b.

World Meteorological Organization: Atmospheric Deposition, https://public.wmo.int/en/our-mandate/focus-areas/environment/atmospheric-deposition, last access: 27 October 2022, 2019.

Yang, X., Palmason, B., Sattler, K., Thorsteinsson, S., Amstrup, B., Dahlbom, M., Hansen-Sass, B., Pagn Nielsen, K., and Petersen, G.: IGB, the upgrade to the joint operational HARMONIE by DMI and IMO in 2018., Aladin-Hirlam Newsletter, 11, 93–96, 2018.

Yang, Y., Fu, Y., Lin, Q., Jiang, F., Lian, X., Li, L., Wang, Z., Zhang, G., Bi, X., Wang, X., and Sheng, G.: Recent Advances in Quantifying Wet Scavenging Efficiency of Black Carbon Aerosol, Atmosphere, 10, 175, https://doi.org/10.3390/atmos10040175, 2019.

Yankee Environmental Systems: TPS_3100 Total Precipitation Sensor. Installation & User Guide Version 2.01, 2012.

Ye, H., Zhang, R., Shi, J., Huang, J., Warren, S. G., and Fu, Q.: Black carbon in seasonal snow across northern Xinjiang in northwestern China, Environ. Res. Lett., 7, 44002, https://doi.org/10.1088/1748-9326/7/4/044002, 2012.

Yen, Y.-C.: Review of Thermal Properties of Snow, Ice, and Sea Ice, U.S. Army, Corps of Engineers, Cold Regions Research and Engineering Laboratory, 1981.

Yu, B. and Gan Chowdhury, A.: Gust Factors and Turbulence Intensities for the Tropical Cyclone Environment, Journal of Applied Meteorology and Climatology, 48, 534–552, https://doi.org/10.1175/2008JAMC1906.1, 2009.

Zahn, M., Akperov, M., Rinke, A., Feser, F., and Mokhov, I. I.: Trends of Cyclone Characteristics in the Arctic and Their Patterns From Different Reanalysis Data, J. Geophys. ;Res., 123, 2737–2751, https://doi.org/10.1002/2017JD027439, 2018.

Zampieri, L., Kauker, F., Fröhle, J., Sumata, H., Hunke, E. C., and Goessling, H. F.: Impact of Sea-Ice Model Complexity on the Performance of an Unstructured-Mesh Sea-Ice/Ocean Model under Different Atmospheric Forcings, J. Adv. Model. Earth Syst., 13, https://doi.org/10.1029/2020MS002438, 2021.

Zanatta, M., Herber, A., Jurányi, Z., Eppers, O., Schneider, J., and Schwarz, J. P.: Technical note: Sea salt interference with black carbon quantification in snow samples using the single particle soot photometer, Atmos. Chem. Phys., 21, 9329–9342, https://doi.org/10.5194/acp-21-9329-2021, 2021.

Zuanon, N. (Ed.): IceCube, a portable and reliable instrument for snow specific surface area measurement in the field, 1020-1023, 2013.

Zweigel, R. B., Westermann, S., Nitzbon, J., Langer, M., Boike, J., Etzelmüller, B., and Vikhamar Schuler, T.: Simulating Snow Redistribution and its Effect on Ground Surface Temperature at a High-Arctic Site on Svalbard, J. Geophys. Res. Earth Surf., 126, https://doi.org/10.1029/2020JF005673, 2021.

Acknowledgements

There are many people to whom I would like express my thanks for supporting and accompanying me during the last years. First and foremost, I want to thank Frank Kauker and Andreas Herber for guiding me through the last years, for hours of intense discussions, honest feedback and invaluable support, not only professionally but also personally. I thank Christian Haas, Andreas Herber and Frank Kauker for making this dissertation possible.

I am also thankful to Olaf Eisen, who took me on as his PhD student, for reviewing my thesis and supporting me with constructive remarks together with Marie Dumont. I would also like to extend my sincere gratitude to my other PhD committee members: Christian Haas, Frank Kauker, Andreas Herber, Stefanie Arndt and Marco Zanatta, you gave me great advice and feedback for my work. Thank you Frank Kauker, Andreas Herber, Stefanie Arndt and Arttu Jutila for supporting me during the writing process of my dissertation.

I thank Christof Lüpkes and the Polar Meteorology Section for taking me on. I am thankful for the great graduate school POLMAR for offering so many useful courses and support with various questions. In particular, I want to thank the POLMAR Claudias Hanfland and Sprengel.

During my time as a PhD student, I have been extremely lucky to have the opportunity of taking part of one exceptional field expedition drifting with the research vessel Polarstern through the Arctic Ocean (MOSAiC). I am thankful for all the support, planning, and logistics work that enabled the realisation of the expedition. I am grateful for having such a great MOSAiC Leg2+ team, for all the experiences I was allowed to gain, the insides I got in various research fields and measurement methods, the great spirit and time we had together, and for meeting so many new friends and colleagues around the world. My special thanks goes to Martin Schneebeli who taught me how to measure the wonderful material called snow, Christian Katlein for the conversations we had and teaching me how to be your ROV-Co-Pilot, Marcus Huntemann for having an open ear, Christian Haas for being a great cruise leader, Arttu Jutila and all my friends of the Leg2+ team for sharing all these great memories and going through difficult times together.

Thank you to all former and current colleagues at the Sea Ice Physics section, especially my office mates Philipp Anhaus and Arttu Jutila, for the great working environment and the countless numbers of coffee breaks, pizzas and discussions about our work. My special thanks go to Arttu Jutila and Luisa von Albedyll. You are not only colleagues but became close friends and accompanied me also in difficult times. Thank you all for making my time at AWI a great time.

Lastly, I want to express my deepest gratitude to my friends and family, especially to Hanna and Christina, my grandparents, my mother, my brother, Helmut and Thomas. Danke für eure ständige Unterstützung, eure Ermunterungen und eure Geduld. Danke, dass ihr immer für mich da seid, auch wenn ihr zwischendurch ewig nichts von mir hört.